# MEASUREMENTS AND DATA ANALYSIS FROM A BALLOON-BORNE FOURIER TRANSFORM SPECTROMETER

by

Debra Wunch

A thesis submitted in conformity with the requirements
for the degree of Doctor of Philosophy
Graduate Department of Physics
University of Toronto

# Abstract

Measurements and Data Analysis from a
Balloon-Borne Fourier Transform Spectrometer

Debra Wunch

Doctor of Philosophy

Graduate Department of Physics

University of Toronto

2006

The Middle Atmosphere Nitrogen TRend Assessment (MANTRA) campaigns consist of a high-altitude balloon launch supported by a ground-based campaign. Campaigns were held in Vanscoy, SK, when stratospheric zonal winds change from easterly to westerly: a time of year called turnaround. An investigation of the climatology and predictability of turnaround is presented. The study determined that the timing of turnaround cannot be predicted from stratospheric zonal wind speeds earlier in the summer. The climatology showed that there is a launch window which contains August 26 through September 5, wherein stratospheric zonal wind speeds are low enough to facilitate a launch.

The University of Toronto's Fourier transform spectrometer (U of T FTS) was converted from a ground-based FTS to a balloon- and ground-based FTS through an extensive electronics and software redevelopment. Its functionality was shown by its successful flight on the MANTRA 2004 balloon payload, recording two spectra on each detector, and its ground-based data, recorded during the 2004 campaign. Its balloon and ground-based data were compared with other ground-based instruments on-site and the Microwave Limb Sounder (MLS) satellite instrument.

The U of T FTS participated in a ground-based intercomparison campaign in Toronto with the Toronto Atmospheric Observatory Fourier transform spectrometer (TAO-FTS) and the Portable Atmospheric Research Interferometric Spectrometer for the Infrared

(PARIS-IR). The resolutions of these three instruments are significantly different. The two lower-resolution instruments (PARIS-IR and the U of T FTS) were found to measure 4-day average total columns of $O_3$, HCl, $N_2O$ and $CH_4$ to within 3.5% of the TAO-FTS total columns. The largest errors were produced by the total column retrievals of the stratospheric species ($O_3$ and HCl). In order to achieve this 3.5% agreement for the stratospheric species, the instrument line shape of the U of T FTS and PARIS-IR instruments had to be taken into account. Much of the remaining error can be attributed to the averaging kernels of the lower-resolution instruments.

# Acknowledgements

There are many people to whom I am indebted, and whom I cannot possibly thank properly.

I would like to thank Jim Drummond for lending his support and expertise, and imparting upon me his enthusiasm for lab work. Many thanks are due to Kim Strong for her unwavering support and patience and for her dedication to the MANTRA campaigns and their unique and important role of training tomorrow's scientists.

I must also thank two people who have become important mentors: Tom McElroy and Ted Shepherd. They have both provided insightful discussions and have, at one point or another, kept me on the right track.

A special thank-you goes to Clive Midwinter. Despite his overwhelming expertise in the lab, he has always been happy to seriously consider my ideas and opinions. I cannot imagine a better teacher.

Experimental research cannot be done without adept technical support. I have been lucky to receive the help and expertise of Paul Chen, John Olson, Aaron Ullberg, Gus Melo, Barbara Chu, Jim Bean, Peter Hurley, the electrical engineers in PERC, and Gurmit Besla, Alvin Ffrench and the machinists in the U of T mechanical shop. Outside of the lab, I have been fortunate to have many FTS experts at my disposal: Ron Blatherwick, Pierre Fogal, Aldona Wiacek, Jeff Taylor, Dejian Fu and Kaley Walker.

Financial support for this work was provided by NSERC, the University of Toronto, Environment Canada, the Canadian Space Agency and the OGS. The FTS was kindly loaned to the University of Toronto by Hans Fast of Environment Canada. I would like to thank Annemarie Fraser for providing the U of T GBS and SAOZ data, and Bojan Bojkov for providing the MLS data.

Finally, I must thank my parents, Cheryl and my family for their continued support, despite my resistance to entering the "real world," my friends for making this time so difficult to leave, and Kevin, for keeping me firmly grounded through it all.

# Table of Contents

# List of Tables

# List of Figures

# Chapter 1

# Introduction

## 1.1 MANTRA

The stratospheric ozone layer absorbs biologically harmful ultraviolet radiation from the sun before it can reach the Earth [1]. Ozone is a greenhouse gas in both the stratosphere and troposphere, and because of its relatively short atmospheric lifetime (from days to weeks, compared with the longer lifetimes of other greenhouse gases) it is particularly sensitive to atmospheric conditions [2, pp. 43–44]. Any change in ozone, then, is of concern, and warrants investigation.

Global total column abundances of ozone were 3% lower over the 1997–2001 period than they were in the pre-1980 period. In the northern hemisphere mid-latitudes (35°N–60°N), total column abundances were 3% lower than the pre-1980 period whereas in the southern hemisphere mid-latitudes, total column abundances were 6% lower [3]. Chlorine (Cl) and nitrogen (N) chemistry play an important role in the destruction of ozone: radical Cl by its catalytic destruction of ozone and odd nitrogen ($NO_x$) for both its catalytic destruction of ozone and its control of Cl. It is therefore important to measure nitrogen compounds to investigate any changes in $NO_x$ concentrations or in $NO_x$ to inactive nitrogen ($NO_y$) partitioning.

The Middle Atmosphere Nitrogen TRend Assessment (MANTRA) is a series of high-altitude balloon campaigns that aims to investigate the changing chemical balance of the mid-latitude stratosphere, with a focus on the role of nitrogen compounds in the control of ozone. The mission is described in Strong et al. [4]. There have been four flights to date: in 1998, 2000, 2002 and 2004, all of which were launched from Vanscoy, Saskatchewan (52°N, 107°W) in late August. The balloon flights are supported by an extensive ground-based measurement campaign. If possible, the balloon instruments also participate in the ground-based campaign prior to the launch. A Fourier transform spectrometer (FTS), run by the University of Toronto, participated in both the MANTRA ground-based and balloon-based campaigns and will be the focus of this thesis.

There are four scientific objectives for the MANTRA mission: 1) To measure profiles of the relevant chemical species in the ozone budget, including $O_3$, NO, $NO_2$, $HNO_3$, HCl, $ClONO_2$, $N_2O_5$, $N_2O$ and $CH_4$. 2) To determine historical trends of these quantities from balloon campaigns held at mid-latitudes over the past 20 years. 3) To perform intercomparisons between instruments using different measurement techniques, including Fourier transform spectrometers, grating spectrometers, radiometers and sondes, measuring solar absorption, atmospheric emission, and *in situ*. 4) To participate in the validation of satellite data.

The MANTRA mission investigates the role of nitrogen in the mid-latitude ozone budget by focusing solely on mid-latitude atmospheric chemistry. This is achieved by flying high-altitude balloons in late August. This timing has three significant advantages. First, late August is temporally removed from the breakdown of the polar vortex, which decreases the possibility of contaminating mid-latitude ozone with potentially ozone-poor air in the vortex in early spring. Second, in late August at mid-latitudes, there is an atmospheric phenomenon called “turnaround,” at which time the stratospheric winds reverse direction from easterly to westerly. During the summer months, the stratosphere is calm. At this time, atmospheric dynamics and transport are of minimal importance, and so the chemical composition of the atmosphere is primarily controlled by photochemical effects [5]. The late-summer turnaround event marks the end of this period and thus the maximum accumulation of photochemically-controlled effects. Third, low stratospheric wind speeds allow for easy launch and recovery of high-altitude balloon payloads, and allow for longer float times within the telemetry range of the ground station. It is therefore important to be able to predict turnaround in advance of a field campaign for logistic and scientific reasons. The climatology and predictability of turnaround will be discussed in detail in Chapter 2.

The remaining portion of this chapter will outline the chemistry of interest to the MANTRA campaign (§1.2), the physics behind remote measurements of chemical profiles (§1.3) and the role of the University of Toronto's FTS in the context of the MANTRA campaign (§1.4).

## 1.2 Middle Atmosphere Ozone Chemistry

The atmosphere is comprised of a myriad of atmospheric gases. The main constituents are nitrogen ($N_2$) at ∼78%, oxygen ($O_2$) at ∼21% and argon (Ar) at ∼1%. Trace gases comprise the remaining portion of the atmosphere, and although their concentrations are low, they have a large effect on the temperature of the atmosphere. These gases include ozone ($O_3$), water vapour ($H_2O$), hydrogen chloride (HCl), nitrogen compounds, methane ($CH_4$), and many others.

The atmosphere directly above the Earth's surface, called the troposphere, gets colder with altitude until the tropopause. The tropopause can be located anywhere from 8–18 km in altitude. It is at its highest near the equator and lowest at the poles. Above the tropopause is the stratosphere, generally marked by increasing atmospheric temperature with altitude. The stratosphere is where "high-altitude" ozone is produced. The stratosphere ends at the stratopause, followed by a region of the atmosphere called the mesosphere, which is marked by decreasing temperature with altitude. The mesopause ends the mesosphere and begins the thermosphere, which, for our purposes, is outside of the region of interest.

An early theory for the existence of the stratospheric ozone layer, called the Chapman mechanism, will be described, following the treatment in Jacob [1, pp. 164–191]. Molecular oxygen is photolyzed to produce oxygen atoms, which then combine with molecular oxygen to produce ozone. These photons must have wavelengths of less than 240 nm in the ultraviolet, corresponding to energies higher than the bond energy of an $O_2$ molecule:

$$\mathrm{O_2} + h\nu \rightarrow \mathrm{O} + \mathrm{O}, \quad \lambda < 240 \text{ nm} \tag{1.2.1}$$

$$\mathrm{O} + \mathrm{O_2} + M \rightarrow \mathrm{O_3} + M. \tag{1.2.2}$$

$M$ is a third body, in the atmosphere generally either $N_2$ or $O_2$, used to absorb the excess energy from the reaction [1, p. 158]. The ground state oxygen atom labeled O in the equations, is an $O(^3P)$ atom: an oxygen atom with two unpaired electrons $(2s^2 2p_x^2 2p_y^1 2p_z^1)$ which quickly reacts with $O_2$. The $O_3$ molecules photolyze with ultraviolet light ($\lambda <$ 320 nm) producing oxygen atoms:

$$\mathrm{O_3} + h\nu \rightarrow \mathrm{O_2} + \mathrm{O}(^1D), \quad \lambda < 320 \text{ nm} \tag{1.2.3}$$

$$\mathrm{O}(^1D) + M \rightarrow \mathrm{O} + M \tag{1.2.4}$$

$O(^1D)$ is more reactive than $O(^3P)$; it has no unpaired electrons but no electrons in a $2p$ orbital $(2s^2 2p_x^2 2p_y^2)$. The net reaction for Reactions 1.2.3 and 1.2.4 is:

$$Net: \ \mathrm{O_3} + h\nu \rightarrow \mathrm{O_2} + \mathrm{O}. \tag{1.2.5}$$

This does not act as a sink for $O_3$, since O can participate in Reaction 1.2.2 to produce $O_3$ again. To destroy $O_3$, we must have a terminal loss reaction, which, in the Chapman mechanism, is:

$$\mathrm{O_3} + \mathrm{O} \rightarrow 2\mathrm{O_2}. \tag{1.2.6}$$

While the Chapman mechanism properly reproduces the general shape of the $O_3$ layer, the observed concentrations are lower than the Chapman mechanism predicts. There must, therefore, be other loss mechanisms for $O_3$.

### 1.2.1 Catalytic Ozone Depletion

Stratospheric ozone is depleted by a number of catalytic reactions, notably by hydrogen oxides, odd nitrogen and radical chlorine.

#### Hydrogen Oxides

Water vapour is transported to the stratosphere from the troposphere, and produced in the stratosphere through the oxidation of methane ($CH_4$) [1, p. 211]:

$$\mathrm{CH_4 + 10O_2 \rightarrow CO_2 + H_2O + 5O_3 + 2OH} \tag{1.2.7}$$

Methane is produced in the troposphere from both natural sources (wetlands, termites, etc.) and anthropogenic sources (livestock, rice paddies, natural gas, etc.) [1, p. 206] and is transported to the stratosphere.

The oxidation of water vapour in the stratosphere,

$$\mathrm{H_2O + O(^1}D\mathrm{) \rightarrow 2OH}, \tag{1.2.8}$$

produces OH radicals which can react with $O_3$, producing $O_2$:

$$\begin{aligned} \mathrm{OH + O_3} &\rightarrow \mathrm{HO_2 + O_2} && (1.2.9)\\ \mathrm{HO_2 + O_3} &\rightarrow \mathrm{OH + 2O_2} && (1.2.10)\\ Net:\ \mathrm{2O_3} &\rightarrow \mathrm{3O_2}. && (1.2.11) \end{aligned}$$

Since $HO_2$ and OH cycle rapidly, we refer to them as the $HO_x$ family. Because $HO_x$ is not depleted through this reaction, it is called a catalyst. The termination of this cycle occurs when $HO_x$ is lost through a reaction such as

$$\mathrm{OH + HO_2 \rightarrow H_2O + O_2}. \tag{1.2.12}$$

#### Nitrogen Oxides

The natural source of nitrogen oxide radicals ($NO_x = NO + NO_2$) in the stratosphere is from transport of $N_2O$, a long-lived species produced by the biosphere. $N_2O$ is produced from natural sources in the oceans and soils, and anthropogenic sources from biomass burning, the chemical industry, cultivated soils and livestock. $N_2O$ reacts with $O(^1D)$ to produce NO:

$$N_2O + O(^1D) \rightarrow 2NO. \tag{1.2.13}$$

$NO_x$ radicals also catalytically deplete $O_3$:

$$\begin{aligned} NO + O_3 &\rightarrow NO_2 + O_2 && (1.2.14) \\ NO_2 + O &\rightarrow NO + O_2 && (1.2.15) \\ Net: \; O_3 + O &\rightarrow 2O_2. && (1.2.16) \end{aligned}$$

The termination of this cycle occurs when $NO_x$ radicals are converted to one of their reservoir species: $HNO_3$ or $N_2O_5$. $HNO_3$ is typically produced during the day, since its production requires OH, which, in turn, requires the photolysis of $O_3$ (reaction 1.2.3) to produce $O(^1D)$ (reaction 1.2.8). $N_2O_5$ is typically produced at night.

| Day | Night |
|---|---|
| $NO_2 + OH + M \rightarrow HNO_3 + M$ | $NO_2 + O_3 \rightarrow NO_3 + O_2$ |
| | $NO_3 + NO_2 + M \rightarrow N_2O_5 + M$ |

These species eventually convert back to $NO_x$ unless $HNO_3$ is transported to the troposphere where it is removed through deposition [1]. The sum of $NO_x$ and its reservoir species is referred to as $NO_y$.

### Chlorine

A significant source of Cl in the stratosphere comes from anthropogenically-produced CFC-11 and CFC-12, which are very stable gases, emitted into the troposphere, that are transported up into the stratosphere. In the stratosphere, CFCs are photolyzed and release Cl radicals. Chlorine concentrations also have a natural stratospheric source from methyl chloride ($CH_3Cl$), produced mainly from tropical plants, biomass burning and the oceans [3].

The chlorine catalytic cycle is analogous to the $NO_x$ catalytic cycle. The $ClO_x$ family is comprised of Cl and ClO:

$$\mathrm{Cl} + \mathrm{O}_3 \rightarrow \mathrm{ClO} + \mathrm{O}_2 \quad (1.2.17)$$

$$\mathrm{ClO} + \mathrm{O} \rightarrow \mathrm{Cl} + \mathrm{O}_2 \quad (1.2.18)$$

$$Net: \ \mathrm{O}_3 + \mathrm{O} \rightarrow 2\mathrm{O}_2. \quad (1.2.19)$$

The termination of this cycle occurs when $ClO_x$ converts to HCl or $ClONO_2$,

$$\mathrm{Cl} + \mathrm{CH}_4 \rightarrow \mathrm{HCl} + \mathrm{CH}_3 \quad (1.2.20)$$

$$\mathrm{ClO} + \mathrm{NO}_2 + M \rightarrow \mathrm{ClONO}_2 + M. \quad (1.2.21)$$

These reservoirs eventually convert back to $ClO_x$. The sum of the $ClO_x$ species and their reservoirs is referred to as $Cl_y$.

In the polar regions, ozone loss is most affected by chlorine through the ClO-ClO dimer cycle [1, p. 182]:

$$\mathrm{ClO} + \mathrm{ClO} + M \rightarrow \mathrm{ClOOCl} + M \quad (1.2.22)$$

$$\mathrm{ClOOCl} + h\nu \rightarrow \mathrm{ClOO} + \mathrm{Cl} \quad (1.2.23)$$

$$\mathrm{ClOO} + M \rightarrow \mathrm{Cl} + \mathrm{O}_2 + M \quad (1.2.24)$$

$$(2\times) \ \mathrm{Cl} + \mathrm{O}_3 \rightarrow \mathrm{ClO} + \mathrm{O}_2 \quad (1.2.25)$$

$$Net: \ 2\mathrm{O}_3 \rightarrow 3\mathrm{O}_2 \quad (1.2.26)$$

and heterogeneous chemistry [1, p. 182]:

$$\mathrm{ClONO}_2 + \mathrm{HCl} \xrightarrow{PSC} \mathrm{Cl}_2 + \mathrm{HNO}_3 \quad (1.2.27)$$

$$\mathrm{Cl}_2 + h\nu \rightarrow 2\mathrm{Cl}. \quad (1.2.28)$$

Hydrogen chloride (HCl) has natural tropospheric sources from land releases and sea-salt, and natural stratospheric sources from direct injection by volcanic eruptions [6].

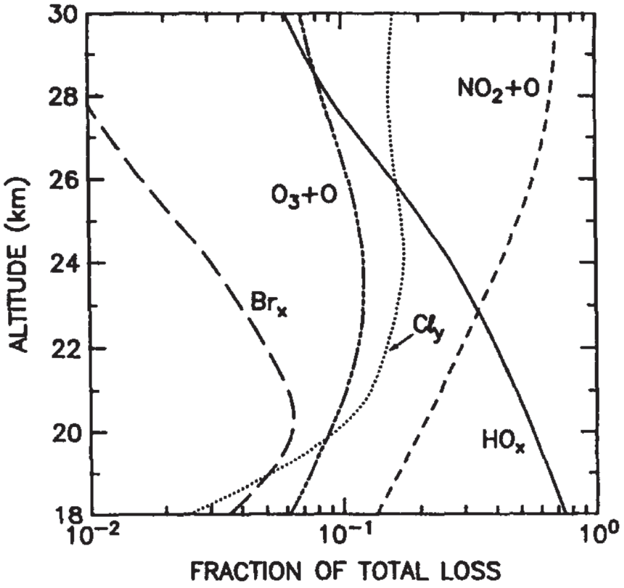

Figure 1.1: Fraction of total ozone loss at midlatitudes (47°) by the individual catalytic cycles. Figure reproduced from McElroy et al. [7].

However, the bulk of the HCl found in the stratosphere is controlled by the anthropogenic releases of CFCs [6].

Figure 1.1, reproduced from the 1992 paper by McElroy et al. [7], shows the fraction of the total ozone loss at midlatitudes (47°) from the individual catalytic cycles. The $NO_x$ cycle (Reactions 1.2.14 and 1.2.15) has the dominant effect in the mid-stratosphere, whereas the $HO_x$ cycle (Reactions 1.2.9 and 1.2.10) dominates in the lower stratosphere. The $Cl_y$ contribution in the figure is from the $ClO_x$ cycle (Reactions 1.2.17 and 1.2.18).[1]

---

[1] The small $Br_x$ contribution is from a catalytic cycle much like the $ClO_x$ cycle (replacing Cl by Br) and also from the the combined reactions

$$\begin{aligned} \mathrm{Br} + \mathrm{O_3} &\rightarrow \mathrm{BrO} + \mathrm{O_2} \\ \mathrm{Cl} + \mathrm{O_3} &\rightarrow \mathrm{ClO} + \mathrm{O_2} \\ \mathrm{ClO} + \mathrm{BrO} &\rightarrow \mathrm{Cl} + \mathrm{Br} + \mathrm{O_2} \\ Net: \ \mathrm{O_3} + \mathrm{O_3} &\rightarrow 3\mathrm{O_2}. \end{aligned}$$

This set of reactions also significantly contributes to polar ozone depletion [1, p. 182].

### 1.2.2 Nitrogen Trends and the Effect of Climate Change on $NO_x$

Nitrous oxide ($N_2O$) surface emissions have steadily increased in the past few decades, with an average rate of increase of ~0.75 ppb/yr (~3%/decade) since the late 1970s [3]. There are few long-term measurements of $NO_x$ compounds. The two longest data sets measuring stratospheric columns of $NO_2$ are located in Lauder, New Zealand (45°S, 170°E, measuring since 1981) [8] and Jungfraujoch, Switzerland (46.5°N, 8°E, measuring since 1985) [3, 9]. From these ground-based measurements, it was determined that stratospheric $NO_2$ column amounts have been increasing by 5±1%/decade since the early 1980s. Since $N_2O$, the source gas for $NO_2$, is only increasing at half that rate, it is thought that the rest of the increase can be mostly attributed to stratospheric ozone loss, since both the daytime and nighttime pathways for the termination of the $NO_x$ cycle require the presence of ozone [3, 10].

Randel et al. [11] have computed $HNO_3$ and $NO_2$ trends measured by the Microwave Limb Sounder instrument on the Upper Atmosphere Research Satellite platform [12] over the 1993-1997 period. The analysis shows a ~2% decrease in $HNO_3$ per year over that period and an increase of approximately half that magnitude in $NO_2$. The Stratoprobe balloon campaigns of the 1970s and 1980s investigated the odd-nitrogen budget in the stratosphere [e.g. 13–21], however, no long-term trends have been published from those data. There do not appear to be other long-term trend analyses of $NO_y$ concentrations in the literature.

Climate change in the stratosphere manifests itself in global-mean cooling [3]. The chemical reaction rates of the $HO_x$, $NO_x$ and $ClO_x$ catalytic cycles all slow with lower temperatures [22] and this will affect the future ozone budget by slowing the catalytic ozone depletion [23, §1.3.2].

## 1.3 Remote Measurements of Trace Gases

There are a variety of ways to measure atmospheric trace gases. Instruments can measure atmospheric properties from the ground, from balloon platforms, from aircraft, from rockets and from space. The measurement techniques can be either passive or active, *in situ* or remote. The discussion that follows will focus on the measurements of atmospheric trace gases made by a certain type of passive remote sounder: Fourier transform spectrometers. The atmospheric signatures that are measured will be discussed in §1.3.1, the viewing geometry for balloon-based and ground-based measurements will be discussed in §1.3.2, and the relevant radiative transfer will be described in §1.3.3.

### 1.3.1 Line Broadening and Absorption Coefficients

The gases in the atmosphere absorb solar radiation at particular wavelengths determined by the quantum selection rules for each molecule [24]. In the infrared, the absorption occurs during molecular vibrational-rotational transitions. The absorptions do not occur at a single wavelength for a molecule in the atmosphere, but are broadened due to the relative thermal motions of the molecules or perturbations due to collisions with other molecules [25, 26].

Broadening due to relative thermal motions of molecules along the line of sight causes Doppler shifting. Because the motions are random, these shifts occur in both directions equally, creating a symmetric, Gaussian distribution referred to as the Doppler line shape, $f_D(\sigma - \sigma_0)$ [25, pp. 107]:

$$f_D(\sigma - \sigma_0) = \frac{1}{\sqrt{\alpha_D \pi}} \exp\left(-\frac{(\sigma - \sigma_0)^2}{\alpha_D^2}\right) \tag{1.3.1}$$

$$\alpha_D = \frac{\sigma_0}{c}\sqrt{\frac{2k_B T}{M_r}} \tag{1.3.2}$$

where $\sigma$ is the wavenumber, $\sigma_0$ is the central wavenumber and $\alpha_D$ is the line width of the line, dependent on $\sigma_0$, the speed of light, $c$, the Boltzmann constant, $k_B$, the temperature, $T$, and the molecular mass, $M_r$.

Collisional, or pressure broadening is well-approximated by the Lorentz line shape, $f_L(\sigma - \sigma_0)$:

$$f_L(\sigma - \sigma_0) = \frac{\alpha_L/\pi}{\alpha_L^2 + (\sigma - \sigma_0)^2} \tag{1.3.3}$$

where $\alpha_L$, the Lorentz line width of the line, is proportional to pressure and weakly dependent on temperature [27, pp. 41–44]:

$$\alpha_L = \alpha_0 \frac{p}{p_s} \left(\frac{T_s}{T}\right)^{n_\alpha}. \tag{1.3.4}$$

Here, $\alpha_0$ is the line width value at standard temperature ($T_s = 296$ K) and pressure ($p_s =$ 1013.25 hPa), and $n_\alpha$ is the temperature exponent [28]. Broadening in this case is due to higher pressures, which cause collisions between molecules. Isolated molecules absorb an almost purely harmonic wave [29]. Collisions cause momentary interruptions to the harmonic wave, changing the phase of the radiation, which broadens the spectral line.

The pressure broadening line width dominates the line shape in the lower atmosphere, and the Doppler broadening line width dominates in the upper atmosphere. The line widths become comparable around 30-40 km [26]. The Voigt profile, $f_V(\sigma - \sigma_0)$, which is a convolution of Doppler and Lorentz line shapes, is used when both Doppler and pressure broadening are important [30].

$$\begin{aligned} f_V(\sigma - \sigma_0) &= f_L(\sigma - \sigma_0) \circledast f_D(\sigma - \sigma_0) && (1.3.5) \\ &= \frac{\alpha_L}{\alpha_D^2} \frac{1}{\pi^{3/2}} \int_{-\infty}^{\infty} \frac{e^{-y^2}}{(\alpha_L/\alpha_D)^2 + (y - (\sigma - \sigma_0)/\alpha_D)^2} dy && (1.3.6) \end{aligned}$$

Figure 1.2 shows the three absorption line shapes.

The absorption coefficient, $k_\sigma$, is the parameter that contains the information necessary to fully describe a line: the line shape, $f(\sigma - \sigma_0)$, the line centre, $\sigma_0$, and the line strength, $S$ [25],

$$k_\sigma = S f(\sigma - \sigma_0) \tag{1.3.7}$$

The line strength, $S$, is defined as

$$S = \int k_\sigma d\sigma, \tag{1.3.8}$$

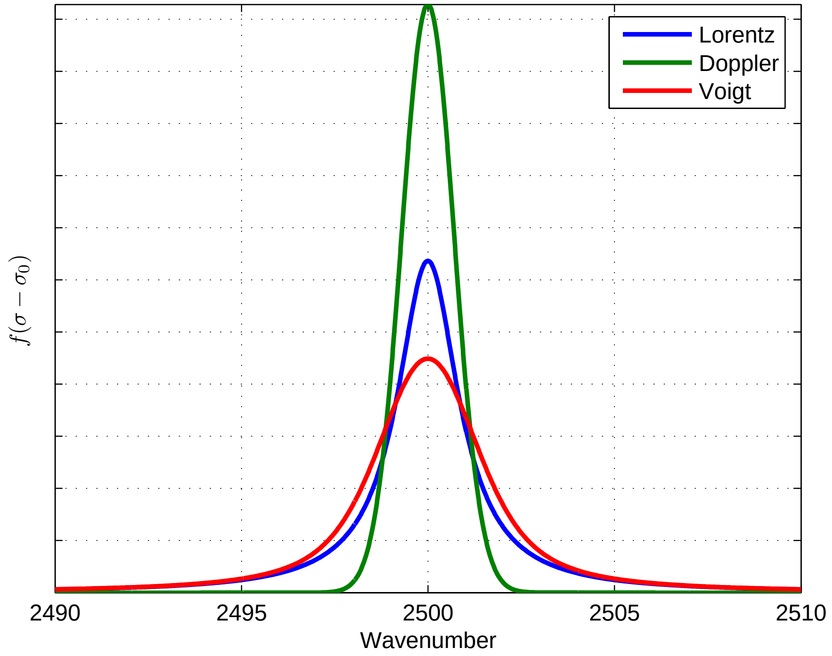

Figure 1.2: Doppler, Lorentz and Voigt lineshapes. The Doppler and Lorentz line shapes have 1 cm$^{-1}$ line widths. The Voigt profile is a convolution of these Doppler and Lorentz line shapes.

integrating over the entire line [e.g. 29, p. 16]. The absorption coefficient, in this case, is said to be normalized.

These spectroscopic line parameters ($\sigma_0$, $\alpha_0$, $n_\alpha$, $S$, and many others) are compiled in a number of databases (e.g. HIgh resolution TRANsmission (HITRAN) [31] and Gestion et Etude des Informations Spectroscopiques Atmosphériques: Management and Study of Atmospheric Spectroscopic Information (GEISA) [32]). The one that will be used throughout this thesis is the HITRAN database, which contains parameters for 39 molecules, including the most relevant atmospheric species.

### 1.3.2 Viewing Geometry

FTS instruments that measure direct solar radiation that has passed through the atmosphere are called absorption FTS instruments; these will be the focus of this thesis. FTS instruments measure the solar spectrum with high resolution, resolving atmospheric

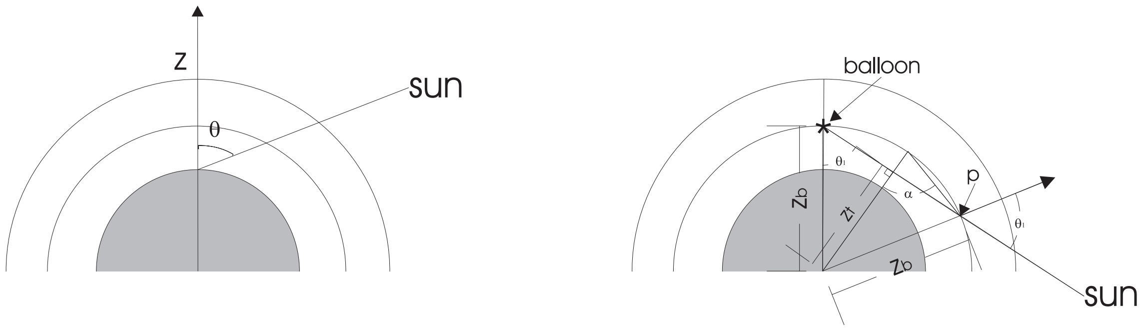

Figure 1.3: Ground-based (left panel) and balloon-based (right panel) viewing geometries. In the balloon-based diagram, the balloon is located at the asterisk, and the point ‘p’ indicates the point above which the viewing geometry is equivalent to the ground-based geometry.

absorption lines from multiple gases simultaneously. Using the line shape, we can determine where in the atmosphere (in the upper or lower atmosphere) the gas resides. The viewing geometry of the FTS is also crucial in determining how well the vertical profile of the gas can be inferred.

I will discuss two viewing geometries for measuring solar absorption by atmospheric trace gases: from the ground and from a balloon platform (Figure 1.3).

Ground-based viewing geometry is much simpler than balloon-based viewing geometry, but gives much lower vertical resolution because all of the vertical information from the spectrum is derived from the line shape. The advantage of ground-based measurements over balloon-based measurements is their temporal coverage and lower cost. Ground-based measurements using absorption FTS instruments can occur during any sunny day throughout the year whereas balloon campaigns last typically only from hours to weeks.

On a balloon platform, FTS instruments can measure with a high vertical resolution if the atmospheric absorption of solar radiation is recorded during sunrise or sunset (called an occultation). From a float altitude, $z_b$, as the sun rises or sets, each spectrum will measure a path defined by a different angle above the nadir ($\theta_1$ in Figure 1.3), and will be most sensitive to the region of the atmosphere that contains the highest airmass (that is, the region between the balloon (indicated by an asterisk) and point p). The point of highest density along this path is at the tangent height: the minimum height to the surface that is reached at each angle ($\mathrm{z_t}$). Above point p, the viewing geometry is identical to ground-based viewing geometry. A sunrise or sunset as seen from 40 km above the surface lasts around 30 minutes at mid-latitudes, and the retrieved vertical resolution of the atmospheric trace gas depends upon the speed at which the FTS records its data.

### 1.3.3 Atmospheric Profile

The change of intensity of a source, $I(\sigma)$, through an atmospheric path of length $ds$ is described by Equation 1.3.9 [27, pp. 10]. This equation implies that the change in intensity at wavenumber $\sigma$ ($dI(\sigma)$) is proportional to the amount of absorber in the path per unit area ($n_x ds$, where $n_x$ is the number density of the absorber $x$) and the source intensity at $\sigma$ ($I(\sigma)$):

$$dI(\sigma) = -k_\sigma I(\sigma) n_x ds. \tag{1.3.9}$$

The constant of proportionality is $k_\sigma$, the molecular absorption coefficient (Equation 1.3.7). We are neglecting scattering out of the path and emission into the path, because these effects are negligible in infrared solar absorption measurements.

Integrating Equation 1.3.9 gives [27, pp. 10–11, 40]:

$$\tau \equiv \frac{I(\sigma)}{I_0(\sigma)} = \exp\left\{-\int_{s_1}^{s_2} k_\sigma n_x ds\right\} \equiv \exp(-\chi), \tag{1.3.10}$$

where $\tau$ is the transmission through the atmosphere and $\chi$ is the optical depth of the atmosphere ($\chi \equiv \int_{s_1}^{s_2} k_\sigma n_x ds$). To relate the path $ds$ to the altitude $dz$, we must know the angle of the sun to the vertical, $\theta$, based on our viewing geometry (§1.3.2). For ground-based measurements, in the absence of refraction,

$$\begin{aligned} \frac{ds}{dz} &= \sec(\theta), && (1.3.11) \\ \chi &= \int_0^\infty k_\sigma n_x \sec(\theta) dz. && (1.3.12) \end{aligned}$$

For balloon-based measurements, in the absence of refraction, the optical depth between the balloon and the tangent point is calculated, multiplied by two and added to the optical depth from point p (labeled in the right panel of Figure 1.3) out to the sun. The tangent height is $z_t$, the balloon height is $z_b$, and the angle above the nadir is $\theta_1$:

$$\frac{ds}{dz} = \begin{cases} 2\tan(\alpha) & \text{if } \mathrm{z_t} \leq z \leq \mathrm{z_b} \\ \sec\theta_1 & \text{if } z \geq \mathrm{z_b} \end{cases} \tag{1.3.13}$$

$$\chi = 2\int_{\mathrm{z_t}}^{\mathrm{z_b}} k_\sigma n_x \tan(\alpha) dz + \int_{\mathrm{z_b}}^{\infty} k_\sigma n_x \sec(\theta_1) dz. \tag{1.3.14}$$

The angle $\alpha$ is related to $\theta_1$ by $\alpha = \frac{1}{2}(90 + \theta_1)$.

Given Equation 1.3.10 and the absorption coefficient (Equation 1.3.7), the transmission spectrum of the atmosphere can be theoretically calculated, if we know the vertical distribution (profile) of gases in the atmosphere.

We talk about vertical profiles of gases in two units: volume mixing ratio (VMR) and number density. The VMR is the volume of the gas per volume of air, and the number density is the number of molecules of gas per unit volume of air. The VMR of gas $x$ ($C_x$) and the number density of gas $x$ ($n_x$) are related by the number density of air, $n_a$ [1, pp. 5-6], which is Avogadro's constant $A_v$, times the number of moles of air $N$ per unit volume of air ($n_a = A_v N/V$). Using the ideal gas law ($PV = NRT$) we can see the pressure ($P$) and temperature ($T$) dependence of $n_x$:

$$n_x = n_a C_x = \frac{A_v P}{RT} C_x \tag{1.3.15}$$

where $R$ is the ideal gas constant.

The total column amount of gas $x$, $\mathrm{m_0}$ (the amount of absorber between the ground and the top of the atmosphere), is the vertically integrated number density:

$$\mathrm{m_0} = \int_0^{\infty} n_x dz. \tag{1.3.16}$$

If the path through which the atmosphere has been measured is at an angle to the zenith (as discussed in §1.3.2), this must be taken into account. The column along a slant path, m, then, is expressed as:

$$\mathrm{m} = \int_0^\infty n_x ds = \int_0^\infty n_x \frac{ds}{dz} dz. \tag{1.3.17}$$

The air mass factor is the ratio of the column density along the slant path to the column density along the vertical path ($\mathrm{m}/\mathrm{m}_0$). To compute the total column from the slant column, the slant column is divided by the air mass factor.

In this thesis, we will discuss both column amounts of gases (especially for the ground-based work) and volume mixing ratio vertical profiles.

## 1.4 The Role of the U of T FTS on MANTRA

Fourier transform spectrometers play an important role in the suite of instruments on board the MANTRA payload. They are high-resolution, broad-band instruments that can simultaneously measure almost every chemical species relevant to the MANTRA science goals. There have been three FTSs on MANTRA payloads over the years: the University of Denver's FTS (DU FTS), the University of Waterloo's FTS called the Portable Atmospheric Research Interferometric Spectrometer for the Infrared (PARIS-IR), and the Meteorological Service of Canada's FTS run by the University of Toronto (U of T FTS).

The DU FTS has a 30-year flight heritage on board a variety of high-altitude balloons. The instrument and results from the MANTRA 1998 campaign are described in Fogal et al. [33]. The PARIS-IR instrument is a ground- and balloon-based version of the Atmospheric Chemistry Experiment FTS (ACE-FTS) [34] that was built in 2003-2004 for ACE-FTS validation. The instrument is described in Fu et al. [35]. The U of T FTS was rebuilt from a commercial model during 2003–2004 and is described in detail in Chapter 4.

All three of the FTS instruments were on board the MANTRA 2004 payload. The DU and U of T FTS instruments were on the MANTRA 2002 payload; the DU FTS was the sole FTS on the MANTRA 1998 payload. All three of these instruments measure in solar occultation mode.

The role of the U of T FTS is four-fold: one, to develop a Canadian capacity for balloon-borne FTS measurements; two, to measure profiles of chemical species of interest to the MANTRA mission; three, to compare results with other instruments, both ground-based and balloon-based; and four, to participate in satellite validation.

The PARIS-IR and U of T FTSs are currently the only two active balloon-borne FTS instruments in Canada, and with these two instruments, we have developed Canadian expertise in balloon-borne Fourier transform spectroscopy.

To contribute to the MANTRA science goals, the U of T FTS is configured to measure HCl, $O_3$, $N_2O$, CO, and $CH_4$. Since HCl is not measured by the DU FTS, it is the main focus of the balloon-borne data from the U of T FTS.

The U of T FTS participated in ground-based instrument intercomparison campaigns, both at Vanscoy during the MANTRA field campaign in 2004, and at the University of Toronto during the summer of 2005. The results from these campaigns will be described in Chapter 5. Problems with the MANTRA 2004 flight limited the scientific results from the flight data, and those details will be discussed in Chapters 4 and 5.

The ground-based campaigns also included data from satellite overpasses. The Microwave Limb Sounder (MLS) instrument on the Aura satellite began science measurements shortly after the ground-based campaign began in 2004 [36, 37]. There were multiple overpasses during the 2004 ground-based campaign, and the results of comparisons with MLS will be discussed in Chapter 5.

This thesis consists of three related projects: the climatology and predictability of turnaround (Chapter 2), the redevelopment of the U of T FTS (Chapter 4), and ground-based intercomparison campaigns (Chapter 5). Chapter 3 details basic FTS theory and Chapter 6 provides a summary of this work and a future outlook for these projects. The turnaround study allows us to better prepare for the late-summer turnaround launches, by providing a launch window-of-opportunity. This work is published as Wunch et al.

[38, 2005]. On the U of T FTS refurbishment project, I worked closely with Clive Midwinter and was involved in every aspect of the work: the wiring, purchasing of new electronics, mechanical design, electrical design, optical design and testing. I wrote all of the software for the instrument from the instrument control software through to the processing of interferograms into spectra. A short summary of this work is published as Wunch et al. [39, 2006]. For the ground-based intercomparison campaigns, I was responsible for running the U of T FTS, processing its data using SFIT2 and synthesizing the results from the three FTSs. A paper describing the 2005 ground-based campaign in Toronto has recently been submitted [40].

# Chapter 2

# Turnaround*

## 2.1 Introduction and Motivation

Vanscoy, Saskatchewan (52°N, 107°W) was the launch site for the MANTRA high-altitude balloon campaigns, which took place in the late summers of 1998, 2000, 2002 and 2004. The original motivation for developing a climatology of winds over the launch site was to determine how early, and with what accuracy, it is possible to predict the optimal launch date in terms of stratospheric winds. The MANTRA mission, as described in §1.1, aims to investigate the chemical interactions that affect ozone. These objectives are met by a launch during late summer, which is dynamically quiescent and closer to photochemical control [5, 41]. Practically, the balloons should be launched when the stratospheric wind speeds are at a minimum in order to ensure that the payload remains within the telemetry range (approximately 500 km) for the duration of mission science (typically 18 hours). Low stratospheric wind speeds occur in mid-latitudes in late summer, during a time of year called "turnaround." The purpose of the work described below is to characterize the late-summer turnaround event and in particular to investigate how far in advance it can be predicted.

In the extratropical stratosphere, there is an annual cycle in temperature. At solstice, the highest temperatures occur over the summer pole and the lowest temperatures occur

---

*The work in this chapter is published in Wunch et al. [38]

over the winter pole. The thermal wind relation 2.1.1 then implies easterly zonal wind vertical shears ($\partial u/\partial z < 0$) in the summer hemisphere and westerly shears ($\partial u/\partial z > 0$) in the winter hemisphere [42, pp. 274]:

$$\frac{\partial u}{\partial z} = -\frac{g}{Tf}\frac{\partial T}{\partial y}. \tag{2.1.1}$$

Here, $u$ is the zonal wind, $T$ is the temperature, $g$ is the gravitational acceleration, $f$ is the Coriolis parameter, $z$ is the vertical coordinate (altitude) and $y$ is the meridional coordinate. The Coriolis parameter is defined as $f = 2\Omega \sin\phi$, where $\Omega$ is the Earth's rotation rate and $\phi$ is the latitude [42]. Over the course of a year, there will be two transitions, during which the zonal wind shear vanishes ($\partial u/\partial z = 0$). In the summer hemisphere stratosphere, the easterly vertical shear is strong enough that the winds become easterly for much of the summer, and so there is a period of time when the zonal winds themselves vanish [43]. It is these transitions, which we call "turnaround" events, that we wish to study.

Rossby waves, or planetary waves, are large-scale disturbances in the atmosphere, which can be observed in the latitudinal displacement of the mid-latitude jet stream. The restoring force for a Rossby wave is the meridional gradient in the Coriolis parameter.

Vertically-propagating Rossby waves are of interest here, because they can disturb the stratosphere. The dispersion relation for a vertically-propagating Rossby wave against a zonal background flow, $\bar{u}$, is [26]:

$$\omega \equiv ck = k\bar{u} - \frac{\beta k}{k^2 + l^2 + \left(f_0^2/N^2\right)\left(m^2 + 1/4H^2\right)}. \tag{2.1.2}$$

where $k$, $l$ and $m$ are the zonal, meridional and vertical wave numbers, respectively, $H$ is the scale height, $N$ is the buoyancy frequency, and $c$ is the phase speed of the wave. The variables $\beta$ and $f_0$ come from the Taylor expansion approximation to the Coriolis parameter: $f \approx f_0 + \beta y$. Rearranging, we get:

$$\bar{u} - c = \frac{\beta}{k^2 + l^2 + \left(f_0^2/N^2\right)\left(m^2 + 1/4H^2\right)}. \tag{2.1.3}$$

For vertical propagation, $0 < m^2 < \infty$, and with $k^2$, $l^2$, $\beta$, $f_0^2$, $N^2$ and $H^2$ all positive-definite, this sets the condition that

$$0 < \bar{u} - c < \bar{u}_c \equiv \frac{\beta}{k^2 + l^2 + (f_0^2/(4N^2H^2))}. \tag{2.1.4}$$

The bulk of the planetary-scale waves (and those that are relevant for this study) remain stationary with respect to topography, and so $c = 0$, leaving us with

$$0 < \bar{u} < \bar{u}_c. \tag{2.1.5}$$

Therefore, vertically-propagating Rossby waves can only exist if the background winds are westerly, but not if they have speeds greater than $\bar{u}_c$. The stratospheric winds in the summer are easterly, and Rossby waves do not propagate into the summer stratosphere. Those waves with small zonal wavenumbers can propagate upwards into the winter stratosphere, which has a mean westerly flow, and so while the winter stratosphere is often disturbed by these large-scale waves, the summer stratosphere is relatively dynamically inactive [43].

Turnaround events occur in early spring and in late summer. The springtime transition is highly irregular, but the late-summer transition is comparatively smooth. The contrast between the two events in the Northern Hemisphere is visible in Figure 2.1, which shows the climatology of 10-hPa zonal winds over Vanscoy using three different data sources (discussed in §2.2). Note the small standard deviation about the mean zonal wind speed as the wind speeds change sign in late summer (around day 240), as compared with the large standard deviation and multiple sign changes in spring (around day 100).

## 2.2 Data Sets

The zonal wind data sets used in this study are the assimilated data from the National Centers for Environmental Prediction / National Center for Atmospheric Research

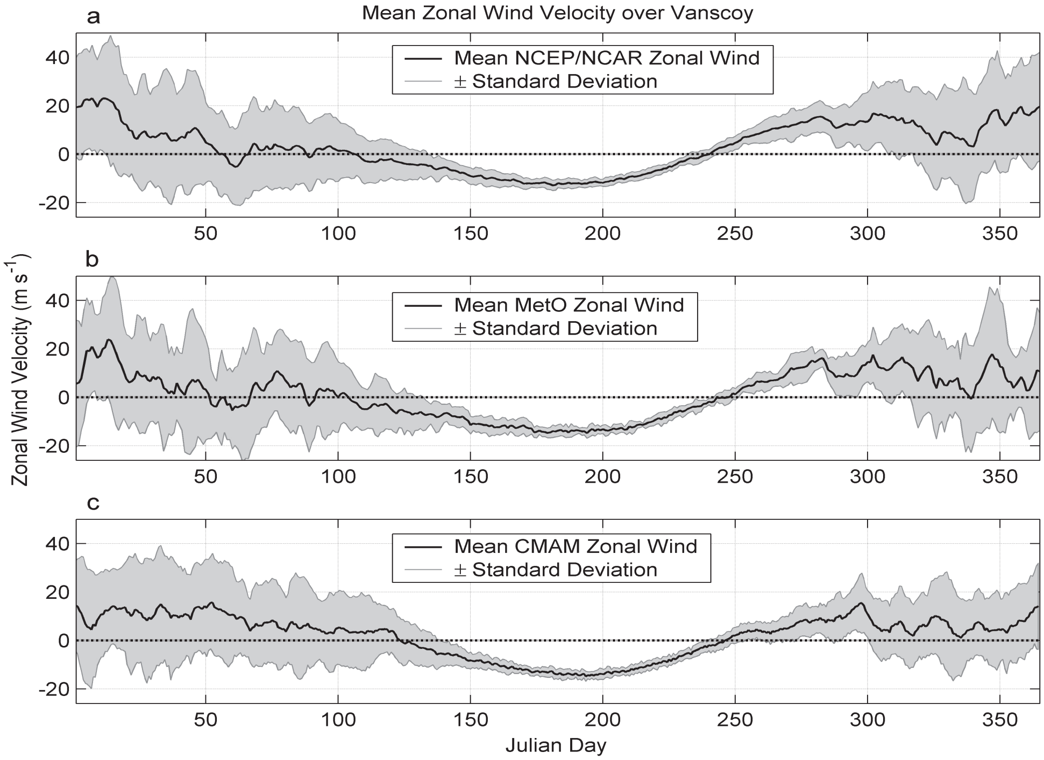

Figure 2.1: Long-term mean of the 10-hPa zonal wind over Vanscoy (solid curve), and the standard deviation of daily data (shading): a) data from the NCEP/NCAR reanalysis (1979-2003); b) data from the MetO analysis (1993-2002); and c) simulations from a 24-year run of the CMAM model for current conditions.

(NCEP/NCAR) reanalysis project [44] and the United Kingdom Meteorological Office (MetO) [45, 46], as well as model data from climate simulations performed with the Canadian Middle Atmosphere Model (CMAM). The NCEP/NCAR reanalysis is provided by the Climate Diagnostics Center with 6-hourly data combined into a daily average zonal wind over a grid of 144 longitudes by 73 latitudes, on 17 pressure levels, for the period 1948-2003. The closest grid point to Vanscoy is (52.5°N, 107.5°W). The reanalysis data has several limitations from the perspective of this study. Most importantly, its ceiling is 10 hPa, while the MANTRA balloons float at about 5 hPa. Only the reanalysis record from 1979 onward is used in this study since satellite data were integrated into the model after that time [44], creating a more self-consistent data set, and because the focus of

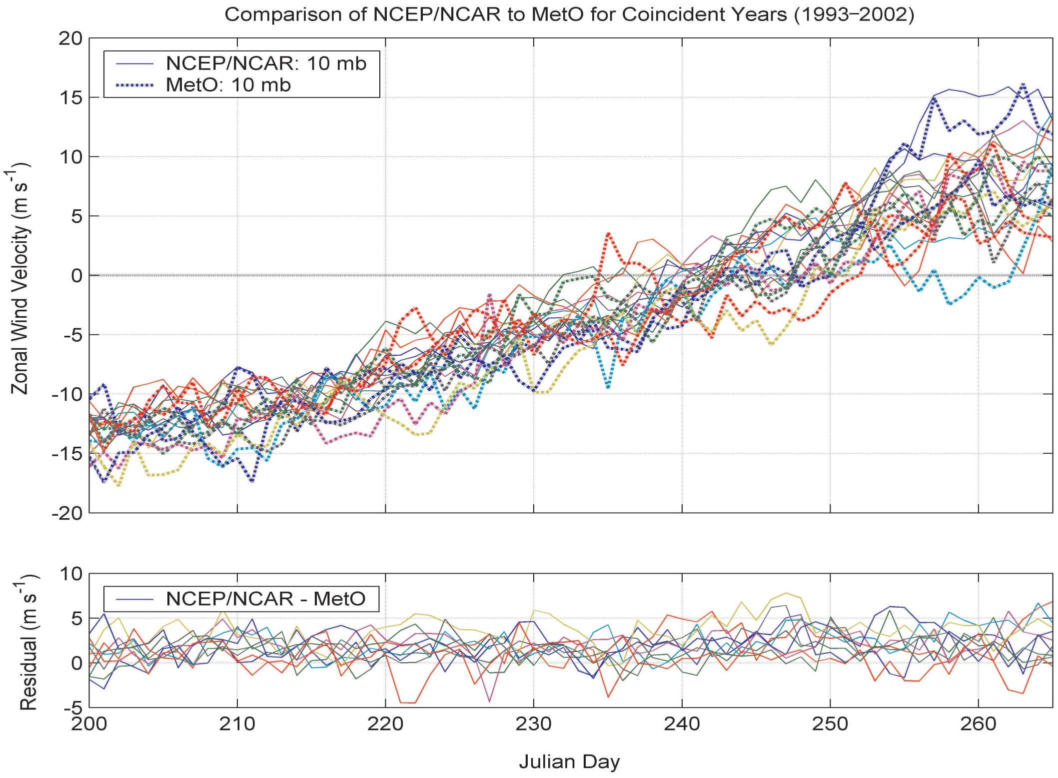

Figure 2.2: A comparison of coincident years of zonal wind velocity at 10 hPa over Vanscoy for NCEP/NCAR (solid) and MetO (dotted). The different colours represent different years. The lower panel shows the residuals.

this work is on predicting the turnaround phenomenon over Vanscoy for future launches. The effect of including the entire record is addressed in §2.4.2.

The MetO data set used in this study is a stratospheric extension of the United Kingdom Meteorological Office weather forecasting operational analysis [45]. The MetO lid is at 0.32 hPa. The closest grid point to Vanscoy is (52.5°N, 108.75°W). However, the MetO data set only extends back to late 1991, which places limitations on the statistical analysis. The MetO and NCEP/NCAR data sets were compared for coincident years at 10 hPa, and the results are shown in Figure 2.2. NCEP/NCAR is generally more westerly than MetO by about 2 m/s, on average, and differences can often reach 5 m/s. Turnaround in the late summer is relatively unchanging with altitude or pressure above 10 hPa (see Figure 2.3); thus, because of the overall similarity of the MetO and

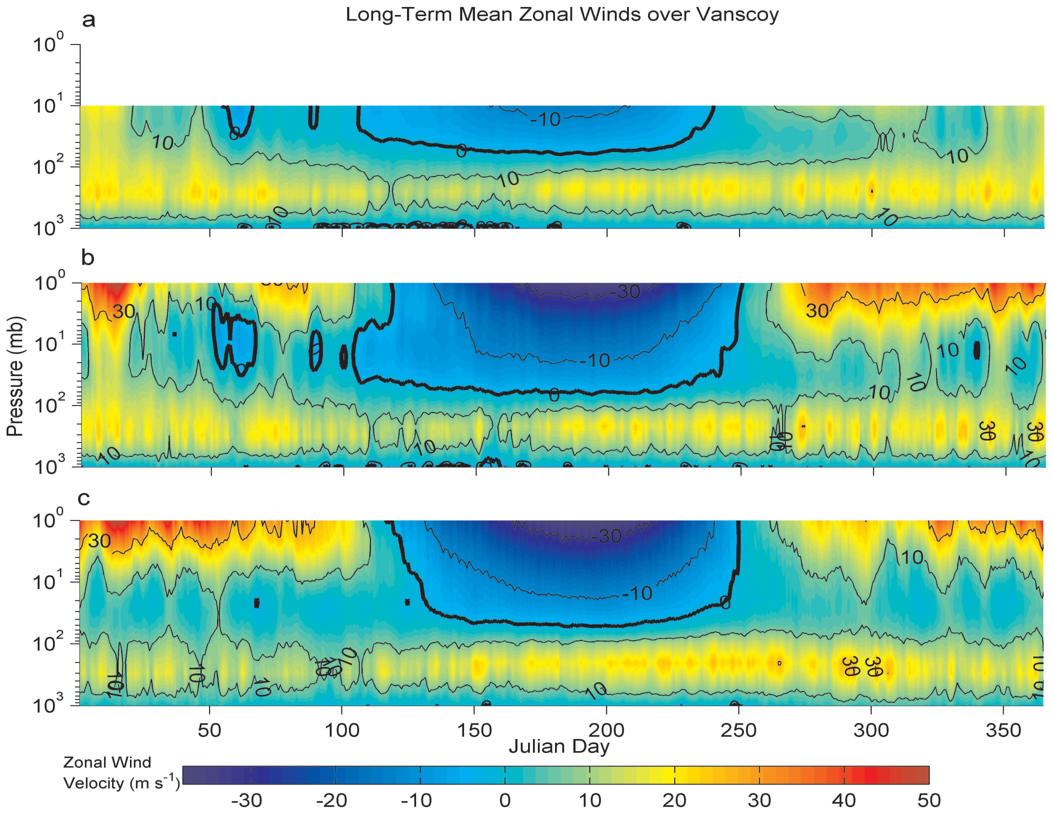

Figure 2.3: The temporal-vertical picture of turnaround: a) NCEP/NCAR long-term average from 1979-2003 on 17 pressure levels; b) MetO mean for 1993-2002 on 22 pressure levels; and c) CMAM mean for 24 years on 16 pressure levels.

NCEP/NCAR data sets at 10 hPa, we have primarily used NCEP/NCAR at 10 hPa, to take advantage of its longer data record. However, in light of the differences with MetO, we ensure that all conclusions are also supported by the MetO data.

The CMAM is a three-dimensional climate simulation model with fully interactive chemistry that extends from the surface of the Earth to approximately 100 km altitude (0.001 hPa) [47, 48]. The data we have used here is from the '2000 Run' as described by Austin et al. [49] which models current conditions. The years analyzed here are the last 24 of a 39-year simulation. The closest CMAM grid point to Vanscoy is (50.625°N, 108.75°W); the data is output every 18 hours.

## 2.3 The Climatology of Turnaround

Our main goal was to see if we could predict, some weeks before a campaign, when turnaround is likely to occur. If we could narrow down the window of opportunity, we could much more easily plan our campaigns and incur less risk. A climatology of the phenomenon is then necessary to begin this work. To fully characterize turnaround, we first need to study the temporal structure of turnaround, which we have already seen briefly in Figure 2.1. Second, we need to look more closely at the vertical-temporal structure in Figure 2.3. Third, the horizontal-spatial structure for a single year is shown in Figure 2.5 and sheds light on the time evolution of turnaround over North America.

From Figure 2.1, we can see the time evolution of the 10-hPa zonal winds over Vanscoy from NCEP/NCAR in panel ‘a’, from MetO in panel ‘b’ and from CMAM in panel ‘c’. The 1-$\sigma$ standard deviation from the mean is shown in the shaded area. It is clear from this picture that the springtime turnaround event is much more variable than the late summer event. The low variability is seen from approximately Julian day 130 through 250, when stratospheric winds are easterly, and there is no propagation of planetary waves into this region. From the figure, one can see that for the NCEP/NCAR data set, the climatological mean zonal wind crosses the zero line at Julian day 239 with a standard deviation of 10.8 days. The corresponding dates for MetO and CMAM, are 247.2 and 246.1, respectively, with standard deviations of 4.7 and 7.6 days.

In order to determine whether the difference in turnaround dates between data sets was due to the different time series length, Figure 2.4 shows the same means as in Figure 2.1 for the MetO and CMAM data sets but restricting the NCEP/NCAR mean to years corresponding to the MetO data set. The turnaround date for NCEP/NCAR for these later years is 240.9. Since this does not account for the entire difference between the turnaround dates for NCEP/NCAR and MetO, the time series cannot be the only reason for the difference. While NCEP/NCAR agrees quite well with MetO during the disturbed winter–spring period, during the summertime period, NCEP/NCAR appears

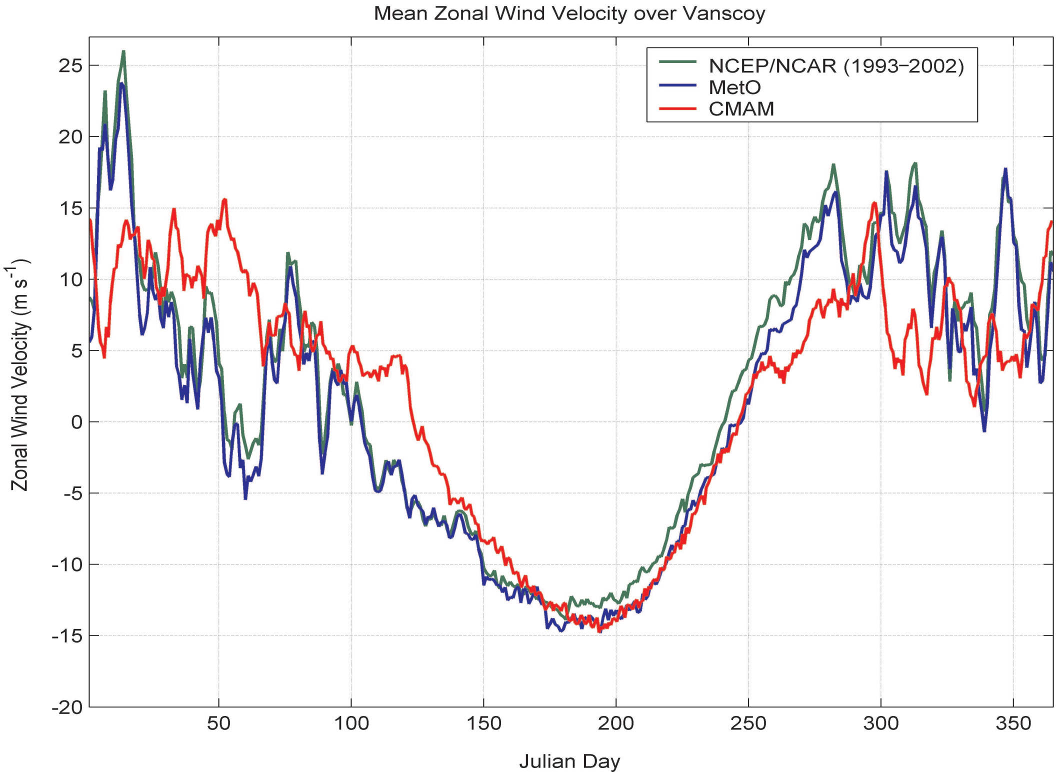

Figure 2.4: A comparison of NCEP/NCAR (1993-2002) (green), MetO (1993-2002) (blue) and CMAM (24 years) (red) long-term means of 10-hPa zonal wind velocity over Vanscoy.

to have a systematic westerly bias. We would not expect exact agreement in the winter–spring period between the CMAM and either the NCEP/NCAR reanalyses or the MetO analyses, due to the limited (10-year) time period.

The vertical-temporal structure illustrated in 2.3 shows that the zero wind speed (the thick black curve) occurs at all altitudes above 100 hPa nearly simultaneously during the late-summer turnaround event. This is especially clear in the CMAM data in panel ‘c’ around Julian day 250. Below 100 hPa, winds are westerly throughout the year, with a maximum around 300 hPa at the jet stream. No other contour appears to have such a uniform vertical extent. This represents the ideal launch conditions, since at any given altitude above 100 hPa, the balloon will remain effectively stationary.

Figure 2.5 shows the horizonal-spatial wind speeds at 10 hPa over North America for a number of days before and after turnaround in 1998. The star on the figure indicates

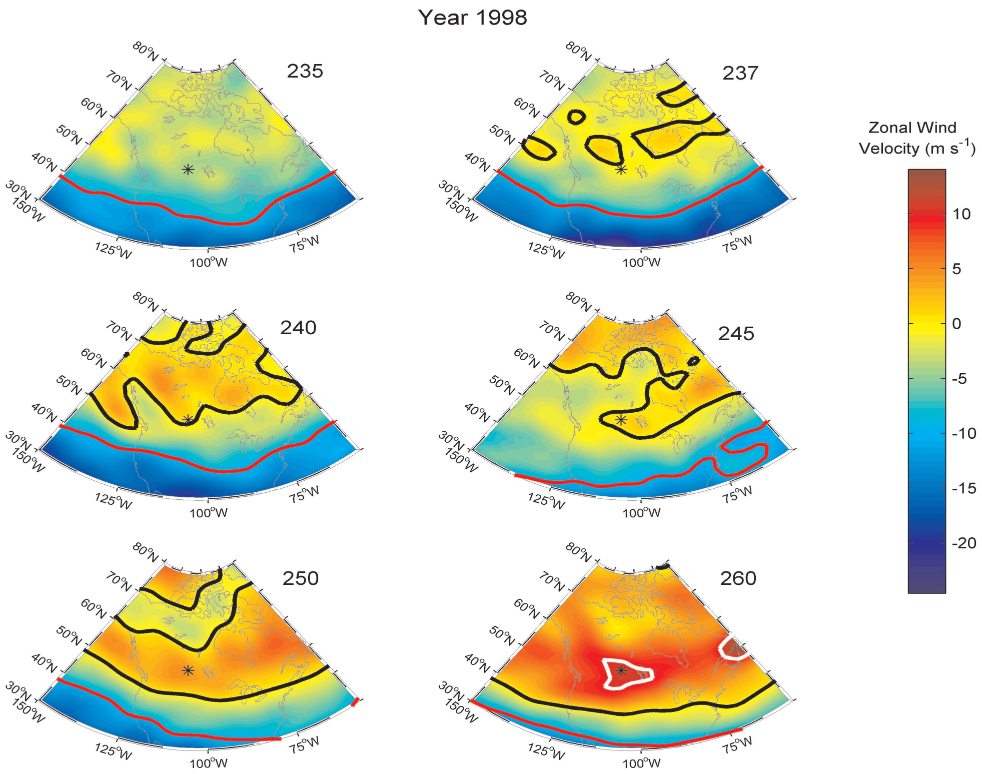

Figure 2.5: The time evolution of turnaround in 1998 at 10 hPa over North America. The NCEP/NCAR data set is used, and days 235, 237, 240, 245, 250 and 260 are shown. The red, black and white curves mark, respectively, the contours of -10, 0 and +10 m/s zonal wind velocities.

the location of Vanscoy, Saskatchewan, and the red, black and white curves represent the -10, 0 and +10 m/s zonal wind contours, respectively. The zero contour first appears in small isolated closed contours at high latitudes (between 50°N and 80°N) in late August. These are relatively evenly distributed zonally across the planet. The zero contours then coalesce into a distinct line, which is roughly zonally symmetric, between 45°N and 55°N. This zero contour drifts uniformly south for several weeks, to a latitude of about 30°N in early October. Each year's turnaround event has a different temporal extent. Two extreme examples are seen in Figure 2.6, where the 1985 turnaround event happened over five days, whereas the 1987 turnaround event took place over more than a month.

To accommodate for the temporal extent of turnaround, we will define turnaround

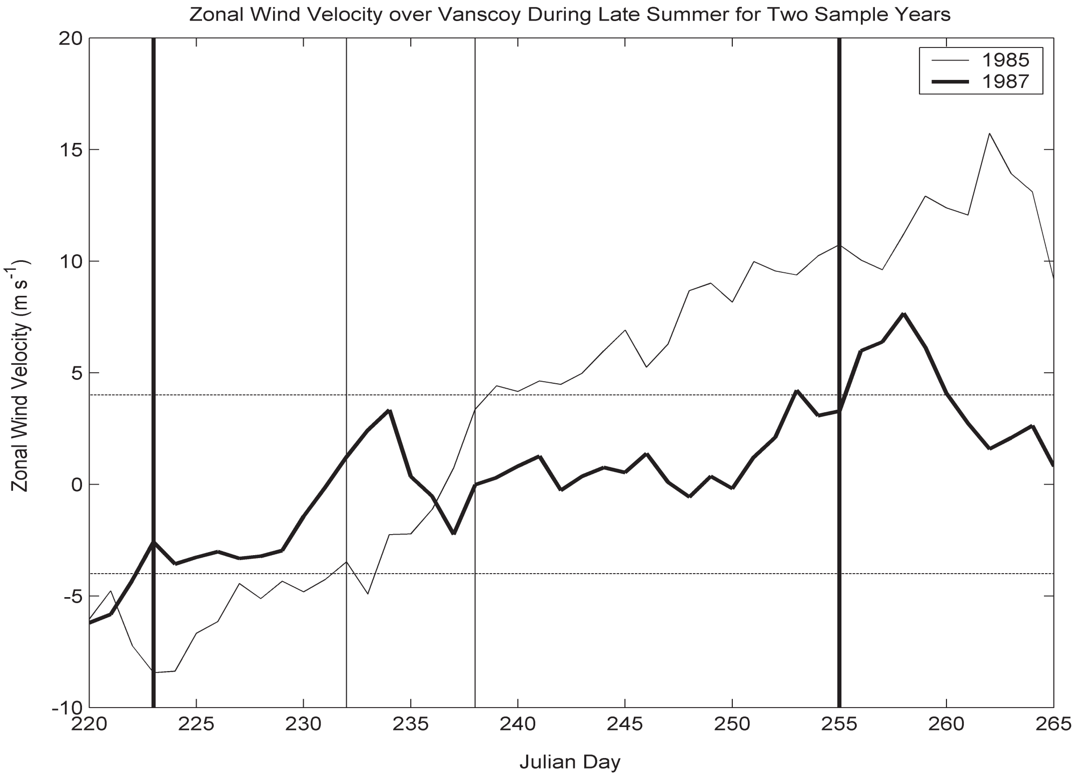

Figure 2.6: Differences in the turnaround interval. Here are two extreme examples of the extent of turnaround, using the NCEP/NCAR reanalysis. The horizontal lines indicate the ±4 m/s limits and the vertical lines show where the two curves cross those limits.

for the rest of this chapter as the interval during which the zonal wind speeds change sign. The interval is the set of dates in a given year for which the zonal wind speeds lie between the first day for which $u \geq -4$m/s and the last day for which $u \leq +4$m/s, where $u$ is the 10-hPa zonal wind over Vanscoy. The value of ±4 m/s was chosen to ensure that the MANTRA balloon reaches neither Lake Winnipeg nor the Rocky Mountains during its flight – two undesirable payload recovery sites. From the perspective of ballooning, the turnaround interval defined here is one in which suitable launch days are likely.

Each year was characterized according to this definition and the results are plotted in Figure 2.7. Each day in late summer was then assigned a score, according to the number of years in which a particular day was in the turnaround interval. The normalized statistics from this analysis are shown in Figure 2.8. There are four panels in this figure, the first

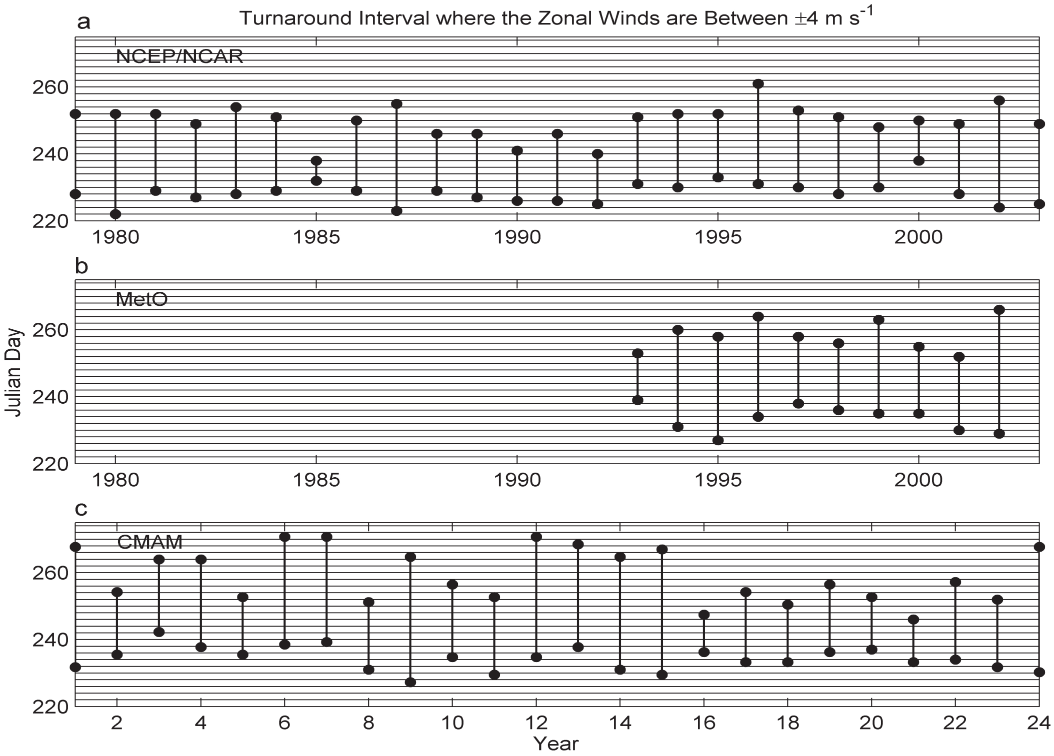

Figure 2.7: The duration of turnaround in different years at 10 hPa. The range of days indicated by the vertical lines shows the days in which the winds were within the turnaround interval. Panels a), b) and c), respectively, are for NCEP/NCAR, MetO and CMAM.

from the NCEP/NCAR record from 1979-2003, the second reducing the time line from the NCEP/NCAR record to 1993-2002, matching the MetO time line, which is shown in the third panel. The fourth panel shows the equivalent CMAM plot. Aside from the saturation of these probability distributions, which indicates that certain dates fell within the turnaround interval in every year, panels ‘a’ through ‘c’ appear quite Gaussian. The CMAM distribution clearly is non-Gaussian, with turnaround events unrealistically prolonged. The reasons behind this are not yet understood. The middle two panels, however, give us some valuable information: in every year between 1993 and 2002, an appropriate launch window has included days 238-248 (August 26 through September 5).

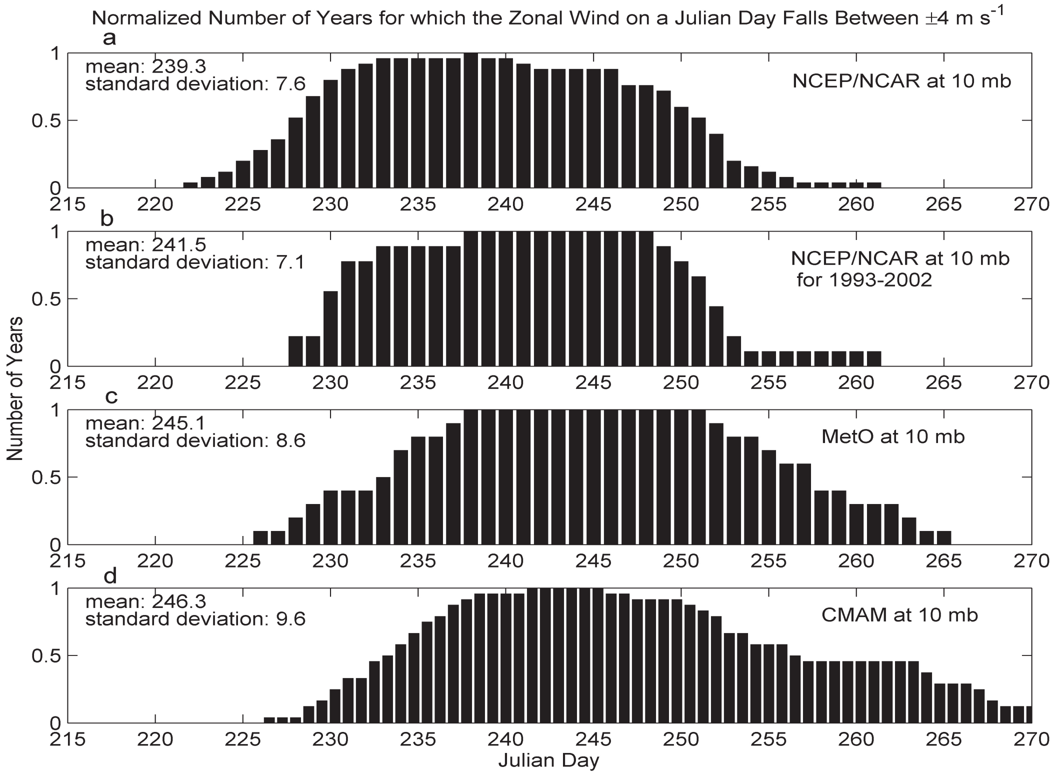

Figure 2.8: The normalized probability distribution of a late-summer Julian day falling within the turnaround interval, using the data from Figure 2.7: a) NCEP/NCAR for 1979-2003; b) NCEP/NCAR for 1993-2002; c) MetO for 1993-2002; d) CMAM for 24 years.

## 2.4 The Predictability of Turnaround

Our first attempt at predicting the launch window from earlier in the year was to fit a simple $5^{th}$-order polynomial to the zonal winds over Vanscoy from Julian day 150 to 270 for each year. This process was an attempt to see if the time of maximum easterly zonal wind speed and the time of minimum zonal wind speed (i.e. turnaround) were correlated in a simple manner. No significant correlation was found although the means calculated were comparable to those from previous methods (Julian day 240.7 with a standard deviation ($1\sigma$) of 3.2 days).

It became clear that we needed to explore what possible parameters might produce a statistically significant correlation with the turnaround date.

### 2.4.1 Correlations

For a time series consisting of $n$ years of data, the correlation coefficient, $r$, of zonal wind, $u$, at day $i$ with $u$ at day $j$ is defined by

$$r = \frac{\sum_{k=1}^{n} u'_k(i) u'_k(j)}{\sqrt{\sum_{k=1}^{n} [u'_k(i)]^2 \sum_{k=1}^{n} [u'_k(j)]^2}}, \qquad (2.4.1)$$

where $u'_k(i)$ is the deviation of the zonal wind at day $i$ in year $k$ from its long-term mean for that day. That is $u'_k(i) = u_k(i) - \frac{1}{n}\sum_{k=1}^{n} u_k(i)$.

Using Equation 2.4.1, we looked for correlations between different parameters: we calculated correlation coefficients for zonal winds over Vanscoy with zonal winds over Vanscoy, zonal mean zonal winds at the latitude of Vanscoy with zonal winds over Vanscoy, and zonal mean zonal winds at the latitude of Vanscoy with zonal mean zonal winds at the latitude of Vanscoy. The only statistically significant correlation that we found was when zonal mean zonal winds at 52°N were correlated with themselves[1]. Thus, for the rest of this chapter, we will look only at autocorrelations for zonal-mean zonal winds.

Figure 2.9 shows the autocorrelation coefficients for the zonal mean zonal wind over Vanscoy at 10 hPa, using the NCEP/NCAR reanalysis data in panel 'a' and the CMAM data in panel 'b'. The autocorrelations are shown relative to the wind 10, 20, 30 and 40 days ahead of the average turnaround date for that data set. From Figure 2.9a, one can see the persistence of high autocorrelations early in the summer for days separated by more than a month. However, before turnaround, the correlations drop off drastically, diminishing the predictability of turnaround. The statistical significance of the coefficients at the mean turnaround date is marginal. The CMAM does not fully capture the persistence of high correlations during the summer months, but it does capture the abrupt drop-off of the correlations just before turnaround, with similarly marginal statistical significance.

---

[1] For clarity, the zonal means were over 144 latitude grid points for the NCEP/NCAR reanalysis, 96

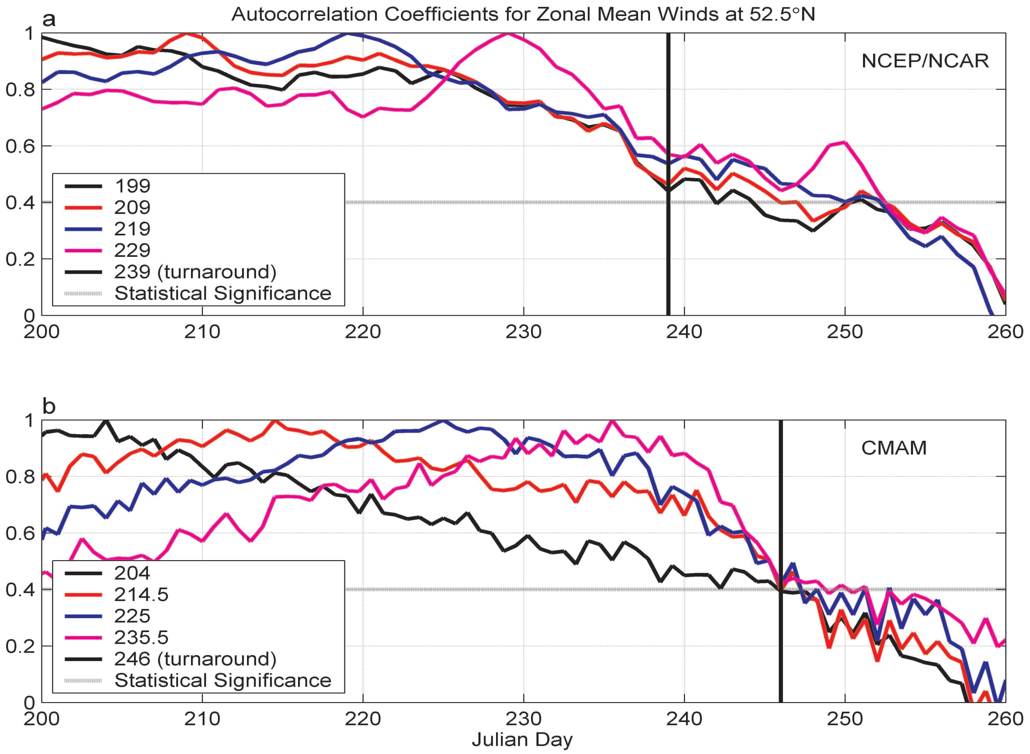

Figure 2.9: Autocorrelation coefficients between the 10-hPa zonally averaged zonal wind. The coefficient will be unity when correlated with itself. a) NCEP/NCAR reanalysis for 1979-2003; b) 24 years of CMAM. A value above 0.4 is statistically significant for both data sets.

Figure 2.10 shows the complete autocorrelation matrix from which rows of the matrix were extracted to produce Figure 2.9. From Figure 2.10, it is clear that there is a block of time during the summer months when the autocorrelations are high, but these correlations drop off sharply around day 239.

### 2.4.2 A Warning about Reanalyses

The full NCEP/NCAR reanalysis data set spans 1948 through to the present, using a consistent data assimilation scheme for all years. The reanalysis assimilates operational data (from sondes, ground-based measurements, satellites, etc.) with model data (for

---

grid points for the MetO analysis and 97 grid points for the CMAM output.

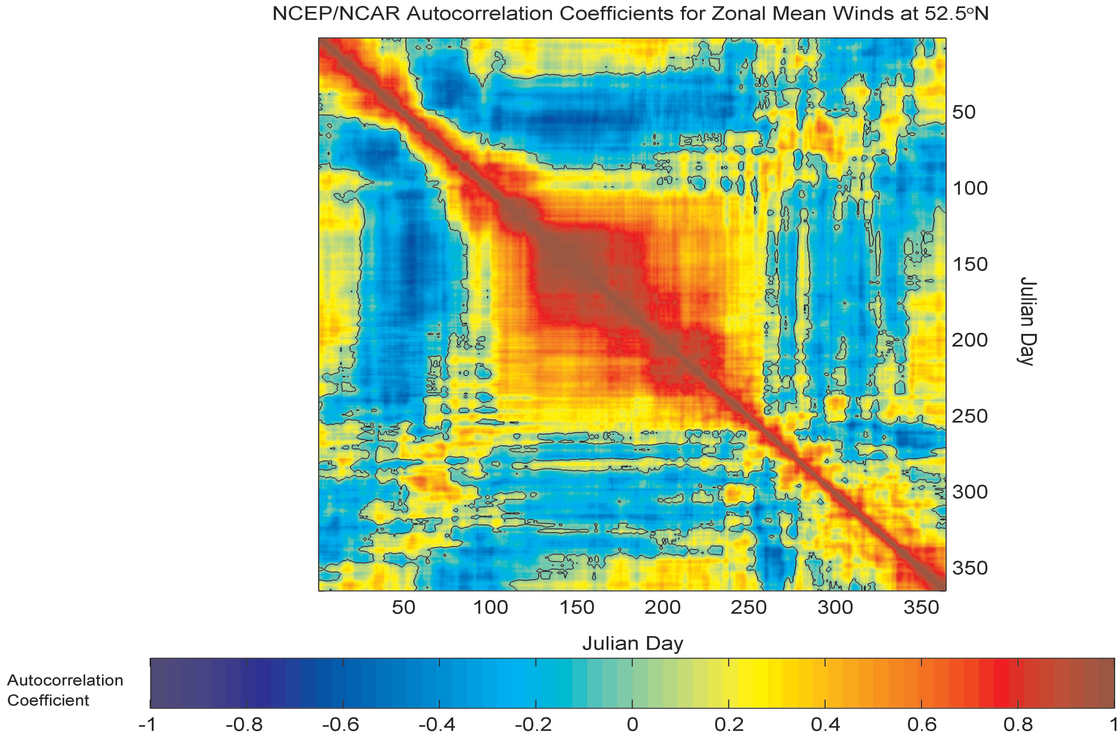

Figure 2.10: Autocorrelation coefficients for the 10-hPa zonally averaged zonal winds, at 52.5°N, calculated using years 1979-2003 of the NCEP/NCAR reanalysis.

details, refer to §2.2 and Kalnay et al. [44]). Over the course of this time line, there have been three well-defined observing regimes [50]: between 1948 and 1957, very few data were input into the assimilation scheme; after the International Geophysical Year, and between 1958 and 1978, upper air observations were available; and from 1979 to the present, the modern satellite network was used. These changes in data source and availability create an inhomogeneity in the time series of many of the reanalysis fields. Figure 2.11 shows the zonal wind velocity at 10 hPa over Vanscoy for the entire NCEP/NCAR reanalysis data set, with the three observing regimes indicated. There is a clear trend prior to 1970, and, whether this is real or not, it causes spuriously high autocorrelations. Figure 2.12 shows the strong autocorrelation coefficients that result from an autocorrelation analysis of years 1948 through 1969, as compared with those from Figure 2.10.

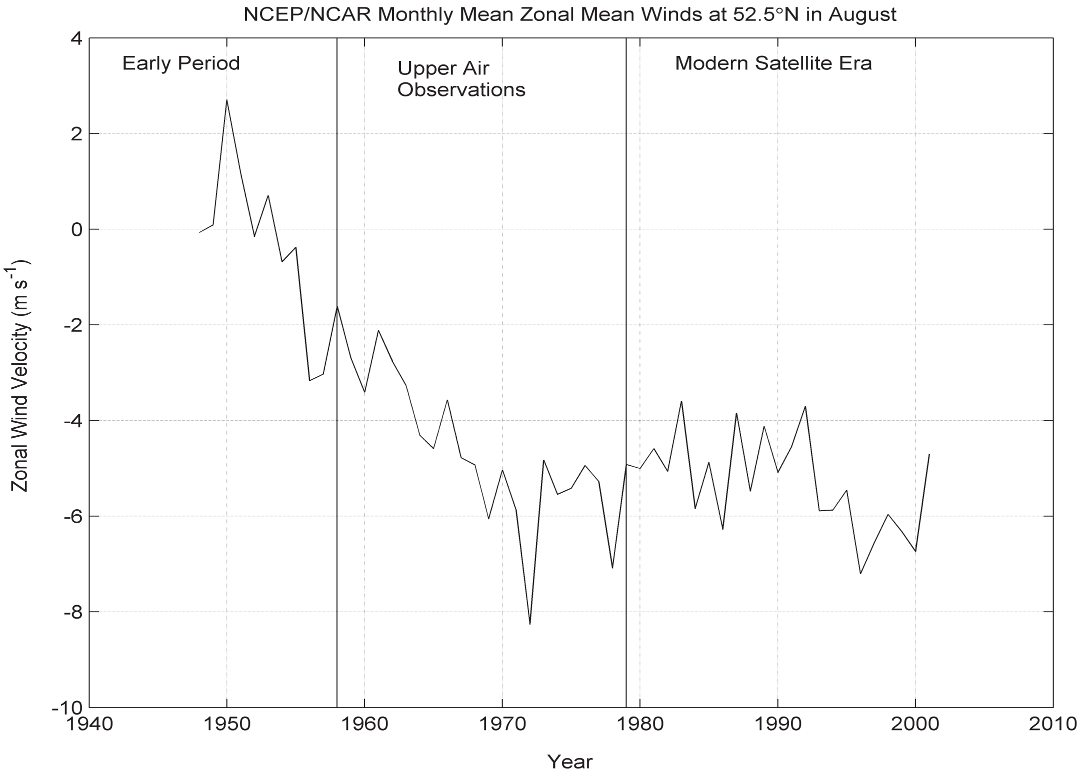

Figure 2.11: An illustration of the three observing regimes during the NCEP/NCAR time series. Zonal wind velocity is plotted against time. The three regimes are indicated by the vertical lines.

## 2.5 Discussion and Conclusions

The work shown in this chapter had the ultimate goal of determining when turnaround is likely to occur in a given year. Figures 2.9 and 2.10 show that, while we have quite high correlations between zonal mean zonal winds throughout the summer, suggesting that that time of year is highly predictable, the correlations drop off just before turnaround. It appears as though the stratosphere loses all its predictability as Rossby waves are allowed to propagate up into it.

Interestingly, from Figure 2.5, it would appear that the predictability of turnaround at lower latitudes would be higher than that at 52°N. This is, in fact, the case. Figure 2.13 shows the autocorrelation coefficients for zonal mean zonal winds at 30°N latitude, which

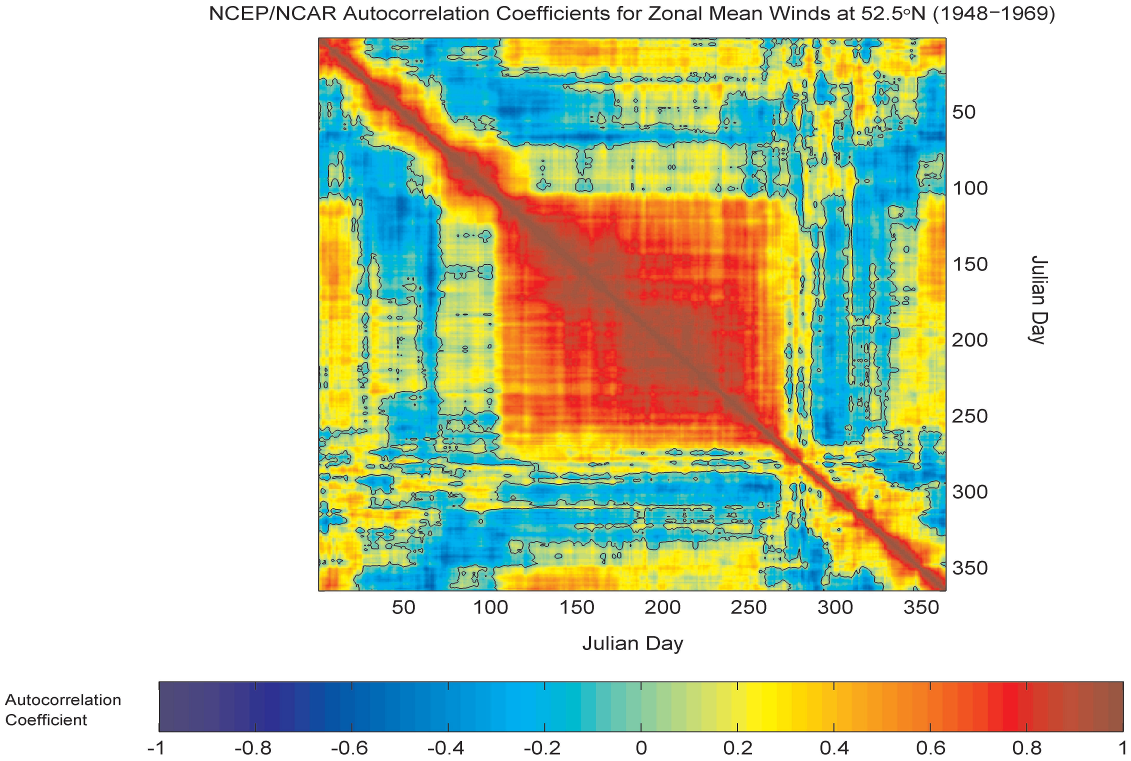

Figure 2.12: Autocorrelation coefficients for the 10-hPa zonally averaged zonal winds, at 52.5°N, calculated using years 1948-1978 of the NCEP/NCAR reanalysis. Note the high correlation as compared with Figure 2.10.

is close to another launch site in Palestine, TX (31.8°N, 95.7°W). The winds remain highly correlated past the average turnaround date at that latitude (which is, of course, much later than turnaround over Vanscoy). While the MANTRA science goals required the launch be from the Canadian mid-latitudes, other groups may find this information of use.

Not all is lost at mid-latitudes, however, since from the turnaround interval defined in §2.3, we defined a launch window that has provided good launch conditions in every year from 1993-2002. It is expected that this launch window will continue to hold into the future, since, upon examination of Figure 2.11, there does not appear to be a significant trend in zonal wind speeds over the 1979–2001 period. The launch window includes days 238-248 (August 26 through September 5). These dates are consistent with both data

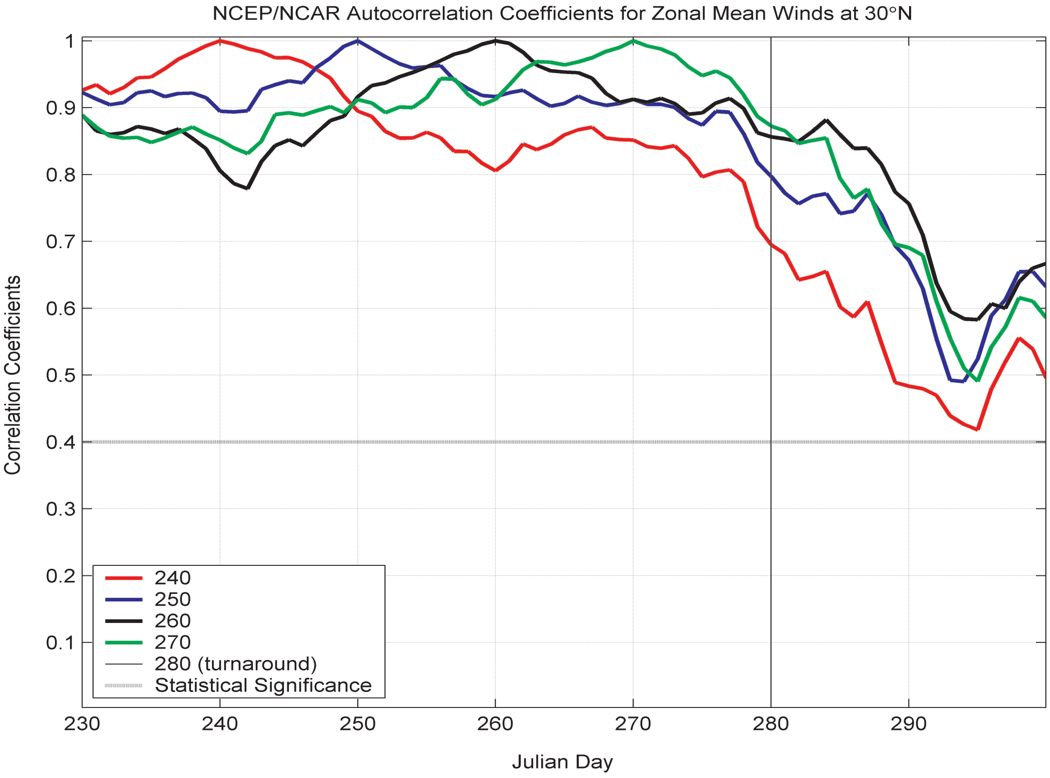

Figure 2.13: Autocorrelation coefficients between the 10-hPa zonally averaged zonal winds at 30°N for the NCEP/NCAR reanalysis for 1979–2003. A value above 0.4 is statistically significant.

sets: the NCEP/NCAR reanalysis and the MetO analysis data. The launch dates for the MANTRA balloons have all fallen within or very close to the window as well: in 1998, the balloon was launched on August 24; in 2000, August 29; in 2002, September 3; and 2004, September 1 and September 14. The September 14 launch, discussed in §4.4.4, was launched after turnaround was over.

# Chapter 3

# Fourier Transform Spectrometers and Balloon-Borne Constraints

## 3.1 Introduction

Solar absorption Fourier transform spectrometers (FTSs) have been used for decades both from the ground and on balloon platforms. These measurements have led to many important advances in our understanding of ozone chemistry at mid-latitudes, of which I will only describe a small selection. In her review paper, de Mazière [51] focuses on ground-based FTS measurements of atmospheric observations. She points out that ground-based networks, such as the Network for the Detection of Atmospheric Composition Change, have helped to develop our understanding of natural atmospheric variability and trends of the major atmospheric trace gases that affect climate (e.g. Rinsland et al. [52], Notholt et al. [53]), their transport, and their chemical correlations (e.g. Rinsland et al. [54]). These network measurements have also helped differentiate the naturally-derived from the anthropogenically-caused changes to our atmosphere (e.g. Trolier et al. [55], Griffith et al. [56]) and to assess the efficacy of international agreements such as the Montreal Protocol and its amendments.

The main advantages of measuring solar absorption by atmospheric trace gases from a balloon platform are the high spectral resolution, high vertical resolution and high signal-to-noise ratio [57]. Due to balloon-based FTS measurements, new spectroscopy has been discovered (e.g. Goldman et al. [58]); the first vertical profiles of HCl were measured (Farmer et al. [59]) and many nitrogen compound profiles were measured: NO and $NO_2$ (Rinsland et al. [60]), $HNO_3$ (Goldman et al. [61]), and $N_2O$ (Rinsland et al. [62]). More recently, an $NO_y$ budget was derived along with airborne and model estimates (Kleinböhl et al. [63]).

This chapter will discuss the basic theory behind Fourier transform spectroscopy (§3.2), as well as three common errors associated with Fourier transform spectrometers and their well-established solutions (§3.3.1, §3.3.2 and §3.4). A discussion will follow in §3.5 about the particular constraints on balloon-borne Fourier transform spectrometers and the common solutions that have been applied. The particular work that is the crux of this thesis will be discussed in Chapter 4.

## 3.2 Basic FTS Theory

A Fourier transform spectrometer (FTS) such as the U of T FTS passes collimated light through an input aperture, to be split by a beamsplitter into two paths (see Figure 3.1). One path reflects off a stationary mirror; the other off a moving mirror, controlled by a scan motor. The light recombines at the beamsplitter, and the recombined light reflects off of a focussing mirror (off-axis paraboloid), which focuses the light onto a detector. This intensity interference pattern (called an interferogram) produced at the detectors is then recorded with respect to the optical path difference (OPD) between the two mirrors. A Fourier transform is taken to derive a spectrum from the interferogram. The following mathematical treatment borrows from Griffiths and de Haseth [64], Bernardo [65], Davis et al. [66] and Chamberlain [67].

Mathematically, we consider a uniform, monochromatic plane wave, $\Psi$, with amplitude $2a$, angular frequency $\omega$ and wavenumber $\vec{k}$, traveling in direction $\vec{r}$ in time $t$:

$$\Psi(\vec{r},t) = 2a \cdot \exp[i(\omega t + \vec{k} \cdot \vec{r})].$$

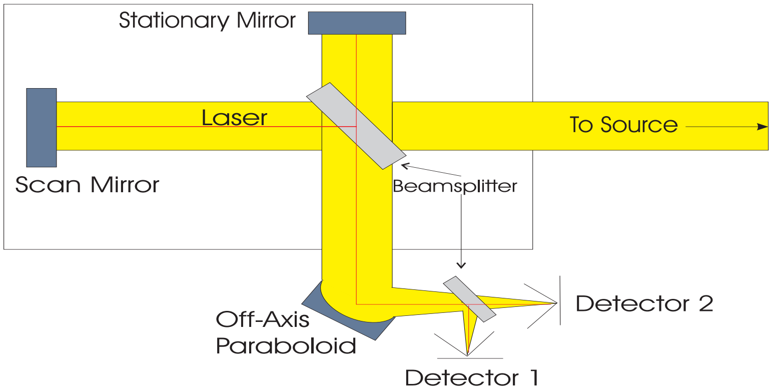

Figure 3.1: A schematic of a Fourier transform spectrometer. Light enters the spectrometer from the right, is split by the beamsplitter into two paths and recombined onto the detectors. The purpose of the laser will be discussed in §3.2.2.

This wave enters the interferometer and is split into two paths by the beamsplitter: one with a longer path than the other. We will denote the difference in path length between the two paths by setting the travel time of the wave in the second path to $t + \tau$.

$$\Psi_1(\vec{r}, t) = a \cdot \exp[i(\omega t + \vec{k} \cdot \vec{r})] \tag{3.2.1}$$

$$\Psi_2(\vec{r}, t) = a \cdot \exp[i(\omega(t + \tau) + \vec{k} \cdot \vec{r})] \tag{3.2.2}$$

When the two waves recombine at the beamsplitter, we get:

$$\begin{aligned} \Psi_{total}(\vec{r}, t) &= \Psi_1 + \Psi_2 \\ &= a \cdot \exp[i(\omega t + \vec{k} \cdot \vec{r})] + a \cdot \exp[i(\omega t + \vec{k} \cdot \vec{r})] \exp[i\omega\tau] \\ &= a \cdot (1 + \exp[i\omega\tau]) \exp[i(\omega t + \vec{k} \cdot \vec{r})]. \end{aligned} \tag{3.2.3}$$

Our detectors record only the intensity information from the recombined wave in Equation 3.2.3, which is related to the amplitude $A$ of the wave by $I = AA^*$, and so we need to consider only the amplitude of the wave:

$$A = a \cdot (1 + \exp[i\omega\tau]).$$

At this stage, we can convert to units that are more natural for Fourier transform spectrometry: the optical path difference (OPD) between the two arms of the interferometer,

$x$, and the wavenumber, $\sigma$. We know that $\sigma = \omega/(2\pi c)$, where $c$ is the speed of the wave, and that the distance traveled in the long path $x = c\tau$, so $\omega\tau = 2\pi\sigma x$, and:

$$A = a \cdot (1 + \exp[i2\pi\sigma x]). \tag{3.2.4}$$

The intensity is then:

$$I = 2a^2 \cdot (1 + \cos[2\pi\sigma x]).$$

Our detectors are AC-coupled: they record only the AC component of the signal, and so we keep only the cosine term of the equation:

$$I = 2a^2 \cdot \cos(2\pi\sigma x). \tag{3.2.5}$$

For polychromatic sources (such as the sun), we must integrate this over all $\sigma$, remembering that $a$, the source amplitude, is dependent on $\sigma$ as well:

$$I(x) = \int_0^\infty 2a^2(\sigma) \cdot \cos(2\pi\sigma x) d\sigma. \tag{3.2.6}$$

Since $a(\sigma)$ is real, this is mathematically equivalent to:

$$I(x) = \int_{-\infty}^{\infty} a^2(\sigma) \cdot e^{-i2\pi\sigma x} d\sigma. \tag{3.2.7}$$

We define $S(\sigma) \equiv a^2(\sigma)$ as the spectral intensity (the spectrum), and so we are left with a Fourier transform relating the interferogram, $I(x)$ and the spectrum $S(\sigma)$:

$$I(x) = \int_{-\infty}^{\infty} S(\sigma) e^{-i2\pi\sigma x} d\sigma \tag{3.2.8}$$

$$S(\sigma) = \int_{-\infty}^{\infty} I(x) e^{i2\pi\sigma x} dx. \tag{3.2.9}$$

If the interferogram is real and symmetric about the zero path difference (i.e. $I(x) = I(-x) = I^*(x)$), the sine part of the integral vanishes, and we are left with a cosine Fourier transform. This takes the form:

$$I(x) = \int_{-\infty}^{\infty} S(\sigma) \cos(2\pi\sigma x) d\sigma \tag{3.2.10}$$

$$S(\sigma) = \int_{-\infty}^{\infty} I(x) \cos(2\pi\sigma x) dx. \tag{3.2.11}$$

In a real instrument, the interferogram is digitized and has a finite optical path difference. The integrals then become sums of $N$ terms, where $N$ is the number of points making up the interferogram:

$$\begin{aligned} I(n) &= \sum_{k=1}^{N} S(k) \cos\left(\frac{2\pi(k-1)(n-1)}{N}\right), \quad n = 1, 2, ..., N && (3.2.12) \\ S(k) &= \sum_{n=1}^{N} I(n) \cos\left(\frac{2\pi(k-1)(n-1)}{N}\right), \quad k = 1, 2, ..., N. && (3.2.13) \end{aligned}$$

We can define our wavenumbers, $\sigma$, in units of $\text{cm}^{-1}$, and our optical path difference, $x$, in cm, given the sampling frequency of our interferogram, $\Delta x$, in cm:

$$\begin{aligned} \sigma_k &= \frac{k-1}{\Delta x \cdot N} && (3.2.14) \\ x_n &= (n-1) \cdot \Delta x. && (3.2.15) \end{aligned}$$

The resolution of a spectrum, $\delta\sigma$, is defined by the inverse of the maximum optical path difference (MOPD), $L$. The spectral range, $\Delta\sigma$, is defined by the sampling frequency.

$$\begin{aligned} \delta\sigma &= \sigma_k - \sigma_{k-1} = \frac{1}{\Delta x \cdot N} = \frac{1}{L} && (3.2.16) \\ \Delta\sigma &= \sigma_N - \sigma_1 = \frac{1}{\Delta x}\left(1 - \frac{1}{N}\right). && (3.2.17) \end{aligned}$$

In a typical FTS, $N$ is on the order of one million points, and Equation 3.2.17 becomes $\Delta\sigma \approx 1/\Delta x$.

### 3.2.1 Extended Source

The preceding analysis assumed a perfectly collimated point source, which is not realistically achievable. Any source will have a finite extent, subtending a solid angle $\Omega$. This causes beams of slightly different path lengths to recombine, replacing the path difference, $x$, in Equation 3.2.8 by an effective path difference, $x_{eff}$, that is dependent on $x$ and the divergence angle, $\theta$, by $x_{eff} = x \cos\theta$ (see Figure 3.2) [68, pp. 144]. Because $\theta$ should be very small:

$$x_{eff} \approx x\left(1 - \frac{\theta^2}{2}\right). \qquad (3.2.18)$$

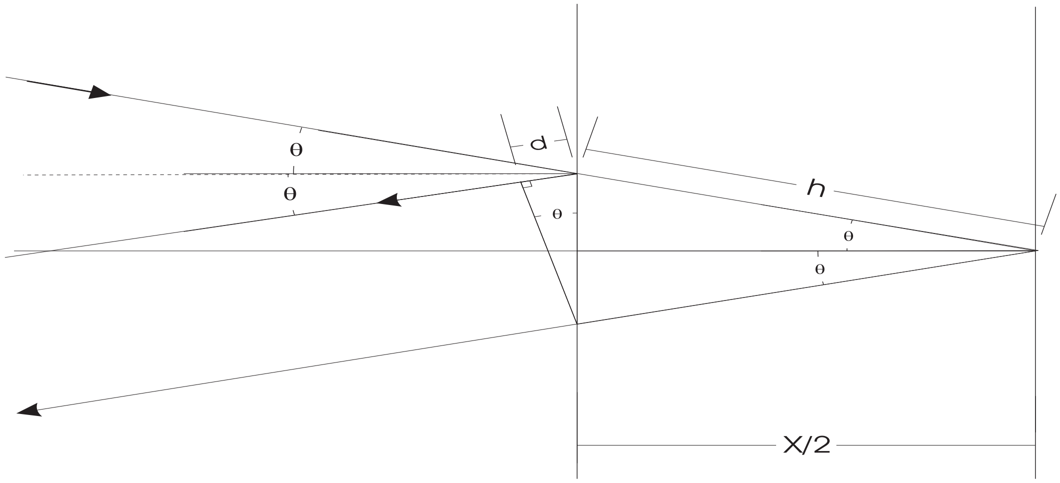

Figure 3.2: Extended source. The two vertical lines represent the two mirrors of the FTS, and so the path difference between them for an on-axis ray is $x$. Light enters from the top left at an angle $\theta$ to the on-axis ray, which is subtended by the source of finite extent. The distance 2h−d is $x_{eff}$. Figure reproduced from Bell [68].

The solid angle[1] is $\Omega = \pi\theta^2$, which yields,

$$x_{eff} = x\left(1 - \frac{\Omega}{2\pi}\right). \tag{3.2.19}$$

When this is replaced in 3.2.8, we get:

$$S_\Omega(\sigma) = \int I(x) e^{i2\pi x\sigma(1-\Omega/2\pi)} dx. \tag{3.2.20}$$

This represents the Fourier transform of the product of the two functions $I(x)$ and $e^{-i2\pi x\sigma\Omega/2\pi}$. We know the Fourier transform of $I(x)$: it is $S(\sigma)$. The Fourier transform of $e^{-i2\pi x\sigma\Omega/2\pi}$ is

$$\int e^{-i2\pi x\sigma\frac{\Omega}{2\pi}} e^{i2\pi x\sigma} dx = \delta\left(\sigma - \sigma\Omega/2\pi\right). \tag{3.2.21}$$

The delta-function ($\delta\left(\sigma - \sigma\Omega/2\pi\right)$) shifts the wavenumber from $\sigma$ to $\sigma\Omega/2\pi$ for a ray with the maximum angle in the solid angle. But we have multiple rays from different parts of the solid angle, so we essentially have multiple solid angles, ranging from zero (the on-axis ray) to $\Omega_m$, the largest solid angle. We therefore must integrate $\delta\left(\sigma - \sigma\Omega/2\pi\right)$ from

---

[1]
$$\Omega \equiv \int_0^{2\pi} d\phi \int_0^{\theta} \sin\theta d\theta = 2\pi(1-\cos\theta) \approx \pi\theta^2$$

$\Omega = 0$ to $\Omega = \Omega_m$, which results in a rectangular function that spans from 0 to $\sigma\Omega_m/2\pi$. In spectral space, then, we convolve the ideal spectrum, $S(\sigma)$, with a boxcar function of width $\sigma\Omega_m/2\pi$ [69].[2] This causes a "smearing" out of the wavelengths, reducing the resolution to $\overline{\delta\sigma}$. The central wavenumber, $\sigma_0$, is also shifted lower to $\overline{\sigma}$, because only wavelengths longer than the central path length will interfere at any given mirror position[3]:

$$\overline{\delta\sigma} = \frac{\sigma_0 \Omega}{2\pi} \tag{3.2.22}$$

$$\overline{\sigma} = \sigma_0 \left[1 - \frac{\Omega}{4\pi}\right] \tag{3.2.23}$$

To ensure that the desired resolution can be achieved, the solid angle must be limited, as the resolution is proportional to the solid angle in Equation 3.2.22. This can be done by reducing the solid angle subtended by the focussing mirror and aperture size of the detector. The desired resolution of the instrument ($\delta\sigma = 1/L$) can serve to limit the solid angle: we can insist that the resolution defined by Equation 3.2.22 be no greater than $1/L$. The maximum allowable solid angle would be:

$$\frac{\sigma_0 \Omega}{2\pi} = \frac{1}{L}, \tag{3.2.24}$$

$$\Omega = \frac{2\pi}{\sigma_0 L}. \tag{3.2.25}$$

The solid angle of a focussing mirror is defined by the focal length, $f$, and the radius of

---

[2] Alternatively, we can reverse the order of integration in 3.2.20, using the cosine transform for simplicity, first integrating with respect to $\Omega$:

$$S_\Omega(\sigma) = \int I(x) \int_0^{\Omega_m} \cos\left\{2\pi x\sigma\left(1 - \frac{\Omega}{2\pi}\right)\right\} d\Omega dx.$$

The central integrand reduces to

$$\int_0^{\Omega_m} \cos\left\{2\pi x\sigma\left(1 - \frac{\Omega}{2\pi}\right)\right\} d\Omega = \pi\Omega_m \mathrm{sinc}\left(\frac{\sigma x \Omega_m}{2\pi}\right) \cos\left(2\pi\sigma x\left(1 - \frac{\Omega_m}{4\pi}\right)\right).$$

The envelope of this function is a sinc function ($\mathrm{sinc}(x) \equiv \frac{\sin \pi x}{\pi x}$), which, upon Fourier transformation with respect to $x$, becomes a rectangular function with width $\sigma\Omega_m/2\pi$. The cosine function, which Fourier transforms into a delta function, implies that there is a shift of $\sigma - \sigma\Omega_m/4\pi$.

[3] The 4 in Equation 3.2.23 comes from a shift of half the maximum shift, since we must average over all incident angles within the solid angle, from 0 to $\Omega_m$.

the aperture, $r$, by the relation [66, pp. 71–72]:

$$\Omega = \frac{\pi r^2}{f^2}. \tag{3.2.26}$$

Substituting Equation 3.2.26 into 3.2.25, we get

$$r^2 = \frac{2f^2}{\sigma_0 L}. \tag{3.2.27}$$

For an instrument that measures at a maximum of 5000 cm$^{-1}$, with a MOPD of 50 cm ($L$ = 500 mm) and a focussing mirror with a focal length of 100 mm, the maximum radius for the detector element or aperture size is 0.28 mm.

### 3.2.2 Sampling and the Fast Fourier Transform

We need to sample the interferogram at exactly equally-spaced OPD positions. Since scanning motors do not have perfectly constant speeds, a laser beam is typically passed through the centre of the optics, creating a simple cosine interference pattern that is a function only of the OPD and not the speed of the scanning motor. The cosine signal is typically converted to a square wave, and the rising edge (or the falling edge or both edges) of the wave is then used to trigger the sampling of the interferogram at precise OPD positions. The laser that one chooses for this purpose defines the spectral range of the FTS; from Equation 3.2.17, we can see that the more often we sample an interferogram, the higher the frequency we can resolve. We can resolve frequencies up to half of the sampling frequency, a point called the Nyquist frequency. For example, if we use a HeNe laser, with a frequency of 15798 cm$^{-1}$, sampling on every rising edge, our Nyquist frequency is 7899 cm$^{-1}$. The spectral range in this case is limited to 0–7899 cm$^{-1}$. The spectral range is further limited by the main optical components in the FTS: the beamsplitter and the detectors.

An efficient algorithm for computing discrete Fourier transforms, called the fast Fourier transform (FFT), was most recently developed by Cooley and Tukey [70]. One of the peculiarities of the Cooley-Tukey algorithm is that it is most efficient when the number of points in the interferogram is $2^N$ where $N$ is any integer. This is because the algorithm takes advantage of the symmetry of the Fourier series, and divides up the problem into quickly computable pieces that can then be easily reconstructed [71]. To process the FFT most efficiently, we take the interferogram, $I(n)$, and add zeros after the MOPD point to increase the number of points to the nearest power of two, a process called zero-filling or zero-padding. Zero-padding an interferogram adds no information to the resulting spectrum, it simply interpolates between existing points (see Figure 3.3). The result of the FFT is the spectrum of interest.

The method described above applies to fully symmetric interferograms. Most real FTS instruments do not record perfectly symmetric interferograms, and in the next section (§3.3), we will discuss the most common error that occurs when recording an interferogram: phase errors.

## 3.3 Phase Errors and their Correction

There are two types of phase errors that can occur when recording an interferogram: errors that are wavenumber-dependent and those that are optical path difference-dependent. Wavenumber-dependent phase errors occur most commonly because the zero path difference position is not sampled, and also because optical components in the FTS respond differently at different wavenumbers. These phase errors are routinely corrected for, in a manner which will be described below.

Optical path difference-dependent phase errors occur due to sampling errors and alignment errors (such as scan tube shear or scan mirror tilt) [72]. These errors are typically minimized through careful optical alignment and although there has been at least one attempt to formulate a correction for them (Raspollini et al. [72]), they are typically quantified and characterized as the instrument line shape (ILS). The ILS will be discussed in §3.3.2.

Practical interferometers generally produce one of two types of interferograms: single-

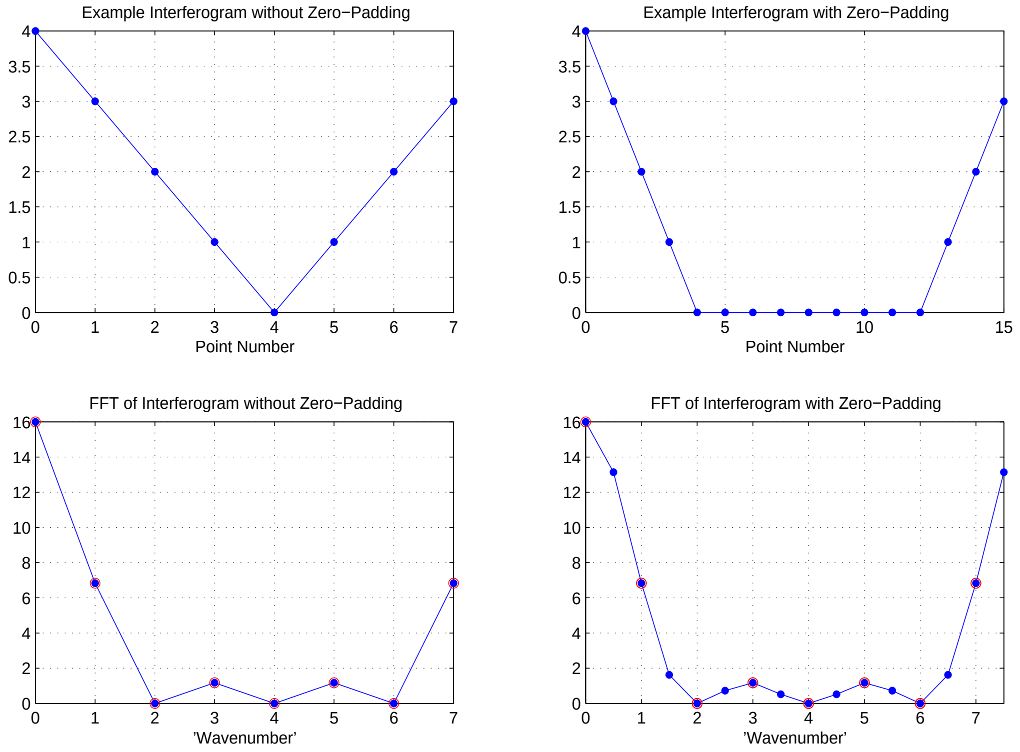

Figure 3.3: Zero-padding an interferogram does not add any information to the spectrum. In the top left panel, there is an interferogram without zero-padding. The top right panel shows the same interferogram with zero-padding. The panels below each of the interferograms show the FFT of the interferograms. The bottom left panel contains the same information as the bottom right panel, shown by the red circles, however, the bottom right panel has been interpolated. (Note the different x-axis ranges on the bottom two panels. The point located at wavenumber ∼7.5 in the bottom-right panel is required by the periodicity of the FFT.)

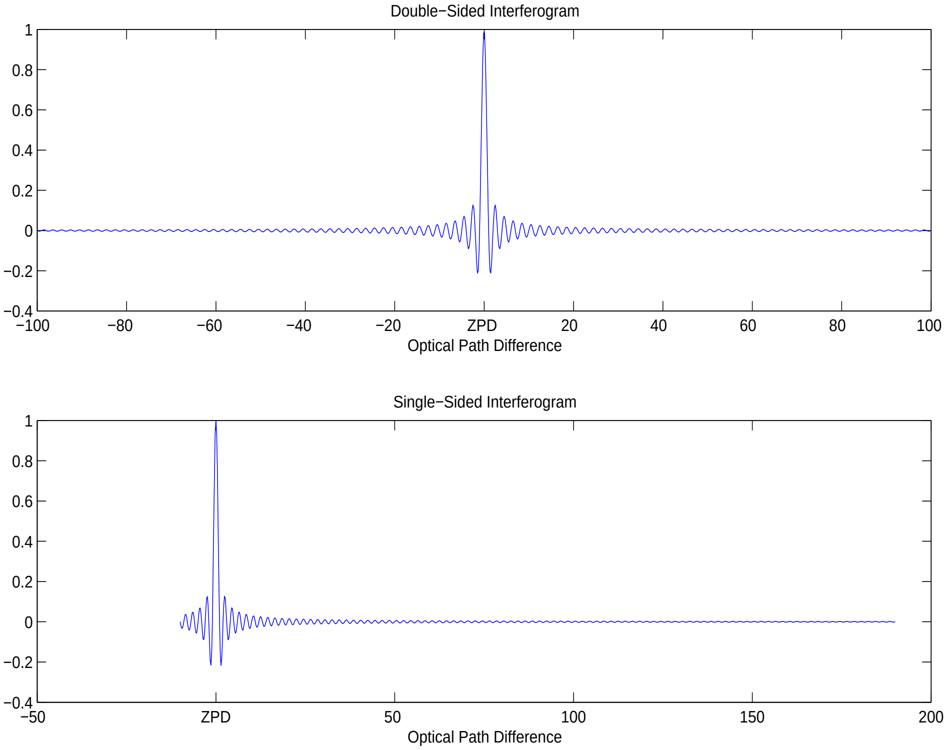

Figure 3.4: Double-sided (top panel) and single-sided (lower panel) interferograms. Each interferogram has an equal number of points. The single-sided interferogram has nearly twice the resolution of the double-sided interferogram.

sided or double-sided. Double-sided interferograms contain an (approximately) equal number of points on either side of the zero path difference (ZPD) position (see Figure 3.4). Single-sided interferograms contain far more points on one side of the ZPD than the other. The advantage of single-sided interferograms over double-sided ones is the savings in data storage, processing time and instrument size for spectra of equal resolution. The disadvantage of single-sided interferograms is that any phase errors they contain are more difficult to correct.

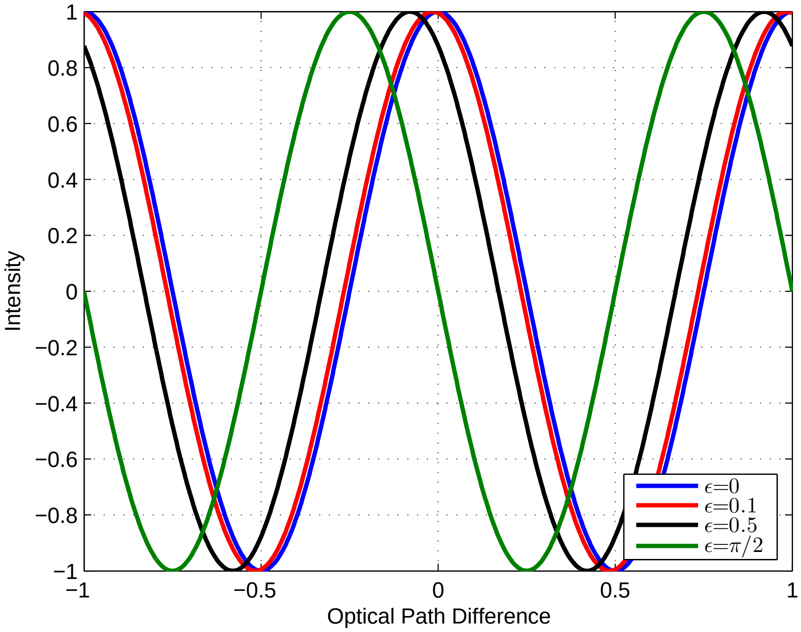

Figure 3.5: Cosine interferogram with different phase errors, $\epsilon$.

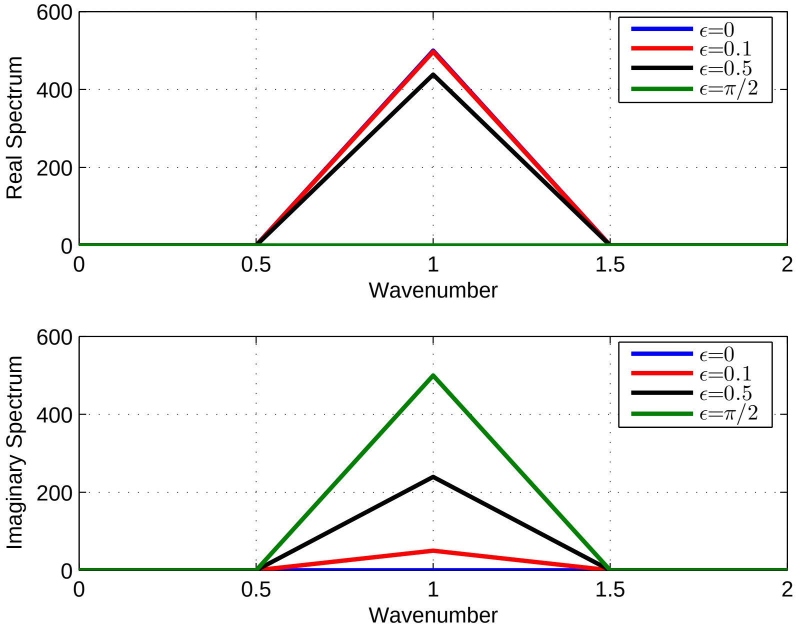

Figure 3.6: FFT of a cosine interferogram with different phase errors, $\epsilon$. Note that the larger we make $\epsilon$, the more information is transferred from the real part of the spectrum (top panel) to the imaginary part (lower panel), until we reach $\pi/2$, when the cosine function becomes a sine function and all the information is now contained in the imaginary part.

### 3.3.1 Wavenumber-Dependent Phase Errors

Wavenumber-dependent phase errors add an extra term, $\epsilon$, that is a function of wavenumber ($\sigma$), into the argument of the exponential function of Equation 3.2.8:

$$I(x) \quad = \quad \int_{-\infty}^{\infty} S(\sigma) e^{-i(2\pi\sigma x + \epsilon(\sigma))} d\sigma. \tag{3.3.1}$$

When taking the Fourier transform of an asymmetric real function, as in the examples in Figure 3.5, some of the information from the real part of the spectrum is shifted into the imaginary part (Figure 3.6).

Taking the modulus of the complex spectrum incorporates the imaginary component into the real component, however a double-sided interferogram is needed to create a full complex spectrum in this manner since we must know the asymmetry of the interferogram for each OPD point. If we only have single-sided interferograms, a better option is to correct for any phase errors in the interferogram and shift all the information into the real part of the spectrum.

There are two methods of correcting the phase errors in an interferogram: the Mertz method and the Forman method. The Forman method has the advantage that it can be applied iteratively, and so I will discuss that method here.

#### Forman Phase Correction

Forman, Steel, and Vanasse [73] demonstrated that a single-sided interferogram with only a short section of the interferogram in the negative OPD region is sufficient to fully reconstruct the spectrum. The main assumption is that the phase error, referred to as the phase angle, $\epsilon(\sigma)$, smoothly varies with wavenumber.

In this method, we symmetrize the originally asymmetric single-sided interferogram produced by the FTS. This is done by computing the phase spectrum and the transform of the phase spectrum, called the phase interferogram. The phase interferogram is then convolved with the original asymmetric interferogram to produce a phase-corrected, symmetric interferogram. The normal method of processing the interferogram, discussed in §3.2, is then used to create the desired (real) spectrum.

We begin with Equation 3.3.1, renaming our asymmetric interferogram $M(x)$:

$$M(x) = \int_{-\infty}^{\infty} S(\sigma) e^{-i\epsilon(\sigma)} e^{-2\pi i \sigma x} d\sigma. \tag{3.3.2}$$

The complex spectrum is defined by $m(\sigma) \equiv S(\sigma)e^{-i\epsilon(\sigma)}$. The phase spectrum, $e^{-i\epsilon(\sigma)}$, however, can be computed only from a double-sided interferogram, because it is a measure of how asymmetric the interferogram is about ZPD. So we use $n$ points from the short arm and $n$ points from the long arm of the asymmetric interferogram to compute a low-resolution complex spectrum by taking the Fourier transform.

Designate the short, double-sided portion of the asymmetric interferogram $M_s(x)$, the low-resolution complex spectrum $m_s(\sigma)$, and the low-resolution real spectrum $S_s(\sigma)$. Thus:

$$m_s(\sigma) = \int M_s(x) e^{2\pi i \sigma x} dx, \tag{3.3.3}$$

and $\epsilon(\sigma)$ can be computed by[4]:

$$\epsilon(\sigma) = -\arctan \frac{\Im(m_s(\sigma))}{\Re(m_s(\sigma))}. \tag{3.3.4}$$

We ultimately want to find the symmetric interferogram, $I(x)$, as seen in Equation 3.2.8:

$$I(x) = \int_{-\infty}^{\infty} S(\sigma) e^{-2\pi i \sigma x} d\sigma = \int_{-\infty}^{\infty} S(\sigma) e^{-i\epsilon(\sigma)} e^{i\epsilon(\sigma)} e^{-2\pi i \sigma x} d\sigma. \tag{3.3.5}$$

---

[4] Using $m_s(\sigma) = S_s(\sigma)e^{-i\epsilon(\sigma)} = S_s(\sigma)\cos(\epsilon(\sigma)) - iS_s(\sigma)\sin(\epsilon(\sigma))$, we get that

$$\begin{aligned} \Re(m_s(\sigma)) &= S_s(\sigma)\cos(\epsilon(\sigma)) \\ \Im(m_s(\sigma)) &= -S_s(\sigma)\sin(\epsilon(\sigma)) \end{aligned}$$

and, dividing $\Im(m_s(\sigma))$ by $\Re(m_s(\sigma))$, we get

$$-\tan(\epsilon(\sigma)) = \frac{\Im(m_s(\sigma))}{\Re(m_s(\sigma))}$$

which leads directly to 3.3.4.

We define a phase interferogram, $F(x)$, as the Fourier transform of $e^{i\epsilon(\sigma)}$, our phase spectrum:

$$F(x) = \int_{-\infty}^{\infty} e^{i\epsilon(\sigma)} e^{-2\pi i x\sigma} d\sigma. \tag{3.3.6}$$

Because the phase interferogram was created by truncating the asymmetric interferogram, $M(x)$, we have, mathematically, multiplied $M(x)$ by a boxcar function of length $2n$. The Fourier transform of boxcar function is a sinc function ($\text{sinc}(x) \equiv \frac{\sin(\pi x)}{\pi x}$), which has oscillations that extend to infinity. To avoid the spurious oscillations, the phase interferogram, $F(x)$, should be apodized. Forman suggests using the apodizing function

$$\left[1 - \left(\frac{\tau}{n}\right)^2\right]^2, \tag{3.3.7}$$

where $\tau$ is a vector spanning $-n$ to $n-1$. This eliminates the oscillations, but introduces a small error into the phase correction procedure [73].

Using the notation $\mathfrak{F}^{-1}(F(x))$ to represent the inverse Fourier transform of $F(x)$, and recognizing that $\mathfrak{F}^{-1}(M(x)) = S(\sigma)e^{-i\epsilon(\sigma)}$ (Equation 3.3.2) and that $\mathfrak{F}^{-1}(F(x)) = e^{i\epsilon(\sigma)}$ (Equation 3.3.6), we can substitute into Equation 3.3.5 to get:

$$I(x) = \int_{-\infty}^{\infty} \mathfrak{F}^{-1}(M(x))\mathfrak{F}^{-1}(F(x))e^{-i2\pi\sigma x} d\sigma. \tag{3.3.8}$$

Making use of the fact that the Fourier transform of the product of two functions is the convolution of the Fourier transforms of each of those two functions, we have:

$$I(x) = M(x) \circledast F(x). \tag{3.3.9}$$

Practically, this is an extremely useful relation. It means that one can symmetrize the asymmetric interferogram, $M(x)$, by convolving it with the Fourier transform of $e^{i\epsilon(\sigma)}$. The convolution can be computed with unequal sized vectors, as we have here, since $M(x)$ is the full interferogram and $F(x)$ is calculated from $M_s(x)$. We can compute $\epsilon(\sigma)$, and hence $e^{i\epsilon(\sigma)}$, from Equation 3.3.4, and so all the information we require is known.

The Mertz method differs from the Forman method at Equation 3.3.8. In the Mertz method, the phase spectrum, $e^{i\epsilon(\sigma)}$, is linearly interpolated to the resolution of the full complex spectrum. This is a valid process, since we have assumed that $\epsilon(\sigma)$ varies smoothly with $\sigma$. The full complex spectrum, $m(\sigma) = S(\sigma)e^{-i\epsilon(\sigma)}$, is multiplied by the phase spectrum to produce a corrected spectrum, $S(\sigma)$. The advantage of the Forman method over the Mertz method is that because the Forman method produces a corrected interferogram instead of a spectrum, should residual asymmetries still exist in the interferogram, the process can be iterated. Once the corrected interferogram is found, a cosine FFT can be applied to compute the spectrum.

### 3.3.2 Instrument Line Shape

After correcting the wavenumber-dependent phase errors, we are left to consider the optical path difference (OPD)-dependent ones. The line shape of an ideal FTS is a sinc function. This results from the fact that an interferogram has a finite path length, and so the infinite interferogram is multiplied by a boxcar function. In spectral space, this implies a convolution of the infinitesimal-resolution spectrum with a sinc function. A delta-function absorption line at $\sigma_0$ becomes a sinc function centred on $\sigma_0$.

Deviations from a perfect sinc function ILS (asymmetries, reduced sidelobes, etc.) are caused by OPD-dependent errors, and, given a well-constructed FTS, they can be minimized with careful optical alignment of the beamsplitter, flat mirrors, focussing mirror and detectors. The detector alignment causes the most common alignment error, since it must be placed with the correct aperture or element size (discussed in §3.2.1) in exactly the focal plane of the image. Detector alignment errors will be discussed below.

The measure of the attenuation of the signal as a function of OPD is called the effective apodization[5], which is computed from the real component of the Fourier transform of the ILS. The ideal effective apodization for each OPD position is unity. Imperfect alignment will reduce the effective apodization at large OPD.

The OPD-dependent phase error is a measure of the asymmetry of the ILS. It is

---

[5] Effective apodization is sometimes also be referred to as the "modulation efficiency." Both of these terms will be used throughout the thesis.

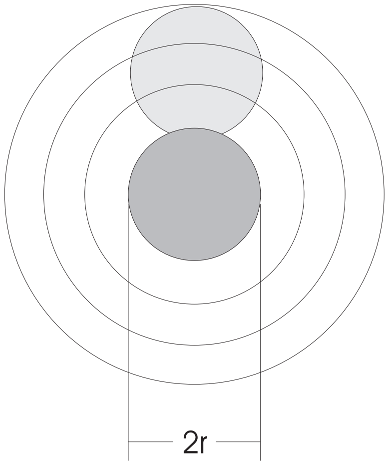

Figure 3.7: Off-axis detector. The dark shaded region is the aperture placed properly on-axis. The light shaded region is the aperture placed off-axis, increasing the effective aperture size. The black circles indicate possible locations of peaks and troughs of the Airy disk about the axis.

the angle between the real and imaginary parts of the Fourier transform of the ILS. An increase in the magnitude of the phase error indicates where the scan mirror tilts or the scan tube is sheared.

The ILS is calculated by measuring absorption lines of a gas whose properties (temperature, pressure, line parameters) are very well-known. Given this information, we can calculate the ideal absorption line widths and shapes, convolve them with a guess of the ILS, compare the results with the measured lines, and adjust tunable parameters to minimize the difference between them. This is done iteratively. Hase et al. [74] describe their widely-used software package called LINEFIT that is designed for this purpose.

### Detector Alignment Errors

Guelachvili [69] and Kauppinen and Saarinen [75, 76] discuss the line shape errors that occur due to placing the detector off-axis or out of focus. An off-axis placement of the detector increases the effective aperture size and hence solid angle, and unevenly illuminates the detector (Figure 3.7). This changes both the position and shape of a spectral line, shifting the central wavenumber down and broadening the lines.

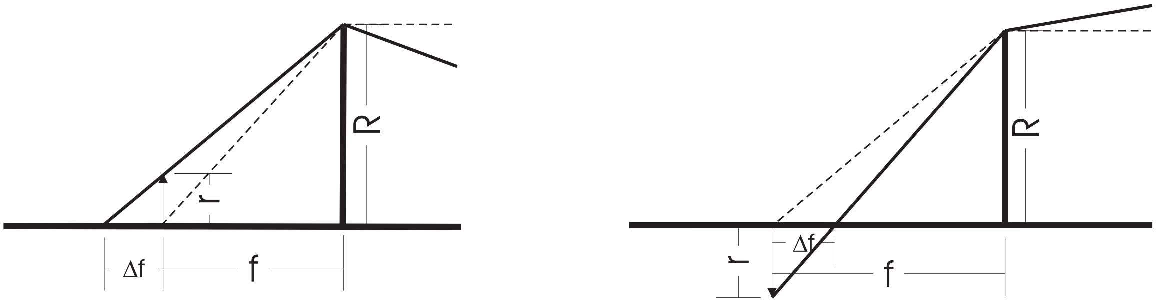

Figure 3.8: Off-focus detector. Left panel: Detector is further from the collimator (of radius R) than the focal point. Right panel: Detector is closer to the collimator than the focal point. The dashed lines are the on-focus rays.

An off-focus detector also shifts and smears the spectral line in the same way as the extended source does compared with a point source. Moving a point source $\Delta f$ away from the focal point of a collimator, effectively creates an extended source of radius $r$ at the actual focal point (Figure 3.8).

These errors are not easily corrected after the measurement has been taken. The best way to minimize these errors is to perform a very careful detector alignment, testing the alignment by retrieving the lineshape as described in §3.3.2.

In the next section, another common problem in FTS instruments will be addressed: the stability of the scanning mechanism.

## 3.4 Dynamic Alignment

As mentioned in §3.2, no real scanning mechanisms can control a mirror with perfectly smooth, constant speed: there will always be some variation in speed, which necessitates the use of a laser to record the precise mirror positions. Also unavoidable are slight changes in the angle of the mirror. With such changes, photons incident on one side of the mirror travel farther than those at the other, and when the light recombines at the beamsplitter, there will be photons from different OPDs recombining, yielding an error in the interferogram, essentially smearing out information. This is a problem that must be solved, and different FTS manufacturers solve it in different ways.

Brüker, a German company that manufactures FTS instruments, solved this problem by using corner cubes instead of mirrors, ensuring that the beam reflects exactly back along its original path, regardless of the angle of the corner cube. One drawback of this method is that the position of the moving corner cube with respect to the optical axis defined by the beamsplitter and stationary corner cube must be precisely on-axis, or errors in the instrumental lineshape will occur that mimic the error of an off-axis detector [75]. These errors are not dynamically adjustable, but must be adjusted manually. This problem is further complicated by the fact that the moving corner cube may have a variable displacement from the optical axis throughout the scan length.

ABB Bomem, a Canadian company, solved the problem by adjusting the angle of the stationary mirror to compensate for the scanning mirror. This is a process called Dynamic Alignment (DA). Because the FTS involved in this work was manufactured by ABB Bomem, and because a significant amount of effort was required to preserve this system in the final product, as discussed in §4.4.1, the DA system will be described in some detail here.

The DA system makes use of a beam-expanded laser (the laser that is also used for sampling), since its position will be measurably affected by the change in angle of the scanning mirror. The DA system measures the intensity and phase difference between five points on the laser image after it has passed through the interferometer [77, 78]. These points are called TX, TY, X, Y and R, and are measured by individual diodes.

The intensity is measured to ensure that the laser signal detected after the laser has passed through the instrument produces a cosine wave (what we will call fringes). If the laser signal is not producing fringes, then the two paths of the laser are not recombining properly, indicating a large difference in angle between the stationary mirror and the scanning mirror (assuming, of course, that there is no other physical blockage in the system). Signals TX and TY are focussed signals and are used to determine two things: one, whether fringes are detected as the scanning mirror moves down the scan tube, and two, whether the amplitude of the fringes is sufficiently large. If the fringes are not detected or the amplitude is not sufficiently high, the first mode of the dynamic alignment is activated: the spiral search pattern. In this case, the instrument is considered to be out of alignment. The spiral search pattern is the coarse search mode of the stationary mirror, to which the dynamic alignment pen motors are attached. The spiral begins in the centre of the stationary mirror's range of motion and expands first out to the edges and then back into the centre.

Once fringes of sufficient intensity are detected on TX and TY, only small adjustments to the angle of the stationary mirror become necessary in order to maintain the alignment of the system. Signals X, Y and R on the remaining three diodes compare the phase of the fringes. If the phase of the fringes between the three diodes is the same, then there is no angular difference between the two paths: the instrument is well-aligned. If there is a phase difference between the diodes, voltages are sent to the pen motors to finely adjust them to compensate for the phase difference. Proper interferograms can still be recorded during this mode of the DA because the adjustments are smaller than the wavelength between fringes.

One of the dangers of this DA system is that the system can think that it is properly aligned when, in fact, it is out by one fringe. The phase comparison and the intensity comparison can be within the tolerance range, but the angle is such that the recombined laser signal is 180° out of phase. This problem does occur occasionally, but it can be detected by carefully monitoring the external signal levels (a blackbody, the sun, etc.) at ZPD. If the ZPD signal is much lower than expected, then this might be the cause. However, once the DA system finds the proper alignment, it maintains its alignment well.

## 3.5 Balloon-Borne Fourier Transform Spectrometers

Engineering a balloon-borne FTS requires extra considerations that would not be required of a ground-based FTS. There is limited power available for a balloon-borne FTS, limited space on the gondola and mass restrictions. The FTS must be relatively compact, able to withstand environmental constraints, able to function autonomously and be commanded remotely, and able to send its data to the ground during a flight. The instrument must also have a sunseeker, since our FTS instruments measure solar absorption during sunrise and sunset.

In some cases (and in the case of the MANTRA campaigns), a launch crew supplies the balloon platform, which includes a telemetry system with uplinks for sending commands to the instruments, and downlinks to relay data back down to the ground.

### 3.5.1 Environmental Constraints and Solutions

When engineering an FTS for high-altitude measurements, one must ensure that the instrument can withstand pressures below 5 hPa and ambient temperature swings from 20°C to −60°C.

The pressure constraint affects three aspects of the instrument: moving hardware, the control computer hard drive, and the electronics. Low pressures affect lubricants in moving parts by breaking them down or increasing their viscosity. This can be alleviated by using vacuum-rated motors and lubricants.

Commercial hard drives require air pressure to function properly. The head of the reader sits on a small cushion of air, to ensure that the head does not scratch the surface of the drive. At high altitudes, this air is no longer available. There are two solutions to this problem: the first is to pressurize a hard drive, the second is to use a Compact Flash (CF) card or other solid state drive. The advantage of using a pressurized hard drive is that storage sizes are large, the drives themselves are relatively inexpensive, and installing software and operating systems is simple. The disadvantages are that building a pressurized case is difficult and expensive, and the drives tend to be heavier and larger as a result. The second option, using CF cards, has the advantage of requiring no pressurized case. Moreover, CF cards are very small (9 $cm^2$) and lightweight, have sufficient storage for a single balloon flight (currently up to 8 GB) and are fairly inexpensive. The disadvantage to using a CF card to replace a hard drive is that it is recognized by most operating systems as a removable device, and so many current off-the-shelf operating systems cannot be installed on it. Using custom-made or older operating systems is the typical solution to this problem. Another disadvantage to using a CF card is the limited number of read/write cycles per card. This is not a serious problem, however, because the cards are inexpensive and can be replaced frequently.

In electronics that draw significant power, the pressure constraint becomes a heat dissipation problem, as most off-the-shelf electronics cool by convection. Convection is very inefficient at low pressures, leaving radiation and conduction as the only two options to remove heat from the electronics. Because conduction is far more efficient than radiation, most electronics are fitted with conductive metals to pull heat away from the heat-generating part of the instrument, into a metal plate, or even the payload itself. Another reason to limit power consumption for a balloon-borne instrument is that all instruments on a balloon platform run on batteries. These batteries are expensive, heavy and disposable. The capacity of a battery is limited, and so instruments that require a lot of power must balance power consumption with a mass increase to their instrument. An increase in mass to the payload affects the ultimate altitude (called the float height) that the balloon can reach. Typically, stratospheric balloon campaigns such as MANTRA require that the float altitude be well above the ozone peak ($\sim$24km), to satisfy their scientific requirements (e.g. measure full vertical profiles of $O_3$).

The size of the gondola also constrains the size of the instrument. The MANTRA gondola is around 2 m by 2 m by 2 m, and up to 15 instruments must fit on the payload simultaneously. The FTS instrument must therefore be shorter than 2 m in any dimension in order to fit within the gondola structure.

### 3.5.2 Control Software

Control software, beyond controlling the basic functions of the instrument (the scan motor, dynamic alignment, and data storage), must be robust: it should be able to receive commands from the ground, send data down to the ground, and function usefully even if there are communications breakdowns.

Typically, flight software will contain an automatic schedule that dictates when to record data, at what resolution and how quickly. The schedule is modified if the instrument receives confirmed commands from the ground. It is wise to both downlink the interferograms during the flight and also store the data on-board for retrieval after the payload has landed. This will ensure that in the unlikely event that the payload is destroyed upon landing, the data will have been safely recorded on the ground, but if a problem arises with the telemetry system, the complete data set can be retrieved after the flight.

Recording and monitoring the instrument's housekeeping data, which consists of temperatures, voltages and other instrument status information, is critical during a flight. The more information we have about the status of the instrument, the better equipped we are to prevent damage and understand and analyze the data.

### 3.5.3 Solar Pointing

To retrieve vertical information about atmospheric composition from a balloon-borne FTS, solar absorption by atmospheric trace gases is measured during sunrise and sunset. We must, then, have a reliable method of ensuring that the sun is properly directed into the instrument. This requires a solar tracker.

Sunset or sunrise on a balloon platform at an altitude of, say, 40 km, would cover a set of elevation angles from $-6°$, when the sun is just at the horizon, to 0 degrees, when the sun is at a 90° zenith angle. For a tangent height, $H_t$, radius of the Earth, $R_e$,

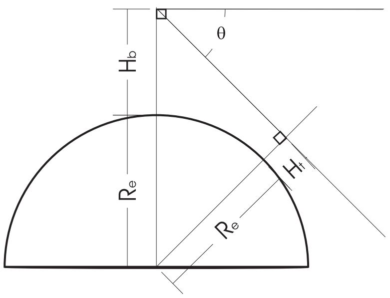

Figure 3.9: Occultation solar angle geometry

balloon height, $H_b$, and the elevation angle, $\theta$, as in Figure 3.9, we have the relation:

$$\cos\theta = \frac{R_e + H_t}{R_e + H_b}.$$

With a tangent height of zero and balloon height of 40 km, the lowest angle at which the sun can be seen is $\theta = -6.4°$.

There are three methods of tracking the sun on board a balloon platform. The first method is to have no gondola control, and use a dedicated sunseeker that tracks the sun 360° in azimuth and $0 - 180°$ in the zenith. Integrating the instrument onto the payload is trivial in this case, because the sunseeker does not depend on the orientation of the gondola to track the sun. One (rare) problem with this method is that if the payload happens to be oriented in such a way that the gondola's structure blocks the sun to the sunseeker, there is no way to recover. These sunseekers also tend to be heavy [79], costly, consume a lot of power and each instrument with pointing needs would require their own sunseeker. This would be a viable option if the FTS were the only instrument on the payload.

The second method is to control the gondola itself, with both azimuth control and a pointing table for elevation control, such as the system designed by Quine et al. [80]. The instruments can then be coupled to the pointing table for their solar beam. In practice, however, this has two main drawbacks. The first is that the gondola pointing control, particularly the azimuthal control, is rarely sufficient for FTS measurements, which require ∼1 arcmin precision (∼0.02°).[6] The second drawback is that even if the azimuthal control were good enough, we would need precise alignment with the pointing system. On the MANTRA 2004 payload, as an example, there were five instruments that measured solar absorption by occultation. The solar alignment of such instruments on a gondola structure is a notoriously difficult problem, especially from a logistic point of view. Gondolas are not built to optical precision and so alignment must occur outdoors on a clear day. (Some rough alignment can be done with a lamp source, but all final positions are determined with the sun.) Each instrument ideally needs at least a few hours with the gondola without other instruments on board, during a day when the skies are clear, creating significant delays in flight preparation.

The third method combines the advantages of each of the first two methods. This method was also used by Hawat et al. [81]. The method depends on some azimuthal control from the main gondola pointing system, and uses a small suntracker that has a tracking range covering a small range of azimuthal and elevation angles (a "delta-tracker"). The advantage of this third method is that the trackers remain small, low mass, and draw little power, while still allowing for a much simpler method of aligning the instrument with the payload. First, the instrument can be aligned to the delta-tracker off the payload, then integrated onto the payload without any further adjustment, since the delta-tracker will take care of any small differences between the instrument and the gondola pointing system.

---

[6] This number is a conservative approximation that is also found in Hawat et al. [81]. The U of T FTS field of view, for example, is 5 mrad, which is ∼0.3°. The solar diameter is ∼0.5°. It is desirable to ensure that the pointing accuracy does not allow the edges of the solar disk to enter into the FTS field of view, and so the pointing accuracy (in both azimuth and elevation) must be much better than 0.1°, and should probably be better than half that (0.05°).

# Chapter 4

# The University of Toronto's Balloon-Borne FTS*

## 4.1 Introduction

This chapter will focus on the specific work that was done on the U of T FTS, in order to prepare it for flight aboard the MANTRA 2002 and 2004 balloon payloads.

In §4.2, I will describe the U of T FTS as it was received in 2001 from the Meteorological Service of Canada (MSC). In §4.3, I will discuss the changes made to the U of T FTS for the 2002 launch, and describe the 2002 flight. In §4.4, I will describe the extensive upgrade to the FTS, and how it fared on the MANTRA 2004 balloon. Section 4.5 will discuss the results of this work.

## 4.2 The FTS in Its Original State

The MSC loaned the FTS to the University of Toronto in 2001, an instrument that was built by ABB Bomem (then called Bomem, Hartmann and Braun) in the 1980s. It is a DA-series FTS and was updated in the mid-1990s with the most modern electronics available at the time, including what is still today the most modern dynamic alignment electronics. It is a Michelson-type FTS with a maximum optical path difference of 50 cm, a 5-cm input aperture and a spectral range of 1200–5000 cm$^{-1}$ (2–8.3 $\mu$m), constrained by

---

*A summary of this work is published in Wunch et al. [39]

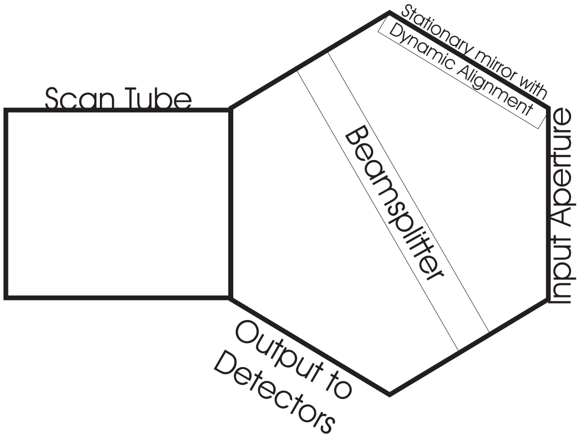

Figure 4.1: The U of T FTS hexagon.

a $CaF_2$ beamsplitter, germanium solar filter and two simultaneously-measuring detectors: a mercury cadmium telluride (MCT, or HgCdTe) detector and an indium antimonide (InSb) detector. The instrument had originally been designed as a ground-based solar absorption FTS, and during its upgrade in the 1990s, had its laser hermetically sealed with the intention of one day completing the work required to create a balloon-borne FTS.

The instrument came in two pieces: an electronics box and the spectrometer itself. The electronics box contained the power supplies, a 486 computer and an electronics card cage. The original software was embedded in the BIOS chip of the 486 motherboard and manually controlled all the main functions of the spectrometer in a simple and repeatable way. The software controlled 8 electronics boards: a microprocessor, through which the other boards were controlled, the sampling board, which controlled the data collection by two analog-to-digital converter boards, a speed and search control board that controls the scan motor through the dynamic alignment, a solenoid board that controlled a white light source inside the instrument and two miscellaneous electronics boards. A second, external, computer was necessary for the interface between the spectrometer and the user. The interface software is called “PCDA”.

The heart of the spectrometer hardware is the hexagon, which houses the beamsplitter

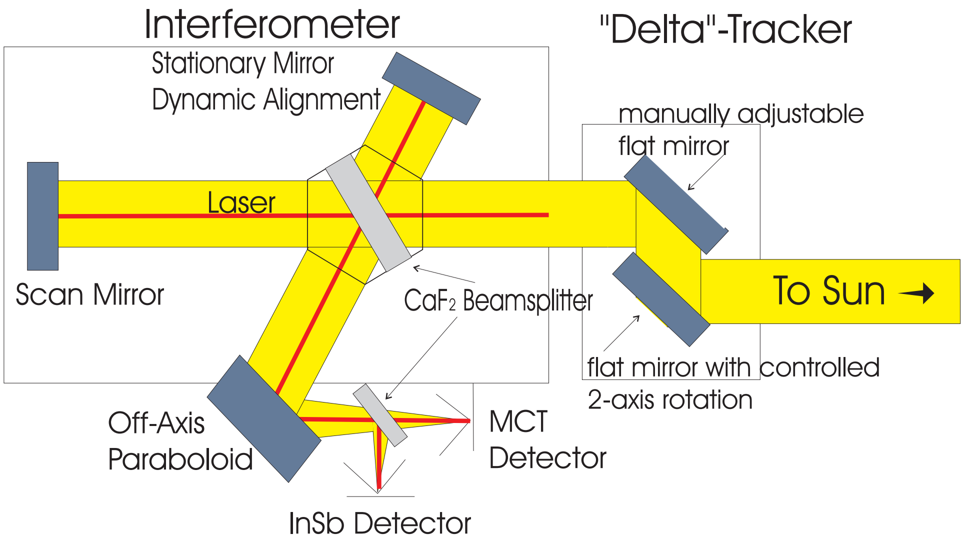

Figure 4.2: U of T FTS optical layout.

and stationary mirror, and connects the scan tube to the laser optical board and the detector mount (Figure 4.1). The scan tube is a rigid aluminum tube that contains the scanning mirror, motor and drive belt. The scan motor is a brushless tachometer that is used because of its zero backlash and its relatively smooth motion [77]. The moving mirror sits on the drive belt that runs the length of the scan tube. At either end of the scan tube there is a mechanical switch that is used in the software to reverse the direction of the mirror. The laser optical board sits atop the hexagon and holds the laser and all the laser optics and detectors. The laser beam passes through a beam expander, and then through prisms that deflect it through the optical centre of the interferometer. The interfering beams are then reflected back onto the laser optical board, where the beam spans 5 diodes, resulting in the signals X, Y, R, TX and TY, described in §3.4.

The detector mount connects to the hexagon and holds the two detectors and the off-axis parabolic mirror that focuses the collimated light from the interferometer. The InSb detector is housed in a down-looking dewar that holds liquid nitrogen to cool the detector and reduce noise. The MCT detector is mounted in a side-looking liquid-nitrogen dewar. Figure 4.2 shows a schematic of the U of T FTS optical layout.

## 4.3 The U of T FTS on MANTRA 2002

The obvious things that needed to be addressed for the 2002 flight were the power supplies, the software, the detector mounting system, and the solar pointing system. The power supplies in the U of T FTS were not vacuum-rated and so they were replaced with off-the-shelf VICOR DC/DC converters that are very efficient (up to 80%). This also helped to reduce the mass and power consumption of the FTS.

While PCDA is suitable for ground-based lab measurements, it is insufficiently robust for ballooning, which requires autonomous and remote control, and the ability to access all the housekeeping information. To add automated control to the PCDA software, a software control layer was written in LabVIEW, using a Dynamic Data Exchange (DDE) link between the LabVIEW program and PCDA. Unfortunately, the DDE link only allowed for one-way information exchange—to be exact, LabVIEW could send commands to PCDA, but not receive any information from it. This caused problems creating control software that is robust and reliable: intelligent decision-making on the part of the LabVIEW software was next to impossible. For example, if signal levels were too low, PCDA could not record data and would give no indication that it had stopped recording. (This particular problem was solved by monitoring the filenames written to the hard drive and if the expected filename did not exist, re-sending the scan command, but PCDA could not be forced to record data under low-signal conditions.)

Another problem was that the housekeeping data that PCDA monitored could not also be monitored by the LabVIEW program. Kaley Walker, with assistance from Tom McElroy, David Barton, and Akira Ogyu put together electronics to monitor the housekeeping data. Temperatures and voltages were read in to a Field Programmable Gate Array (FPGA) and sent to the ground using a slow, 300-baud downlink, independent from the instrument.

The detector mount was not durable enough for flight—any force on the mount bent the metal. Further, the mounts had no fine adjustments to precisely direct the light onto the detectors, other than manually moving the detector in its mount. Since alignment must be precise to ≪0.5 mm, very fine, repeatable adjustment capabilities are required. Spectral Applied Research rebuilt the detector mount, and installed a two-axis micrometer stage to hold the off-axis parabolic mirror, and an adjustable beamsplitter between the two detectors. This improved the detector alignment enormously; however, since they only addressed two of the three axes required for full alignment, the detector position had to be manually adjusted in the third axis.

Our solar pointing for the 2002 flight was controlled by the main gondola's pointing system, using a pick-off mirror mounted to its pointing table. The gondola pointing system is described by Quine et al. [80]. The pointing table performed fine elevation control to ±0.086° ($1\sigma$), and the entire gondola was stabilized in azimuth to ±3.1° ($1\sigma$). This pointing accuracy was not sufficiently precise for the FTS.

### 4.3.1 The MANTRA 2002 Flight

The launch of MANTRA 2002 occurred on September 3rd at 02:02 local time. As the payload passed through the tropopause, the top mount, the joint between the cables that attach to the gondola and the flight train, froze and could not rotate (see Figure 4.3). This meant that the payload could not be decoupled from the flight train and the pointing system could not stabilize the payload in azimuth. The payload, as a result, rotated through sunrise and most of the day. During sunset, the pointing system parameters were optimized, and the payload briefly stopped rotating. The payload was, however, oscillating in azimuth enough that signal levels were too low for PCDA to record data.

No scientific data was retrieved from the U of T FTS during the MANTRA 2002 launch. The housekeeping electronics, however, worked well, and indicated that the instrument hardware performed well—the voltages and temperatures were all within acceptable levels and, except for the processor temperature, were stable (see Figures 4.4–4.6). The vertical lines indicate the times of launch, sunrise, high-sun, and sunset. Be-

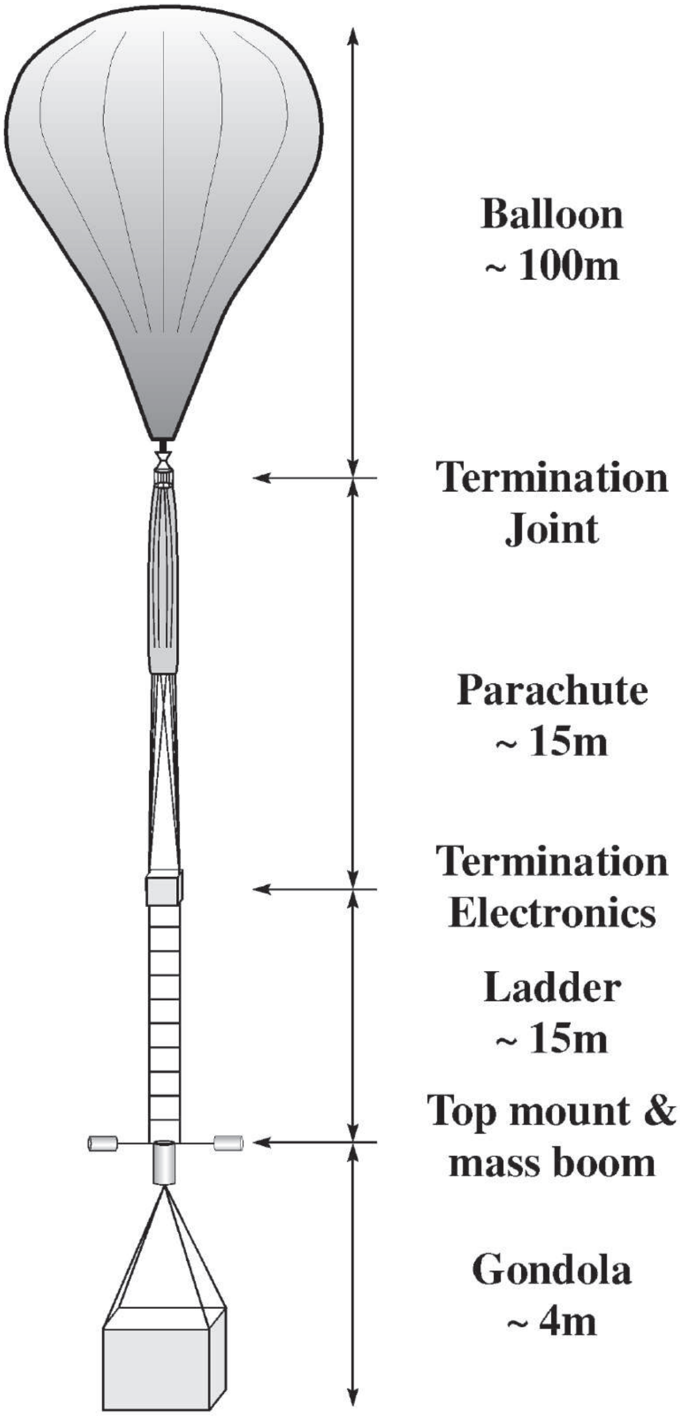

Figure 4.3: A typical flight train. Figure reproduced from Quine et al. [80].

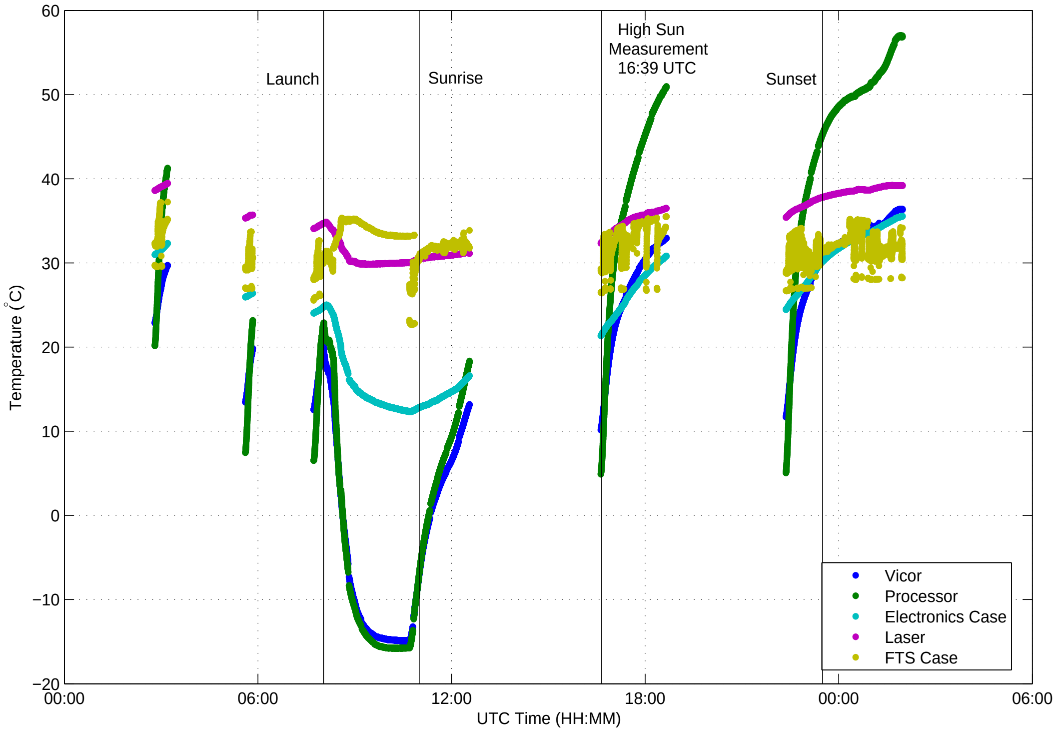

Figure 4.4: Temperatures from the U of T FTS during the MANTRA 2002 flight. The vertical lines indicate the launch, sunrise, high sun, and sunset times. The instrument and computer were off when there is no data, and during the time between launch and sunrise, the computer was left on while the instrument was turned off.

tween launch and sunrise, the instrument was turned off to conserve power, but the computer was left on, which is the cause of the sudden drop in FTS voltages and temperatures. The 28-volt line in Figure 4.5 measured the battery input to the FTS, which also powers the computer, so it will not drop to zero when the instrument is off and the computer is on. The laser intensity signals are invalid while the instrument is off (Figure 4.6). These housekeeping data show that a better method of removing heat from the processor was needed. The lack of interferometric data indicated that the pointing accuracy of the gondola pointing system was not sufficient to acquire solar spectra.

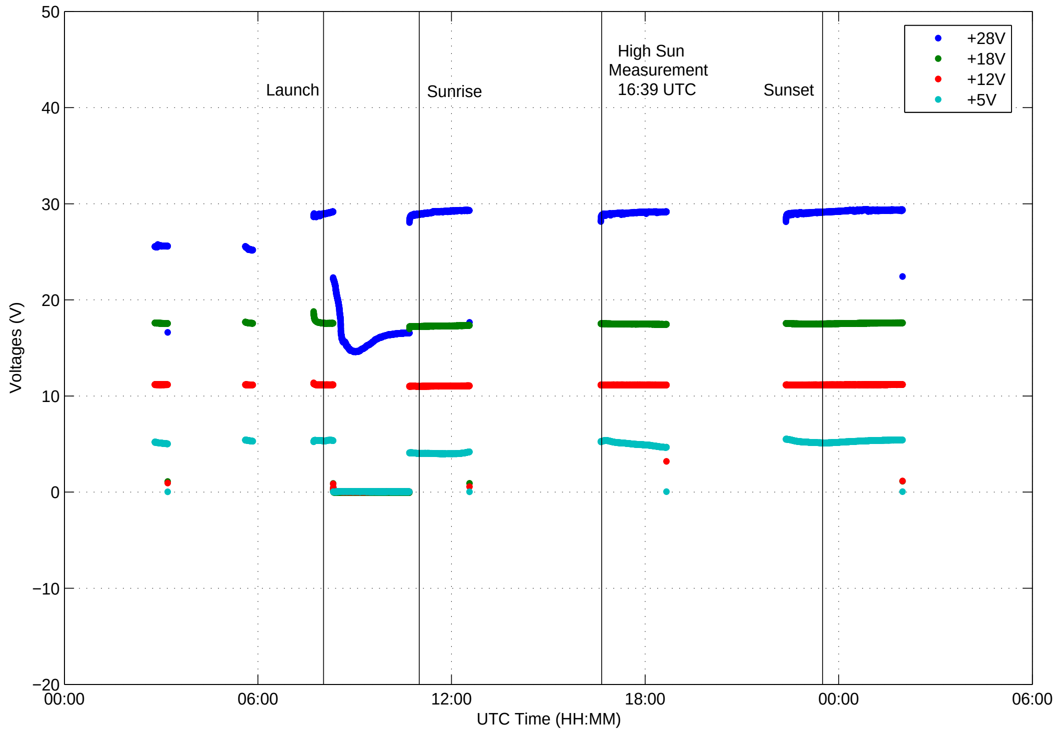

Figure 4.5: Voltages from the U of T FTS during the MANTRA 2002 flight. The vertical lines indicate the launch, sunrise, high sun, and sunset times. The instrument and control computer were off when there is no data, and during the time between launch and sunrise, the control computer was left on while the instrument was turned off. The 28-volt line was measuring the battery voltage, which does not drop to zero when the instrument is turned off. The 18V line measured the preamplifier voltage to the detectors, the 12V and 5V lines measured the power to the PCDA computer (not the control computer).

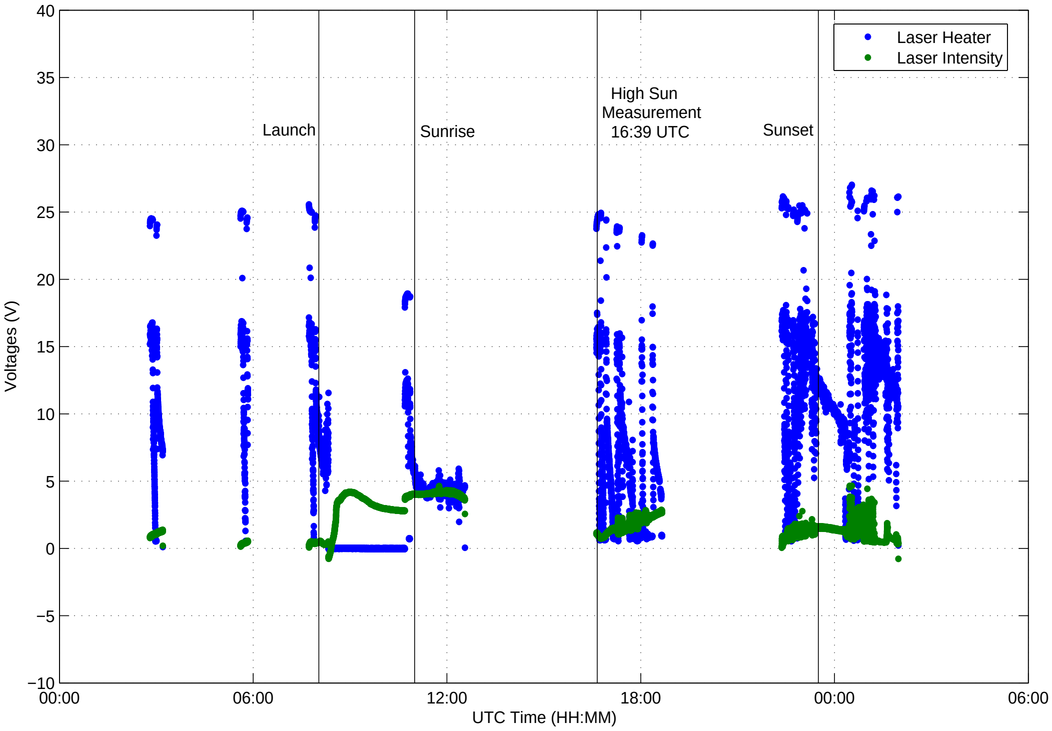

Figure 4.6: Laser status from the U of T FTS during the MANTRA 2002 flight. The vertical lines indicate the launch, sunrise, high sun, and sunset times. The instrument and computer were off when there is no data, and during the time between launch and sunrise, the computer was left on while the instrument was turned off.

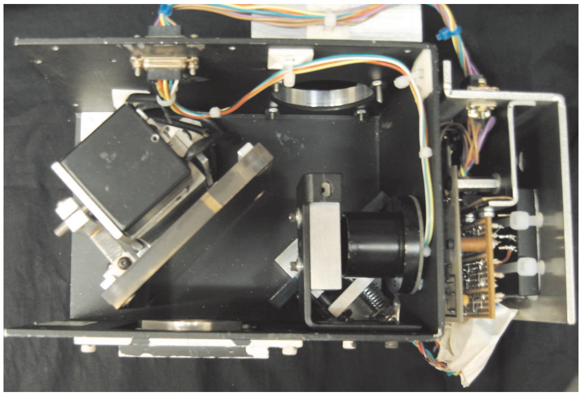

Figure 4.7: The delta-tracker. Light enters from the bottom left of the tracker onto the gold mirror in the centre of the tracker, which is attached to two pen motors that control its angle. Light is reflected off the mirror onto a 45° mirror and into the FTS through the hole on the top right of the tracker.

## 4.4 The U of T FTS on MANTRA 2004

The main lessons learned from the 2002 launch of the U of T FTS were: one, to ensure that the U of T FTS is less dependent on the pointing system (especially in azimuth) and devise a better method of solar alignment with the pointing system; two, to obtain new detectors, as the old ones were borrowed from the University of Denver; three, to modify the detector mounts to include z-translation capability for the InSb detector (the MCT detector already had z-axis adjustment); and, four, to remove PCDA, replacing it with robust LabVIEW control software with embedded housekeeping records.

To address the first item, a delta-tracker, which had flown in previous balloon campaigns on a different FTS, was acquired from Environment Canada. The tracker has a ±10° tracking range in elevation and azimuth and an electronics board that independently controls it from the instrument (Figure 4.7). This was ideal for use on board the payload in order to complement the gondola pointing system's azimuth control. Integrating the U of T FTS with the rest of the payload became simple, and ground-based measurements could be set up by adding two mirrors in front of the tracker. The extra mirrors were necessary because during mid-day, the sun can reach up to 45° in elevation, outside of the range of the delta-tracker.

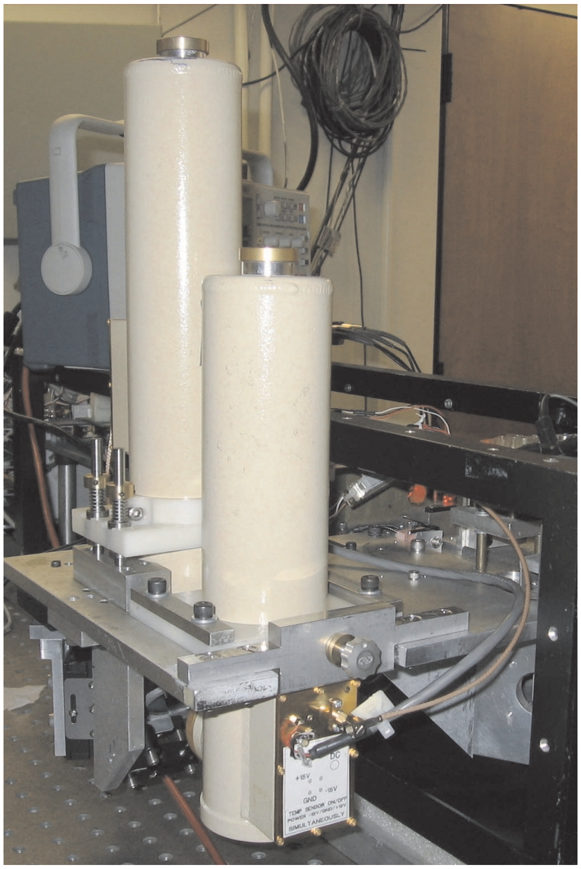

Figure 4.8: Detector mount. There is a precision screw controlling the x-translation of the MCT detector (the detector closer to the camera). On the InSb detector, there are bearings that slide around three posts (two of which are visible) and a precision screw (not visible) that guide its z-translation adjustment.

To address the second item, we purchased new detectors, with 24-hour dewars and preamps mounted inside the jacket of the detectors. This improved the noise levels of the detectors because the preamp connections are shorter, reducing pickup noise. Both detectors (InSb and MCT) are photovoltaic. MCT detectors are typically photoconductive; however, over a range of input intensities, photovoltaic detectors produce a more linear output voltage.

To address the third item, we made further modifications to the detector mount, adding some more fine control to the mount by allowing the detectors to slide in their third axis more easily. Since the MANTRA 2004 launch, we have also included micrometer control in the third axis of each of the detectors, for more accurate and repeatable detector

| Original Board | Replacement |
|---|---|
| Microprocessor | EPIA 500 MHz computer |
| Sampling Board | Schmidt Trigger; 32-bit LabJack digital counter |
| Analog-to-Digital Converters | MCC 16-bit ADC (4 simultaneous channels) |
| Speed and Search Control | Unchanged |
| Solenoid Board | None |

Table 4.1: Replacement boards for the original Bomem electronics.

alignment (see Figure 4.8).

To address the fourth item, we looked to PCDA to determine how it controlled the FTS. There are three main components of the U of T FTS that must be controlled to have a working interferometer: the scanning motor, the dynamic alignment and the data collection (including interferograms and housekeeping data). All of these components are controlled through the PCDA interface, and so it had to be replaced in order to have full control over the instrument. This required the removal of the computer inside the electronics box, because the control software is hard-coded into the BIOS of that computer. Since there was little documentation as to how the control software interacted with the electronics, we had to deconstruct the electronics system with circuit diagrams and a logic analyser. Most of the boards were straight-forward and we found inexpensive off-the-shelf boards to replace them. Table 4.1 lists these replacements. Because nearly eight years had passed since the last electronics upgrade to the FTS, the off-the-shelf components we used were smaller and more efficient than the originals. Our main concern was to keep intact the speed and search control board that controls the scan motor and dynamic alignment system.

The microprocessor and embedded computer were replaced by a 500 MHz EPIA computer and LabVIEW software (discussed in §4.4.2). The sampling boards were replaced by a Schmidt trigger filter to condition the laser signal, which was then digitized by a 32-bit digital counter. Housekeeping signals were brought in from the instrument to three LabJack 12-bit analog-to-digital converters (ADCs). We monitor all internal voltages (±28 V, ±15 V, +5 V), a variety of temperatures and a number of other important signals: the laser heater, laser intensity and the sunseeker mirror positions. The LabJack board contains the 32-bit counter channel used for the laser sampling.

The original ADCs had built-in electronics to perform a gain change after a certain (programmable) number of fringes. An interferogram has a centreburst (the part of the interferogram that is recorded at and near ZPD) which contains much more signal than points further down the path, although this information is no less important. The ratio of intensities between the maximum and minimum signal levels of the interferogram is called the dynamic range. Because the information in both of these parts of the interferogram are equally important, we must digitize the information in both regions of the interferogram with as much accuracy as possible. This means we need a digitizer (ADC) that has an input range larger than that of the centreburst, while also distinguishing the low-signal spectral information from the ADC noise at the ends of the interferogram. If the spectral signal near MOPD is not larger than the ADC noise, the overall resolution of the spectrum will be reduced.

The dynamic range, $D$, of an ADC is measured in bits. An estimate of the dynamic range required to record an interferogram with a given spectral SNR, spectral range, and resolution is: [64, pp. 65–67]:

$$D = \log_2 \left[ SNR \sqrt{\frac{\sigma_{max} - \sigma_{min}}{\delta\sigma}} \right]. \tag{4.4.1}$$

The required ADC for $\sigma_{max} = 5000$ cm$^{-1}$, $\sigma_{min} = 1200$ cm$^{-1}$, $\delta\sigma = 0.02$ cm$^{-1}$ and SNR=300 is 17 bits.

We replaced the old analog-to-digital converters by a 16-bit ADC with 8 independent channels from the Measurement Computing Corporation (MCC). For each detector, we record the data twice: once at a gain of 1 to capture the centreburst and the other at a gain of 2, 5 or 10 to capture the detail at the ends of the interferogram, increasing our ADC resolution. This causes two potential problems when stitching the two channels together to create the interferogram: one, that the channel gain is not exactly the prescribed value, and the other, that there is a phase difference between the two channels. The gain specification on the MCC ADC board is that the gains are correct to within 0.05%, which, for a gain of 5, a typical setting, is 5.0025. Alternatively, one could determine the gain ratio from the high and low gain data channels themselves. The disadvantage of this method is that because interferograms oscillate about zero, dividing the two channels entails a possible division by zero or very small numbers, causing a larger error than that from the gain uncertainty of 0.05%. The phase difference between the two channels can be monitored by comparing a section of the interferogram that is not saturated in the high gain channel with the corresponding points in the low gain channel. The residuals between the two channels over this range show no apparent structure, which would be an indication of a phase difference between the two channels.

A second option would have been to purchase an 18 or 20-bit ADC, for which only one interferogram need be recorded, but this option is more costly and would have required a custom-made electronics board.

The solenoid board is used for controlling the white light source in the FTS. The white light source is used when the environmental conditions are very stable, and one wishes to average interferograms before they are phase-corrected and converted into spectra. The white light source indicates exactly where zero path difference (ZPD) is located since its ZPD intensity is much larger than its side-lobes. The white light source is not a necessary component, and is, in fact, undesirable when measuring solar absorption in occultation, because the environmental conditions change far too rapidly to justify interferogram averaging. The solenoid board was removed and not replaced.

Replacing old electronics and detectors with new ones had the added advantage that we also reduced our power consumption and the need for some voltages entirely. Therefore, we did not need the same number of DC-DC converters as we originally had in the FTS, so the number of the VICOR modules was reduced, further reducing the mass of the instrument.

The 500MHz computer draws 12W of power, and a custom aluminum heat sink was

| | $\widetilde{CS}$ | $\widetilde{RD}$ | A8 | $\widetilde{WR}$ | D0 | D1 | D2 | D3 | D4 | D5 | D6 | D7 |
|---|---|---|---|---|---|---|---|---|---|---|---|---|
| Read | 0 | 0 | 0 | 1 | UNUSED (0) | DIR | SPEED | | | | ALIGN | |
| Write | 0 | 1 | 0 | 0 | STANDBY (0) | TRIM (1) | AUTO ALIGN (0) | DIR | SPEED | | | |

Table 4.2: Line descriptions on the dynamic alignment board

built for it, in order to conduct heat away from the chip. We wanted to run the instrument off a Windows XP operating system, to optimize the performance of the 16-bit ADC. Our hard drive is a Compact Flash card, due to its small size, ruggedness and ability to function nominally under vacuum. XP, however, cannot be installed on a CF card, because it is recognised as removable media and cannot be partitioned. Our solution to this problem was to build a custom XP-like operating system using Windows XP Embedded, a development tool that creates an instrument-specific operating system, with only the components necessary to run the computer and software. XP Embedded has the added advantage of being smaller than 1GB, and so relatively cheap and easily obtained CF cards could be used. XP Embedded can also be directly copied from one CF card to another, and multiple copies of the same operating system can be made and switched in the event of a CF card corruption.

### 4.4.1 The Speed and Search Control

The speed and search control board controls the scan motor speed and direction as well as the dynamic alignment mirror through a feedback loop. The scan motor direction and speed can also be controlled through analog voltages applied directly to the motor itself, but because the dynamic alignment of the interferometer is so precisely influenced by the scan motor position, the two mechanisms must be controlled in tandem. These are controlled by a programmable microchip containing a proprietary program to which we do not have access. We wanted to keep the program because it is reliable and robust, so we had to determine the dynamic alignment signals. This was accomplished using a logic analyser while running the instrument through PCDA. Through a controlled set of

| Speed | D2 (D4) | D3 (D5) | D4 (D6) | D5 (D7) |
|---|---|---|---|---|
| 0.1 cm/s | 0 | 1 | 0 | 1 |
| 0.15 cm/s | 0 | 1 | 1 | 0 |
| 0.2 cm/s | 0 | 1 | 1 | 1 |
| 0.3 cm/s | 1 | 0 | 0 | 0 |
| 0.5 cm/s | 1 | 0 | 0 | 1 |
| 0.7 cm/s | 1 | 0 | 1 | 0 |
| 1.0 cm/s | 1 | 0 | 1 | 1 |
| 1.5 cm/s | 1 | 1 | 0 | 0 |
| 2.0 cm/s | 1 | 1 | 0 | 1 |

Table 4.3: Data lines on the dynamic alignment board read (write) cycle

experiments, including different scan directions, speeds and states of dynamic alignment, the bit pattern was determined for the 12 digital input and output lines to the microchip. These twelve lines include four control lines (a Chip Select ($\widetilde{CS}$), a Read ($\widetilde{RD}$), a Write ($\widetilde{WR}$) and a Register Select (A8)) and 8 bits of data (D0-7), summarized in Table 4.2. The scan speed is determined by four bits that increase bit-wise (D2–5 in the read cycle; D4–7 in the write cycle). The scan direction is determined by one bit (D1 for the read cycle; D3 for the write cycle). The speed direction is away from ZPD if high, and toward ZPD if low. The alignment indicators are read by two bits in the read cycle: bits D6 and D7. In the read cycle, D0 is an unused bit and is always low. There are no alignment signals sent in the write cycle, and so there are an extra three bits (D0–D2) in the write cycle that set the system mode, the speed trim and the automatic alignment mode. The system mode is kept out of standby mode (low), the speed trim is always disabled (high), and the automatic alignment mode is always left on (low). Tables 4.3 and 4.4 list signals that are written to and read from the data lines. From these signals, we can determine and control the speed of the scan motor and determine the state of the dynamic alignment (aligned, search or partial alignment).

With the information from the speed and search control, together with the sampling information from the LabJack counter, we now have a precise method of determining the exact position of the motor, and hence the resolution of the spectrum. We have

| Alignment Status | D6 (TY) | D7 (TX) |
|---|---|---|
| Aligned | 1 | 1 |
| Only TX Aligned | 0 | 1 |
| Only TY Aligned | 1 | 0 |
| Search | 0 | 0 |

Table 4.4: Alignment status on the dynamic alignment board read cycle

full control over the interferometer: the scan motor, dynamic alignment and with the software, discussed in §4.4.2 below, the data collection.

### 4.4.2 Software

The control software, which was written in LabVIEW, was separated from the analysis software, written in MATLAB, so that the strengths of both languages could be exploited. LabVIEW has a strong instrument control package and an extensive hardware driver library, whereas MATLAB is ideal for matrix calculations, statistical analysis and graphing.

#### Control Software

The LabVIEW software integrates the scan motor, controlled through digital commands to the dynamic alignment (speed and search control), the data acquisition, and the housekeeping information. The software contains an instrument control module called a state machine and an automated scheduler. The state machine controls the basic functions of the instrument: sampling and mirror scan direction, finding the beginning of scan switch, initializing the analog-to-digital converters, and stopping the scan motor. The automated scheduler allows a pre-determined experiment to be run without user intervention. The scheduler includes the ability to record data with different scan lengths and speeds during certain time intervals: for example, pre-set sunrise and sunset intervals.

The software also contains uplink and downlink capabilities through three RS-232 connections (one 300 baud (bits/s) uplink shared by all instruments on the payload, one dedicated 9600 baud housekeeping downlink and one dedicated 115 kbaud data downlink), so that the instrument can be controlled from the ground during a flight. The housekeeping downlink includes a centreburst from the instrument, so that the data quality can be monitored in near-real time. The 115 kbaud data line is not fast enough to downlink the entire interferogram in real time. Complete interferograms for both detectors are 6 MB each and are recorded every 50 seconds, giving a data rate of 960 kbaud. Data are both downlinked during the flight (which will take a few hours) and also stored on-board for retrieval after the payload has landed.

An occultation takes approximately 30 minutes from the MANTRA float altitude, and adding on 15 minutes before and after the occultation to ensure that the entire occultation is measured, the data volume is about 430 MB per occultation. We aim to measure through two occultations, and so we need, at minimum, a 1 GB hard drive to record the data from one flight. We chose to record our data on a 2 GB flash card, separate from that of the operating system, so we could insert a new flash card before flight.

The software has many advantages for this application. First, all instrument housekeeping information is recorded and easily accessible. All post-processing can therefore be done with full knowledge of the state of the instrument. This is also extremely important during a balloon flight, when ambient temperatures can dip to as low as −60°C, and when direct sunlight hits the instruments, the instrument cases can reach 80°C. Since the electronics have only radiative and conductive means of cooling, monitoring the temperatures during a flight can indicate when an instrument must be turned off to avoid overheating or when heaters must be turned on to avoid freezing. (Most heaters, however, turn on automatically using a thermostat.)

The second advantage of this software is that it allows for post-processing flexibility. It is preferable to do no processing of the data on board the balloon so we have the ability to process the data in any manner desired after the flight. Processing on-board has typically been used in the past to reduce data volume, because on-board storage was expensive [79]. That is no longer an issue.

In the U of T FTS, since both a high-gain and a low-gain channel for each detector are stored on-board, we do not need to institute a mid-interferogram gain change, eliminating the need for this on-board processing procedure. In fact, we do not perform on-board processing of any kind (fast Fourier transforms (FFTs), apodization, digital filtering, etc.).

### Analysis Software

The MATLAB data analysis software decodes the binary data from the LabVIEW program, performs a Forman phase correction to symmetrize the interferograms, and computes a fast Fourier transform to produce an atmospheric spectrum. The mathematical details were described in §3.2 and §3.3. Here, I will describe the details of the processing code that I have written.

### Forman Phase Correction

The high and low gain channels must be put together into one vector. This is done by first fitting a line to the interferogram and subtracting off any offset in each channel, then multiplying the low gain channel by the ratio of the high gain value to the low gain value. The high gain channel then replaces the interferogram from the multiplied low gain channel after a certain number of points. This number is chosen to ensure that the data from the high gain channel that is appended to the low gain channel is not saturated. In the code, the number of points was set to 5000. The entire interferogram contains 780,000 points. The asymmetric interferogram is $M(x)$, from Equation 3.3.2.

The next step is to take equal numbers of points around ZPD to create a low-resolution, double-sided interferogram: $M_s(x)$. We take 256 points. The phase spectrum, $m_s(\sigma)$, is calculated from the FFT of $M_s(x)$. The phase angle, $\epsilon(\sigma)$, is calculated from $m_s(\sigma)$, using Equation 3.3.4, and the phase interferogram, $F(x)$, is computed by taking the FFT of $\mathrm{e}^{i\epsilon(\sigma)}$. The apodization function (Equation 3.3.7) is applied, where

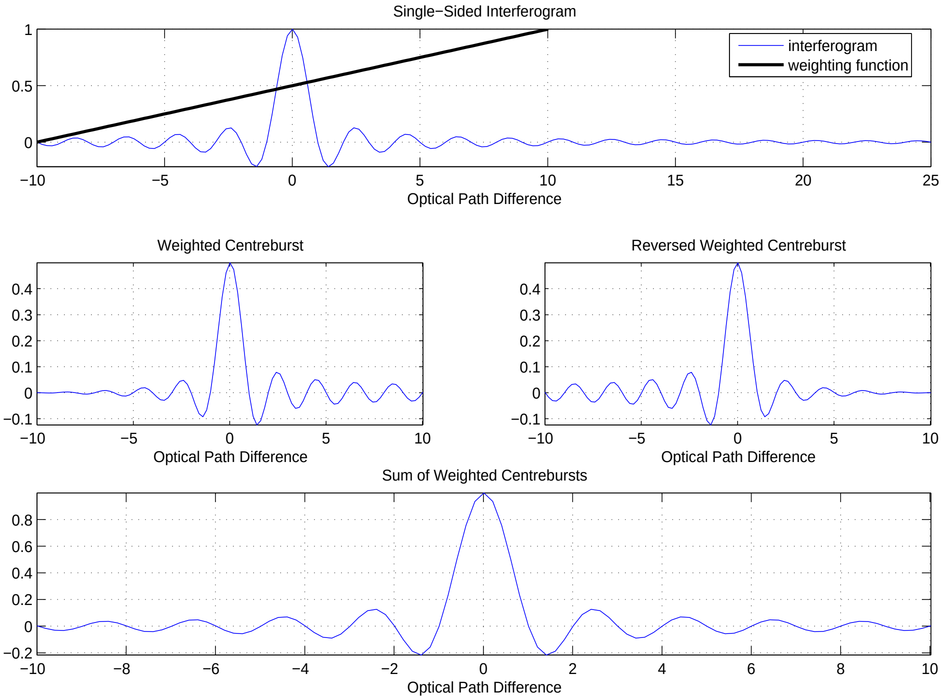

Figure 4.9: The linear weighting function applied to the phase-corrected interferogram, before computing the FFT. The top panel shows the phase corrected interferogram in blue, and the weighting function in black. The centre-left panel shows the weighting function applied to the central portion of the interferogram (the “centreburst”). The centre-right panel shows the reversed weighted interferogram. The bottom panel shows the sum of the two weighted interferograms.

$\tau$ is a vector spanning -128 to 127 and $n$ is 128. The asymmetric interferogram, $M(x)$, is then convolved with the apodized phase interferogram to produce a phase-corrected interferogram.

### Fourier Transform Scheme

The Fourier transform routine uses a built-in MATLAB FFT function. In preparation, however, for the FFT, ABB Bomem uses a procedure in their processing code, which I have adopted in mine, to ensure both that data are used from the short arm of the phase-corrected interferogram and that we have a perfectly symmetric interferogram to work with.

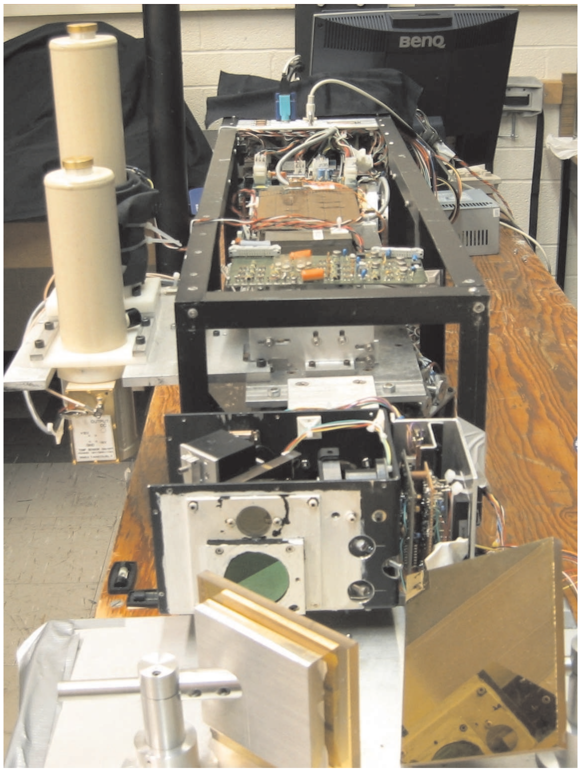

Figure 4.10: The U of T FTS with delta-tracker attached. The laser (gold box) and laser detector electronics sit on top of the hexagon (not visible) mid-way down the FTS. The electronics are housed under the plate near the rear of the instrument.

In order to use the short arm of the interferogram, a linear weighting function, increasing from 0 to 1, is multiplied across equal numbers of points on either side of ZPD (see Figure 4.9). The vector is then reversed and added to itself, to create a perfectly symmetric interferogram. The short arm of the interferogram is then removed, and replaced by the long arm to create a double-sided interferogram. The zero path point in the interferogram is shifted to the first point in the vector (essentially swapping the left and right halves of the vector). Zeros are inserted between the two halves of the shifted interferogram to increase the number of points to $2^N$, where $N$ is an integer (see Figure 3.3). The MATLAB FFT routine is applied to the interferogram to compute the spectrum.

Once the upgrade to the U of T FTS was complete, it was run under vacuum to test its temperature stability, and upon successful completion of the vacuum test, was

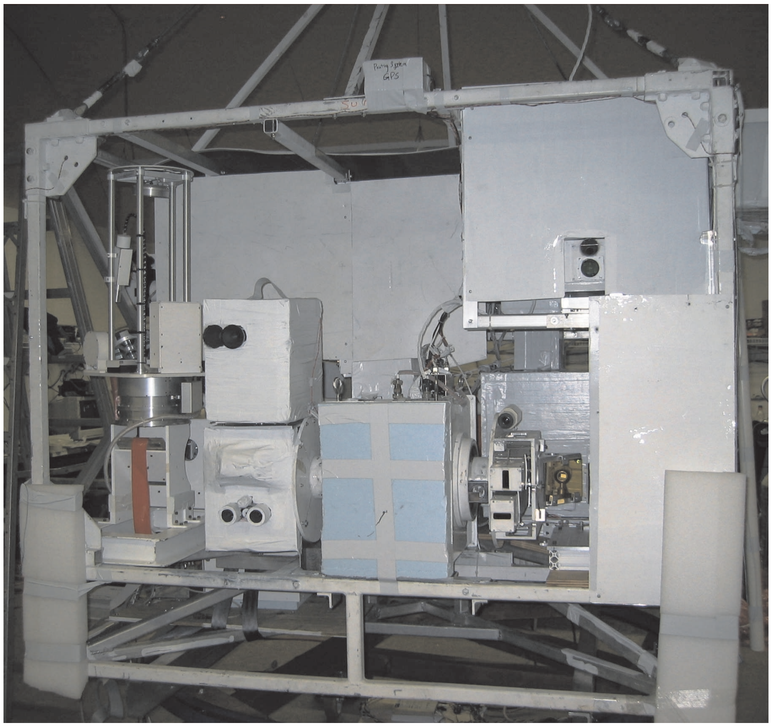

Figure 4.11: The payload just before the first MANTRA 2004 launch. The U of T FTS is located in the top right-hand corner of the gondola.

shipped out to Vanscoy to participate in the MANTRA 2004 campaign. A photograph of the U of T FTS is shown in Figure 4.10.

### 4.4.3 MANTRA 2004 Launch #1

The first launch was at 08:34 local time on September 1st. The payload is shown in Figure 4.11. Because the launch was in the late morning, the first occultation opportunity was at sunset. The launch itself was a success and all the instruments were launched while running: the pointing system in solar pointing mode and the U of T FTS in its scheduler mode. All commanding capability, however, was lost shortly after launch, which meant that no commands could be sent to the instruments. This also meant that the data downlink line was inaccessible to the U of T FTS, since the 115 kbaud downlink was to be shared by all three FTSs in succession, initially connected to the DU FTS. The housekeeping downlink for the U of T FTS was intact.

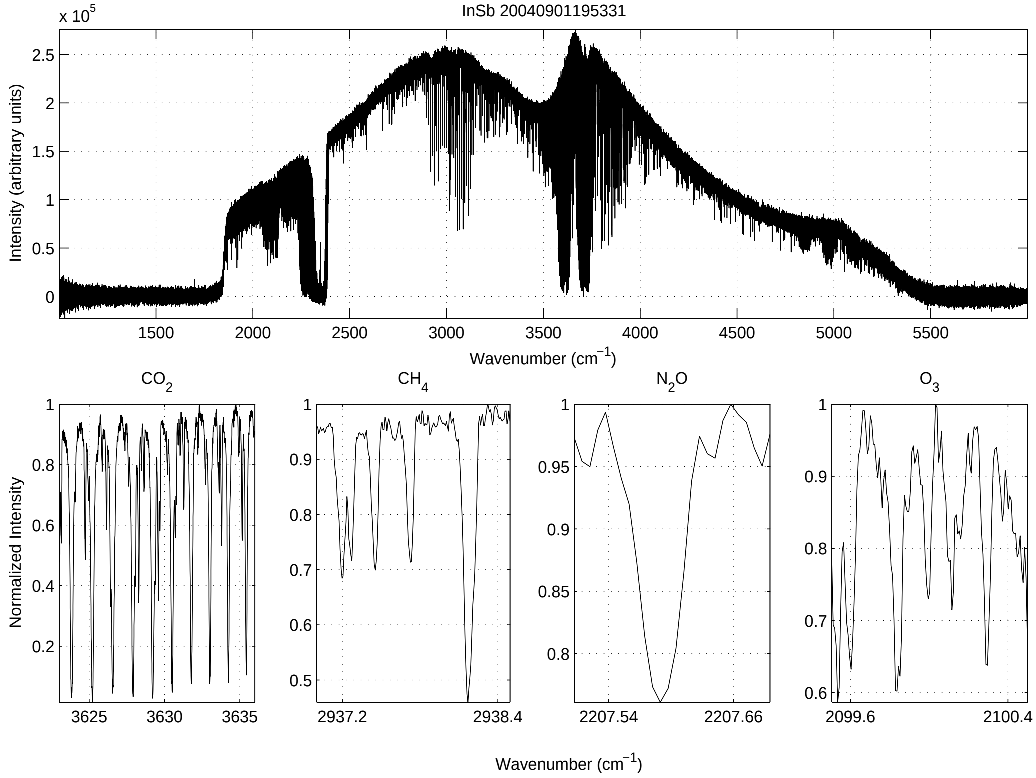

Figure 4.12: InSb spectrum from the first MANTRA 2004 flight.

There was no automated scheduler in the pointing system, and so the pointing system, which was supposed to take limb mode data (pointing 90° from the sun and scanning the vertical) during the day, continued to follow the sun. Because it was in direct sun throughout the hottest time of the day, the pointing system overheated and shut down three hours before sunset. As a result, the payload began to slowly rotate, and continued to do so during sunset. During sunset, the payload was within $\pm 10°$ of azimuth for around 5 minutes, long enough for the U of T FTS to record two spectra on each detector at a zenith angle of $\sim 89°$ (see Figure 4.12 and Figure 4.13). The payload was not facing the sun long enough during sunset to acquire a full occultation. However, without the delta-tracker, no spectra would have been recorded at all. The payload was terminated immediately following sunset.

The new control software on the U of T FTS worked well. Housekeeping data are

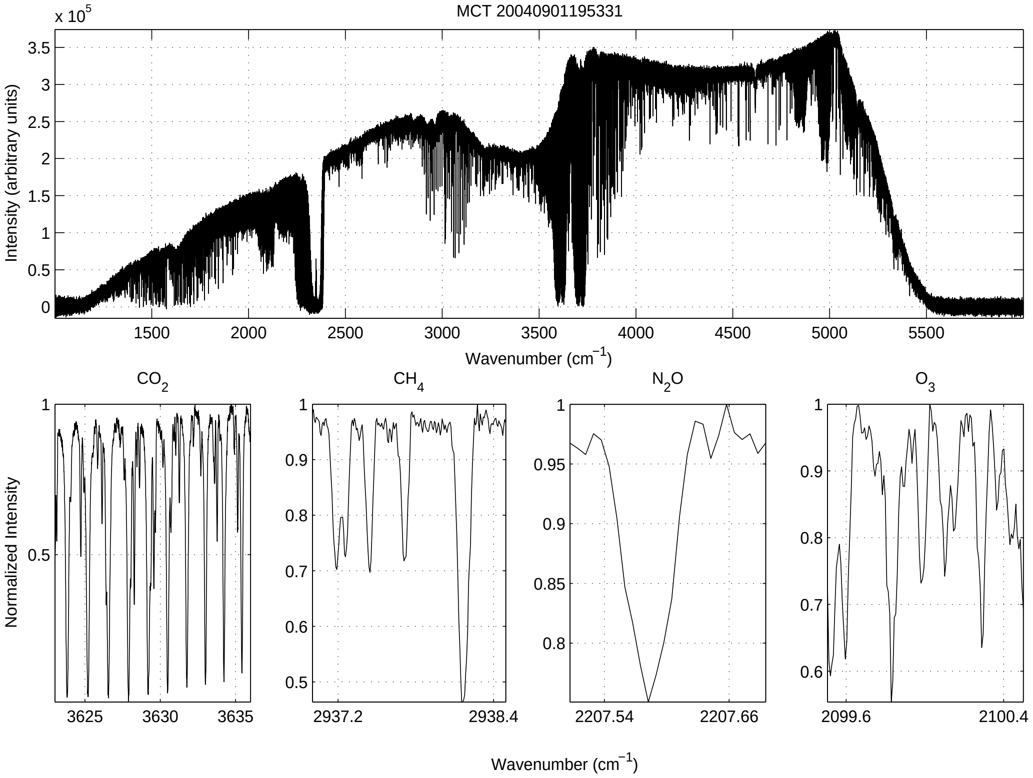

Figure 4.13: MCT spectrum from the first MANTRA 2004 flight.

shown in Figures 4.14, 4.15, 4.16 and 4.17. The housekeeping data were useful during the flight, giving us constant information about the status of the instrument, and even information about the direction in which the payload was facing, by noting increases in temperature as the sunlight was incident upon the preamplifier (which is near the front of the instrument) and the power supply (which is at the back of the instrument); see Figure 4.15. We monitored the voltages, temperatures and laser status constantly, and the instrument performed optimally in the low-pressure environment. The temperatures dip below −40°C during the ascent through the tropopause, but remain between +10 and +55°C once the float height is reached. The voltages were constant throughout the flight, and the housekeeping data showed the expected signals. The laser heater cycles to maintain the laser temperature stability, and is constant when the spectra were recorded. The laser intensity was also constant when the spectra were recorded. One extra spec-

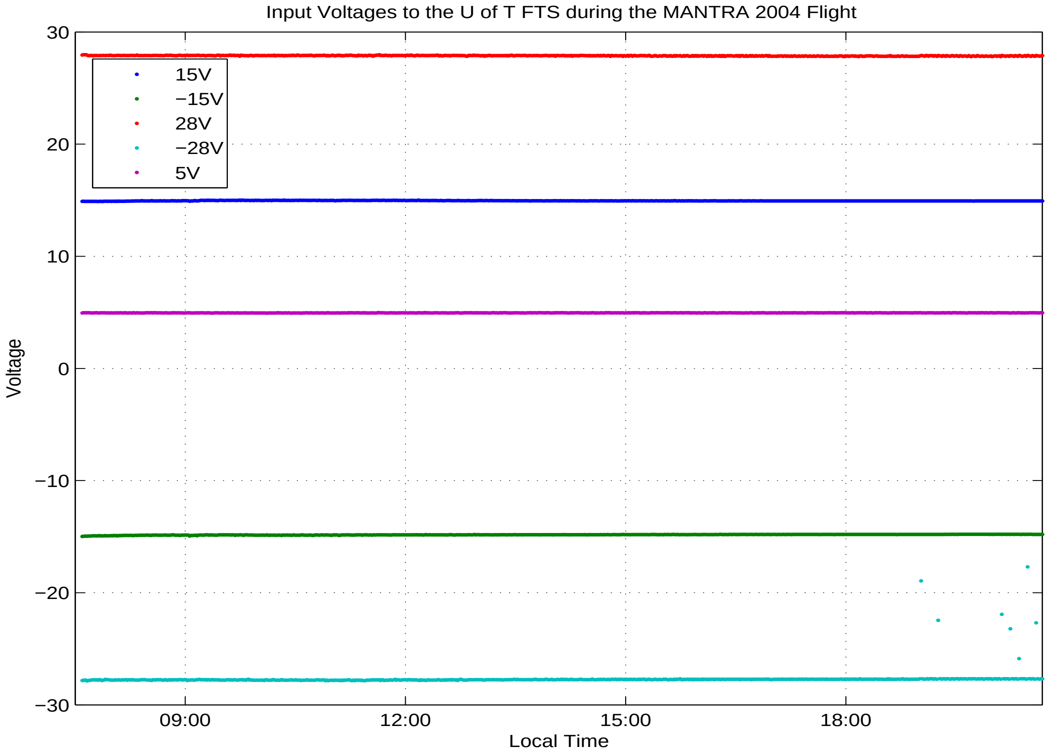

Figure 4.14: Housekeeping voltages from the MANTRA 2004 flight. The +15V and -15V supplies power the detector preamplifiers. The +28V and -28V lines supply power to the scan motor, dynamic alignment motor, laser and laser heater. The +5V line powers the dynamic alignment board.

trum that could have been recorded during this period was lost to misalignments in the scanning mirror that were not compensated for by the dynamic alignment system. This is possibly due to a small misalignment in the laser detector board or low laser intensity. The sun azimuth and elevation signals are the voltages sent to the delta-tracker pen motors, and the period of time during which the suntracker was able to lock onto the sun is evident from Figure 4.17. (The gaps between sets of instrument status data are times when the centreburst, voltages, and temperatures are being recorded. This happens approximately once every 90 seconds.)

The instruments were recovered, and there was some damage to the U of T FTS. The landing had been a hard one, with a direct upright landing, followed by the payload

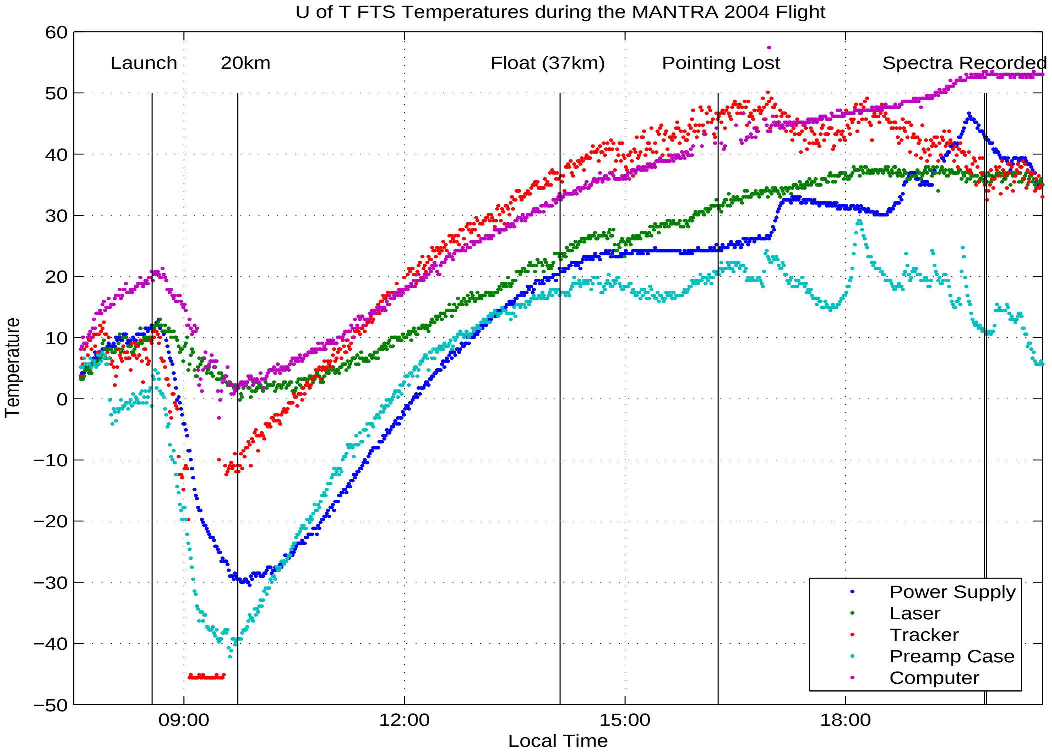

Figure 4.15: Housekeeping temperatures from the MANTRA 2004 flight. The vertical lines indicate the time of launch, ascent through the tropopause, the time that the float altitude was reached, when the pointing system shut down, and when the two spectra were recorded. The tracker temperature saturates as the payload rises through the tropopause because its thermal sensor is located on the outside of the tracker. The computer temperature sensor was placed on the hottest part of the motherboard.

tipping over onto one side (see Figure 4.18). This shear caused the vibration mounts that connected the U of T FTS to its base plate to tear out, the baseplate itself to fracture and the instrument to crash through part of the gondola. Not surprisingly, while the hexagon, scan tube and detector mount were still intact (though not aligned), the whole system was at a 30-degree angle to the vertical. The system had to be hammered back into its proper alignment, and the optical alignment had to be redone. After a week or so, the problems had been fixed and the instrument was recording ground-based data, though of poorer quality than before the flight.

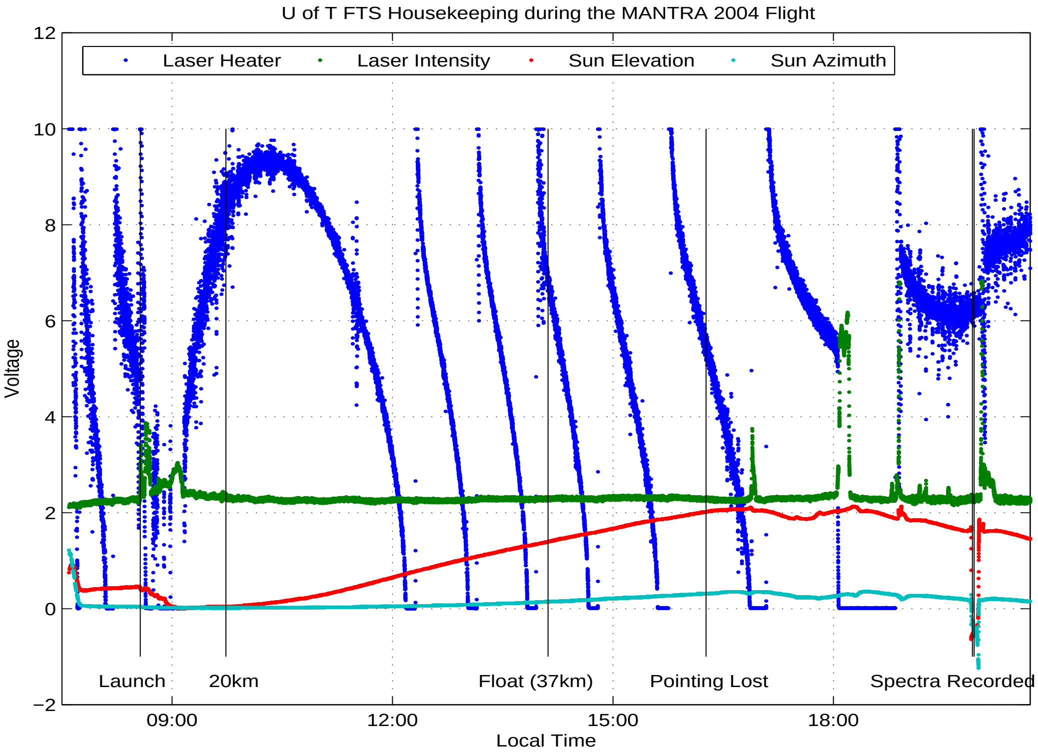

Figure 4.16: Housekeeping instrument status from the MANTRA 2004 flight. The sun elevation and azimuth signals are the voltages applied to the tracker pen motors.

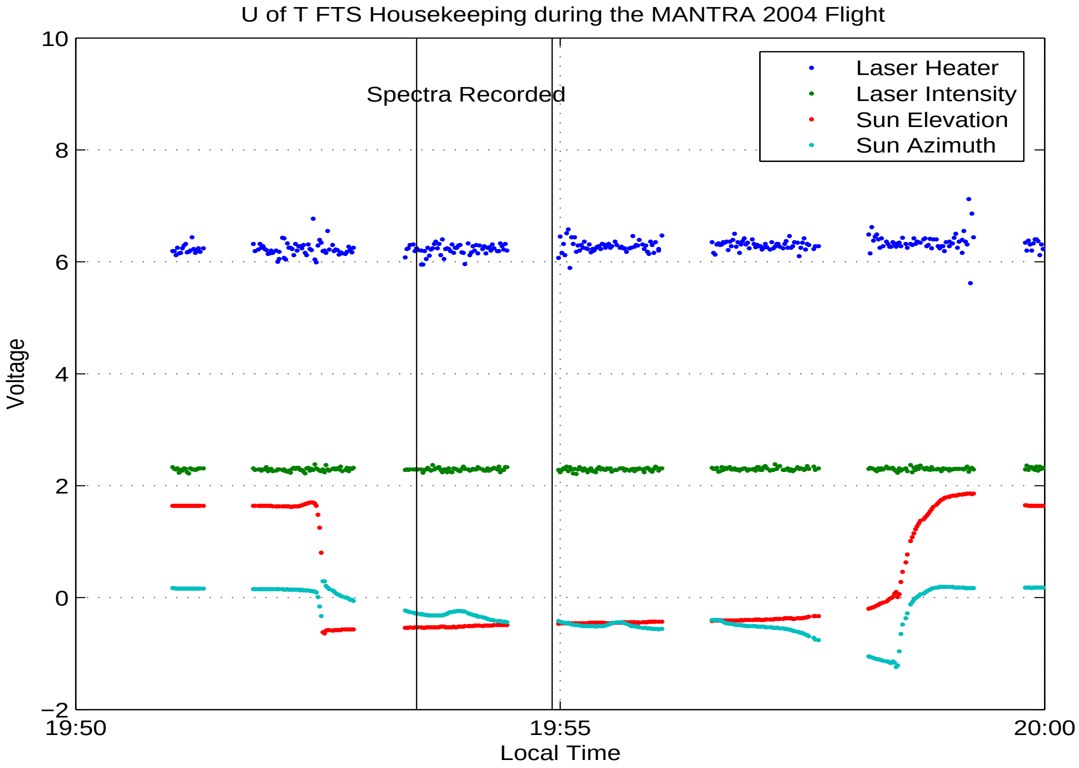

Figure 4.17: Housekeeping instrument status from the MANTRA 2004 flight. This shows the housekeeping data when the two spectra were recorded. The sun azimuth voltage changes as it tracks the sun while the payload slowly rotates.

Figure 4.18: The U of T FTS after landing. Figure courtesy SIL.

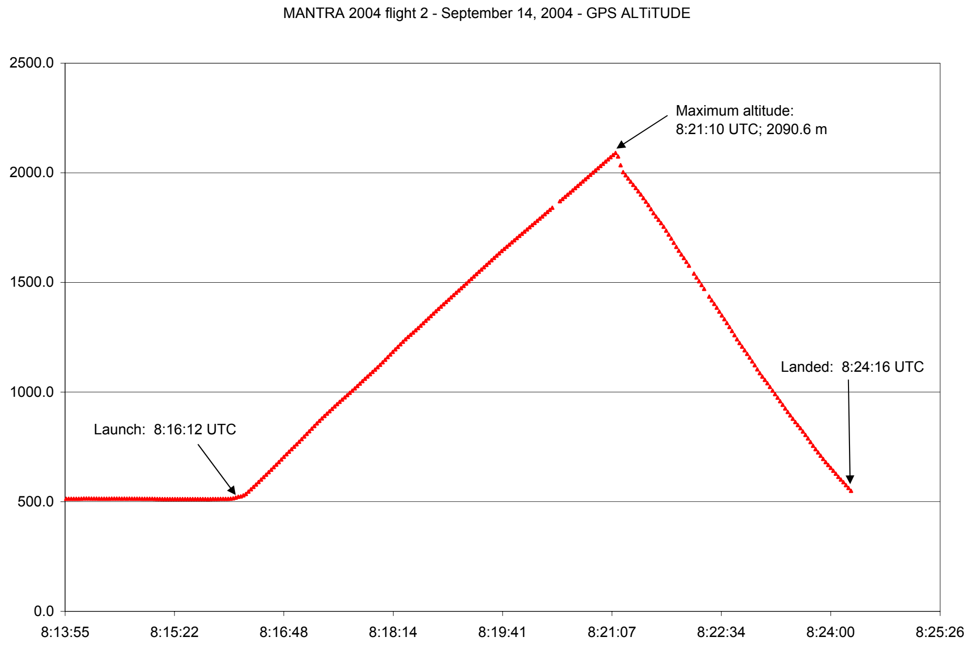

Figure 4.19: The second MANTRA 2004 flight (figure courtesy Prof. Kaley Walker). The x-axis is time in UTC, and the y-axis is altitude in m.

### 4.4.4 MANTRA 2004 Launch #2

The decision was made to attempt a second launch, and ground-based measurements continued between launches. The second launch occurred at 02:16 local time on September 14th. Shortly after, the termination devices fired prematurely, and the payload ended up on the ground in a field less than 1 km away from the launch site (see Figure 4.19).

## 4.5 Results

The new design of the U of T FTS worked well. The integration of the FTS onto the payload was smooth. The instrument was lifted into place after being aligned and tested on the ground, and, because the delta-tracker was attached to the FTS, no precise

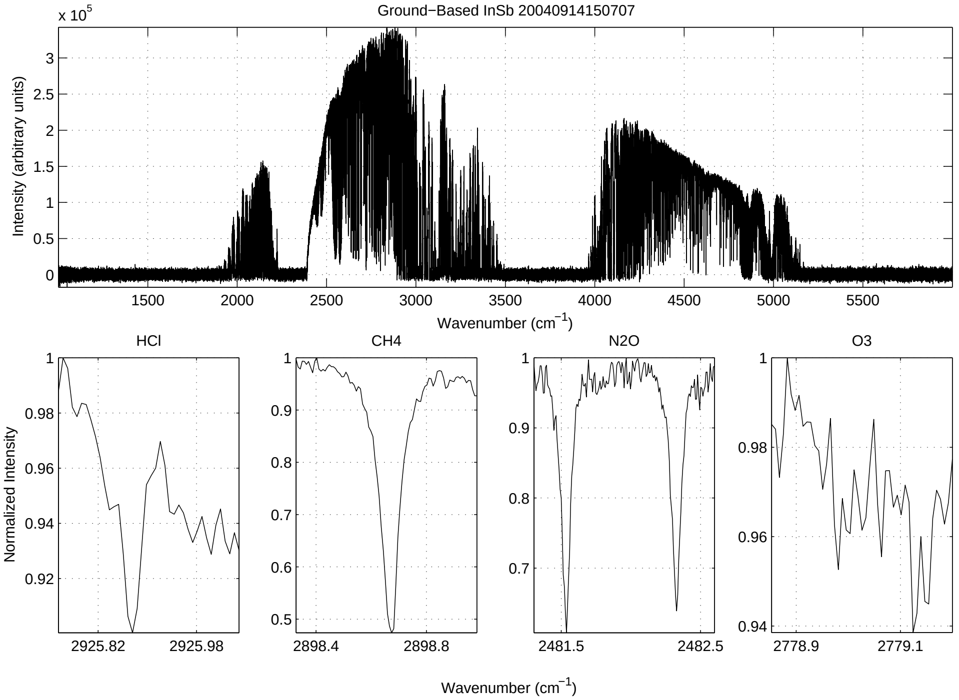

Figure 4.20: InSb spectrum from the MANTRA 2004 ground based campaign. The top panel shows the entire spectrum, while the lower four panels show microwindows from which we retrieve HCl, $CH_4$, $N_2O$ and $O_3$, respectively.

alignment was necessary with the payload.

A fortunate result of the work done on this FTS is that both the power consumption and the mass of the instrument were significantly reduced. The power was reduced from 145 W to 65 W and the mass was reduced from 90 kg to 55 kg. The size was reduced from two pieces to one, with dimensions of approximately 1.5 m by 0.3 m by 0.5 m.

The U of T FTS made solar absorption measurements on the ground in the lead-up to the first MANTRA 2004 flight and between flights. Figures 4.20 and 4.21 show the spectra and atmospheric trace gas microwindows for the ground-based data. Comparing flight spectra in Figures 4.12 and 4.13 with the ground-based spectra in Figures 4.20 and 4.21, one can see striking differences. The most obvious difference is the overall shape of the spectra. There is much less absorption in the balloon spectra, simply due to the lack of water vapour and other tropospheric trace gases in the optical path.

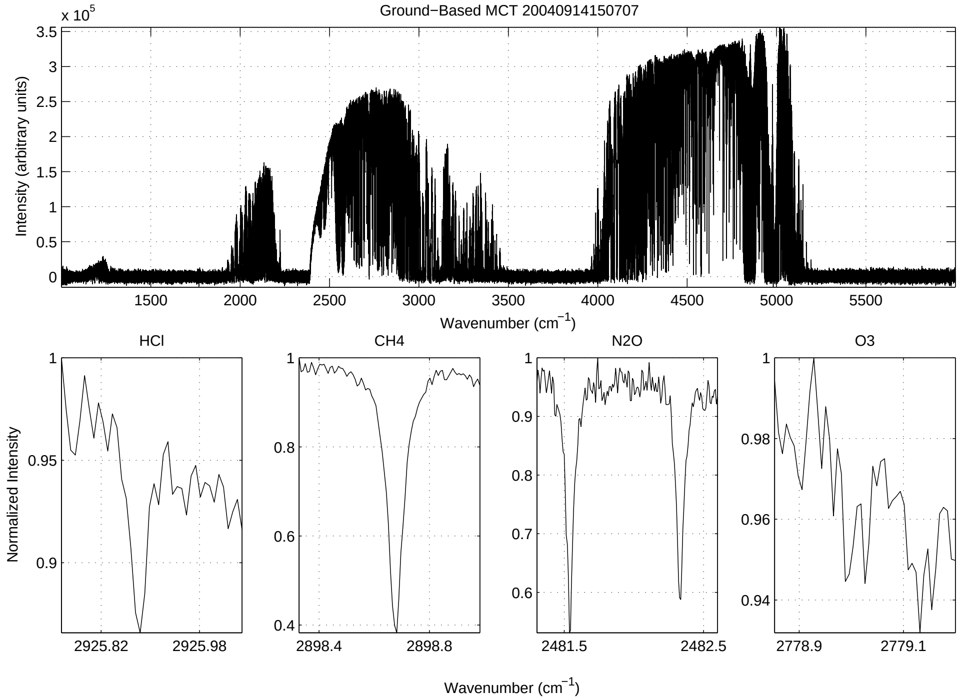

Figure 4.21: MCT spectrum from the MANTRA 2004 ground based campaign. The top panel shows the entire spectrum, while the lower four panels show microwindows from which we retrieve HCl, $CH_4$, $N_2O$ and $O_3$, respectively.

To compare spectral signatures of trace gases, some common microwindows for $CO_2$, HCl, $CH_4$, $N_2O$, and $O_3$ are shown. Since molecules cannot generally be measured in the same microwindows on the ground as from a balloon (since most of the spectral lines present in the balloon spectra are saturated in the ground-based spectra, or obscured by water vapour, and many lines in the ground-based spectra may not be sufficiently strong for balloon spectra), microwindows cannot be directly compared. The microwindows shown here indicate the comparable resolutions and noise levels between the two viewing geometries. This indicates that the instrument suffered few detector alignment problems from the change in environment.

From August 27 onward, a neutral density filter (metal mesh) was placed in front of the input to the FTS, in anticipation of the higher solar signals that would be found at high altitudes as compared with the ground-based signals. One feature to note is that the noise levels appear to be the same in the ground-based spectra and the balloon-based spectra. Since there are many more photons reaching the detectors when the instrument is on the balloon, we would expect an increase in the photon noise for the balloon-based spectra. Because we do not see an increase in noise between the two spectra for the same detector, we can conclude that the interferograms are not photon-limited, and that there is another, larger noise source in the FTS. Suggestions for finding the sources of noise and improving the noise levels will be discussed in Chapter 6.

Chapter 5 will discuss, in detail, the measurements made by the U of T FTS and the results obtained.

# Chapter 5

# U of T FTS Measurements*

## 5.1 Introduction

The U of T FTS recorded flight data from MANTRA 2004 and ground-based data, both in Vanscoy and in Toronto. This chapter will discuss the flight data results and two intercomparison campaigns: the MANTRA 2004 ground-based campaign in Vanscoy, Saskatchewan and the ground-based FTS intercomparison campaign, held in Toronto in May through September, 2005.

A mathematical formalism that allows us to obtain information about the atmosphere from a measurement, called retrieval or inverse theory, will be discussed in §5.2. SFIT2, a commonly-used retrieval program, uses this theory and will be described in §5.3. A discussion of the flight data and intercomparison campaigns themselves will follow.

## 5.2 Retrieval Theory

Retrieving column amounts of a gas in the atmosphere is an inherently ill-posed or underconstrained problem: there is more than one solution that fits the data [82]. The treatment of the inverse problem described in this section will closely follow the optimal estimation method (OEM) of Rodgers [82].

The problem is formulated as follows. For each measurement made (say, an absorp-

---

*The work contained in §5.6 through to the end of this chapter has been submitted to Atmospheric Chemistry and Physics as Wunch et al. [40].

tion line is measured by a number of spectral points), we have a measurement vector, $\mathbf{y}$, of length $m$. The measurement vector is related to the real state of the atmosphere (say, the profile of the gas), called the state vector, $\mathbf{x}$, of length $n$. The forward model, $\mathbf{F}(\mathbf{x}, \mathbf{b})$, relates the state vector to the measurement vector. The forward model contains all the relevant physics of the measurement (the radiative transfer model and the instrument line shape, for example), and the model parameters, $\mathbf{b}$, are quantities that are not retrieved, but influence the measurement and are known to some degree of accuracy. Model parameters can include the absorption coefficient of the gas, the pressure and temperature profile of the atmosphere, the air mass factor at the latitude and time of day, etc. Since there is always some error associated with a measurement, $\boldsymbol{\epsilon}$, and some error associated with the forward model, $\boldsymbol{\Delta}\mathbf{f}$ , we can write

$$\mathbf{y} = \mathbf{F}(\mathbf{x}, \mathbf{b}) + \boldsymbol{\Delta}\mathbf{f} + \boldsymbol{\epsilon}. \tag{5.2.1}$$

What we ideally want is some way of solving this equation for $\mathbf{x}$, the true state of the atmosphere. The forward model is typically not invertible (and is certainly not invertible in our case), and so we need a method of estimating the true state of the atmosphere. We will label estimates with a caret (ˆ)—the estimate of the true state of the atmosphere is $\hat{\mathbf{x}}$.

For simplicity, assume that the problem is linear with Gaussian statistics with $\boldsymbol{\Delta}\mathbf{f} = 0$ and no parameters. These assumptions are not generally applicable, but can be generalized later. Then

$$\mathbf{y} = \mathbf{F}(\mathbf{x}) + \boldsymbol{\epsilon}. \tag{5.2.2}$$

We can linearize this equation by taking the first term of the Taylor expansion about the point $\mathbf{x_0}$:

$$\mathbf{y} =\mathbf{F}(\mathbf{x_0}) + \frac{\partial \mathbf{F}(\mathbf{x})}{\partial \mathbf{x}}(\mathbf{x} - \mathbf{x_0}) + \boldsymbol{\epsilon}. \tag{5.2.3}$$

Define a weighting function matrix, $\mathbf{K}$, which describes the sensitivity of the forward model to the state vector:

$$\mathbf{K} \;=\; \frac{\partial \mathbf{F}(\mathbf{x})}{\partial \mathbf{x}}. \tag{5.2.4}$$

We assume that $\mathbf{F}(\mathbf{x_0}) = \mathbf{K}\mathbf{x_0}$, since $\mathbf{K}$ also represents the forward mapping from state space into measurement space, and the mapping of the origin ($\mathbf{K}\mathbf{x_0}$) should lie at $\mathbf{F}(\mathbf{x_0})$ [82]. We can then rewrite Equation 5.2.3 to get:

$$\mathbf{y} = \mathbf{K}\mathbf{x} + \boldsymbol{\epsilon}. \tag{5.2.5}$$

We ultimately want to know how to update our prior knowledge of the probability of a given state of the atmosphere, $P(\mathbf{x})$, with our particular measurement, $\mathbf{y}$. This is expressed as the probability of the state given a measurement, $P(\mathbf{x}|\mathbf{y})$. By Bayes' theorem, we have the relation

$$P(\mathbf{x}|\mathbf{y}) = \frac{P(\mathbf{y}|\mathbf{x})P(\mathbf{x})}{P(\mathbf{y})}. \tag{5.2.6}$$

The probability of obtaining measurement $\mathbf{y}$ given an atmospheric state $\mathbf{x}$, $P(\mathbf{y}|\mathbf{x})$, is dependent on the forward model and the measurement error covariance, $\mathbf{S}_\epsilon^{\mathbf{-1}}$ [82, pp. 23–24].[1] For the measurement error covariance, we can reasonably assume that there is no off-diagonal contribution, because the measurements are mostly independent of each other. This is not generally the case for covariance matrices.

---

[1] A covariance matrix is defined by the expectation value ($E\{\}$) of the deviation from the mean of each point in the vector to the deviation from the mean of every other point in the vector. Note that when $i = j$, we get the variance ($var(y_i) = \int (y_i - \overline{y}_i)^2 P(y)dy$):

$$S_{ij} \;=\; cov(y_i, y_j) = E\{(y_i - \overline{y}_i)(y_j - \overline{y}_j)\} = \int (y_i - \overline{y}_i)(y_j - \overline{y}_j)P(y)dy \tag{5.2.7}$$

$$\mathbf{S} \;=\; \begin{bmatrix} var(y_1) & cov(y_1, y_2) & \dots & \dots & cov(y_1, y_m) \\ cov(y_2, y_1) & var(y_2) & \dots & \dots & cov(y_2, y_m) \\ cov(y_3, y_1) & cov(y_3, y_2) & \ddots & \dots & cov(y_3, y_m) \\ \vdots & \vdots & \vdots & \ddots & \vdots \\ cov(y_m, y_1) & cov(y_m, y_2) & \dots & \dots & var(y_m) \end{bmatrix}. \tag{5.2.8}$$

Assuming a Gaussian distribution for the measurement error covariance, the probability $P(\mathbf{y}|\mathbf{x})$, then, can be written as[2]

$$P(\mathbf{y}|\mathbf{x}) = \frac{1}{(2\pi)^{m/2}|\mathbf{S}_\epsilon|^{1/2}} \exp\left\{-\frac{1}{2}(\mathbf{y}-\mathbf{Kx})^T\mathbf{S}_\epsilon^{-\mathbf{1}}(\mathbf{y}-\mathbf{Kx})\right\}. \tag{5.2.10}$$

Similarly, if we assume that the prior knowledge of $\mathbf{x}$ is also Gaussian, then

$$P(\mathbf{x}) = \frac{1}{(2\pi)^{n/2}|\mathbf{S_a}|^{1/2}} \exp\left\{-\frac{1}{2}(\mathbf{x}-\mathbf{x_a})^T\mathbf{S_a^{-1}}(\mathbf{x}-\mathbf{x_a})\right\}, \tag{5.2.11}$$

where $n$ is the length of the state vector and $\mathbf{x_a}$ is the *a priori* value. $P(\mathbf{y})$ is simply a normalizing factor, and is not needed here [82, p. 24]. Using Equation 5.2.6, we get

$$P(\mathbf{x}|\mathbf{y}) = C\exp\left\{-\frac{1}{2}\left[(\mathbf{x}-\mathbf{x_a})^T\mathbf{S_a^{-1}}(\mathbf{x}-\mathbf{x_a}) + (\mathbf{y}-\mathbf{Kx})^T\mathbf{S}_\epsilon^{-\mathbf{1}}(\mathbf{y}-\mathbf{Kx})\right]\right\}, \tag{5.2.12}$$

where $C$ is a constant. The argument in the exponent can be expressed as a quadratic in $\mathbf{x}$: $(\mathbf{x}-\hat{\mathbf{x}})^T\hat{\mathbf{S}}^{-\mathbf{1}}(\mathbf{x}-\hat{\mathbf{x}})$, and so we can collect terms quadratic in $\mathbf{x}$ and linear in $\mathbf{x}$. The estimate of the state vector, $\hat{\mathbf{x}}$, in this case is the expectation value of $P(\mathbf{x}|\mathbf{y})$, which makes it both the most likely state of the probability distribution function and the expectation value of $\mathbf{x}$. Collecting terms quadratic in $\mathbf{x}$, we get

$$\mathbf{x}^T\hat{\mathbf{S}}^{-\mathbf{1}}\mathbf{x} = \mathbf{x}^T\mathbf{S_a^{-1}}\mathbf{x} + \mathbf{x}^T\mathbf{K}^T\mathbf{S}_\epsilon^{-\mathbf{1}}\mathbf{Kx} = \mathbf{x}^T(\mathbf{S_a^{-1}} + \mathbf{K}^T\mathbf{S}_\epsilon^{-\mathbf{1}}\mathbf{K})\mathbf{x}. \tag{5.2.13}$$

Collecting terms linear in $\mathbf{x}$, we get

$$\mathbf{x}^T\hat{\mathbf{S}}^{-\mathbf{1}}\hat{\mathbf{x}} = \mathbf{x}^T\mathbf{S_a^{-1}}\mathbf{x_a} + \mathbf{x}^T\mathbf{K}^T\mathbf{S}_\epsilon^{-\mathbf{1}}\mathbf{y} = \mathbf{x}^T(\mathbf{S_a^{-1}}\mathbf{x_a} + \mathbf{K}^T\mathbf{S}_\epsilon^{-\mathbf{1}}\mathbf{y}). \tag{5.2.14}$$

This results in:

$$\begin{aligned}
\hat{\mathbf{S}}^{-\mathbf{1}} &= \mathbf{K}^T\mathbf{S}_\epsilon^{-\mathbf{1}}\mathbf{K} + \mathbf{S_a^{-1}} && (5.2.15)\\
\hat{\mathbf{x}} &= (\mathbf{K}^T\mathbf{S}_\epsilon^{-\mathbf{1}}\mathbf{K} + \mathbf{S_a^{-1}})^{-\mathbf{1}}(\mathbf{K^T}\mathbf{S}_\epsilon^{-\mathbf{1}}\mathbf{y} + \mathbf{S_a^{-1}}\mathbf{x_a}), &&\\
&= \mathbf{x_a} + (\mathbf{K}^T\mathbf{S}_\epsilon^{-\mathbf{1}}\mathbf{K} + \mathbf{S_a^{-1}})^{-\mathbf{1}}\mathbf{K}^T\mathbf{S}_\epsilon^{-\mathbf{1}}(\mathbf{y}-\mathbf{Kx_a}). && (5.2.16)
\end{aligned}$$

---

[2] This is analogous to the scalar version of a Gaussian probability density function [82, pp. 20]:

$$P(\epsilon) = \frac{1}{(2\pi)^{1/2}\sigma_\epsilon} \exp\left\{-\frac{(\epsilon-\bar{\epsilon})^2}{2\sigma_\epsilon^2}\right\}, \tag{5.2.9}$$

where $\bar{\epsilon} = \int \epsilon P(\epsilon)d\epsilon$ is the mean of $\epsilon$, and $\sigma^2 = \int(\epsilon-\bar{\epsilon})^2P(\epsilon)d\epsilon$ is the variance of $\epsilon$.

If we define another matrix, $\mathbf{G}$, as the pre-multiplier of $(\mathbf{y} - \mathbf{K}\mathbf{x_a})$ in Equation 5.2.16,

$$\mathbf{G} = (\mathbf{K}^T\mathbf{S}_\epsilon^{\mathbf{-1}}\mathbf{K} + \mathbf{S}_\mathbf{a}^{\mathbf{-1}})^{\mathbf{-1}}\mathbf{K}^T\mathbf{S}_\epsilon^{\mathbf{-1}}, \tag{5.2.17}$$

we get another matrix, $\mathbf{A}$:

$$\mathbf{A} = \mathbf{G}\mathbf{K} = (\mathbf{K}^T\mathbf{S}_\epsilon^{\mathbf{-1}}\mathbf{K} + \mathbf{S}_\mathbf{a}^{\mathbf{-1}})^{\mathbf{-1}}\mathbf{K}^T\mathbf{S}_\epsilon^{\mathbf{-1}}\mathbf{K}, \text{ and} \tag{5.2.18}$$

$$\mathbf{I} - \mathbf{A} = (\mathbf{K}^T\mathbf{S}_\epsilon^{\mathbf{-1}}\mathbf{K} + \mathbf{S}_\mathbf{a}^{\mathbf{-1}})^{\mathbf{-1}}\mathbf{S}_\mathbf{a}^{\mathbf{-1}}. \tag{5.2.19}$$

Using Equations 5.2.5, 5.2.17 and 5.2.18, we can simplify Equation 5.2.16 to

$$\hat{\mathbf{x}} = \mathbf{A}\mathbf{x} + (\mathbf{I} - \mathbf{A})\mathbf{x_a} + \mathbf{G}\boldsymbol{\epsilon}. \tag{5.2.20}$$

Equation 5.2.20 shows that the retrieved value, $\hat{\mathbf{x}}$ is a weighted average of the true state, $\mathbf{x}$, and the *a priori* state, $\mathbf{x}_a$ by the matrix $\mathbf{A}$, called the averaging kernel. The averaging kernel has a number of very useful properties. It is the sensitivity of the retrieval to the true state:

$$\mathbf{A} = \frac{\partial \hat{\mathbf{x}}}{\partial \mathbf{x}}. \tag{5.2.21}$$

Its rows describe the sensitivity of the retrieval to each grid point (altitude). Ideally, the averaging kernel should be an identity matrix, with the concentration at each altitude being represented by the single diagonal element in each row. In reality, however, the rows have peaked functions: off-diagonal non-zero elements show that the concentration at each altitude has contributions from a number of grid points. The half-width of the peaked function is a measure of the vertical resolution of the observations. The area of the averaging kernel (the sum of the rows) shows at what altitude the retrieval is sensitive to the measurement (i.e. where the values are close to 1) and where the retrieval is dependent on the *a priori* (i.e. where the values are close to 0) [82, pp. 47]. The trace of the averaging kernel, called the degrees of freedom for signal, provides a measure of how many independent pieces of information are contained in the measurement

$$d_s = \mathrm{tr}(\mathbf{A}). \tag{5.2.22}$$

One degree of freedom for signal implies that the measurement contains information about one part of the atmosphere. Two degrees of freedom for signal would imply that there are two independent partial column amounts usually representing different heights in the atmosphere that can be retrieved.

In the work done in the rest of this chapter, we are interested in the total column, which is a function of the profile, described by Equation 1.3.16. The column averaging kernel, $\mathbf{a}_{\boldsymbol{\rho}}$, is a measure of the sensitivity of the retrieved column amount to the profile at each altitude. It is computed by multiplying the averaging kernel, $\mathbf{A}$, by the column vector $\boldsymbol{\rho}$ that converts from a profile of volume mixing ratios (VMRs) to a total column:

$$\mathbf{a}_{\boldsymbol{\rho}} = \boldsymbol{\rho}^{\mathrm{T}}\mathbf{A}. \tag{5.2.23}$$

In this case, $\boldsymbol{\rho}$ must contain the air masses in each layer to convert VMR to number density (Equation 1.3.15) and then must sum them up with a discrete version of Equation 1.3.17, taking refraction and the spherical geometry into account.

Typically, these values are shown normalized: $a_{\rho_i}\rho_i^{-1}$, but because this artificially gives weight to regions of the atmosphere in which there is very little absorption (i.e. the mesosphere in Figure 5.1), the more physically-intuitive density-weighted column averaging kernel, $\mathbf{a}_{\boldsymbol{\rho}}$, will sometimes be used as well. Figure 5.1 illustrates the difference between density-weighted and normalized column averaging kernels.

Returning to Equation 5.2.1, we now add back in the model parameters ($\mathbf{b}$) and forward model error ($\boldsymbol{\Delta}\mathbf{f}$):

$$\mathbf{y} = \mathbf{F}(\mathbf{x}, \mathbf{b}) + \boldsymbol{\Delta}\mathbf{f} + \boldsymbol{\epsilon}$$

Equation 5.2.20 becomes:

$$\hat{\mathbf{x}} = \mathbf{A}\mathbf{x} + (\mathbf{I} - \mathbf{A})\mathbf{x}_{\mathbf{a}} + \mathbf{G}\boldsymbol{\epsilon}_{\mathbf{y}}, \text{ where} \tag{5.2.24}$$

$$\boldsymbol{\epsilon}_{\mathbf{y}} = \mathbf{K}_{\mathbf{b}}(\mathbf{b} - \hat{\mathbf{b}}) + \boldsymbol{\Delta}\mathbf{f} + \boldsymbol{\epsilon}, \tag{5.2.25}$$

where $\mathbf{K}_{\mathbf{b}} = \partial\mathbf{F}(\mathbf{x}, \mathbf{b})/\partial\mathbf{b}$ and $\hat{\mathbf{b}}$ are the estimates of $\mathbf{b}$.

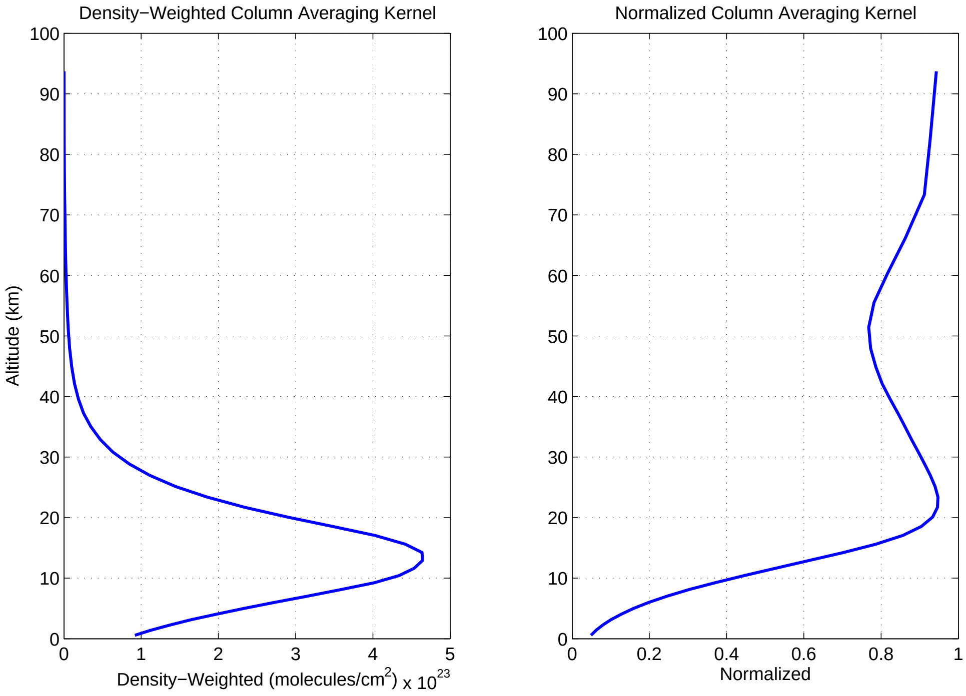

Figure 5.1: Density-weighted and normalized column averaging kernels for a typical ozone profile in the 3040 cm$^{-1}$ microwindow for the U of T FTS MCT detector.

### 5.2.1 Errors

Subtracting the true state vector from the retrieved state ($\hat{\mathbf{x}} - \mathbf{x}$) from Equation 5.2.24 gives us a collection of errors associated with the retrieval. There are four types of errors that arise from this retrieval method. From Rodgers [82, p. 48]:

$$\hat{\mathbf{x}} - \mathbf{x} = \begin{cases} (\mathbf{A} - \mathbf{I})(\mathbf{x} - \mathbf{x_a}) & \ldots \text{ a) smoothing error} \\ + \mathbf{G}\mathbf{K_b}(\mathbf{b} - \hat{\mathbf{b}}) & \ldots \text{ b) model parameter error} \\ + \mathbf{G}\boldsymbol{\Delta}\mathbf{f}(\mathbf{x}, \mathbf{b}, \mathbf{b}') & \ldots \text{ c) forward model error} \\ + \mathbf{G}\epsilon & \ldots \text{ d) retrieval noise} \end{cases} \tag{5.2.26}$$

We assume that the retrieval is an estimate of the true state of the atmosphere, with an error contribution by the averaging kernel matrix $\mathbf{A}$—called the smoothing error. Since we do not know the true state of the atmosphere ($\mathbf{x}$), we can only know the error statistics of the smoothing error ($\mathbf{S_s}$), given an ensemble of real states of the atmosphere. Typically, the mean state is taken to be the *a priori*, $\mathbf{x_a}$, and so the smoothing error is related to the *a priori* covariance matrix $\mathbf{S_a}$.

$$\begin{aligned}\mathbf{S_s} &= E\{(\mathbf{A}-\mathbf{I})(\mathbf{x}-\mathbf{x_a})\cdot(\mathbf{x}-\mathbf{x_a})^T(\mathbf{A}-\mathbf{I})^T\} \\ &= (\mathbf{A}-\mathbf{I})\mathbf{S_a}(\mathbf{A}-\mathbf{I})^T \qquad (5.2.27)\end{aligned}$$

The model parameter errors can be minimized through precise laboratory measurements, or by designing the experiment to minimize the dependence of the result on the parameters. The model parameter error covariance matrix ($\mathbf{S_f}$) is dependent on the covariance matrix of $\mathbf{b}$.

$$\mathbf{S_f} = \mathbf{G K_b S_b}(\mathbf{G K_b})^T \qquad (5.2.28)$$

The forward model error is difficult to evaluate because it must contain all the correct physics for the particular problem.

The retrieval noise is easy to evaluate, because it is dependent on the measurement noise error covariance matrix $\mathbf{S}_\epsilon$, which is normally assumed to be random, unbiased and diagonal.

$$\mathbf{S_m} = \mathbf{G S}_\epsilon \mathbf{G}^T \qquad (5.2.29)$$

The measurement noise is the inverse of the signal-to-noise ratio of the microwindow, which is placed down the diagonal of the $\mathbf{S}_\epsilon$ matrix.

In many OEM retrieval algorithms, elements other than the desired atmospheric state can be retrieved (for example, wavenumber shifts, baseline correction, line shape information) [83]. We will call the true states of these extra elements $\mathbf{e}$ and their *a prioris*, $\mathbf{e_a}$, so the total state vector, now called $\mathbf{s}$, becomes

$$\mathbf{s} = \begin{bmatrix}\mathbf{x} \\ \mathbf{e}\end{bmatrix}.$$

In this case, the averaging kernel becomes

$$\begin{bmatrix}\mathbf{A} & \mathbf{A_{xe}} \\ \mathbf{A_{ex}} & \mathbf{A_{ee}}\end{bmatrix},$$

with additional elements ($\mathbf{A_{xe}}$ and $\mathbf{A_{ex}}$) that could affect the retrieval, leaving $\mathbf{A}$ as the averaging kernel containing only the profile information. Equation 5.2.24 is rewritten as:

$$\hat{\mathbf{s}} - \mathbf{s_a} = \begin{bmatrix} \hat{\mathbf{x}} - \mathbf{x_a} \\ \hat{\mathbf{e}} - \mathbf{e_a} \end{bmatrix} = \begin{bmatrix} \mathbf{A} & \mathbf{A_{xe}} \\ \mathbf{A_{ex}} & \mathbf{A_{ee}} \end{bmatrix} \begin{bmatrix} \mathbf{x} - \mathbf{x_a} \\ \mathbf{e} - \mathbf{e_a} \end{bmatrix} + \begin{bmatrix} \mathbf{G}\boldsymbol{\epsilon_y} \\ \boldsymbol{\epsilon_e} \end{bmatrix}, \tag{5.2.30}$$

where $\boldsymbol{\epsilon_e}$ represents the errors associated with the additional elements. Rearranging this equation, we get:

$$\hat{\mathbf{x}} - \mathbf{x} = (\mathbf{A} - \mathbf{I})(\mathbf{x} - \mathbf{x_a}) + (\mathbf{A_{xe}})(\mathbf{e} - \mathbf{e_a}) + \mathbf{G}\boldsymbol{\epsilon_y}. \tag{5.2.31}$$

This adds a new error term, called the interference error: $\mathbf{A_{xe}}(\mathbf{e} - \mathbf{e_a})$. Its error covariance matrix is:

$$\mathbf{S_e} = \mathbf{A_{xe}}\mathbf{S_{ea}}\mathbf{A_{xe}}^T, \tag{5.2.32}$$

where $\mathbf{S_{ea}}$ is the *a priori* covariance of $\mathbf{e}$. Typically, the total error is taken to be a sum (in quadrature) of the smoothing error, retrieval noise and interference error [83].

## 5.3 SFIT2

A standard program for retrieving trace gas concentrations from measurements made by Fourier transform spectrometers is called SFIT2. It is described by [84–86] and is based on the SFIT1 program [87]. SFIT2 is an optimal estimation program—it uses the maximum point of the probability distribution function to determine the best result; that is, when

$$\frac{\partial P(\mathbf{x}|\mathbf{y})}{\partial \mathbf{x}} = 0, \tag{5.3.1}$$

to obtain Equation 5.2.16:

$$\hat{\mathbf{x}} = \mathbf{x_a} + (\mathbf{S_a^{-1}} + \mathbf{K}^T\mathbf{S}_\epsilon^{-1}\mathbf{K})^{-1}\mathbf{K}^T\mathbf{S}_\epsilon^{-1}(\mathbf{y} - \mathbf{K}\mathbf{x_a}).$$

Because of the nonlinear nature of the problem, SFIT2 uses a Newtonian iteration technique to minimize $P(\mathbf{x}|\mathbf{y})$ from 5.2.12, iterating to obtain the best estimate of the true state of the atmosphere ($\hat{\mathbf{x}}$).

$$\mathbf{x}_{i+1} = \mathbf{x_a} + (\mathbf{S_a^{-1}} + \mathbf{K}_i^T\mathbf{S}_\epsilon^{\mathbf{-1}}\mathbf{K}_i)^{-1}\mathbf{K}_i^T\mathbf{S}_\epsilon^{\mathbf{-1}}[(\mathbf{y} - \mathbf{y}_i) - \mathbf{K}_i(\mathbf{x_a} - \mathbf{x}_i)] \qquad (5.3.2)$$

The $\mathbf{y}_i$ term is what the forward model produces from the $i$th estimate of $\mathbf{x}$: $\mathbf{F}(\mathbf{x}_i)$, or a calculated spectrum. The $\mathbf{K}_i$ matrix is the weighting function matrix $\mathbf{K}$ evaluated at $\mathbf{x}_i$ ($\partial\mathbf{F}/\partial\mathbf{x}|_{\mathbf{x}_i}$).

The inputs to SFIT2 include: the absorption coefficients and line parameters from the HITRAN 2004 database [31]; *a priori* profiles and error covariance matrices for each molecule; an atmospheric pressure-temperature profile provided by data from the NCEP/NCAR analysis [88], selected out by the data from the Goddard automailer [89]; and an atmospheric path calculated by a ray-tracing program called FSCATM [90, 91].

The *a priori* information that is used for all the work in the remainder of this chapter was generated by Aldona Wiacek [92, 93] from climatologies from the HALogen Occultation Experiment (HALOE) satellite instrument [94], supplemented by daytime profiles from the Michelson Interferometer for Passive Atmospheric Sounding (MIPAS) satellite instrument [95], profiles from the Jet Propulsion Laboratory's (JPL's) MkIV balloon FTS [96] and the Kiruna NDACC station *a priori* profiles. The *a priori* profiles were generated for the Toronto Atmospheric Observatory (∼43°N), and used in the analyses both for the measurements recorded in Toronto and those recorded in Vanscoy (∼52°N).The *a priori* covariance matrices were assumed to be diagonal, with 30% standard deviation at each level for all molecules with the exception of ozone for the Vanscoy data, for which a 20% standard deviation was assumed. The lower standard deviation was used in that case because there were ozone sonde profiles recorded every second day throughout the MANTRA 2004 campaign, which agreed within 20% of the *a priori* value.

FSCATM [90, 91] is a nonlinear forward model. It uses an *a priori* state estimate, pressure and temperature profiles, and the measurement latitude, longitude, altitude, and time to numerically calculate the air mass distribution for a model atmosphere, taking atmospheric refraction into account.

Small spectral regions ("microwindows") are chosen to retrieve a target gas. Microwindows are chosen if they contain at least one suitably strong absorption line of the target gas with as few interfering features as possible. The main input file to SFIT2 includes a large number of parameters, including the number of microwindows to be used simultaneously for retrieval of the molecule, what interfering species are present in the microwindow(s), whether or not there are solar lines in the microwindow, and what additional parameters should be retrieved. The main additional parameters of interest in this work relate to the instrument line shape information, called the effective apodization parameter (EAP) and the phase error (PHS)—described in §3.3.2 as the effective apodization and OPD-dependent phase error, respectively.

When retrieving columns of a gas, the absorption line shape (§1.3.1) is important: this shape defines the amount of absorber in the path and where it originates in the atmosphere via Lambert's Law (Equation 1.3.9). The instrument line shape (§3.3.2), is, therefore, also vitally important, so we can distinguish the instrumental effects from the atmospheric ones.

In SFIT2, the EAP and PHS can either be retrieved as a set of polynomial coefficients or as Fourier components. In the work done here, when they are retrieved, they are retrieved as third-order polynomial coefficients. If the EAP and PHS values are known from, say, independent gas cell measurements, tabular values (columns containing EAP or PHS values and the corresponding OPD) can be input into SFIT2 instead of retrieving the PHS and EAP parameters. A standard NDACC method for this uses calibrated HBr cells [97] and a retrieval algorithm that determines ILS information. Hase, Blumenstock, and Paton-Walsh [74] describe their software designed for this purpose, called LINEFIT, which produces a table containing modulation efficiency (a term used interchangeably with effective apodization) and phase error, as a function of OPD.

### 5.3.1 LINEFIT inputs to SFIT2

The modulation efficiency produced from LINEFIT is the attenuation of the signal as a function of OPD, divided by the apodization function intentionally applied to the interferogram. (In the case of the U of T FTS, a triangular apodization is applied.) This should be the correct input to SFIT2, as SFIT2 is supposed to multiply the modulation efficiency by the apodization function before performing the retrieval. This, however, does not provide the best spectral fits to the data. The best fits are found from multiplying the modulation efficiency by the apodization function before inputting it into SFIT2 (Figure 5.2). A comparison between the EAP retrieved from SFIT2 and the LINEFIT modulation efficiency for the U of T FTS is shown in Figure 5.3. This test was also done with a Hamming apodization function, with the same results: that multiplying the modulation efficiency from LINEFIT with a Hamming filter created the best spectral fits. Thus, for all LINEFIT inputs to SFIT2 (notably in §5.6), the LINEFIT modulation efficiency is multiplied by the apodization function.

## 5.4 MANTRA 2004 Flight Data

As described in §4, there were only two spectra recorded on each detector of the U of T FTS during the MANTRA 2004 flight. The following sections will describe the flight data quality, results from the retrievals of HCl, $CO_2$, $N_2O$, CO, $O_3$ and $CH_4$ and comparison with the Microwave Limb Sounder satellite instrument, which measured close to Vanscoy multiple times during the MANTRA 2004 campaign.

The Microwave Limb Sounder (MLS) instrument is on board the Aura spacecraft, which is part of the Earth Observing System (EOS) mission. Aura was launched on July 15, 2004 and MLS began recording science data on August 13, 2004 [36, 37]. The MLS overpasses near Vanscoy for the August 13–September 13 dates are shown in Figure 5.4. MLS on Aura is an improved version of the MLS instrument on the Upper Atmosphere Research Satellite (UARS) [98]. The MLS instrument measures thermal emissions of a

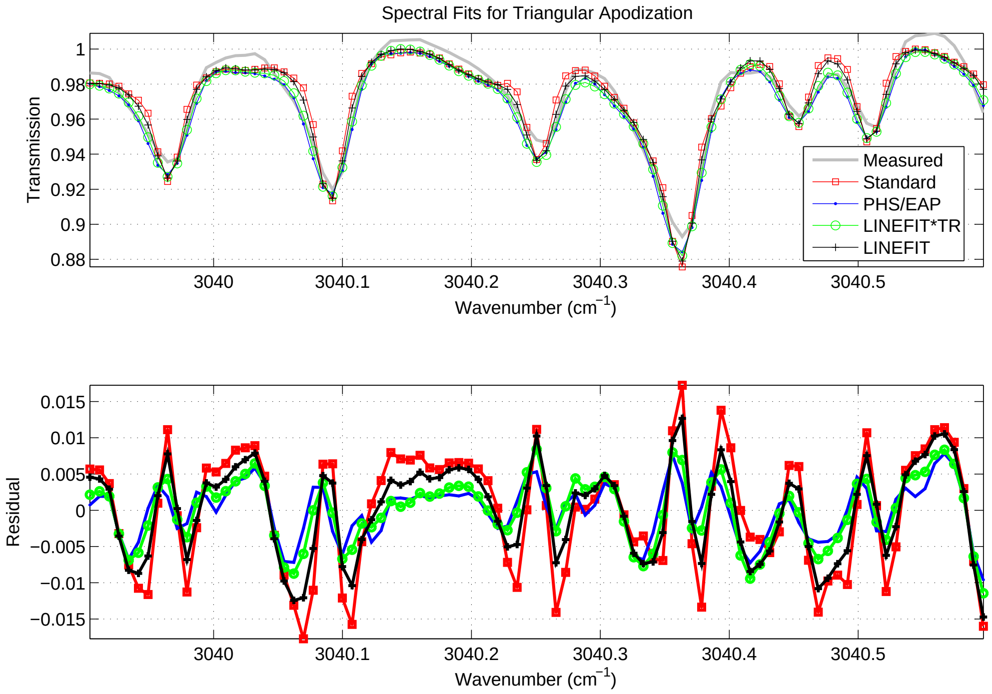

Figure 5.2: Comparison of spectral fits for four retrieval cases: the standard retrieval, where no ILS information is provided to SFIT2, the PHS/EAP retrieved case, where SFIT2 retrieves the ILS information itself, the case when the LINEFIT results are used as a tabular input to SFIT2, and the case when the LINEFIT results, multiplied by a triangular apodization, are used as a tabular input to SFIT2. The PHS/EAP retrieved and LINEFIT*TR cases provide the best spectral fits.

variety of molecules, including $O_3$, HCl, $N_2O$ and CO with high vertical resolution. The results presented in the following sections are some of the earliest comparisons with the MLS instrument on Aura.

## 5.4.1 MANTRA 2004 Flight Data Quality

Because of the rotation of the payload, the delta-tracker on the U of T FTS was required to function at the limits of its tracking range. The errors associated with the delta-tracker and its current electronics increase as the edge of the tracking range is reached because the motors are required to apply more force as the springs that control the mirror are stretched. As a result, one would suspect that the signal-to-noise ratio of the interferogram would be reduced. This is, in fact, apparent in the spectra produced from

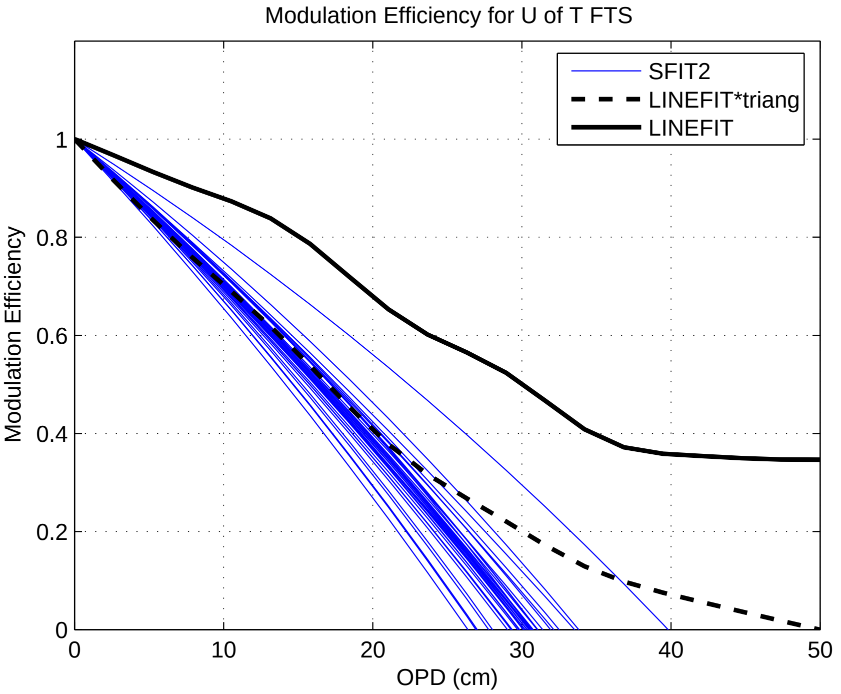

Figure 5.3: Comparison between EAP from SFIT2 and LINEFIT modulation efficiency. The LINEFIT modulation efficiency multiplied by the triangular function (dashed line) is used as the input to SFIT2 for this intercomparison.

the balloon payload.

Further, the instrument line shape of the FTS was unknown—even had the ILS been measured before the flight, this would not guarantee consistency with the ILS during the flight since the ILS is sensitive to temperature. The instrument temperatures during the flight ranged from –40°C to +50°C (see Figure 4.15), and this is potentially a large contributor to ILS changes. For all retrievals below, PHS and EAP parameters are retrieved as part of the state vector, in an attempt to account for the ILS in the retrievals. This method is described in detail in §5.6.2. In that section, it is determined that retrieving PHS and EAP parameters from SFIT2 for stratospheric species is a viable alternative to calculating ILS parameters independently from a gas cell measurement.

A third problem with the data from the flight is time. The on-board FTS computer clock was synchronized to the ground-based computer clocks (which are synchronized to the Microsoft server) prior to launch. However, it is a known problem that BIOS clocks

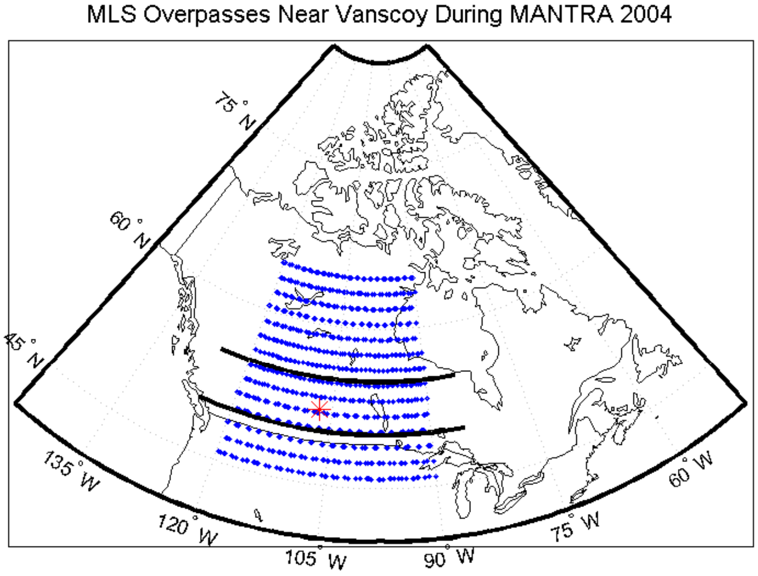

Figure 5.4: MLS profile locations (blue dots) near Vanscoy (red star) during the MANTRA 2004 campaign. The latitudes used for the ground-based comparisons are marked by the black lines.

are sensitive to temperature (and tend to lose time when cold). Unfortunately, the BIOS chip battery was ejected from the flight computer upon landing, and so the time shift could not be estimated. For the results described below, I have assumed that the on-board computer time recorded on each spectrum is the correct time for a number of reasons. First, the $CO_2$ column retrievals are not inconsistent with the *a priori* column (maximum 8% difference—see Table 5.8), indicating that the solar zenith angle calculated for the spectrum time is not seriously in error. Second, the computer was insulated, and its temperature change throughout the flight remained between 0 and 55°C (Figure 4.15). Third, a handwritten log was kept during the flight to record significant events. The times recorded in the log for the acquisition of the spectra are consistent with the times recorded on board (within 3 minutes). There is at least a one-minute delay between the time that the interferogram is recorded and sent down to the ground so the timing is, at most, two minutes off. This translates into a maximum elevation angle error of 0.26°.

| Filename | Detector | Time | Altitude (m) | Location | SZA | Apodization |
|---|---|---|---|---|---|---|
| **040902FI.D13 (I13)** | InSb | 19:53:31 | 35063.4 | 51.5293°N, 108.3410°W | 89.58° | Triangular |
| **040902FI.D14 (I14)** | InSb | 19:54:55 | 35021.7 | 51.5246°N, 108.3461°W | 89.77° | Triangular |
| **040902FI.D15 (I15)** | InSb | 19:53:31 | 35063.4 | 51.5293°N, 108.3410°W | 89.58° | Boxcar |
| **040902FI.D16 (I16)** | InSb | 19:54:55 | 35021.7 | 51.5246°N, 108.3461°W | 89.77° | Boxcar |
| **040902FM.D13 (M13)** | MCT | 19:53:31 | 35063.4 | 51.5293°N, 108.3410°W | 89.58° | Triangular |
| **040902FM.D14 (M14)** | MCT | 19:54:55 | 35021.7 | 51.5246°N, 108.3461°W | 89.77° | Triangular |
| **040902FM.D15 (M15)** | MCT | 19:53:31 | 35063.4 | 51.5293°N, 108.3410°W | 89.58° | Boxcar |
| **040902FM.D16 (M16)** | MCT | 19:54:55 | 35021.7 | 51.5246°N, 108.3461°W | 89.77° | Boxcar |

Table 5.1: The naming convention of the flight spectra.

### 5.4.2 Flight Data and Results

Because raw interferograms are recorded for the U of T FTS, and spectra are produced separately, we have the freedom to choose any apodization function we wish when converting the interferograms into spectra. The four interferograms from the flight were processed using both a boxcar apodization function (unapodized) and a triangular filter that improves the signal-to-noise ratio of the spectra, but also reduces the resolution (see Table 5.1 for the spectrum naming convention). Column amounts of $CO_2$, $O_3$, HCl, $CH_4$, $N_2O$ and CO were retrieved using SFIT2 and SFIT1 [87] in the microwindows listed in Table 5.2. Phase error and effective apodization parameters were retrieved as part of the state vector, based on the results in §5.6.2. SFIT1 is spectral fitting program similar to SFIT2, but it finds the best fit to the microwindow by changing the *a priori* profile by a scale factor rather than changing the *a priori* profile only where the retrieval is sensitive to the spectrum. Because there were only two spectra recorded, and they were of similar solar zenith angle, a profile cannot be retrieved. Also, at the time these spectra were recorded, the solar zenith angles were 89.59° and 89.77°; sunset had not yet begun. However, there is some information in the spectra about the column of the atmosphere above the balloon height.

With the SFIT2 analysis, a density-weighted column averaging kernel can be calculated, which gives the sensitivity of the retrieved column to a particular part of the atmosphere. Not surprisingly, the sensitivities of all molecules were most significant at the lowest altitudes (see Figure 5.5).

| Target Gas | Microwindow | Spectral Range ($cm^{-1}$) | Interfering Species |
|---|---|---|---|
| $O_3$ | 3041 | 3039.90–3040.60 | $H_2O$, $CH_4$ |
| $N_2O$ | 2203 | 2204.60–2204.81 | $O_3$ |
| HCl | 2821 | 2821.45–2821.70 | $H_2O$, $CH_4$, $NO_2$, $O_3$ |
| | | 2843.50–2843.75 | $H_2O$, $CH_4$, $NO_2$, $O_3$ |
| | | 2944.75–2945.05 | $H_2O$, $CH_4$, $NO_2$, $O_3$ |
| | | 2963.15–2963.40 | $H_2O$, $CH_4$, $NO_2$, $O_3$ |
| CO | 2147 | 2146.90–2147.60 | $CO_2$, $O_3$, $N_2O$, $H_2O$ |
| $CH_4$ | 2937 | 2937.05–2938.05 | $H_2O$ |
| $CO_2$ | 3359 | 3356.50–3364.50 | $H_2O$, $N_2O$, HCN |

Table 5.2: Flight data microwindows.

The SFIT1 analysis has no averaging kernel since it assumes equal sensitivity to each layer. Column amounts are retrieved in both cases by applying Equations 1.3.15 and 1.3.16, using the method described in §5.2. The SFIT1 column will deviate most from the *a priori* column because the entire profile has changed by a scale amount, instead of only the layers which are sensitive to the measurement. In order to properly compare the SFIT1 and SFIT2 analyses, one can smooth the SFIT1 analysis with the SFIT2-retrieved averaging kernel by weighting the SFIT1 profile by the SFIT2 averaging kernel, and allowing the SFIT2 *a priori* to provide information where the averaging kernel is insensitive [83]. We use the equation

$$\mathbf{x_s} = \mathbf{A}\mathbf{x_h} + (\mathbf{I} - \mathbf{A})\mathbf{x_a} \tag{5.4.1}$$

where $\mathbf{x_s}$ is the smoothed profile, $\mathbf{A}$ is the averaging kernel, $\mathbf{x_h}$ is the SFIT1 profile and $\mathbf{x_a}$ is the *a priori* profile.

Upon smoothing the SFIT1 retrieved profile with SFIT2, the results are more consistent. Tables 5.3–5.8 contain the vertical column amounts above the balloon (from 35 km to 100 km) and the percent differences from the *a priori* column.

Comparisons with the mean MLS profiles are shown for only the highest U of T FTS SNR fit for each microwindow, which is M13 for ozone, $CO_2$ and $CH_4$. For $N_2O$ and CO, the M14 spectrum gives a better fit. The HCl microwindow shown is M13, even though the SNR is slightly higher for I13 because the HCl M13 fit yields a more stable retrieval.

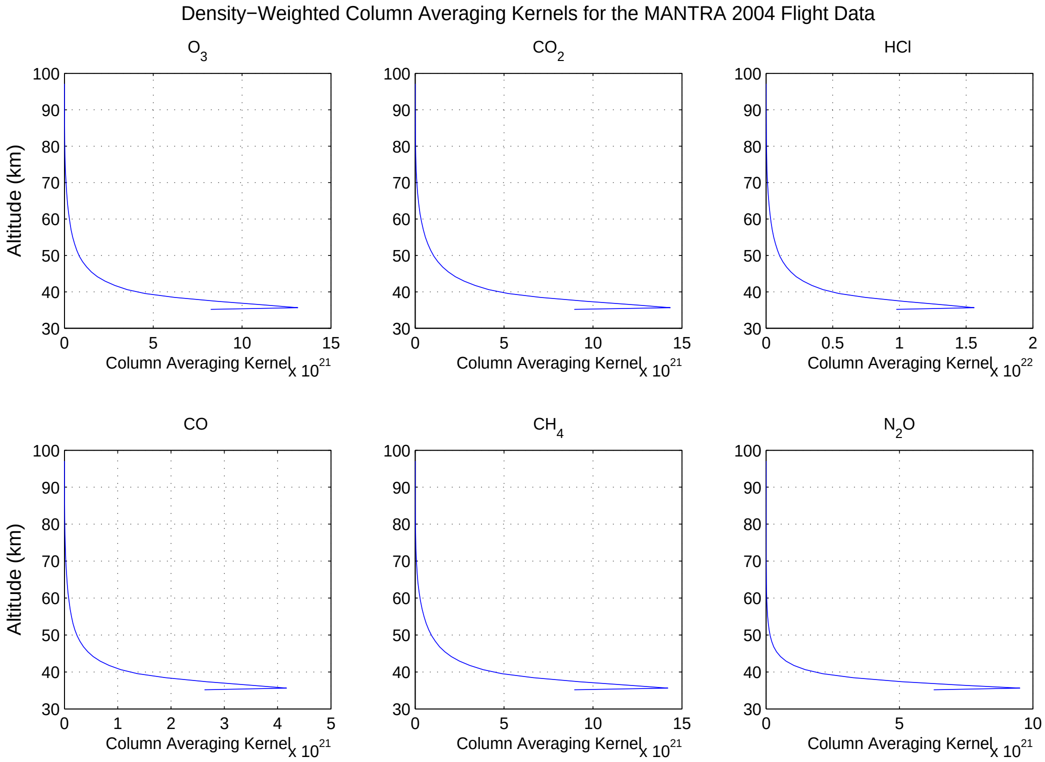

Figure 5.5: Flight column averaging kernels.

The fits are shown in Figures 5.6–5.17. Profile comparisons are shown in Figures 5.18–5.23. The MLS data were constrained to a 51–53°N latitude band, a 90–120°W longitude band and dates including August 27 through September 6th. In general, the SFIT2 and smoothed SFIT1 retrievals are consistent with the profiles generated by MLS. A more quantitative comparison between MLS and the U of T FTS can be achieved by applying the same smoothing procedure from Equation 5.4.1, but with $\mathbf{x_h}$ as the MLS profile. The resulting mean profiles are shown in Figures 5.18–5.23 and the column amounts over the 35 km to 100 km altitude range and percentage differences from the *a priori* are listed in Tables 5.3 through 5.8. The columns retrieved by the FTS and MLS differ at maximum by 15% for ozone, 21% for $N_2O$, 16% for CO and 14% for HCl. The percent difference for spectrum M13 for $O_3$ is 0.03%, M13 for HCl is 3.4%, M14 for CO is 15%, and M14 for $N_2O$ is 19%.

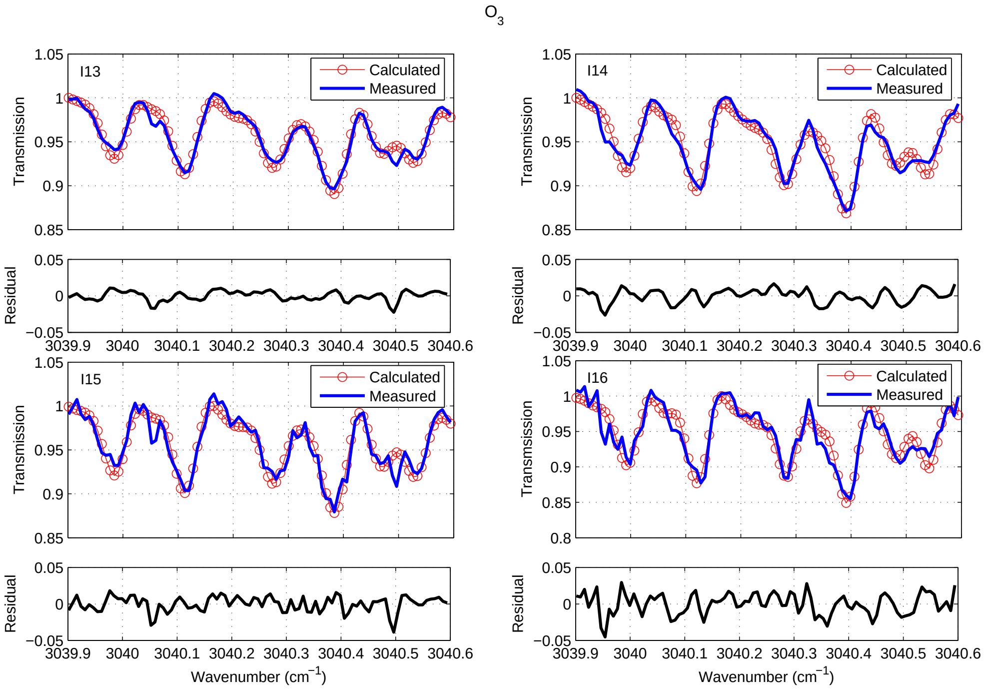

Figure 5.6: Flight data InSb $O_3$ spectral fits. The four panels show the four spectra described in Table 5.1.

As a point of clarity, the FTS profiles shown are not, in fact, true profiles, since these spectra have only ∼1 degree of freedom for signal. The profiles only indicate where the retrieval is sensitive to the measurements and where they differ (and by how much) from the *a priori*.

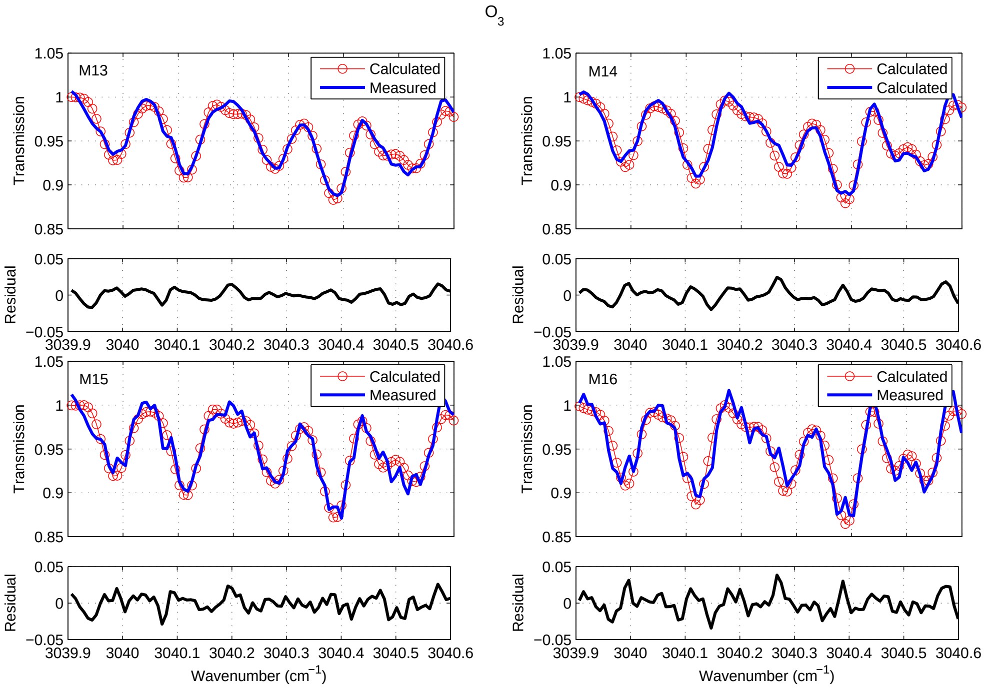

Figure 5.7: As in Figure 5.6, but for MCT $O_3$ spectral fits.

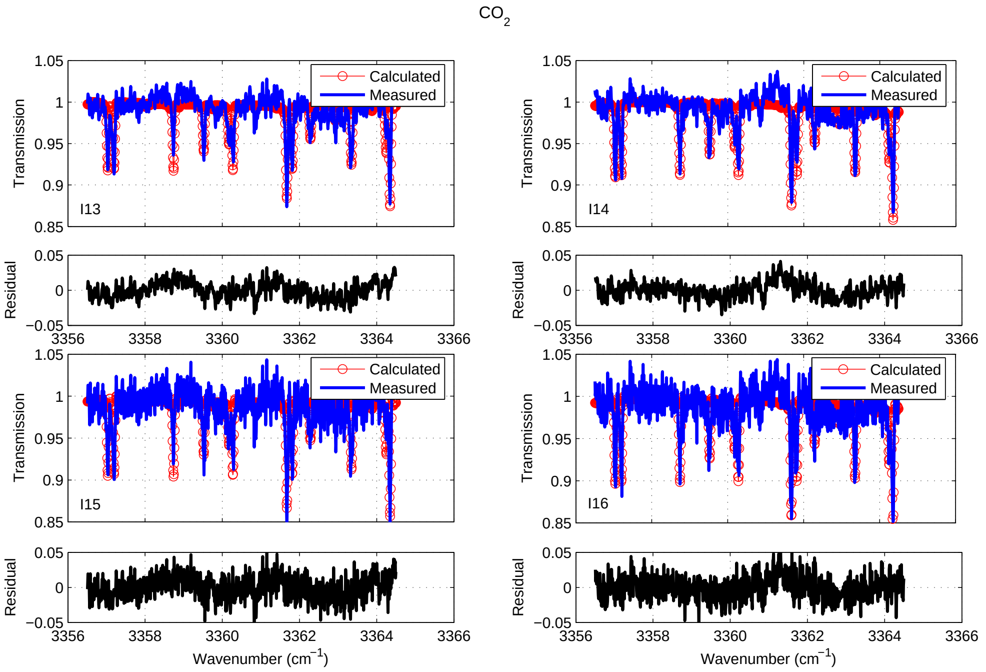

Figure 5.8: As in Figure 5.6, but for InSb $CO_2$ spectral fits.

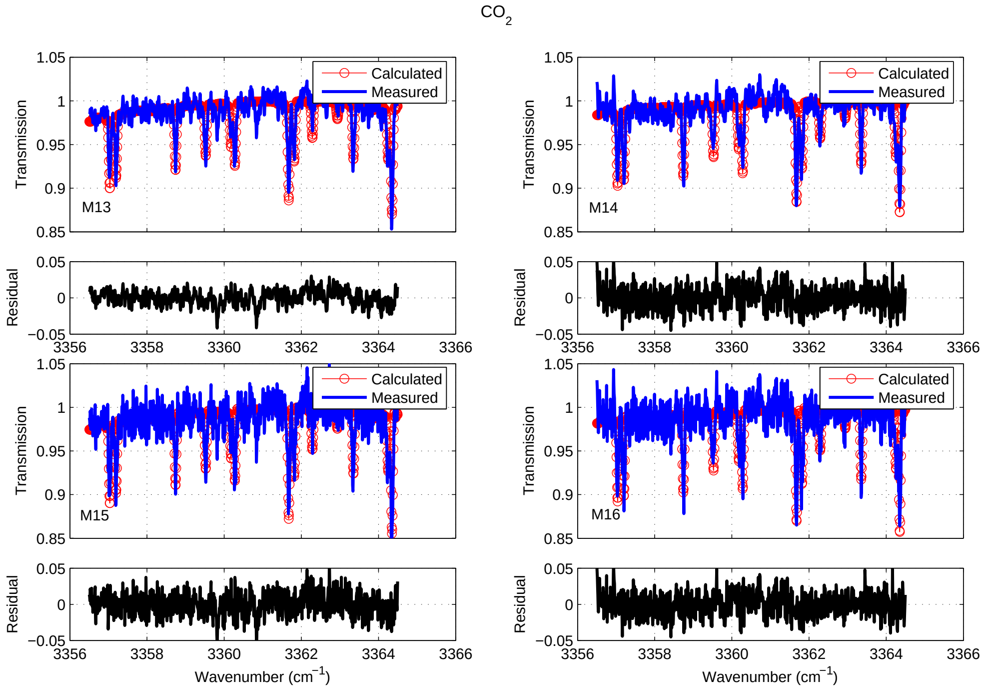

Figure 5.9: As in Figure 5.6, but for MCT $CO_2$ spectral fits.

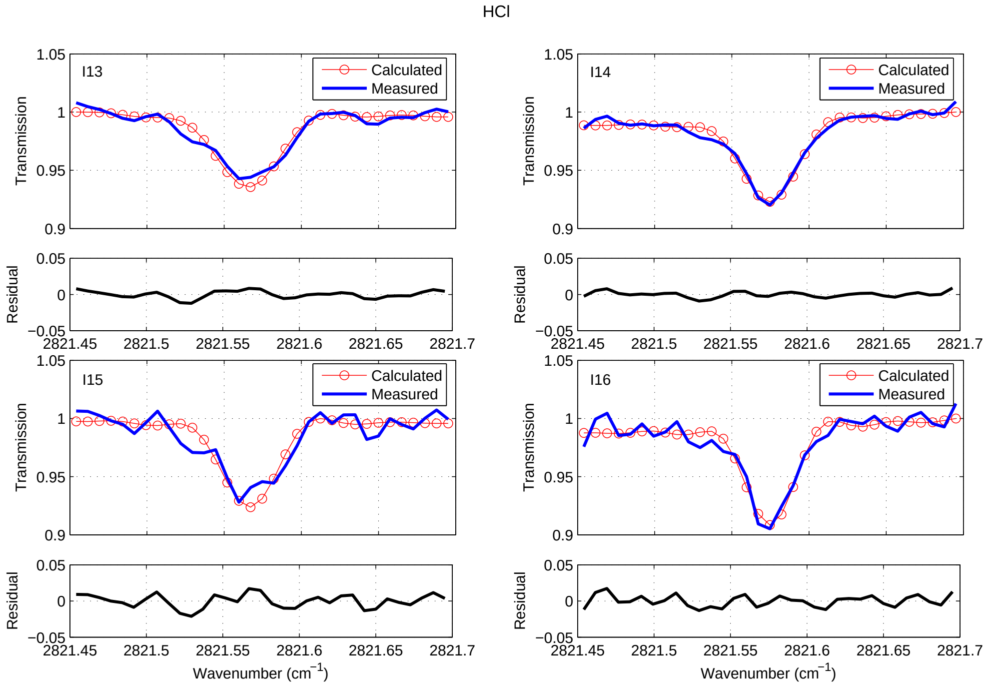

Figure 5.10: As in Figure 5.6, but for InSb HCl spectral fits. Only the first bandpass fit is shown.

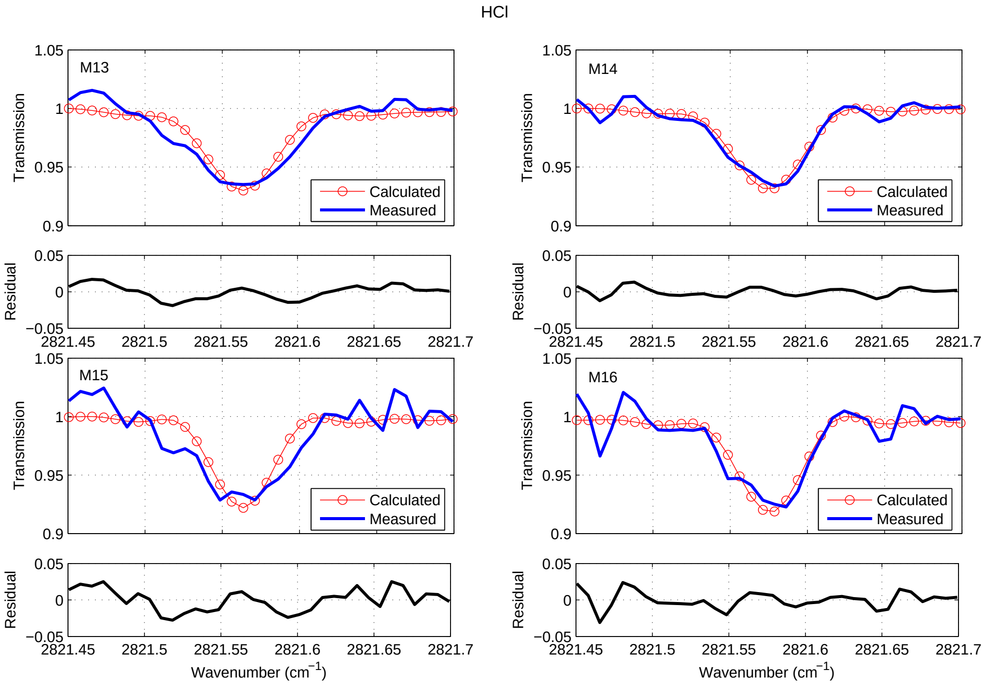

Figure 5.11: As in Figure 5.6, but for MCT HCl spectral fits. Only the first bandpass fit is shown.

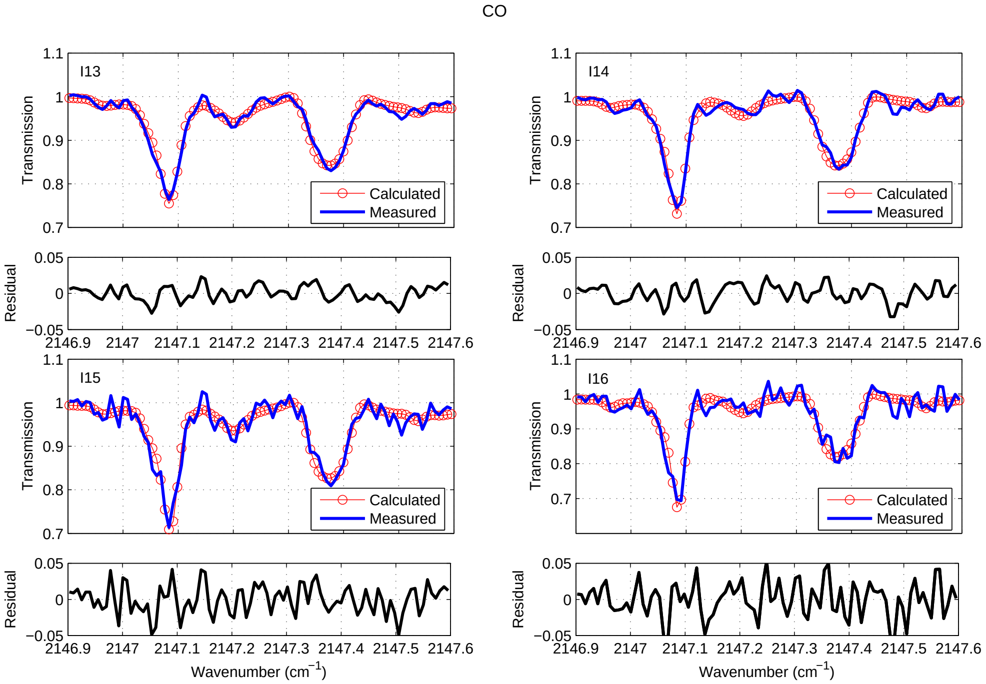

Figure 5.12: As in Figure 5.6, but for InSb CO spectral fits.

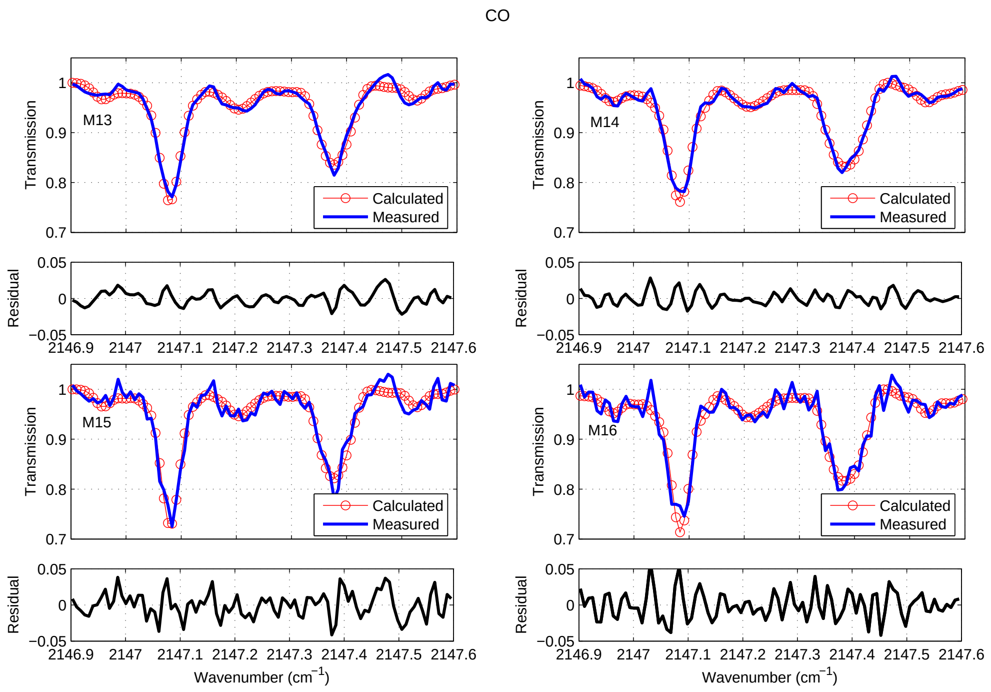

Figure 5.13: As in Figure 5.6, but for MCT CO spectral fits.

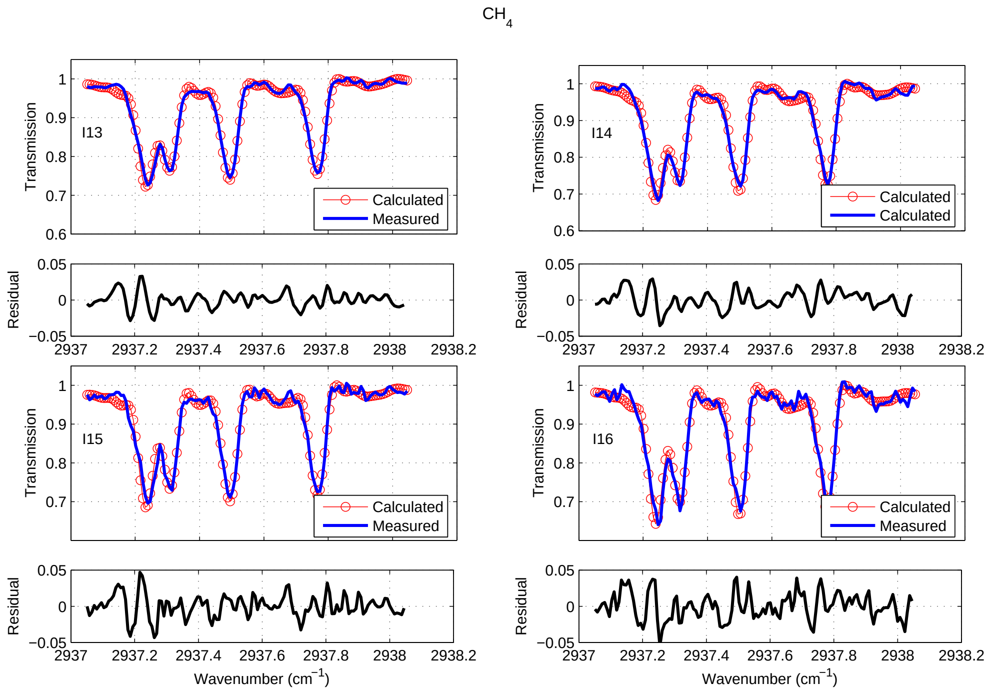

Figure 5.14: As in Figure 5.6, but for InSb $CH_4$ spectral fits.

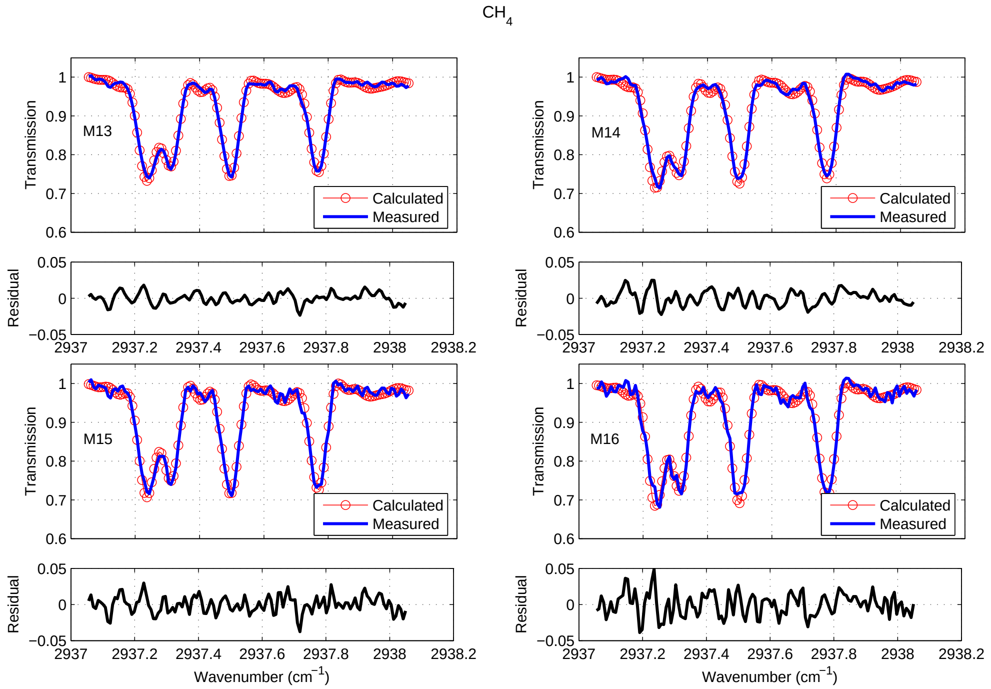

Figure 5.15: As in Figure 5.6, but for MCT $CH_4$ spectral fits.

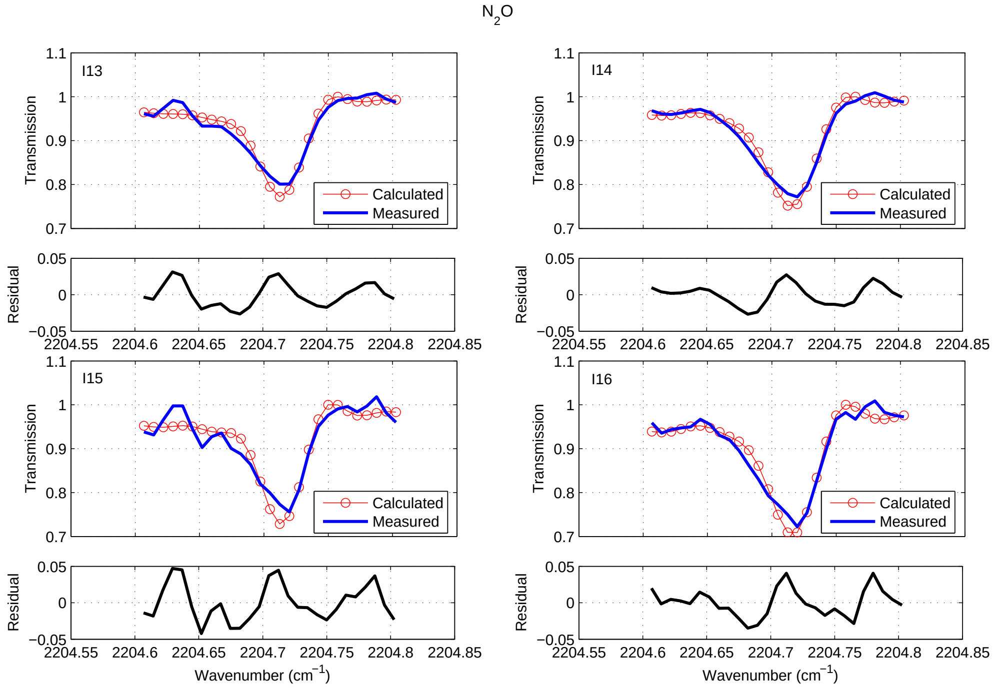

Figure 5.16: As in Figure 5.6, but for InSb $N_2O$ spectral fits.

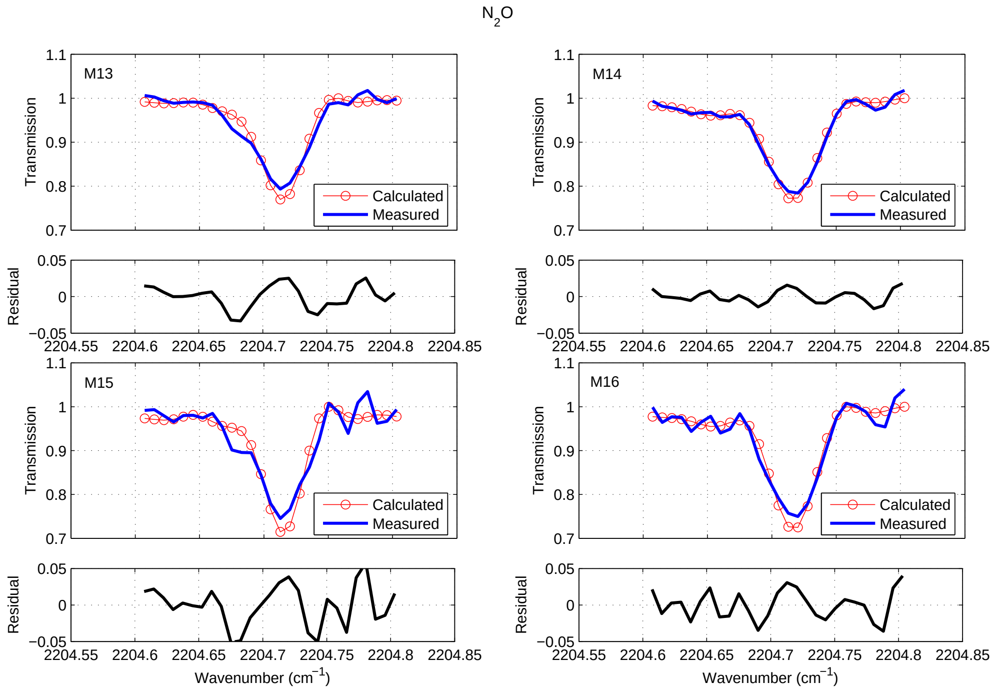

Figure 5.17: As in Figure 5.6, but for MCT $N_2O$ spectral fits.

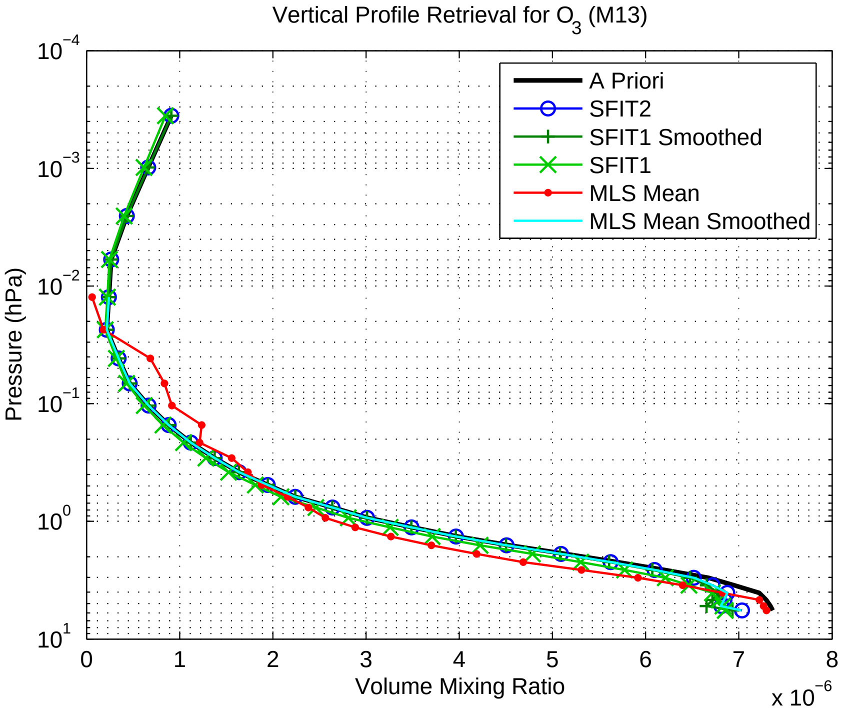

Figure 5.18: The SFIT2 profile, original and smoothed SFIT1 profiles, and original and smoothed MLS mean profiles of ozone in the 3041 cm$^{-1}$ microwindow from the MANTRA 2004 flight data.

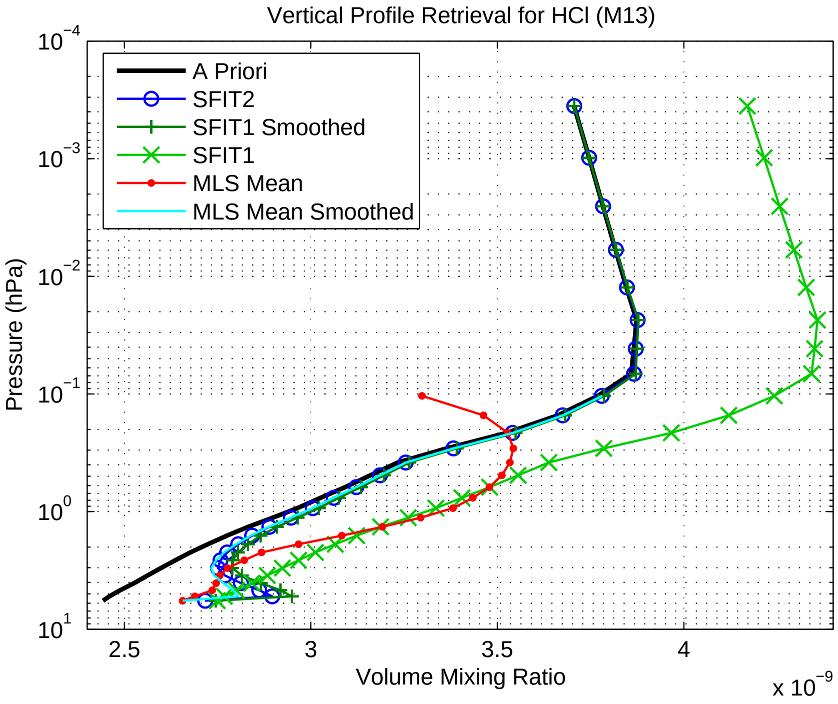

Figure 5.19: The SFIT2 profile, original and smoothed SFIT1 profiles, and original and smoothed MLS mean profiles of HCl from the MANTRA 2004 flight data.

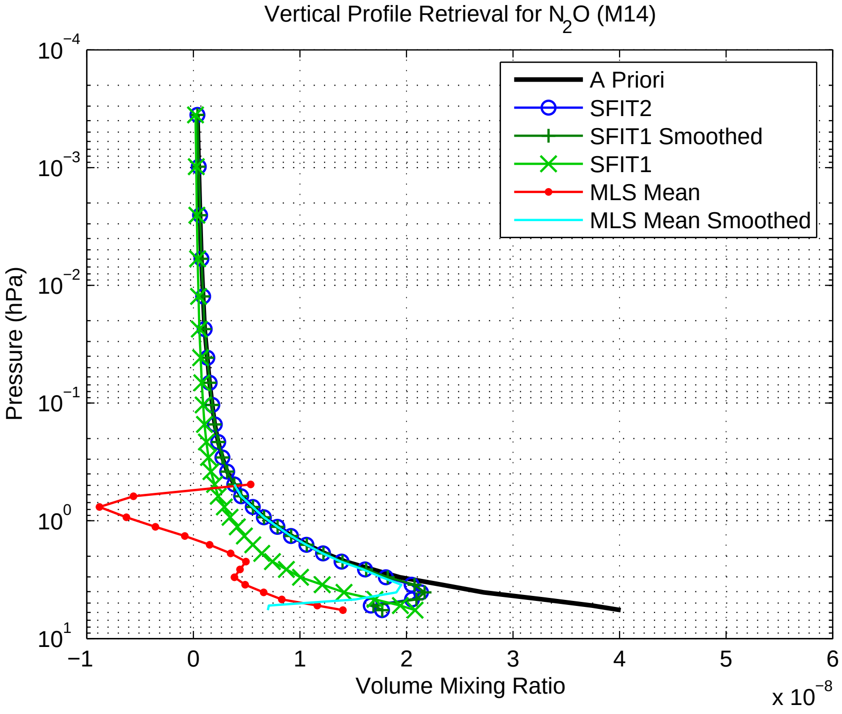

Figure 5.20: The SFIT2 profile, original and smoothed SFIT1 profiles, and original and smoothed MLS mean profiles of $N_2O$ from the MANTRA 2004 flight data.

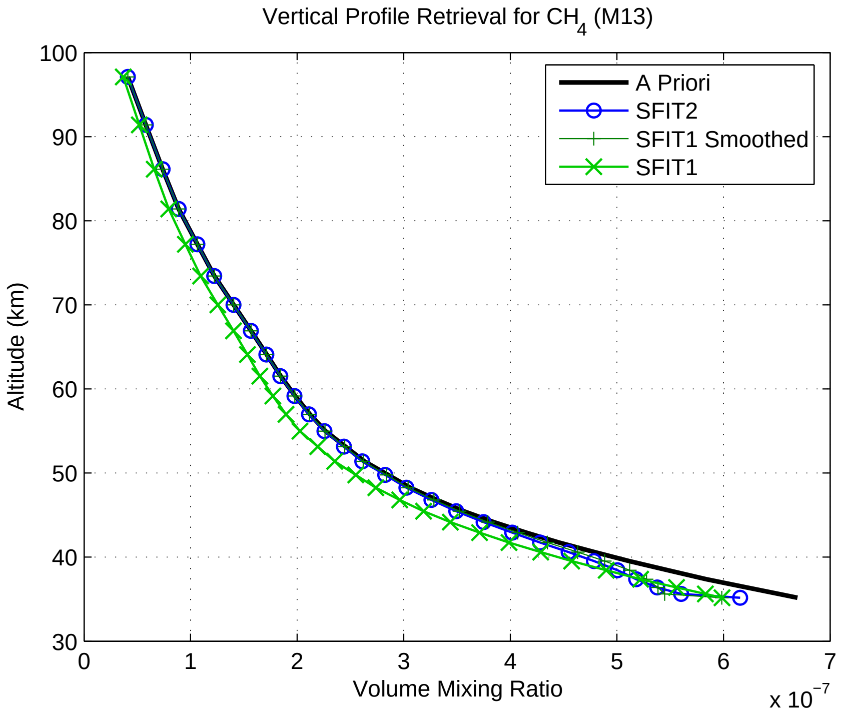

Figure 5.21: The SFIT2, original and smoothed SFIT1 $CH_4$ from the MANTRA 2004 flight data.

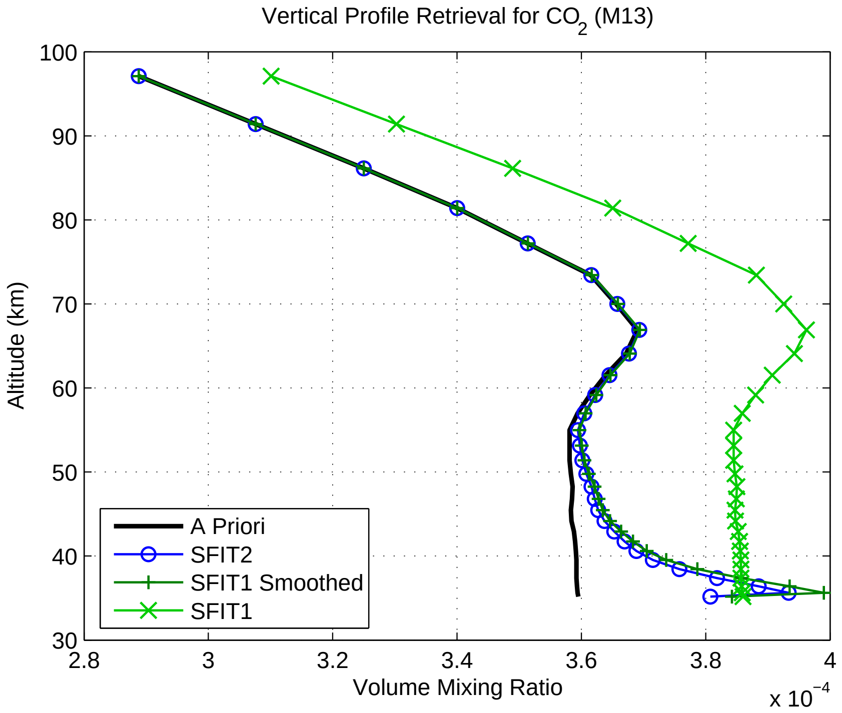

Figure 5.22: The SFIT2, original and smoothed SFIT1 $CO_2$ from the MANTRA 2004 flight data.

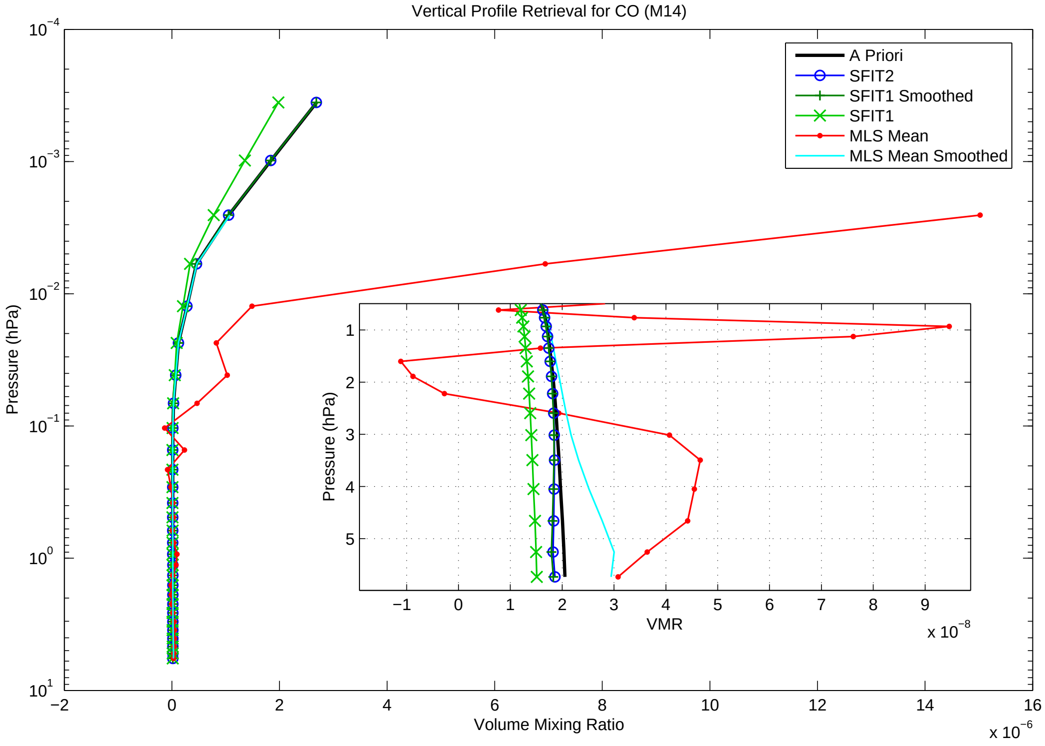

Figure 5.23: The SFIT2 profile, original and smoothed SFIT1 profiles, and original and smoothed MLS mean profiles of CO from the MANTRA 2004 flight data. The inset is an enlargement of the lowest pressure levels.

| | **SFIT2** | **SNR** | % | **SFIT1** | **SNR** | % | **SFIT1 Smoothed** | % | **MLS** | % | **MLS Smoothed** | % | **A Priori** |
|---|---|---|---|---|---|---|---|---|---|---|---|---|---|
| **I13** | 5.87e+017 | 150 | -17.36 | 5.11e+017 | 150 | -28.06 | 5.83e+017 | -17.91 | 6.52e+017 | -8.19 | 6.85e+017 | -3.49 | 7.10e+017 |
| **I14** | 6.26e+017 | 116 | -12.41 | 5.38e+017 | 115 | -24.82 | 6.13e+017 | -14.24 | 6.57e+017 | -8.13 | 6.94e+017 | -2.94 | 7.15e+017 |
| **I15** | 5.77e+017 | 108 | -18.71 | 4.83e+017 | 107 | -31.91 | 5.66e+017 | -20.28 | 6.52e+017 | -8.19 | 6.85e+017 | -3.49 | 7.10e+017 |
| **I16** | 5.95e+017 | 77 | -16.83 | 4.32e+017 | 76 | -39.65 | 5.58e+017 | -22.02 | 6.57e+017 | -8.13 | 6.95e+017 | -2.85 | 7.15e+017 |
| **M13** | 6.85e+017 | 150 | -3.46 | 6.60e+017 | 150 | -6.94 | 6.78e+017 | -4.43 | 6.52e+017 | -8.19 | 6.85e+017 | -3.49 | 7.10e+017 |
| **M14** | 6.50e+017 | 122 | -9.06 | 5.86e+017 | 121 | -18.01 | 6.40e+017 | -10.47 | 6.57e+017 | -8.13 | 6.94e+017 | -2.97 | 7.15e+017 |
| **M15** | 6.61e+017 | 105 | -6.89 | 5.65e+017 | 94 | -20.38 | 6.18e+017 | -12.87 | 6.52e+017 | -8.19 | 6.85e+017 | -3.47 | 7.10e+017 |
| **M16** | 6.38e+017 | 83 | -10.83 | 5.47e+017 | 83 | -23.52 | 6.20e+017 | -13.35 | 6.57e+017 | -8.13 | 6.94e+017 | -2.92 | 7.15e+017 |

Table 5.3: Ozone in the 3041 $\text{cm}^{-1}$ microwindow. These are retrieved vertical column amounts in molecules/$\text{cm}^2$ of $O_3$ over a 35–100-km altitude range from the MANTRA 2004 U of T FTS flight data. The signal-to-noise ratio of each spectrum and the percent difference from the *a priori* column are shown.

| | **SFIT2** | **SNR** | % | **SFIT1** | **SNR** | % | **SFIT1 Smoothed** | % | **MLS** | % | **MLS Smoothed** | % | **A Priori** |
|---|---|---|---|---|---|---|---|---|---|---|---|---|---|
| **I13** | 1.54e+015 | 77 | -37.73 | 4.07e+014 | 41 | -83.57 | 1.49e+015 | -40.02 | 5.16e+014 | -79.18 | 1.60e+015 | -35.41 | 2.48e+015 |
| **I14** | 1.98e+015 | 85 | -20.93 | 1.33e+015 | 82 | -46.95 | 1.95e+015 | -22.26 | 5.26e+014 | -79.00 | 1.64e+015 | -34.69 | 2.51e+015 |
| **I15** | 1.48e+015 | 55 | -40.07 | 4.85e+014 | 45 | -80.43 | 1.57e+015 | -36.76 | 5.16e+014 | -79.18 | 1.64e+015 | -33.86 | 2.48e+015 |
| **I16** | 1.93e+015 | 67 | -23.03 | 1.07e+015 | 56 | -57.18 | 1.83e+015 | -27.04 | 5.26e+014 | -79.00 | 1.64e+015 | -34.62 | 2.51e+015 |
| **M13** | 1.58e+015 | 75 | -36.17 | 8.16e+014 | 70 | -67.06 | 1.69e+015 | -31.75 | 5.16e+014 | -79.18 | 1.61e+015 | -35.02 | 2.48e+015 |
| **M14** | 1.86e+015 | 119 | -25.73 | 1.30e+015 | 117 | -48.11 | 1.88e+015 | -24.93 | 5.26e+014 | -79.00 | 1.56e+015 | -37.82 | 2.51e+015 |
| **M15** | 1.49e+015 | 52 | -39.64 | 6.75e+014 | 51 | -72.73 | 1.68e+015 | -32.35 | 5.16e+014 | -79.18 | 1.66e+015 | -32.97 | 2.48e+015 |
| **M16** | 1.86e+015 | 63 | -25.88 | 1.16e+015 | 62 | -53.79 | 1.88e+015 | -24.91 | 5.26e+014 | -79.00 | 1.66e+015 | -33.92 | 2.51e+015 |

Table 5.4: As in Table 5.3 but for $N_2O$ in the 2203 $\text{cm}^{-1}$ microwindow.

| | **SFIT2** | **SNR** | % | **SFIT1** | **SNR** | % | **SFIT1 Smoothed** | % | **MLS** | % | **MLS Smoothed** | % | **A Priori** |
|---|---|---|---|---|---|---|---|---|---|---|---|---|---|
| **I13** | 3.39e+014 | 183 | -3.75 | 3.31e+014 | 182 | -5.87 | 3.39e+014 | -3.67 | 3.74e+014 | 6.17 | 3.63e+014 | 3.10 | 3.52e+014 |
| **I14** | 3.33e+014 | 159 | -5.93 | 3.17e+014 | 159 | -10.51 | 3.32e+014 | -6.08 | 3.76e+014 | 6.18 | 3.64e+014 | 2.70 | 3.54e+014 |
| **I15** | 3.20e+014 | 105 | -9.02 | 2.96e+014 | 105 | -15.93 | 3.19e+014 | -9.42 | 3.74e+014 | 6.17 | 3.62e+014 | 2.81 | 3.52e+014 |
| **I16** | 3.12e+014 | 100 | -11.82 | 2.76e+014 | 100 | -22.04 | 3.11e+014 | -12.21 | 3.76e+014 | 6.18 | 3.63e+014 | 2.49 | 3.53e+014 |
| **M13** | 3.75e+014 | 174 | 6.53 | 3.96e+014 | 175 | 12.53 | 3.80e+014 | 7.79 | 3.74e+014 | 6.17 | 3.63e+014 | 3.07 | 3.52e+014 |
| **M14** | 3.76e+014 | 168 | 6.20 | 3.90e+014 | 169 | 10.11 | 3.75e+014 | 5.89 | 3.76e+014 | 6.18 | 3.64e+014 | 2.74 | 3.54e+014 |
| **M15** | 3.47e+014 | 103 | -1.53 | 3.27e+014 | 94 | -7.08 | 3.37e+014 | -4.18 | 3.74e+014 | 6.17 | 3.62e+014 | 2.79 | 3.52e+014 |
| **M16** | 3.57e+014 | 98 | 0.84 | 3.60e+014 | 98 | 1.81 | 3.58e+014 | 1.00 | 3.76e+014 | 6.18 | 3.63e+014 | 2.47 | 3.54e+014 |

Table 5.5: As in Table 5.3 but for HCl in the 2821 $\text{cm}^{-1}$ microwindow.

| | **SFIT2** | **SNR** | **%** | **SFIT1** | **SNR** | **%** | **SFIT1 Smoothed** | **%** | **MLS** | **%** | **MLS Smoothed** | **%** | **A Priori** |
|---|---|---|---|---|---|---|---|---|---|---|---|---|---|
| **I13** | 2.65e+015 | 57 | -4.52 | 3.99e+015 | 111 | 43.66 | 2.96e+015 | 6.72 | 7.51e+015 | 170.74 | 3.15e+015 | 13.43 | 2.78e+015 |
| **I14** | 2.79e+015 | 76 | -0.01 | 2.42e+015 | 96 | -13.32 | 2.74e+015 | -1.75 | 7.54e+015 | 170.07 | 3.08e+015 | 10.41 | 2.79e+015 |
| **I15** | 2.63e+015 | 62 | -5.12 | 1.67e+015 | 62 | -39.84 | 2.63e+015 | -5.19 | 7.51e+015 | 170.74 | 3.08e+015 | 10.90 | 2.78e+015 |
| **I16** | 2.73e+015 | 54 | -2.06 | 2.15e+015 | 54 | -23.07 | 2.72e+015 | -2.58 | 7.54e+015 | 170.07 | 3.02e+015 | 8.40 | 2.794e+015 |
| **M13** | 2.67e+015 | 114 | -3.63 | 2.13e+015 | 115 | -23.22 | 2.67e+015 | -3.65 | 7.51e+015 | 170.74 | 3.16e+015 | 13.79 | 2.78e+015 |
| **M14** | 2.69e+015 | 118 | -3.70 | 2.05e+015 | 119 | -26.42 | 2.67e+015 | -4.18 | 7.54e+015 | 170.07 | 3.16e+015 | 13.22 | 2.79e+015 |
| **M15** | 2.69e+015 | 69 | -2.91 | 2.01e+015 | 70 | -27.65 | 2.66e+015 | -4.00 | 7.51e+015 | 170.74 | 3.12e+015 | 12.46 | 2.78e+015 |
| **M16** | 2.67e+015 | 48 | -4.23 | 8.36e+014 | 64 | -70.05 | 2.54e+015 | -9.11 | 7.54e+015 | 170.07 | 3.08e+015 | 10.32 | 2.79e+015 |

Table 5.6: As in Table 5.3 but for CO in the 2147 $cm^{-1}$ microwindow.

| | **SFIT2** | **SNR** | **%** | **SFIT1** | **SNR** | **%** | **SFIT1 Smoothed** | **%** | **A Priori** |
|---|---|---|---|---|---|---|---|---|---|
| **I13** | 5.09e+016 | 103 | -16.10 | 4.64e+016 | 103 | -23.39 | 5.12e+016 | -15.60 | 6.06e+016 |
| **I14** | 6.17e+016 | 81 | 0.99 | 6.21e+016 | 81 | 1.59 | 6.17e+016 | 0.96 | 6.11e+016 |
| **I15** | 4.84e+016 | 71 | -20.13 | 4.23e+016 | 71 | -30.22 | 4.86e+016 | -19.89 | 6.06e+016 |
| **I16** | 5.93e+016 | 62 | -2.93 | 5.79e+016 | 62 | -5.25 | 5.92e+016 | -3.17 | 6.11e+016 |
| **M13** | 5.58e+016 | 137 | -7.89 | 5.42e+016 | 137 | -10.56 | 5.62e+016 | -7.26 | 6.06e+016 |
| **M14** | 6.59e+016 | 108 | 7.77 | 6.95e+016 | 108 | 13.65 | 6.63e+016 | 8.56 | 6.11e+016 |
| **M15** | 5.51e+016 | 98 | -9.12 | 5.27e+016 | 98 | -13.03 | 5.52e+016 | -8.93 | 6.06e+016 |
| **M16** | 6.35e+016 | 69 | 3.89 | 6.57e+016 | 69 | 7.51 | 6.39e+016 | 4.62 | 6.11e+016 |

Table 5.7: As in Table 5.3 but for $CH_4$ in the 2937 $cm^{-1}$ microwindow.

| | **SFIT2** | **SNR** | **%** | **SFIT1** | **SNR** | **%** | **SFIT1 Smoothed** | **%** | **A Priori** |
|---|---|---|---|---|---|---|---|---|---|
| **I13** | 4.71e+019 | 99 | 1.56 | 4.78e+019 | 99 | 2.97 | 4.72e+019 | 1.78 | 4.64e+019 |
| **I14** | 4.95e+019 | 101 | 6.03 | 5.25e+019 | 101 | 12.64 | 5.00e+019 | 7.24 | 4.66e+019 |
| **I15** | 4.54e+019 | 71 | -2.04 | 4.41e+019 | 71 | -4.85 | 4.51e+019 | -2.82 | 4.64e+019 |
| **I16** | 4.82e+019 | 71 | 3.41 | 5.04e+019 | 71 | 8.06 | 4.87e+019 | 4.45 | 4.66e+019 |
| **M13** | 4.82e+019 | 110 | 3.89 | 4.98e+019 | 110 | 7.37 | 4.85e+019 | 4.55 | 4.64e+019 |
| **M14** | 5.04e+019 | 108 | 7.99 | 5.45e+019 | 109 | 16.89 | 5.12e+019 | 9.82 | 4.66e+019 |
| **M15** | 4.66e+019 | 76 | 0.59 | 4.70e+019 | 76 | 1.33 | 4.67e+019 | 0.79 | 4.64e+019 |
| **M16** | 4.87e+019 | 74 | 4.41 | 5.16e+019 | 74 | 10.60 | 4.94e+019 | 5.93 | 4.66e+019 |

Table 5.8: As in Table 5.3 but for $CO_2$ in the 3359 $cm^{-1}$ microwindow.

| | Percent Difference (%) | |
|---|---|---|
| | SFIT1 to SFIT2 | SFIT2 to MLS |
| $O_3$ | 0.7 (6) | 0.03 (16) |
| CO | 0.02 (10) | 9 (16) |
| $N_2O$ | 1 (12) | 2 (21) |
| HCl | 0.08 (3) | 2 (14) |
| $CH_4$ | 0.04 (0.7) | — |
| $CO_2$ | 0.2 (2) | — |

Table 5.9: Flight data vertical column results over a 35–100-km altitude range. The smallest and, in brackets, largest percent differences between the data sets are listed.

### 5.4.3 Flight Data Discussion

It seems clear that had the payload not rotated through sunset, the U of T FTS would have recorded data from a full occultation, allowing us to compute well-resolved vertical profiles of $O_3$, HCl, $N_2O$, $CH_4$ and CO. The four spectra that were recorded revealed that the instrument functioned well in its high-altitude environment. Although no profiles can be computed from the four spectra, slant and vertical columns above the balloon were computed, and were consistent with the corresponding MLS partial columns (Table 5.9). The best comparisons with MLS were from the SFIT2 retrievals of the MCT spectra that were apodized with a triangular function. Apodization with a triangular function also improved the SNR and the spectral fits (Figures 5.6–5.17).

There is a large effect from smoothing the MLS profiles with the U of T FTS averaging kernels. For $O_3$, the MLS profiles were similar to the *a priori* profiles, and well within the 20% standard deviation for the covariance matrices of our *a priori* profile. For HCl, $N_2O$ and CO, the MLS profiles are significantly different in shape. The HCl profile falls within the 30% standard deviation for the covariance matrices. The CO MLS profile oscillates significantly and the $N_2O$ MLS profile contains negative VMRs, both of which are physically unlikely (or impossible) atmospheric states. It is, as a result, difficult to assess the validity of the *a priori* profiles for CO and $N_2O$ from the MLS profiles.

The goal of developing a Canadian capacity for balloon-borne FTS measurements was achieved, and this instrument can be used again on future balloon flights. Given a full data set from this flight, two science goals for the U of T FTS would also have been achieved: measuring vertical profiles of trace gases relevant to ozone concentrations, and satellite validation.

## 5.5 MANTRA 2004 Ground-Based Campaign

MANTRA 2004 included an extensive ground-based campaign. There were daily measurements of $O_3$ from a Brewer Spectrophotometer, the University of Toronto's ground-based UV-VIS spectrometer (U of T GBS) [99], the Service d'Aéronomie's Systeme d'Analyse et d'Observations Zenithales (SAOZ) UV-VIS instrument [100], the CRESTech/York University Acousto-Optic Tunable Filter Spectrometer (AOTF) [4], Environment Canada's SunPhotoSpectrometer (SPS) [101] and Environment Canada's Measurements of Atmospheric Extinction in the Stratosphere and Troposphere Retrieved by Occultation (MAESTRO).

The ground-based instruments measured for 43 days during the MANTRA 2004 campaign, and the U of T FTS collected ground-based spectra for around 10 days. The spectra were recorded during every measurement opportunity—that is, times when both the skies were clear and there were no flight tests being done.

The one molecule that all ground-based instruments measured is ozone. Figure 5.24 shows the comparison of retrieved total columns from the Brewer Spectrophotometer in Vanscoy, a Brewer Spectrophotometer in Regina (<300 km SE of Vanscoy), the U of T GBS and SAOZ. The other instruments' data are not yet available for comparison. The second Brewer from Regina was added to the comparison because there were tests being performed on the Vanscoy Brewer periodically throughout the ground-based campaign. The error bars shown in the figure for the U of T GBS and SAOZ are 5% and 4%, respectively. The U of T GBS errors are computed as a sum, in quadrature, of measurement noise, instrument errors, spectroscopic cross-section errors, fitting residu-

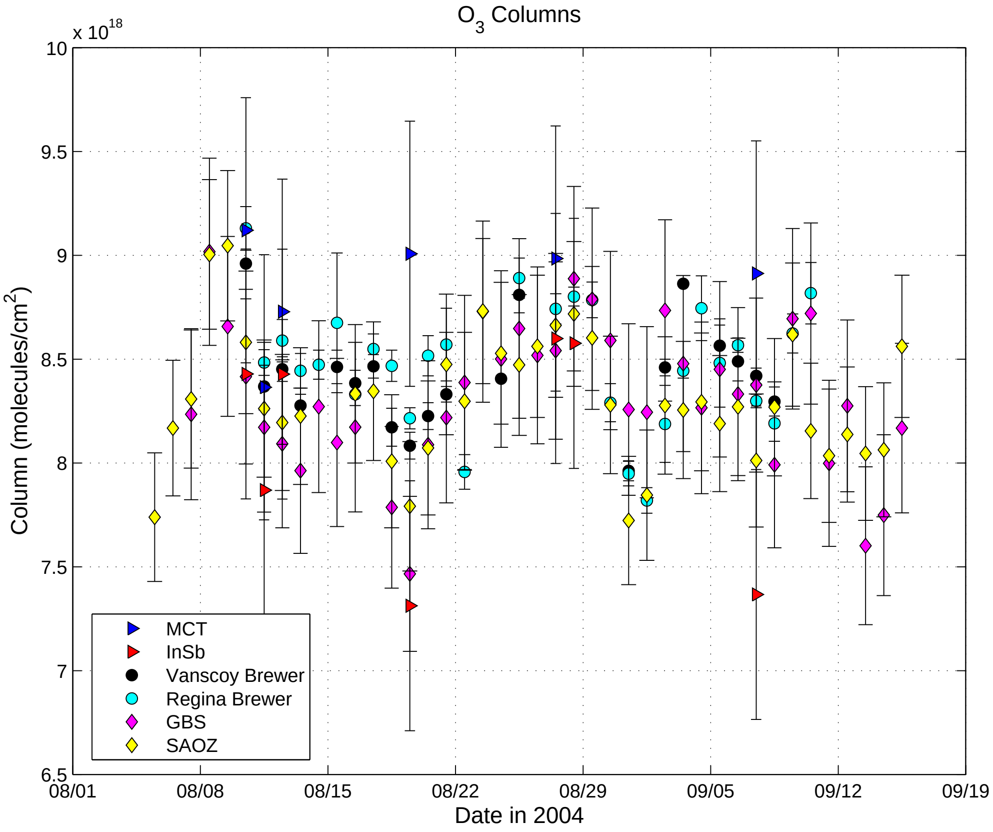

Figure 5.24: Daily average ozone for the MANTRA 2004 ground-based campaign. The two detectors for the U of T FTS are in blue and red triangles. The black circles are from the Vanscoy Brewer, while the cyan circles are from the Regina Brewer. The diamonds are from the ground-based UV-VIS instruments: magenta is the University of Toronto Ground-Based Spectrometer and yellow is the SAOZ instrument.

als, Raman scattering and errors in the air mass factor [99]. The SAOZ errors include measurement noise, errors in the cross-sections, and errors in the air mass factor [100]. The error bars on the daily columns of both Brewer Spectrophotometers consist of the standard deviation from the measurements recorded throughout the day.

The columns and ILS information for the U of T FTS were retrieved using SFIT2, interferograms were apodized with a triangular function and phase error and effective apodization parameters were retrieved as part of the state vector.

### Choice of Averaging Time for MANTRA 2004 Data

The MANTRA 2004 U of T FTS ground-based data have a number of intrinsic problems: first of all, the detector alignment for the InSb detector in particular was poor, since we adjusted the detector position multiple times during the campaign to optimize signal on the sun at ZPD without checking the spectrum to ensure that it had full resolution. Second, the weather in Vanscoy was mostly cloudy over the duration of the campaign. Third, the priority during this period was to prepare the instrument for flight. To ensure that the detectors would not saturate during the flight (which would render the measurement useless, since data from the zero path difference position yields the overall shape of the spectrum) we placed metal mesh in front of the detectors from August 27th onward, cutting the solar signal by a third. As a result of this, the signal-to-noise ratios of some of the ground-based spectra are low. The retrieved profile from a spectrum is a weighted average of the true state and the *a priori* state, weighted by the relative sizes of the error covariance matrices (Equations 5.2.18 and 5.2.20). As a result, if the signal-to-noise ratio is low, the profiles will be weighted toward the *a priori* profile, using less information from the spectrum. To increase the signal-to-noise ratio of the spectra, the spectra can be averaged. Averaging spectra, however, increases the observing time, and one must consider the atmospheric changes that can occur during this time, and balance that against the gain in signal-to-noise ratio.

Schneider [102, pp. 49–53], provides an analysis of the effects of changing solar zenith angle (SZA) on the retrieved profile from averaged spectra.[3] He concludes that the column amounts are not affected by averaging spectra, and that the profile differences are negligible at zenith angles less than 80°, even for long-duration measurements (13 minutes). His measurements were taken at the Izaña Observatory, which is at 28°N,

---

[3] It has been shown mathematically by Kyle and Blatherwick [103] that the smearing of the atmosphere throughout a single interferogram shows a small effect in the spectral lines but has no effect on the column (integrated spectrum).

and for which his 13-minute scans had a maximum change of SZA of less than 3°. This is a significantly lower latitude than at Vanscoy, Saskatchewan (52°N), and so the rate at which the SZA changes will be slower in Vanscoy. Further, the ground-based measurements at Vanscoy were not taken when the SZAs were larger than 65°. To ensure that the SZA does not change more than 3°, a 20-minute averaging time can be used. The FTS during MANTRA 2004 took spectra once every 100 seconds, and so this would increase the SNR by about a factor of three. This, of course, is not possible for all days throughout the ground-based campaign, since the number of spectra during a given time period varied, based on the cloud level. The maximum averaging time is taken to be 20 minutes.

### Justification for the Error Bars in Figure 5.24

August 11 is the best day of data from the ground-based campaign, with the longest period of clear weather. There were 61 individual spectra taken creating 13 20-minute averages, each containing between 2 and 7 spectra in the average. The error bars on the individual columns retrieved from the 13 averaged spectra (on average, 1.8%, with minimum 1.4% and maximum 2.6%), are the sum, in quadrature, of the retrieval noise, the smoothing error and the interference error (described by Equations 5.2.27, 5.2.29 and 5.2.32). The measurement error contributes $\sim$1.5%, the smoothing error contributes $\sim$1% and the interference error contributes a negligible amount ($\ll$1%). These errors, however, do not capture the variability of the column amounts seen during August 11. The standard deviation of the columns for August 11 is a more appropriate measure of the error for the daily average, which is 7%. For other days during the campaign, fewer spectra were recorded, and so the standard deviation for the daily averages during those days will not be representative of a realistic standard deviation. I have, as a result, applied a 7% error bar to each day.

With the 7% error bars, the data agree with the Brewer data, except for the MCT

| Target Gas | Microwindow | Spectral Range ($\mathrm{cm}^{-1}$) | Interfering Species |
|---|---|---|---|
| $O_3$ | 3040 | 3039.90–3040.60 | $H_2O$, $CH_4$ |
| HCl | 2925 | 2925.75–2926.05 | $H_2O$, $CH_4$, $N_2O$, $O_3$ |
| $N_2O$ | 2482 | 2481.30–2482.60 | $CO_2$, $CH_4$, $O_3$ |
| CO | 2058 | 2057.68–2058.00<br>2069.56–2069.76<br>2157.51–2159.14 | $O_3$, $CO_2$, OCS<br>$O_3$, $CO_2$, OCS<br>$O_3$, $N_2O$, $H_2O$ |

Table 5.10: Microwindows for $O_3$, HCl, $N_2O$, and CO used in the MANTRA 2004 ground-based campaign.

detector on August 19. There is a clear high-bias of up to 7% in the FTS MCT data. There are two anomalously low columns retrieved with the InSb data (August 19 and September 7)—both of which can be attributed to poor detector alignment. In these comparisons, averaging kernels can not be taken into account (such as using Equation 5.4.1), because the other ground-based instruments do not retrieve profiles. The disagreement may be due to spectroscopic parameter errors between the infrared, where the U of T FTS measures, and the UV/VIS range, where the other ground-based instruments measure.

### 5.5.1 Partial Column Comparisons with MLS

There were multiple overpasses of the MLS instrument during the 2004 ground-based campaign (Figure 5.4). Partial columns of ozone, HCl, CO and $N_2O$ can be compared with the ground-based MANTRA 2004 data in the same manner as in §5.4.[4] To properly compare partial columns, the MLS data must be smoothed with the U of T FTS averaging kernels over the coincident pressure levels using Equation 5.4.1. The U of T FTS MCT density-weighted column averaging kernels are shown in Figure 5.25, and example spectral fits for each molecule are shown in Figure 5.26. The microwindows are listed in Table 5.10. MLS data were filtered for quality and proximity to Vanscoy. The quality control

---

[4] According to Livesey et al. [104], the MLS averaging kernels are sharply peaked and so it should not be necessary to consider their effect in this case, since the U of T FTS ground-based averaging kernels are very broad.

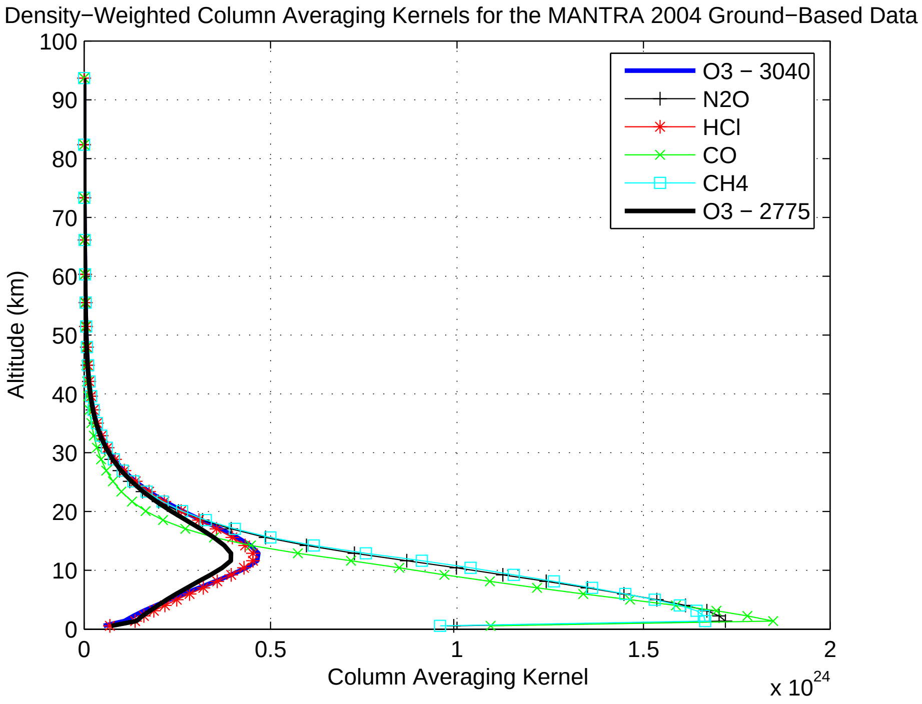

Figure 5.25: Density-weighted column averaging kernels for the U of T FTS ground-based data.

consisted of removing all profiles for which any point in the volume mixing ratio profile had a value of $< -1$ and limiting column retrievals to only vertical levels recommended by the Version 1.5 Level 2 data quality and description document [104]. The latitude range of the data is from 50°N to 55°N, and the longitude range is 90°W to 120°W, approximately centred on Vanscoy (52°N, 107°W). Because this time of year the atmosphere is zonally dynamically quiescent (§2), this range should be suitable for all gases. The partial profile comparisons are shown in Figures 5.27, 5.29, 5.32 and 5.34 and show the variability of the MLS profiles for a single day of measurements and the pressure levels upon which the comparisons take place[5]. Partial column comparisons are shown in Figures 5.28, 5.30, 5.33 and 5.35.

The error bars on the MLS data are the standard deviation from that day's measurements (on average, MLS records ∼10 measurements per day in this latitude and

---

[5] Again, these plots are not meant to imply that the U of T FTS is retrieving profiles: it is meant only to illustrate the altitude range allowed in the comparison and the effect of smoothing the MLS data.

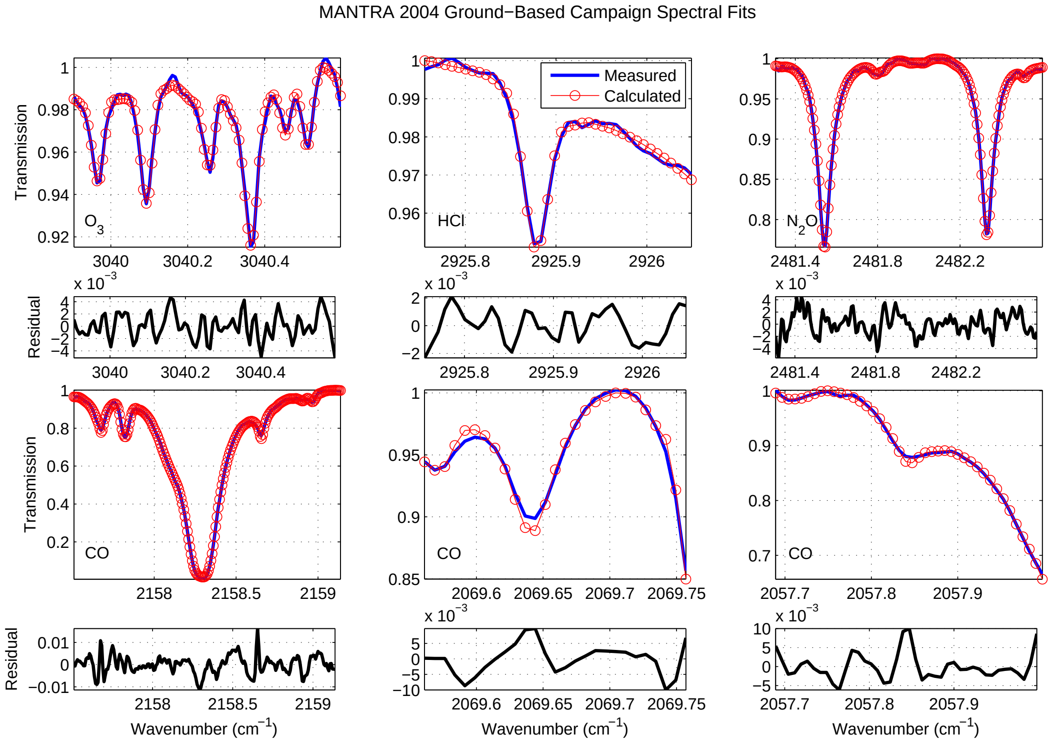

Figure 5.26: Representative examples of MCT spectral fits for the MANTRA 2004 ground-based data.

longitude band), and the error bars on the U of T FTS data are the standard deviation from the August 11 data. The ozone, $N_2O$ and CO partial columns measured by the MCT detector data agree, within error, with the MLS partial columns, except for the August 28 column for CO. The HCl MLS daily mean partial columns are higher than the MCT daily mean total columns by 7%. There is a known ∼0.2–0.4 ppbv (10–15%) high bias of MLS HCl as compared with HALOE [104, 105]. The discrepancy between MLS and HALOE cannot yet be explained. This is also what is seen in Figure 5.29. Since the *a priori* HCl values used in this analysis are from HALOE climatologies [92], this could account for some of the partial column differences. Figure 5.31 shows the (only slight) improvement for retrieving HCl partial columns with the *a priori* multiplied by 1.1 (i.e. an increase of 10% at every level). The difference in this case between the MLS and U of T FTS means is 6%. The comparisons worsen when the *a priori* is increased by 15%

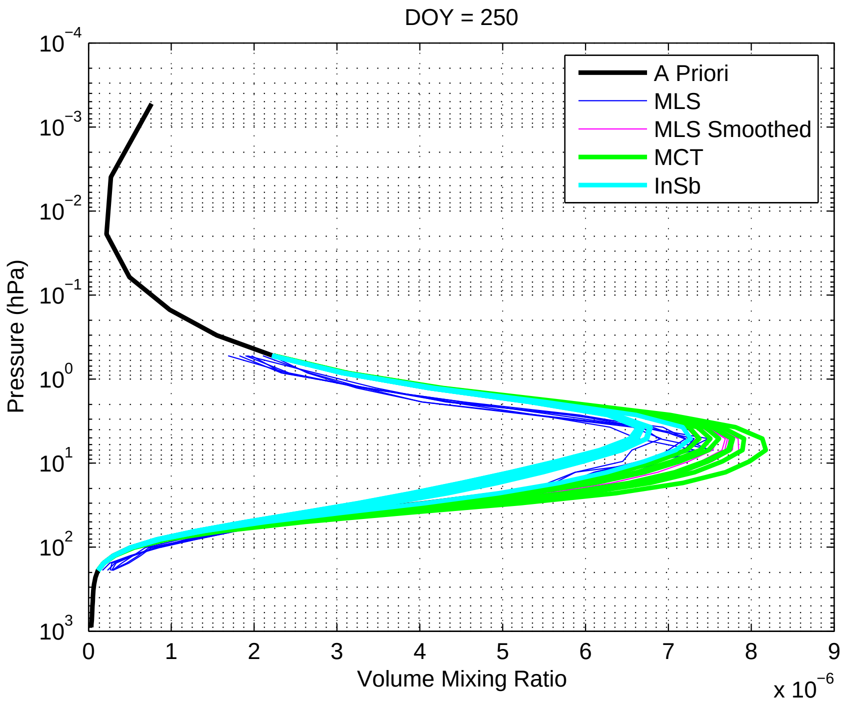

Figure 5.27: Ozone partial profile comparisons with MLS. This figure shows the full *a priori* profile for the U of T FTS data, with the retrieved U of T FTS and MLS profiles over the appropriate pressure range as defined in Livesey et al. [104].

at each level (to 17% percent difference). This is likely due to the increased tropospheric amount, which artificially broadens the expected lineshape, causing SFIT2 to assign less broadening to the ILS and stratosphere and more to the troposphere, where the partial column is insensitive. This would lower the partial columns values, as seen in Figure 5.31.

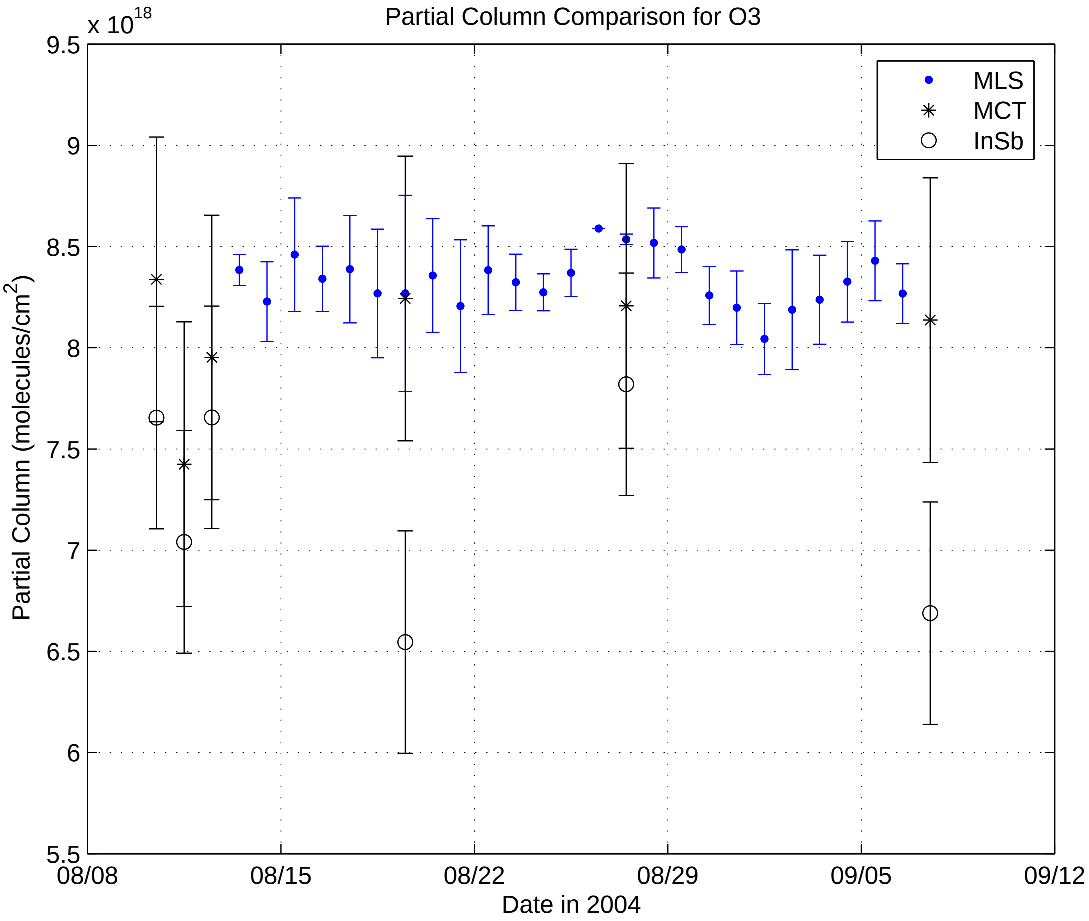

Figure 5.28: Ozone partial column comparisons with MLS.

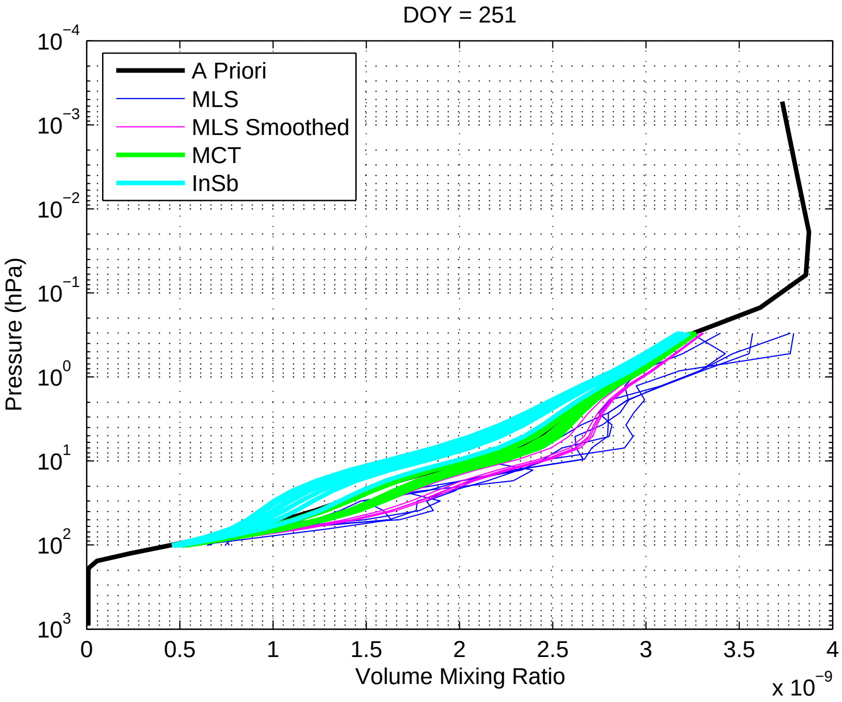

Figure 5.29: Partial profile comparisons as in Figure 5.27, but for HCl.

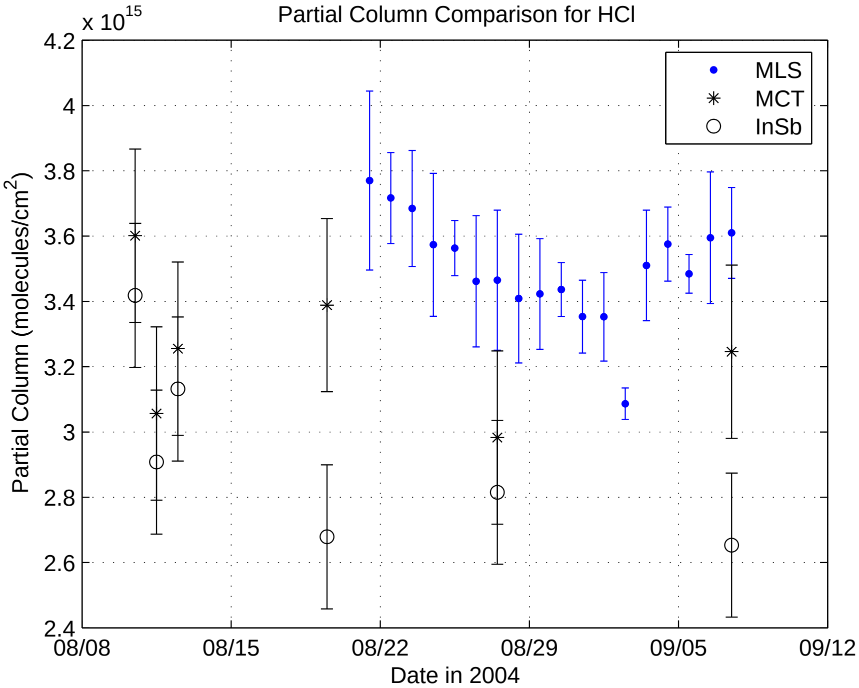

Figure 5.30: HCl partial column comparisons with MLS.

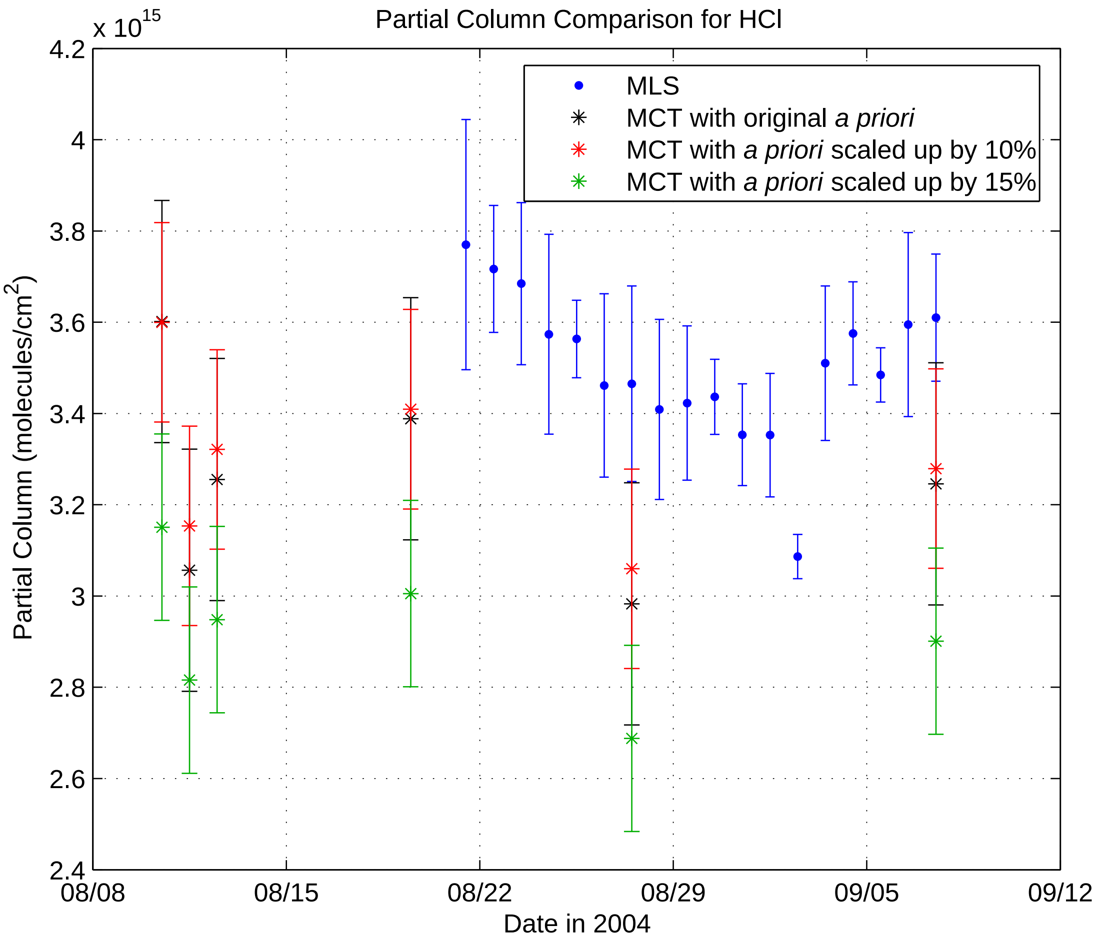

Figure 5.31: HCl partial column comparisons with MLS. The different colours for the U of T FTS partial column data correspond to the different *a priori* profiles used to retrieve HCl partial columns, in an attempt to improve agreement between MLS and the U of T FTS.

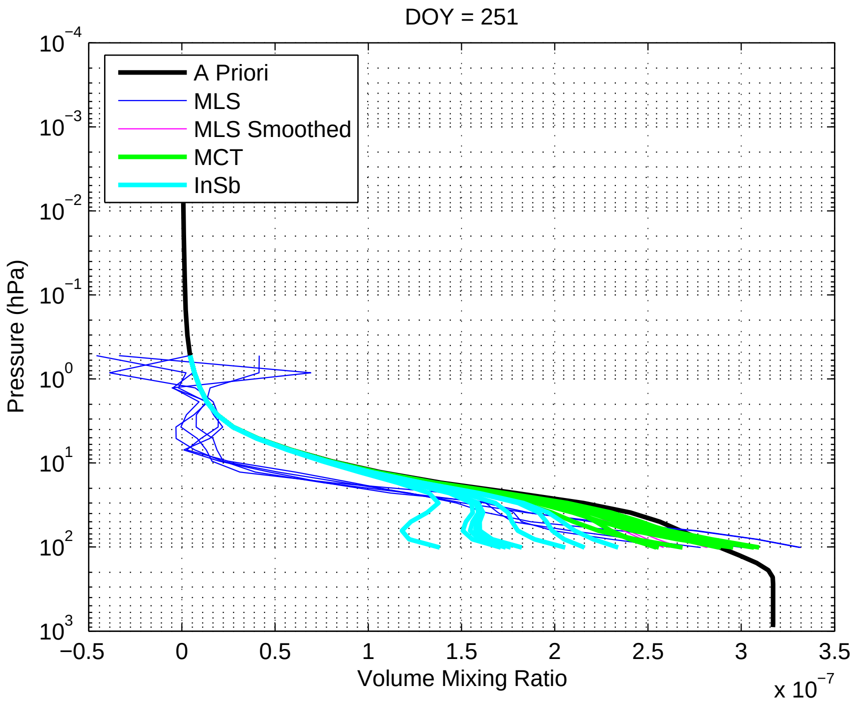

Figure 5.32: Partial profile comparisons as in Figure 5.27, but for $N_2O$.

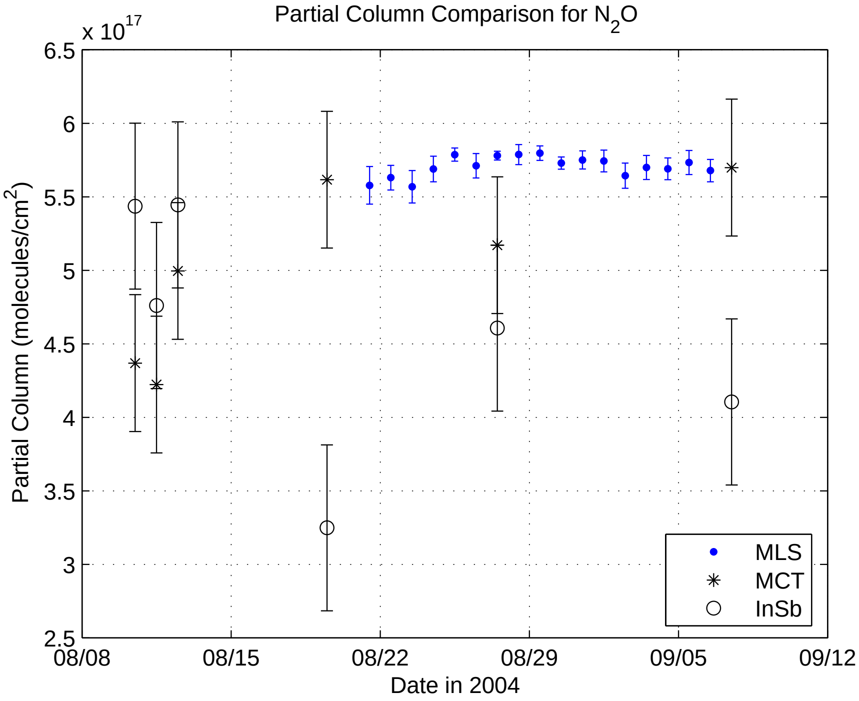

Figure 5.33: $N_2O$ partial column comparisons with MLS.

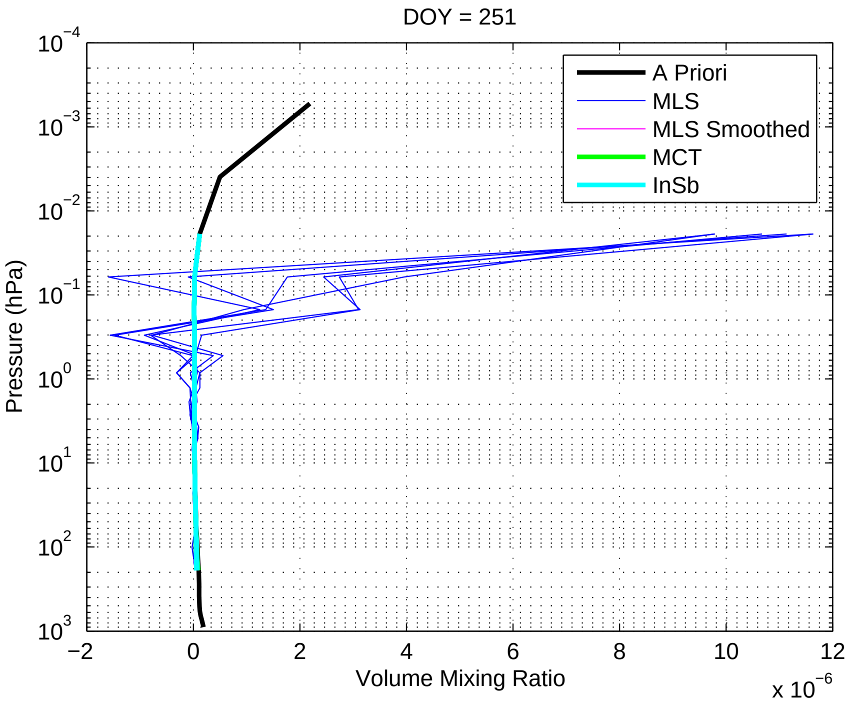

Figure 5.34: Partial profile comparisons as in Figure 5.27, but for CO.

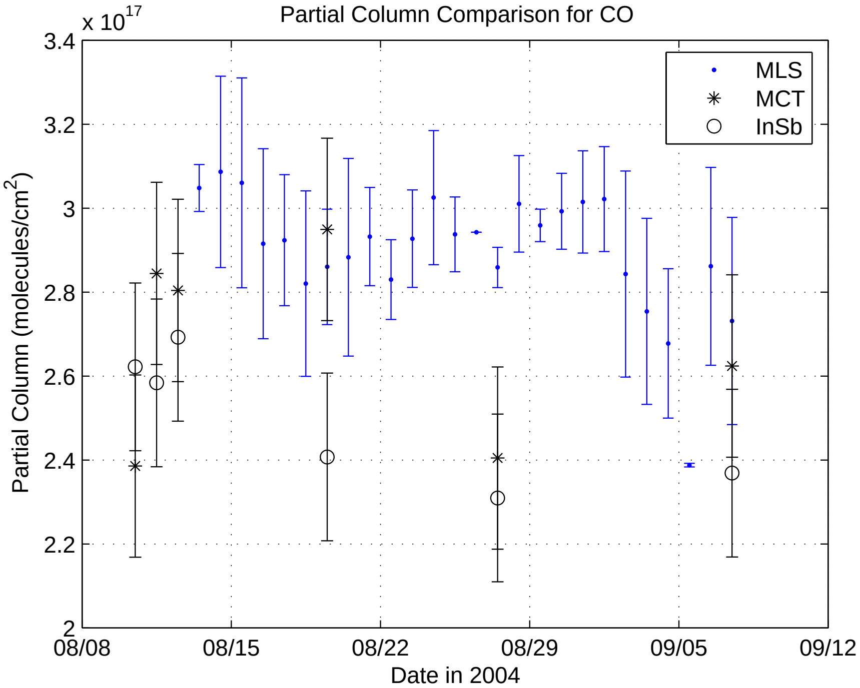

Figure 5.35: CO partial column comparisons with MLS.

### 5.5.2 MANTRA 2004 Ground-Based Discussion

The main limitations to the ground-based data from the MANTRA 2004 campaign were weather and signal-to-noise ratio. The weather reduced the total number of clear-sky days during the seven-week campaign to only six. The metal mesh, used to ensure that the interferograms did not saturate when the FTS was on the balloon, reduced the signal-to-noise ratio of the data, increasing the error. Despite these limitations, the U of T FTS total columns of ozone agree within 7% with the total columns computed by the U of T GBS, SAOZ and the Brewer Spectrophotometers (Figure 5.24), all on-site in Vanscoy, all of which are UV-VIS instruments. Some of this difference may be due to spectroscopic errors between the UV-VIS and the IR, which can lead to systematic differences of 5.5% in IR/UV-VIS absorbance ratios [106]. A possibility for the larger errors found between SAOZ and the U of T GBS and the U of T FTS than between the U of T FTS and the Brewer Spectrophotometers is their respective viewing geometries. The U of T GBS and SAOZ measure scattered light only at dawn and dusk, whereas the Brewers and the U of T FTS measure direct sunlight throughout the day, and so have the same viewing geometry.

Partial column comparison with the MLS satellite instrument show excellent agreement (within the error of the MCT detector on the U of T FTS) for all molecules except for HCl. The difference between the HCl partial columns is still unclear, and a similar discrepancy is seen for HCl profiles between MLS and HALOE that is as yet unexplained [105]. This discrepancy is not seen between the MLS and ACE-FTS profiles, indicating that this is not an IR/UV-VIS spectroscopy problem. These will have been some of the first intercomparisons with MLS data, as it began recording science data on August 13, 2004.

## 5.6 Ground-Based FTS Intercomparisons in Toronto

The U of T FTS recorded ground-based measurements alongside two other FTS instruments: the Toronto Atmospheric Observatory FTS (TAO-FTS) and the Portable Atmospheric Research Interferometric Spectrometer for the Infrared (PARIS-IR). These instruments will be described in §5.6.1.

Previous intercomparisons of ground-based FTS observations have mainly focused upon the agreement of the retrieved quantities with instruments of similar resolution [107–110] based on different analysis techniques [84, 108] or addressed how the influence of individual instrument performance impacts the retrieved vertical column concentrations [108–110]. Paton-Walsh et al. [107] compared two instruments operating at a 0.005 $\text{cm}^{-1}$ resolution for retrieving total columns of HCl, $N_2O$ and $HNO_3$, and at 0.07 $\text{cm}^{-1}$ for retrieving HF columns. Goldman et al. [108] compared $N_2$, HF, HCl, $CH_4$, $O_3$, $N_2O$, $HNO_3$ and $CO_2$ total columns measured by four FTIRs at 50 cm optical path difference (OPD). Meier et al. [109] compared total columns of HCl, HF, $N_2O$, $HNO_3$, $CH_4$, $O_3$, $CO_2$ and $N_2$ from two high-resolution instruments (the OPD used is unspecified in the paper). Griffith et al. [110] compared total columns of $N_2O$, $N_2$, $CH_4$, $O_3$, HCl, $HNO_3$ and HF with two FTIRs operating both at 180 cm OPD (for all molecules except HF) and at 150 cm OPD (for HF). There are no comparisons, to our knowledge, that look at total columns produced by data from instruments with significantly different resolutions.

The goals of the intercomparison are to determine what effect resolution has on retrieved total column amounts of $O_3$, HCl, $N_2O$, and $CH_4$, and what retrieval parameters allow for the best comparison results. The results will be discussed in §5.6.3.

### 5.6.1 Instruments

#### TAO FTS

The Toronto Atmospheric Observatory (43°N, 79°W, 174.0 m) was established in 2001 with the installation of a high-resolution, DA8 model infrared Fourier Transform Spectrometer manufactured by ABB Bomem Inc. The TAO-FTS was designated a complementary instrument of the Network for the Detection of Atmospheric Composition Change, NDACC (formerly the Network for the Detection of Stratospheric Change (NDSC) [111]), in March, 2004. Since then, the TAO-FTS has taken part in both satellite validation activities (Mahieu et al. [112], Dils et al. [113]) and scientific process studies (Wiacek et al. [114]).

The optical design of the TAO instrument consists of a vertically oriented, linear Michelson interferometer with a maximum optical path difference of 250 cm, providing a maximum unapodized resolution of 0.004 $\text{cm}^{-1}$ [93]. The modulation efficiency and phase error are shown in the left-most panels of Figure 5.36. For reference, the U of T FTS MCT modulation efficiency and phase error are shown in the middle panels of Figure 5.36. The U of T FTS ILS is poor, and to increase the SNR of the spectra, while minimizing the resolution loss, interferograms are apodized with a triangular filter.

Infrared solar absorption spectra are nominally recorded on InSb and MCT detectors using a potassium bromide (KBr) beamsplitter to cover from 750–4400 $\text{cm}^{-1}$. All of the internal optics, including the detectors, are kept under vacuum to maintain an ambient pressure of approximately 0.06 Torr, and the detectors are actively cooled using liquid nitrogen. The external optical components include a dedicated elevation-azimuth tracker (manufactured by AIM Controls Inc.) which actively tracks direct solar radiation throughout the day.

Observations are usually taken by sequencing through six different narrow-band optical interference filters which are widely used within the NDACC InfraRed Working Group (IRWG) (Table 5.11). For the purposes of this campaign, only Filter 3 was used with the InSb detector, reducing the spectral range to 2420–3080 $\text{cm}^{-1}$ (3.2–4.2 $\mu$m). This range is ideal for this study because it contains signatures of the four molecules of interest ($O_3$, HCl, $CH_4$ and $N_2O$) in a spectral region that overlaps those of the other two instruments. Each spectrum consists of co-adding four interferograms, resulting in

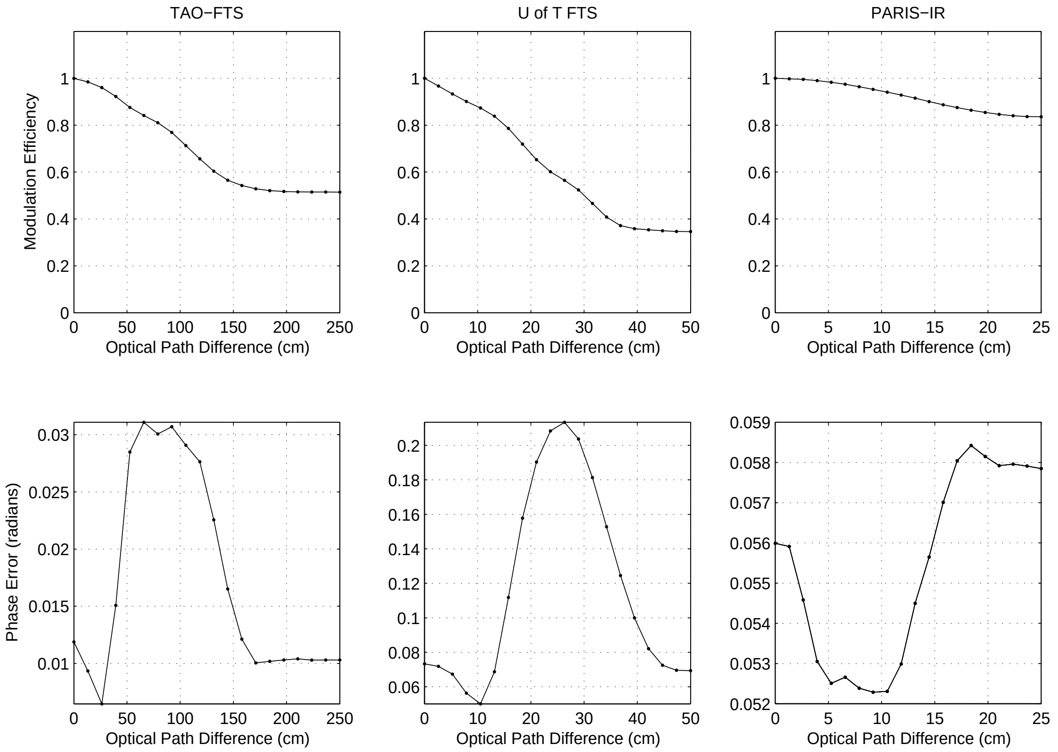

Figure 5.36: Typical modulation efficiency and phase error for all three instruments. These are computed from gas cell measurements using LINEFIT. The top panels contain the modulation efficiency and the lower panels contain the phase error (note the different y-axis scales on the phase error plots). The left-most panels show unapodized TAO-FTS data, recorded August, 2005. The central panels show U of T FTS data, apodized with a triangular filter and recorded September, 2005. The right-most panels show unapodized PARIS-IR data, recorded August, 2005.

one spectrum attained over a period of approximately 20 minutes. Interferograms are unapodized.

### PARIS-IR

The Portable Atmospheric Research Interferometric Spectrometer for the Infrared is a new, compact, portable FTS built by ABB Bomem for the Waterloo Atmospheric Observatory (43°N, 80°W, 319.0 m) [35]. PARIS-IR was primarily constructed from spare flight components that were manufactured for the Atmospheric Chemistry Experiment Fourier Transform Spectrometer (ACE-FTS) [34] and consequently has a very similar op-

| NDACC Filter | Wavenumber Range ($\mathrm{cm}^{-1}$) | Wavelength Range ($\mu$m) | Chemical Species |
|---|---|---|---|
| 1 | 4020–4290 | 2.33–2.49 | HF |
| 2 | 3000–3820 | 2.62–3.33 | $C_2H_2$, HCN, $H_2O$ & isotopes |
| **3** | **2420–3080** | **3.25–4.13** | **$CO_2$, $H_2O$, HDO, HCl, $O_3$, $N_2O$, $CH_4$, $NO_2$, $C_2H_6$** |
| 4 | 2020–2570 | 3.89–4.95 | OCS, CO, $N_2$ |
| 5 | 1590–2150 | 4.65–6.29 | NO, $COF_2$ |
| 6 | 670–1351 | 7.40–15 | $C_2H_2$, $C_2H_4$, $ClONO_2$, $O_3$, $N_2O$, $HNO_3$, $NH_3$, $CCl_2F_2$, $CHF_2Cl$ |

Table 5.11: NDACC filters. Filter 3 (bold) was used for this intercomparison campaign.

tical design with the same maximum OPD (25 cm) and spectral range (750–4400 $\mathrm{cm}^{-1}$). The photoconductive sandwich detectors are corrected for nonlinearity. The spectrometer has a mass of approximately 66 kg, dimensions of 60 cm by 60 cm by 42 cm, and an average power consumption of 62 W. To obtain a sufficiently long optical path difference within this compact volume, ABB Bomem used a "double pendulum" interferometer and "entrance mirror" to pass radiation through the interferometer twice. In addition to the MANTRA 2004 balloon campaign, PARIS-IR has also participated in three ground-based ACE validation campaigns in the Canadian high Arctic at Eureka, Nunavut [115]. Currently, the instrument is regularly operated at the Waterloo Atmospheric Observatory (WAO) for recording atmospheric absorption spectra. Its modulation efficiency and phase error are shown in the right-most panels of Figure 5.36. PARIS-IR interferograms are unapodized.

### 5.6.2 Observation Strategy and Analysis Method

The observation strategy for the campaign was constructed to focus on the effects of the instrument resolution on the retrieved column amounts. This was achieved by measuring simultaneously from the same location, in the same spectral range and using similar retrieval methods with identical *a priori* information, line parameters and forward model. Retrievals for all three instruments were executed using SFIT2 (v.3.82beta3) [86, 116] and

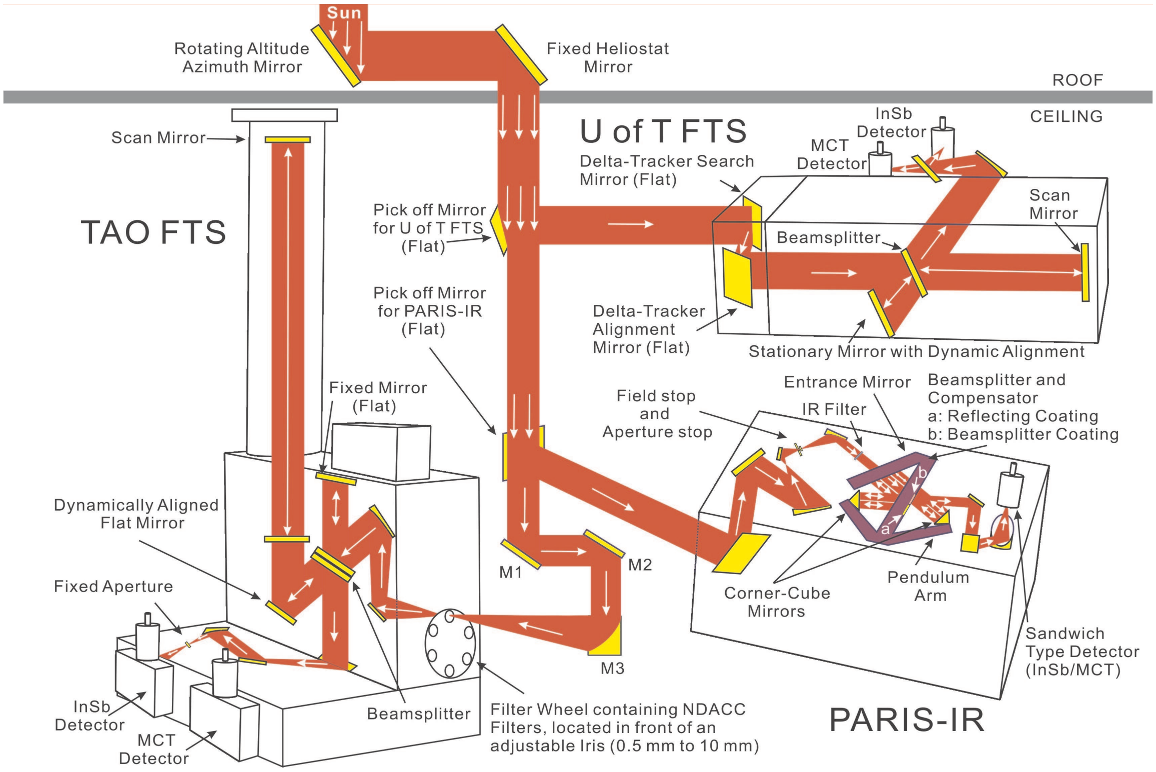

Figure 5.37: The experimental setup. Figure courtesy Dejian Fu.

the same input parameters. All three instruments were located at TAO for the duration of the campaign. The data presented here were recorded on August 24, August 26, September 1 and September 2, 2005, with at least 14 spectra recorded by the TAO-FTS on each day.

To measure the same atmospheric path simultaneously with all three instruments, two small pick-off mirrors were placed in the solar beam to deflect a portion of the light into the U of T FTS and PARIS-IR (Figures 5.37 and 5.38). Every attempt was made to ensure that TAO incurred a minimal loss of signal, and the loss of SNR was less than 10%. To further ensure simultaneity, the U of T FTS and PARIS-IR co-added individual spectra that were recorded during the 20-minute interval required to produce one TAO-FTS spectrum. The PARIS-IR instrument measures the largest number of spectra per unit time, with a 20-second scan time, whereas the U of T FTS measures one interferogram in 50 seconds. The TAO instrument, as described in §5.6.1 requires ∼20

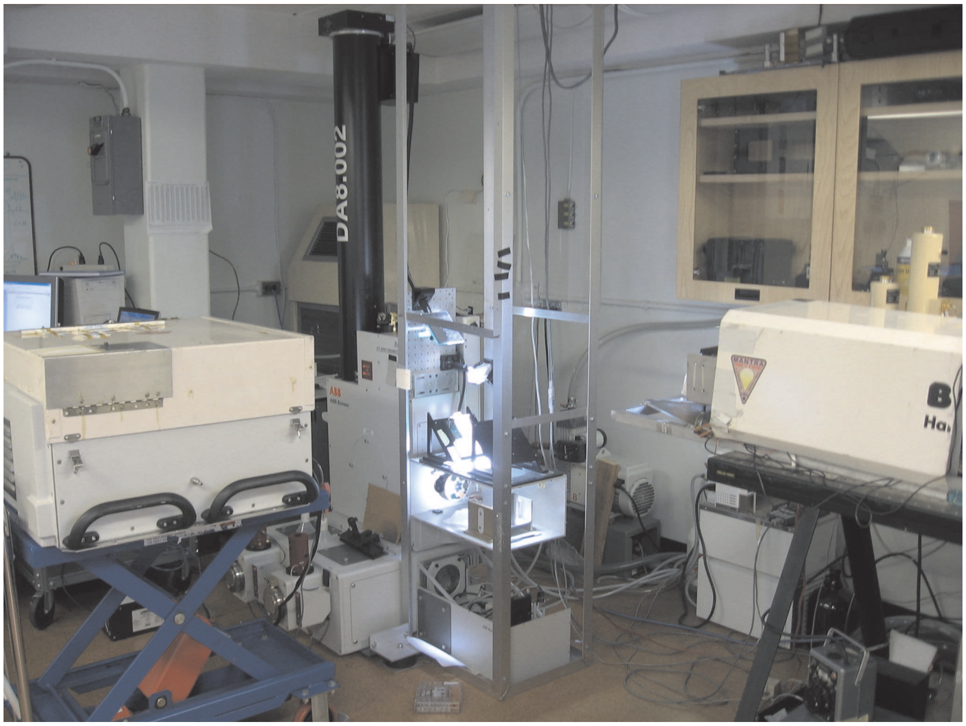

Figure 5.38: Photograph of the experimental setup. The PARIS-IR is on the left of the picture, the U of T FTS is on the right, and the TAO-FTS is located in the centre.

minutes to create one spectrum. Table 5.12 summarizes the instrument details.

The three FTS instruments measured solar absorption by $O_3$, $CH_4$, HCl, and $N_2O$ in the same spectral ranges. The five microwindows chosen for this campaign are listed in Table 5.13. Two microwindows for ozone (near 3040 $cm^{-1}$ and 2775 $cm^{-1}$) were chosen because they yielded the highest degrees of freedom for signal for the lower resolution instruments in the considered spectral range, compared with the more commonly used 3045 $cm^{-1}$ microwindow (e.g. Goldman et al. [108] and Griffith et al. [110]). It should be noted that the best ozone retrievals for the PARIS-IR instrument come from the 1000 $cm^{-1}$ band, but in the interest of maintaining consistency with the other two instruments, retrievals of ozone are considered only in the spectral ranges measured by all three instruments.

The only difference between the three retrieval methods is that the PARIS-IR retrievals were performed on a 29-layer grid, whereas the TAO and U of T FTS retrievals

| | PARIS-IR | U of T | TAO |
|---|---|---|---|
| Maximum Optical Path Difference (cm) | 25 | 50 | 250 |
| Scan Time (s) | 20 | 50 | 300 |
| Spectral Range ($cm^{-1}$) | 750–4400 | 1200–5000 | 750–4400<br>(2420–3080) |
| Measurement Span | Aug. 24–Sept. 2 | May 26–Sept. 12 | Year-round |

Table 5.12: Instrument configuration. The second line of the spectral range for the TAO-FTS indicates its spectral range using NDACC filter 3, which is the spectral range used in this intercomparison. The scan time is the time it takes to record a single interferogram.

| Target Gas | Microwindow | Spectral Range ($cm^{-1}$) | Interfering Species |
|---|---|---|---|
| $O_3$ | 3040 | 3039.90–3040.60 | $H_2O$, $CH_4$ |
| $O_3$ | 2775 | 2775.68–2776.30 | $CH_4$, $CO_2$, HCl, $N_2O$ |
| | (2778) | 2778.85–2779.20 | $CH_4$, HDO, $N_2O$ |
| | (2782) | 2781.57–2782.06 | $CH_4$, HDO, $N_2O$, $CO_2$ |
| HCl | 2925 | 2925.75–2926.05 | $H_2O$, $CH_4$, $N_2O$, $O_3$ |
| $N_2O$ | 2482 | 2481.30–2482.60 | $CO_2$, $CH_4$, $O_3$ |
| $CH_4$ | 2859 | 2859.83–2860.21 | — |
| | (2898) | 2898.32–2898.98 | — |
| | (2904) | 2903.60–2904.16 | $H_2O$, HCl, $O_3$ |

Table 5.13: Microwindows for $O_3$, HCl, $N_2O$, and $CH_4$ used in this intercomparison. The 2775 $cm^{-1}$ $O_3$ and $CH_4$ microwindows each consist of three separate bandpasses retrieved simultaneously. The names of the individual bandpasses are in brackets.

were performed on a 38-layer grid. As discussed in §5.6.2, this made only a small difference in the resulting column amounts.

By eliminating atmospheric condition differences between measurements, eliminating differences in line parameter characterization and minimizing the differences in the retrieval methods, the bulk of the discrepancies can be attributed to differences in instrument resolution.

### Instrument Line Shape

The importance of considering the influence of an individual instrument line shape (ILS) for ground-based comparisons has been previously addressed (Pougatchev et al. [86], Griffith et al. [110]) and is particularly important in this case because of the pronounced differences in the resolution of the three instruments. Pougatchev et al. [117] produced synthetic spectra with a 10% error in the effective apodization parameter at 500, 150 and 50 cm MOPDs, showing that ozone total column errors increase with decreasing MOPD, accruing total column errors of 4.1% at 50 cm MOPD. Retrieving ILS information is very important for the retrievals of stratospheric species, such as $O_3$ and HCl, since their absorption lines are much narrower than the resolution of the U of T FTS and the PARIS-IR instruments. Because of this, most of the broadening of these lines can be attributed to the instrument line shape, and so the ILS will serve an important role. Tropospheric species like $N_2O$ and $CH_4$, however, have pressure-broadened absorption lines that have widths that are on the order of the resolution of the U of T and PARIS-IR instruments.

As mentioned in §5.3, one can input tabular values for PHS and EAP from LINEFIT results, or retrieve PHS and EAP coefficients from the solar spectrum itself with SFIT2. Tabular inputs from LINEFIT are appropriate for ground-based measurements, where the ILS ideally remains constant for several months at a time. For balloon-based measurements, however, temperatures change significantly between daytime and nighttime and both the atmospheric temperature and pressure vary significantly between the ground and float altitude. Both temperature and pressure can affect the instrument alignment and thus the ILS. Because of this, we may wish to calculate the EAP and PHS coefficients for each spectrum individually. Without a permanent gas cell fixed to each spectrometer during solar measurements (which none of these instruments possess), a method for retrieving ILS information from the solar spectrum itself is necessary.

In the sections that follow, when we discuss "tabular" ILS information, we are referring to LINEFIT results used as an input to SFIT2[6]. Retrievals using the LINEFIT tabular inputs will be labeled "ILS input". LINEFIT version 9.0 was used for the U of T FTS and TAO-FTS and version 11.0 for the PARIS-IR. Version 11.0 includes a temperature correction that version 9.0 does not have, although the results were negligibly different between the two versions. The U of T FTS and TAO-FTS measured blackbody

---

[6] See §5.3.1 for a description of this procedure.

radiation through an HBr cell to calculate the ILS, and PARIS-IR measured blackbody radiation through an $N_2O$ cell. When we discuss "polynomial" ILS information, we are referring to the PHS and EAP parameters retrieved from SFIT2. Retrievals that contain PHS and EAP parameters from SFIT2 will be referred to as "PHS/EAP retrieved". When neither the LINEFIT tabular nor SFIT2 polynomial ILS information is included in a retrieval, we will call this our "standard retrieval". The TAO-FTS regularly retrieves a simple phase parameter (SPHS) from SFIT2. SPHS is a single-parameter description of the asymmetry of a spectral line, and is included in all three retrieval types (ILS input, PHS/EAP retrieved and the standard retrieval).

The U of T FTS and PARIS-IR instruments retrieve PHS and EAP information somewhat differently. The method employed for the U of T FTS spectra retrieves third-order polynomial PHS and EAP parameters from the same microwindow as the retrieved species (that is, only one retrieval is necessary for each molecule). The method employed for the PARIS-IR data, however, retrieves third-order PHS and EAP parameters from a very broad $N_2O$ band in the 2806.1–2808.1 $cm^{-1}$ microwindow, and fixes the daily mean of those values for all spectra when retrieving the other species. (This method could also be used for each spectrum individually on a balloon platform, but for this ground-based study, it is more efficient to use the daily mean of the PHS and EAP values.) The PARIS-IR method was attempted for the U of T FTS data with less success than directly retrieving the parameters from the same microwindow as the molecule of interest. We believe that the success of the second, dedicated microwindow for retrieving the ILS parameters for the PARIS-IR instrument may be in part due to the lower degrees of freedom for signal ($<1$) retrieved by the PARIS-IR spectra. Instead of retrieving VMR, PHS and EAP information from a given microwindow with limited information, we are providing extra ILS information from the same spectrum, but in a different microwindow. Table 5.14 lists the PARIS-IR instrument's mean degrees of freedom for signal for each microwindow after retrieving the PHS and EAP values from the $N_2O$ microwindow.

| Target Gas | Signal-to-Noise Ratio | | | Degrees of Freedom for Signal | | | Retrieved ILS Parameters | | | | |
|---|---|---|---|---|---|---|---|---|---|---|---|
| | TAO | U of T | PARIS | TAO | U of T | PARIS | TAO | U of T FTS | | PARIS-IR | |
| | | | | | | | SPHS | SPHS | PHS/ EAP | SPHS | PHS/ EAP |
| $O_3$ (3040) | 200 | 360 | 140 | 2.4 | 1.32 | 1.03 | ✓ | ✓ | ✓ | ✓ | ✓ |
| $O_3$ (2775) | 400 | 900 | 100 | 2.1 | 1.35 | 0.83 | ✓ | ✓ | ✓ | ✓ | ✓ |
| HCl | 680 | 760 | 95 | 3.1 | 1.23 | 0.67 | ✓ | ✓ | ✓ | ✓ | ✓ |
| $N_2O$ | 460 | 600 | 130 | 4.2 | 2.85 | 2.31 | ✓ | ✓ | ✓ | ✓ | |
| $CH_4$ | 420 | 350 | 130 | 4.0 | 2.68 | 2.38 | ✓ | ✓ | | ✓ | |

Table 5.14: Signal-to-noise ratio, degrees of freedom for signal and retrieval parameters for the intercomparison microwindows. The mean degrees of freedom for signal were obtained from retrievals performed using the retrieval parameters listed in columns 8–12. SPHS is the simple phase parameter. PHS and EAP are the third order phase and effective apodization polynomial coefficients. The TAO-FTS always retrieves the simple phase parameter (SPHS), but does not retrieve PHS or EAP polynomial parameters.

### Effects of Resolution

To simulate the effect of resolution on total column amounts, an ensemble of 16 spectra were simulated for the same atmospheric conditions for each of 12 cm, 25 cm, 50 cm, 100 cm, 150 cm, 200 cm, and 250 cm OPD. The signal-to-noise ratio was set to 250 for each spectrum to simulate a typical measurement noise value between the TAO-FTS and PARIS-IR values listed in Table 5.14, and all four molecules were retrieved using the same *a priori* values as our data from September 1st. Identical phase and effective apodization errors were applied to each spectrum, with values similar to the TAO instrument (left panels of Figure 5.36). All results below are consistent with an ensemble of measured spectra from a single day of TAO measurements for which the interferograms were truncated with a triangular apodization function to the same set of OPD values.

In Figures 5.39–5.43, the column amounts of $O_3$, HCl, $N_2O$, and $CH_4$ are shown as a function of the optical path difference. The figures show the mean column amounts with the $2\sigma$ standard deviation for two sets of retrievals: one that retrieves third-order polynomial coefficients for the PHS and EAP functions ("PHS/EAP retrieved") from the microwindow itself, and one that does not retrieve coefficients (our "standard retrieval").

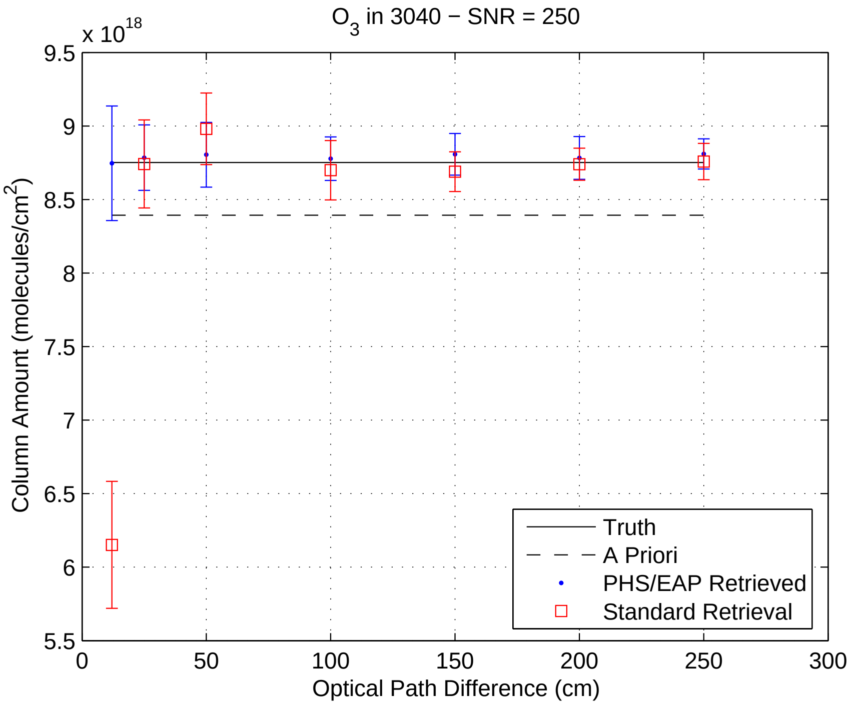

Figure 5.39: Simulated retrievals of ozone columns in the 3040 cm$^{-1}$ microwindow, assuming SNR=250, as a function of OPD.

The *a priori* column value and the "truth" are plotted for reference. The truth in this case is the column amount used to create the model spectra.

For ozone in the 3040 cm$^{-1}$ microwindow (Figure 5.39), there is less than 0.67% difference in column amounts retrieved at 250 cm OPD between the standard and PHS/EAP retrieved cases, with the standard retrieval being essentially indistinguishable from the truth (∼0.07% larger). The PHS/EAP retrieved case changes less than the standard retrieval between the different OPD values, and retrieves columns that are closer to the truth at the lowest OPDs (except for 25 cm). The results are within 1% of the truth for all OPDs for the PHS/EAP retrieved case and differ by more than 1% from the truth for the 50 cm OPD and 12 cm OPD standard retrieval. We would expect, then, good results from the lower resolution instruments using this microwindow if they retrieve PHS and EAP parameters.

Ozone in the 2775 cm$^{-1}$ microwindow is shown in Figure 5.40. At 250 cm OPD, the

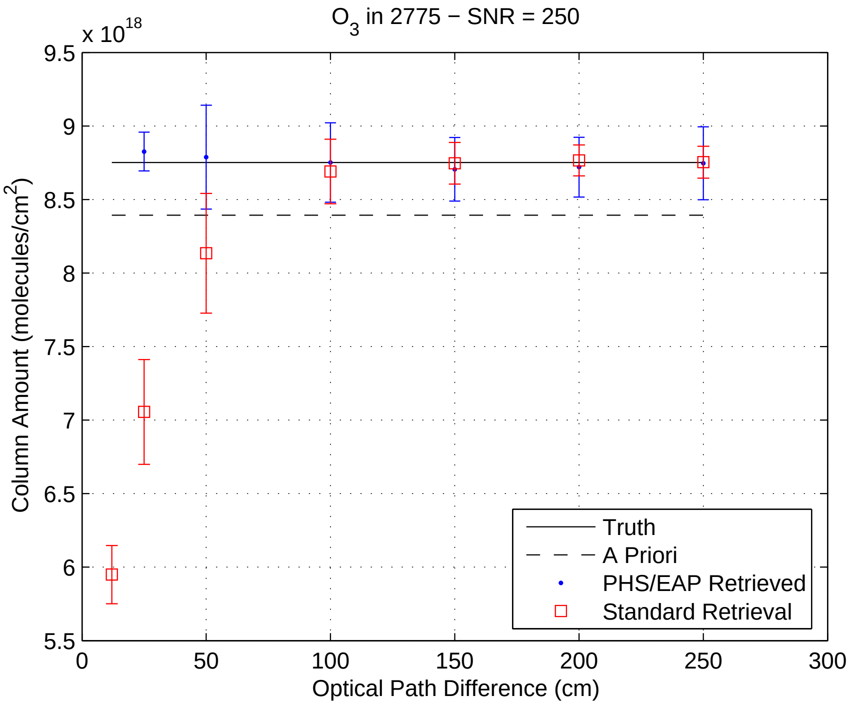

Figure 5.40: Simulated retrievals of ozone columns in the 2775 cm$^{-1}$ microwindow, assuming SNR=250, as a function of OPD. The small error bars on the PHS/EAP retrieval for 25 cm OPD are due to the small number of retrievals that converged for this OPD. The error bars are, as a consequence, not representative of the true standard deviation.

columns differ by less than 0.06% from the truth, obtained by either the standard retrieval or the PHS/EAP retrieved case. The column average for the standard retrieval begins to decrease significantly below 100 cm OPD with the column mean over the ensemble differing by <7% from the truth at 50 cm OPD. The PHS/EAP retrieved case has less than 1% difference down to 25 cm OPD, whereas the standard retrieval gives a mean that is 19.4% smaller than the true value at 25 cm OPD. The simulated retrievals did not converge for the PHS/EAP retrieval at 12 cm OPD, so are not plotted here. We may expect, then, that we should get good results for ozone for the lower-resolution instruments if they retrieve PHS/EAP parameters.

For HCl (Figure 5.41), the difference in columns retrieved between the standard retrieval at 250 cm OPD and the truth is 0.27% and between the PHS/EAP retrieved case at 250 cm OPD and the truth is 0.36%. The column amounts are within 1% of the

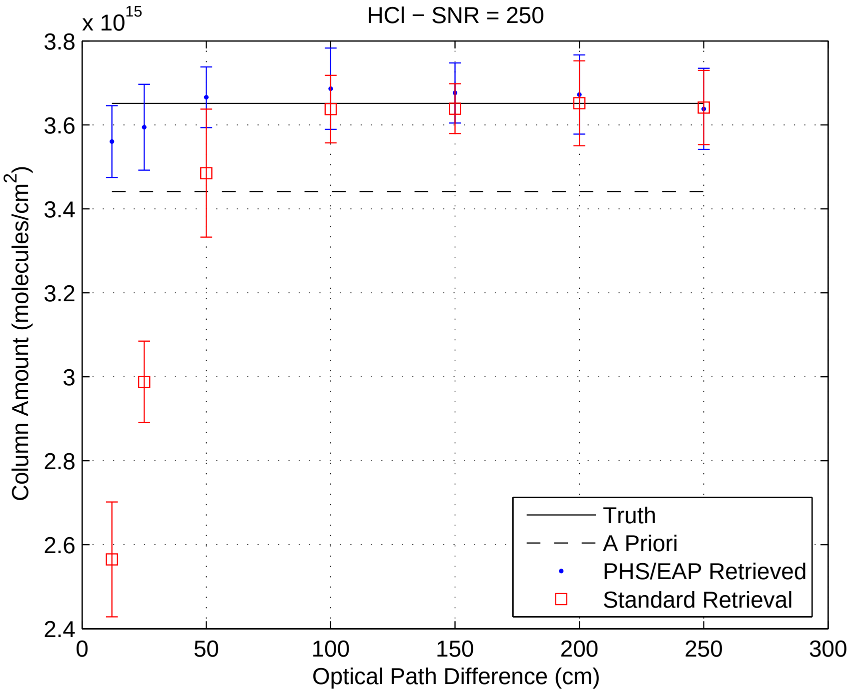

Figure 5.41: Simulated retrievals of HCl columns, assuming SNR=250, as a function of OPD.

truth until 50 cm OPD for the standard retrieval, and 25 cm OPD for the PHS/EAP retrieved case. At and below 50 cm OPD, the percent difference from the truth increases in both cases, with the PHS/EAP retrieved case showing significantly better agreement than the standard case. We would expect, then, reasonable agreement for HCl for the lower resolution instruments if PHS and EAP parameters are retrieved.

For $N_2O$ (Figure 5.42), the difference between the columns retrieved with the standard retrieval at 250 cm OPD and the truth is ~0.5%, and the difference in columns between the PHS/EAP retrieval at 250 cm OPD and the truth is ~0.02%. The $N_2O$ columns show good agreement with the truth (<1%) for all OPDs for the PHS/EAP retrieved case, and good agreement with the truth for all OPDs at or larger than 100 cm for the standard retrieval. Below 100 cm OPD, the standard retrieval stays within ~2% of the truth, and does not have the drastic decrease that the stratospheric species show. We would expect, then, that all three instruments would have good agreement for $N_2O$ if

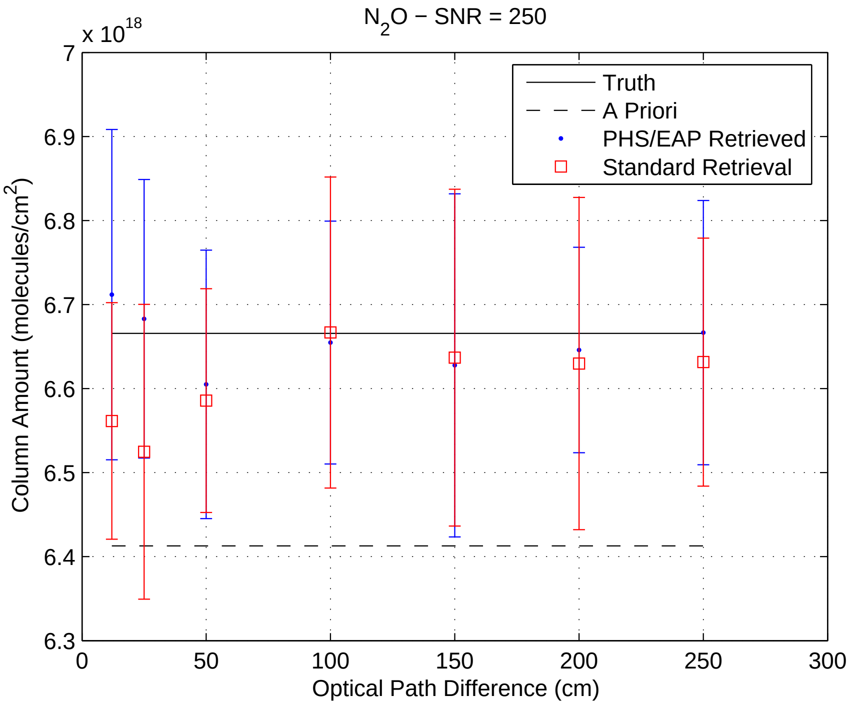

Figure 5.42: Simulated retrievals of $N_2O$ columns, assuming SNR=250, as a function of OPD.

they perform either retrieval, but better results may be obtained from the lower resolution instruments if they retrieve PHS and EAP parameters.

For $CH_4$ (Figure 5.43), the difference between columns retrieved using the standard retrieval at 250 cm OPD and the truth is ∼0.34%, and the difference in columns between the PHS/EAP retrieval at 250 cm OPD and the truth is ∼0.22%. The $CH_4$ columns show good agreement with the truth (<1%) for all OPDs for the PHS/EAP retrieved case, except for 100 cm OPD, where the percent difference from the truth is ∼1.05%. There is good agreement with the truth for all OPDs for the standard retrieval, except for 25 cm OPD where the difference is ∼2.35%. Again, as for $N_2O$, the two retrieval cases stay within ∼2.5% of the truth, and do not show a significant decrease at smaller OPD. We would expect, then, that all three instruments would have good agreement for $CH_4$ if they perform either retrieval.

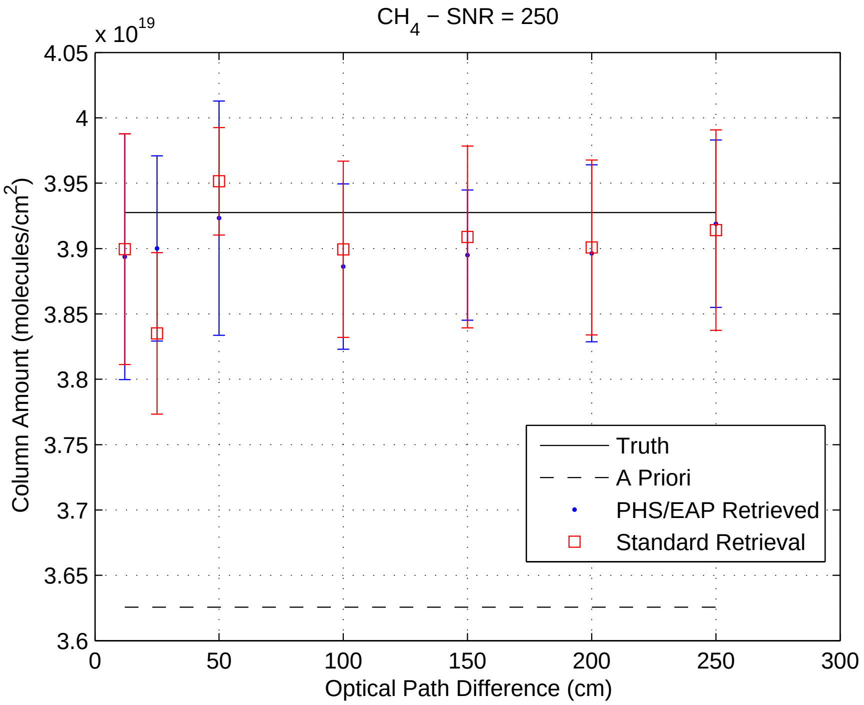

Figure 5.43: Simulated retrievals of $CH_4$ columns, assuming SNR=250, as a function of OPD.

### Comparison of Columns using Retrieved ILS and LINEFIT Predetermined ILS

It has been noted by Griffith et al. [110] that stratospheric species ($O_3$ and HCl) that have narrow absorption lines are highly sensitive to ILS distortions, while pressure-broadened tropospheric species ($N_2O$ and $CH_4$) are less sensitive to them. We have confirmed this and have investigated column differences obtained when retrieving the EAP and PHS with SFIT2 as compared with columns retrieved when using LINEFIT results as inputs to SFIT2. The first test run retrieved PHS and EAP parameters ("PHS/EAP retrieved") using the microwindow itself in the U of T FTS case, and the $N_2O$ microwindow in the PARIS-IR case. The second test run used tabular LINEFIT inputs ("ILS input") obtained from a gas cell measurement. The third test run used only SPHS ILS information ("standard retrieval"). No significant differences in retrieved column amounts between the three ILS cases are seen for the TAO-FTS. Therefore, for our purposes, TAO-FTS

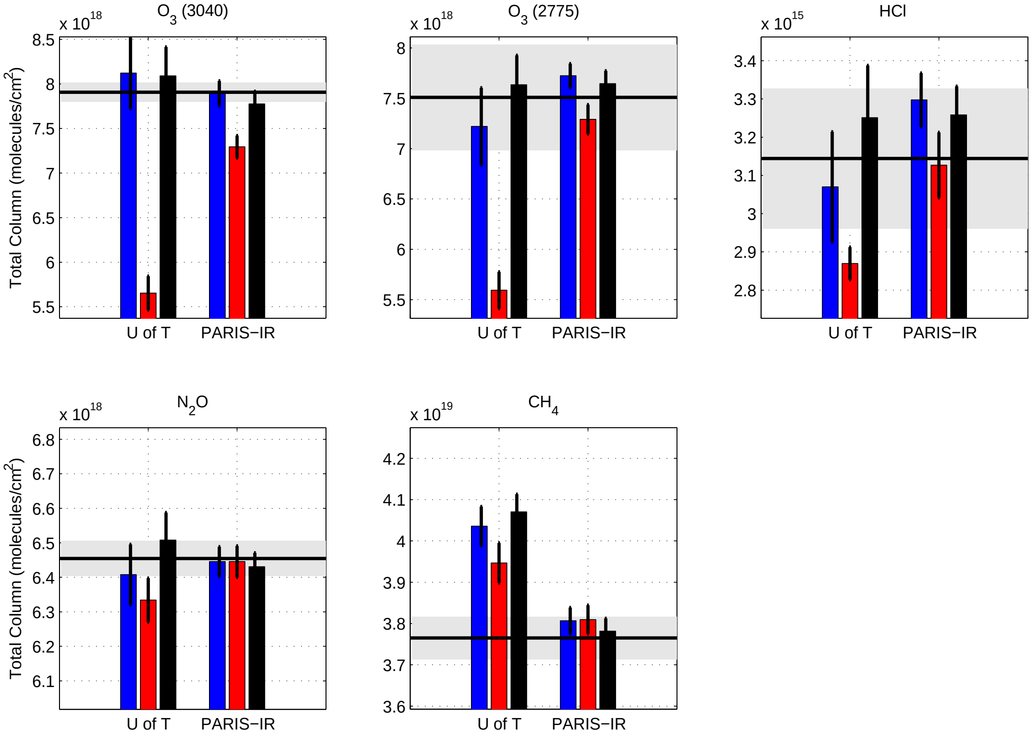

Figure 5.44: Mean column differences from data recorded on September 2, using the PHS/EAP retrieval (blue), the standard retrieval (red) and the ILS input retrieval (black). The thick black horizontal line indicates the TAO-FTS mean and the grey shading is the standard deviation of the TAO-FTS retrieved values. The error bars on the bars indicate the standard deviation of the retrieved values.

data is considered to be closest to the truth.

For the U of T FTS, the best ozone column comparisons were from using the ILS input run (Figure 5.44). For ozone in the 3040 cm$^{-1}$ microwindow, the ILS input run is only slightly closer to the TAO-FTS mean values (by $\sim$ 0.4%) than the PHS/EAP retrieval and both are more than 20% higher than the values from the standard run. The spectral fits from the PHS/EAP retrieved and ILS input cases also show smaller residuals (see Figure 5.45). The PARIS-IR results are similar—retrieving PHS/EAP parameters improved the agreement in the column amounts by $\sim$8% over the standard retrieval (Figure 5.44). Similar results are found for ozone in the 2775 cm$^{-1}$ microwindow (Figure

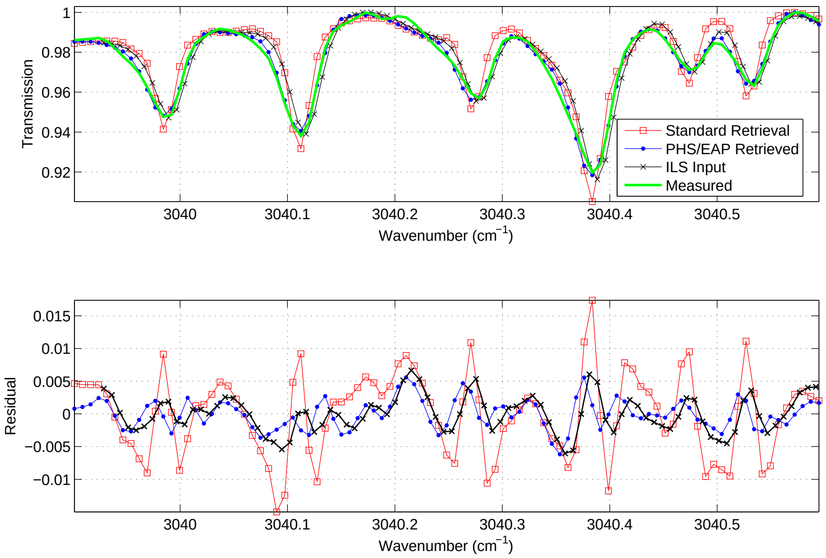

Figure 5.45: $O_3$ spectral fits for the U of T FTS (upper panel), and the residuals between the measured retrieval and the spectral fits (lower panel).

5.44).

The sensitivity of the U of T FTS HCl retrieval to the ILS is also high, as illustrated in Figures 5.44 and 5.46, with the PHS/EAP retrieved case being closer (by $\sim 1\%$) to the TAO-FTS columns than the ILS input run. The difference in HCl columns between the PHS/EAP retrieved and standard retrievals for the PARIS-IR instrument is $\sim$2%, with the standard retrieval mean slightly closer to the TAO retrieved values (Figure 5.44). Residuals from the spectral fits for both the U of T FTS and PARIS-IR show, like in $O_3$, that the PHS/EAP retrieval and ILS input cases are smaller than for the standard retrieval.

The U of T FTS $N_2O$ retrieval is much less sensitive to the ILS, as illustrated in Figures 5.44 and 5.47, although the PHS/EAP retrieved case values are slightly closer to the TAO-FTS values. The sensitivity of the PARIS-IR retrieval in the PHS/EAP retrieved case is also quite low. There is only a $\sim$0.4% difference between the PHS/EAP and standard cases (Figure 5.44). The residuals from the spectral fits for both the U of T FTS and PARIS-IR instruments show only slightly better results for the PHS/EAP

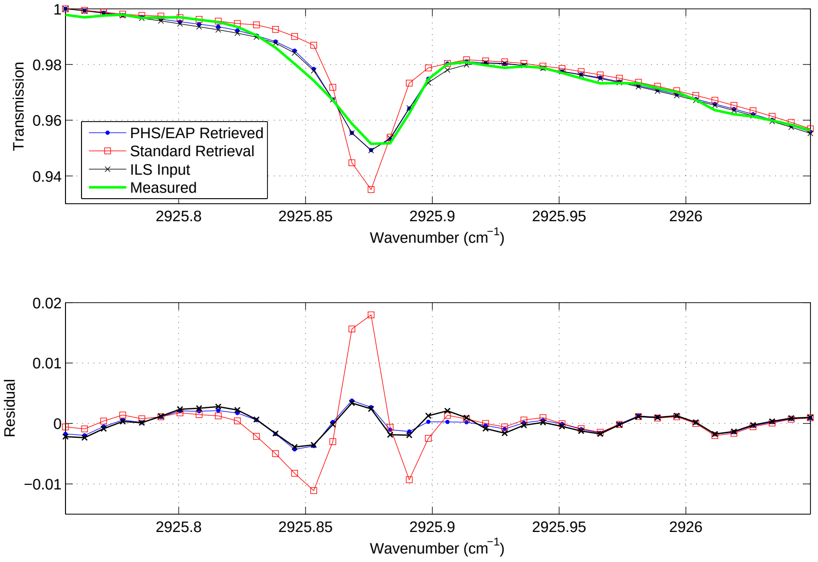

Figure 5.46: HCl spectral fits for the U of T FTS (upper panel), and the corresponding residuals (lower panel).

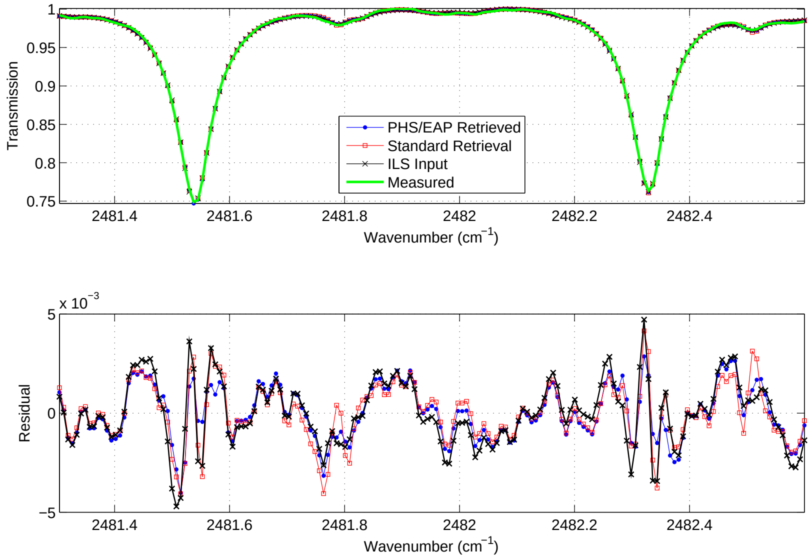

Figure 5.47: $N_2O$ spectral fits for the U of T FTS (upper panel), and the corresponding residuals (lower panel).

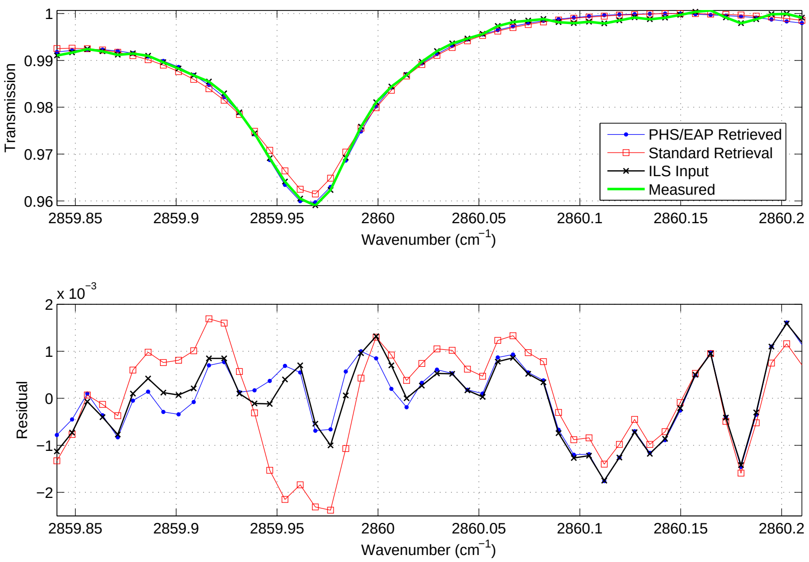

Figure 5.48: $CH_4$ spectral fits for the first $CH_4$ bandpass of the U of T FTS (upper panel), and the corresponding residuals (lower panel).

retrieval and ILS input cases than for the standard retrieval.

The sensitivity of the U of T FTS $CH_4$ retrievals to the ILS is also lower than for $O_3$ and HCl, as illustrated in Figures 5.44 and 5.48–5.50. Retrieving the PHS and EAP parameters for the U of T FTS data produces poorer comparisons with the TAO-FTS data, because it induces spurious oscillations in the profile. There is systematic structure in the residuals from the $CH_4$ spectral fits for all three retrieval cases for both the PARIS-IR and the U of T FTS. The TAO-FTS residuals also show systematic structure, pointing to a possible problem with the methane spectroscopy. The sensitivity of the PARIS-IR retrieval of $CH_4$ to the ILS is very low, with only ∼0.6% difference between the PHS/EAP retrieved and standard retrievals (Figure 5.44).

Because the U of T FTS ILS is much poorer than that of PARIS-IR, the difference in total columns retrieved by the U of T FTS between the PHS/EAP retrieved case and the standard retrieval will be exaggerated for the stratospheric species. Nevertheless, using either the PHS/EAP retrieved or the ILS input cases for both lower-resolution instruments results in reasonable agreement with the TAO-FTS.

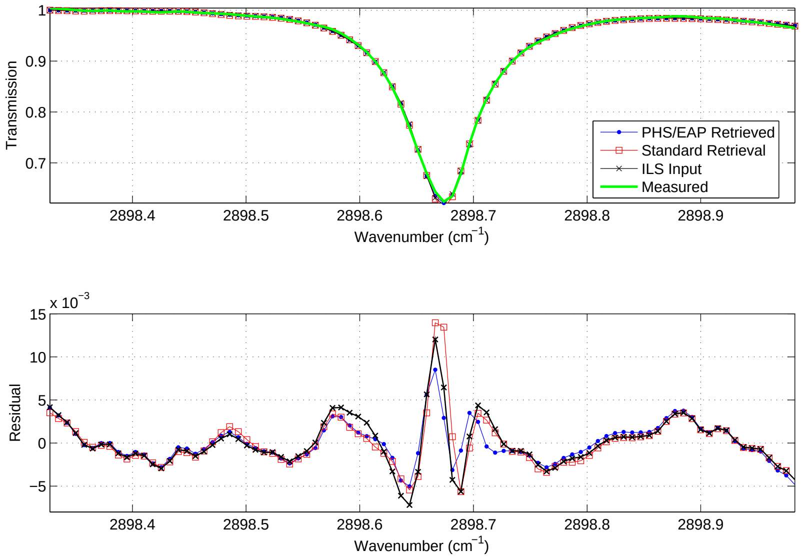

Figure 5.49: $CH_4$ spectral fits for the second $CH_4$ bandpass of the U of T FTS (upper panel), and the corresponding residuals (lower panel).

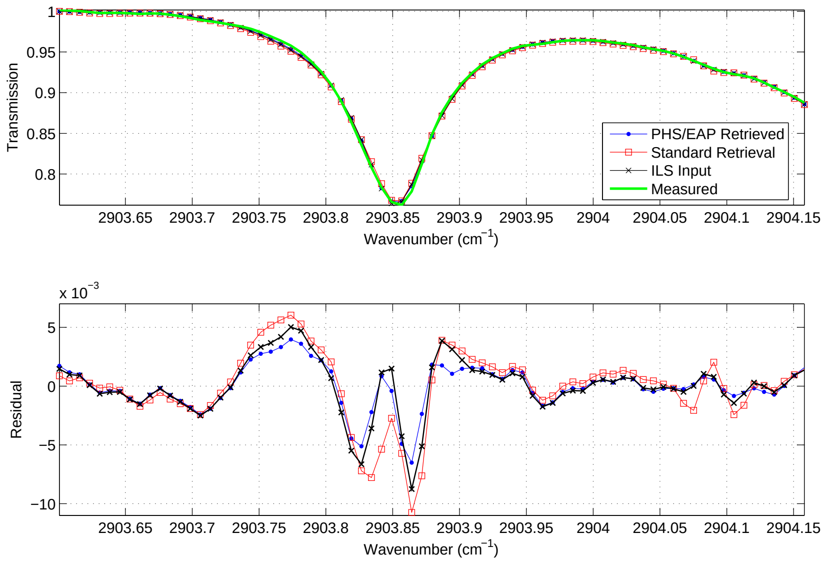

Figure 5.50: $CH_4$ spectral fits for the third $CH_4$ bandpass of the U of T FTS (upper panel), and the corresponding residuals (lower panel).

Using the results from this section, for what follows, we use the PHS/EAP retrieved case to compute columns of $O_3$, HCl and $N_2O$ for the U of T FTS. The standard retrieval is used for $CH_4$. For PARIS-IR, the PHS/EAP retrieved case is used for $O_3$ and HCl, and the standard retrieval is used for $N_2O$ and $CH_4$. Since the TAO-FTS line shape is significantly narrower than both the stratospheric and tropospheric absorption lines, it is much less sensitive to instrument line shape distortions, and the standard retrieval is always used. Retrieving the PHS and EAP parameters for the TAO-FTS makes only small changes (<1%) in total columns retrieved. Table 5.14 summarizes the retrieval parameters for these results.

### Number of Grid Levels

The PARIS-IR analysis retrieves profiles on a 29-layer vertical grid, whereas the TAO FTS and U of T FTS retrieve profiles on a 38-layer grid. The 29-layer vertical grid was chosen for the PARIS-IR retrievals to reduce the size of the state vector, in order to compensate for the lower resolution of the measurements. To ensure that the number of grid levels does not significantly affect the results from this intercomparison, we compared column amounts retrieved for a single day of measurements from the PARIS-IR instrument both on a 29-layer grid and a 38-layer grid.

For $N_2O$ and $CH_4$, there was no noticeable difference ($< 0.1\%$) in column amounts retrieved from the PARIS-IR data between retrieving on a 29-layer grid and a 38-layer grid. For ozone in the 3040 $cm^{-1}$ microwindow, the 38-layer results were $\sim$0.2% lower than the 29-layer results. For ozone in the 2775 $cm^{-1}$ microwindow, the 38-layer results were $\sim$0.6% higher than the 29-layer results. For HCl, the 38-layer results were $\sim$0.4% higher than the 29-layer results. The number of grid levels, therefore, is not a significant influence on the results in this comparison. Figures 5.51–5.55 show the PARIS-IR data retrieved on both a 29- and 38-layer grid for all five microwindows, for the “ILS Input” case.

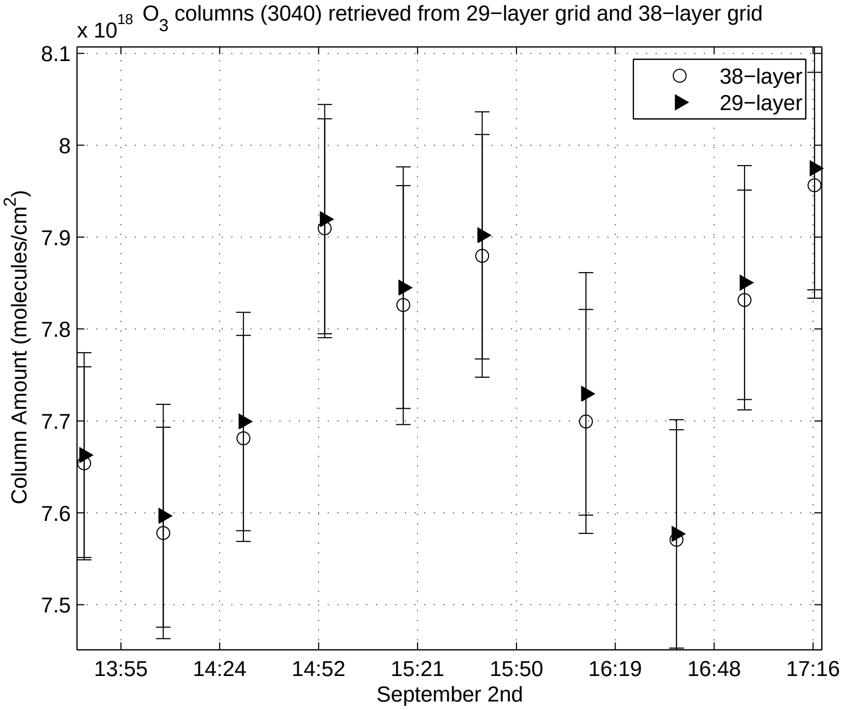

Figure 5.51: $O_3$ columns retrieved for 38- and 29-grid layers for PARIS-IR.

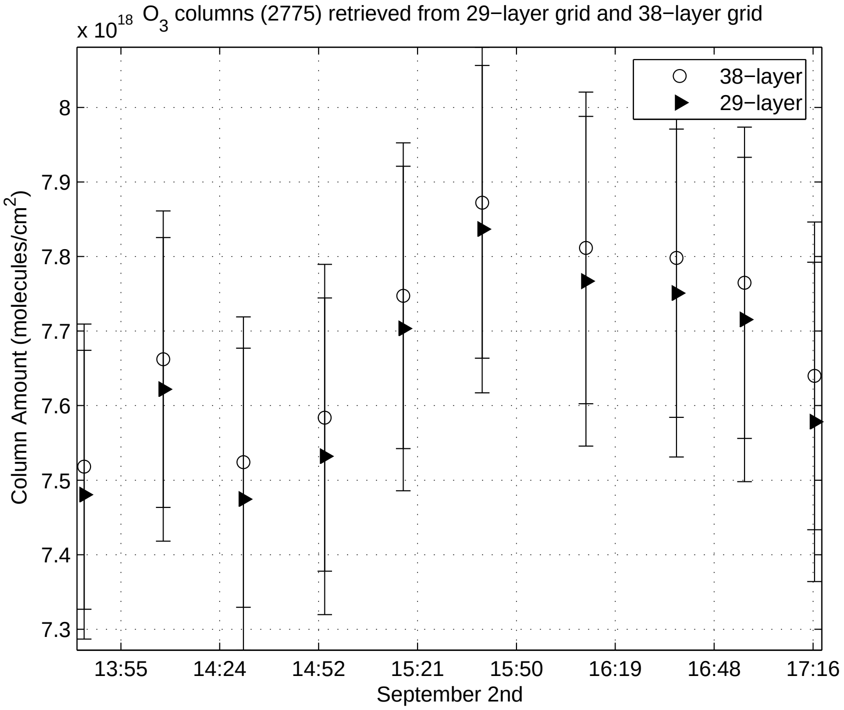

Figure 5.52: $O_3$ columns retrieved for 38- and 29-grid layers for PARIS-IR.

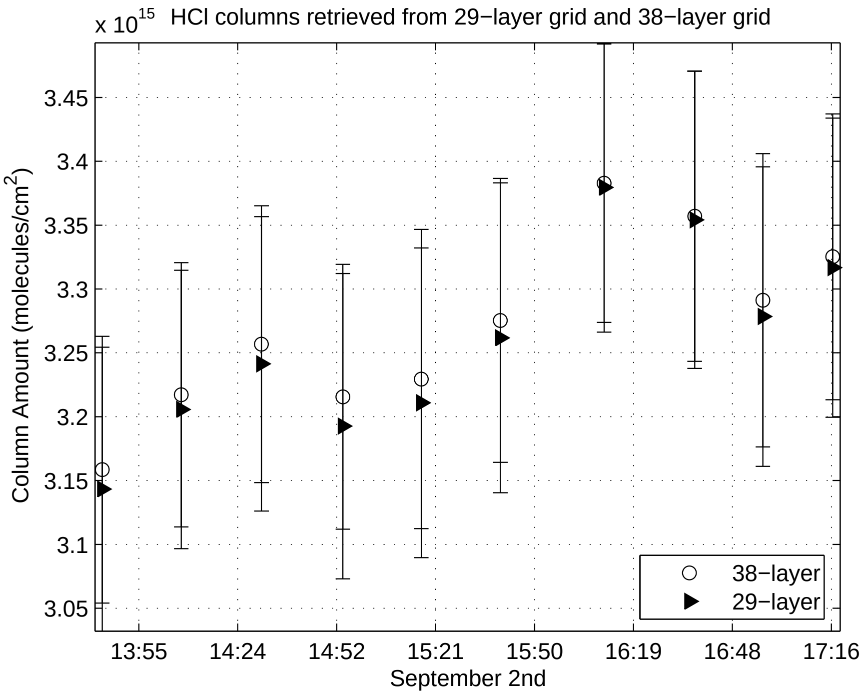

Figure 5.53: HCl columns retrieved for 38- and 29-grid layers for PARIS-IR.

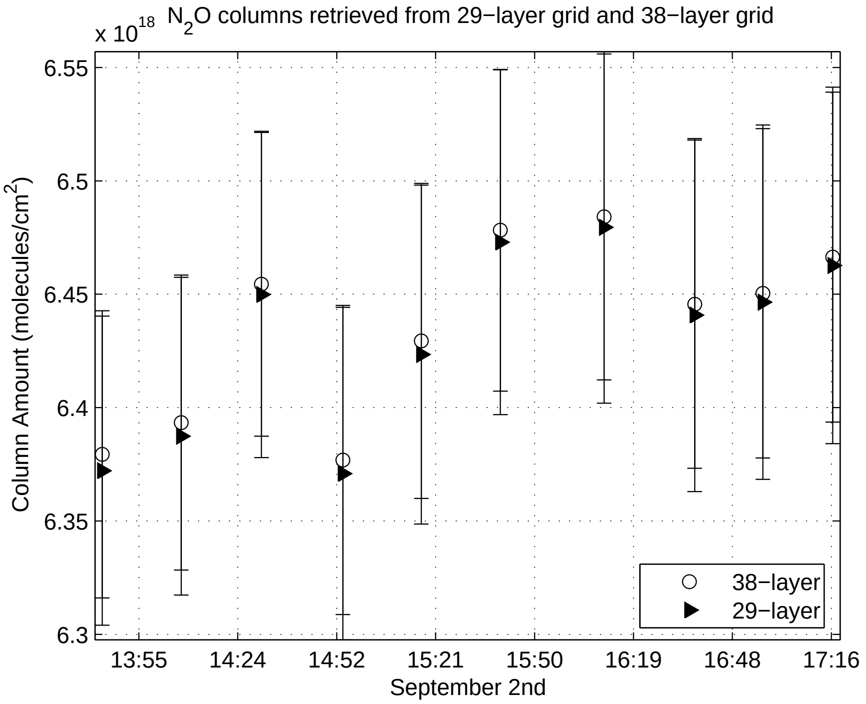

Figure 5.54: $N_2O$ columns retrieved for 38- and 29-grid layers for PARIS-IR.

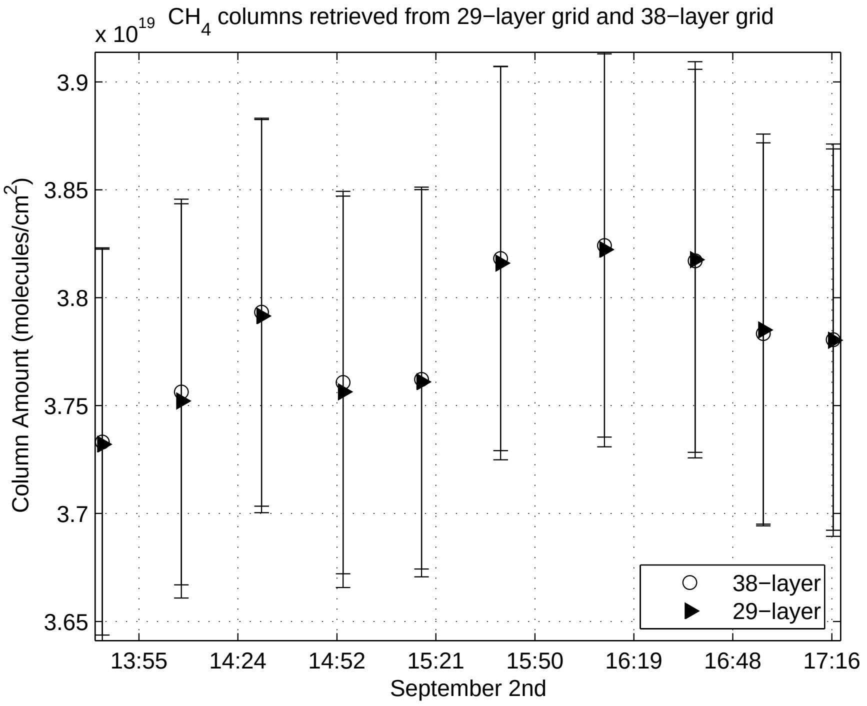

Figure 5.55: $CH_4$ columns retrieved for 38- and 29-grid layers for PARIS-IR.

### 5.6.3 Intercomparison Results

Total column amounts of $O_3$, HCl, $N_2O$ and $CH_4$ were retrieved from PARIS-IR, the U of T FTS and the TAO FTS. Measurements were averaged during coincident 20-minute periods and the total column amounts from these averaged spectra were compared directly. Interferograms were averaged in the case of the TAO-FTS and PARIS-IR, and spectra were averaged for the U of T FTS. The day-to-day variability of the daily mean total column amounts for the TAO instrument over the duration of the intercomparison was small for the tropospheric species (1.7% for $N_2O$ and 0.9% for $CH_4$) and larger for the stratospheric species (7.8% for HCl, 6.3% for $O_3$ in the 3040 $\text{cm}^{-1}$ microwindow and 10% for $O_3$ in the 2775 $\text{cm}^{-1}$ microwindow)[7]. Total column amounts are plotted as a function of solar zenith angle (SZA) in Figures 5.56–5.60 to point out a SZA-dependent error.

---

[7] These values were computed by taking the maximum daily mean column, $\bar{c}_{max}$, subtracting the minimum daily mean column, $\bar{c}_{min}$ and dividing by the mean of the daily mean column amounts $\bar{c}_{mean}$: $(\bar{c}_{max} - \bar{c}_{min})/\bar{c}_{mean}$.

The total column errors in the figures consist of the retrieval noise, smoothing error, and interference error (Equations 5.2.27, 5.2.29 and 5.2.32). There is a clear discrepancy (most pronounced for $CH_4$) between the column amounts at angles larger and smaller than 40 degrees SZA. This may be due to suntracker error near solar noon, and so data taken at angles less than 40 degrees are not included in our means. The total column means over the four days of measurements, given in Table 5.15, show that the lower-resolution instruments are capable of retrieving column amounts of all species to within 3.5% of the TAO-FTS. The statistical significance of the data is tested using the Student's t-test[8]. The agreement is worse than the agreement found in the Meier et al. [109] paper (also listed in the table) with high-resolution instruments of the same resolution, and so this may give an upper bound on the ability to measure total column amounts of these species by lower-resolution instruments.

Methane shows larger errors than would be expected from a tropospheric species retrieval, with significantly different retrieved columns obtained from the three FTSs. This is possibly caused by the more poorly understood spectroscopy of methane due to the lack of accurate air-broadening coefficients and temperature dependencies, which has been noted by Rothman et al. [31], Brown et al. [119], and Worden et al. [120].

A possibility for the differences in the stratospheric retrieved total column amounts is due to the instruments' respective density-weighted column averaging kernels (Equation 5.2.23). In Figure 5.61, the $\mathbf{a}_{\boldsymbol{\rho}}$ are shown for each instrument and in Figure 5.62, the normalized kernels are shown for reference. There are significant differences between the averaging kernels of the three instruments, with the PARIS-IR results showing the lowest sensitivity.

To test the sensitivity of the U of T FTS and PARIS-IR retrievals to the stratosphere,

---

[8] The t-test equation used here is

$$t = \frac{\mu_1 - \mu_2}{\sqrt{\sigma_1^2/N + \sigma_2^2/N}},$$

where the $\mu$ are the means of each data set, the $\sigma$ are the standard deviations of each data set and $N$ is the number of data points (always the same for the two data sets) [118, §6.6.5, p. 113].

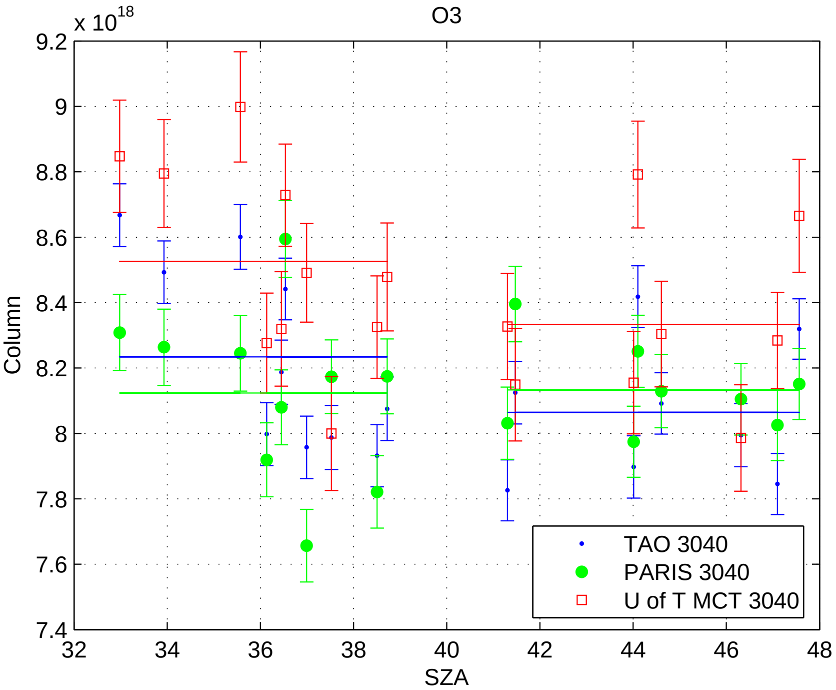

Figure 5.56: $O_3$ column amounts retrieved in the 3040 $cm^{-1}$ microwindow as a function of solar zenith angle, using the parameters listed in Table 5.14. The horizonal lines show the means of the columns over the SZA range indicated. The error bars include the smoothing error, interference error, and the retrieval error added in quadrature.

the averaging kernels were applied to a profile that was 20% larger than the *a priori* profile at each level and the total column was computed. That is,

$$\hat{\mathbf{x}} = \mathbf{A}(\mathbf{1.2x_a}) + (\mathbf{I} - \mathbf{A})\mathbf{x_a} = (0.2\mathbf{A} + \mathbf{I})\mathbf{x_a}. \quad (5.6.1)$$

$$\hat{c} = \boldsymbol{\rho}^{\mathrm{T}}(0.2\mathbf{A} + \mathbf{I})\mathbf{x_a} = (0.2\mathbf{a}_{\boldsymbol{\rho}} + \boldsymbol{\rho}^{\mathrm{T}})\mathbf{x_a}. \quad (5.6.2)$$

In this case, shown in Figure 5.63, there are significant column differences between the TAO-FTS results and the U of T FTS and PARIS-IR results. The red lines indicate the *a priori* column and the green lines indicate the *a priori* column scaled up by 20% (the "truth," here). Results with the *a priori* increased by a larger amount show larger differences between the retrieved columns and the truth.

For $O_3$ in the 3040 $cm^{-1}$ microwindow, the percent differences from the TAO-FTS are: −0.9% for the U of T FTS and −1.8% for PARIS-IR; for ozone in the 2775 $cm^{-1}$

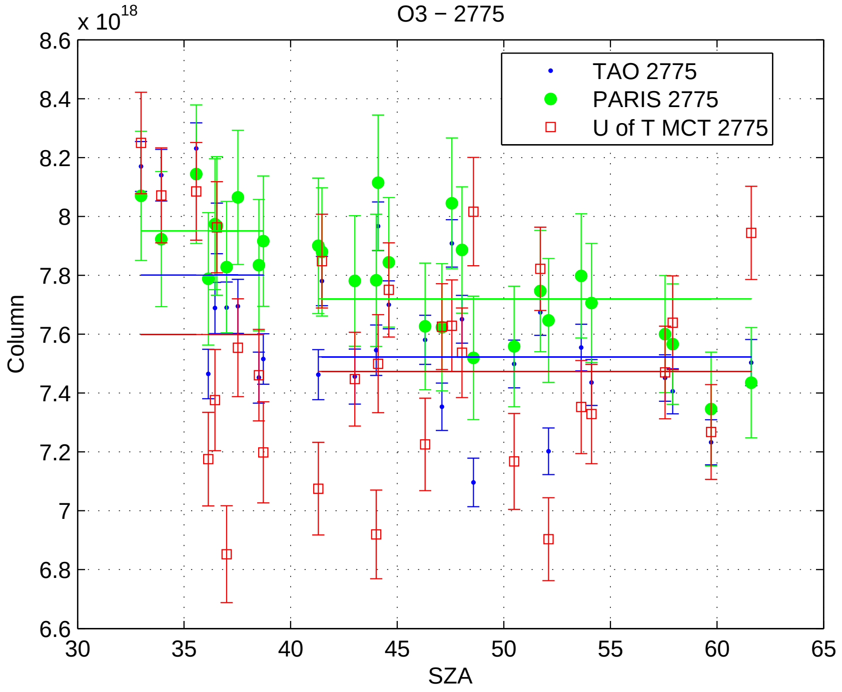

Figure 5.57: As in Figure 5.56, but for $O_3$ in the 2775 $cm^{-1}$ microwindow.

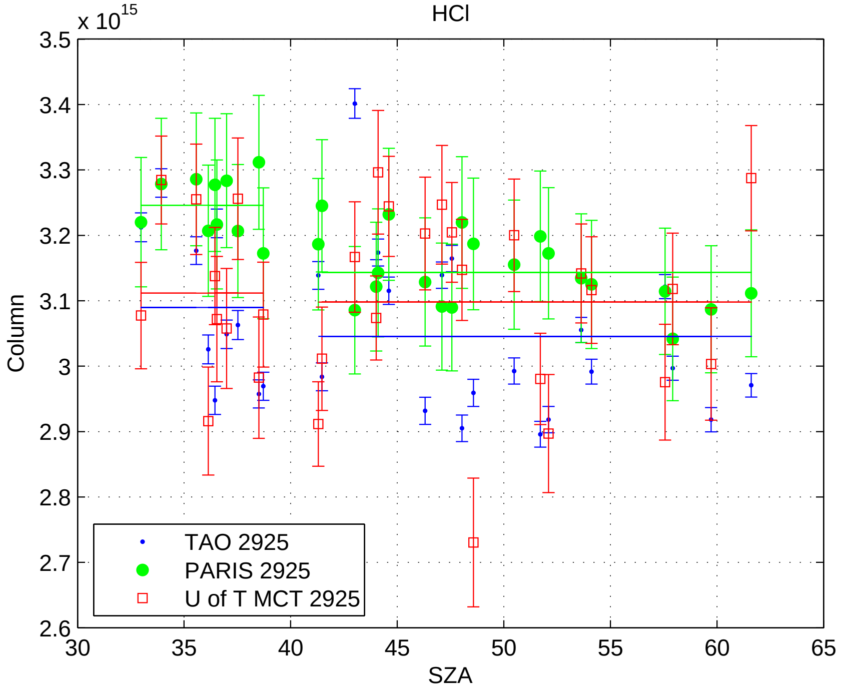

Figure 5.58: As in Figure 5.56, but for HCl.

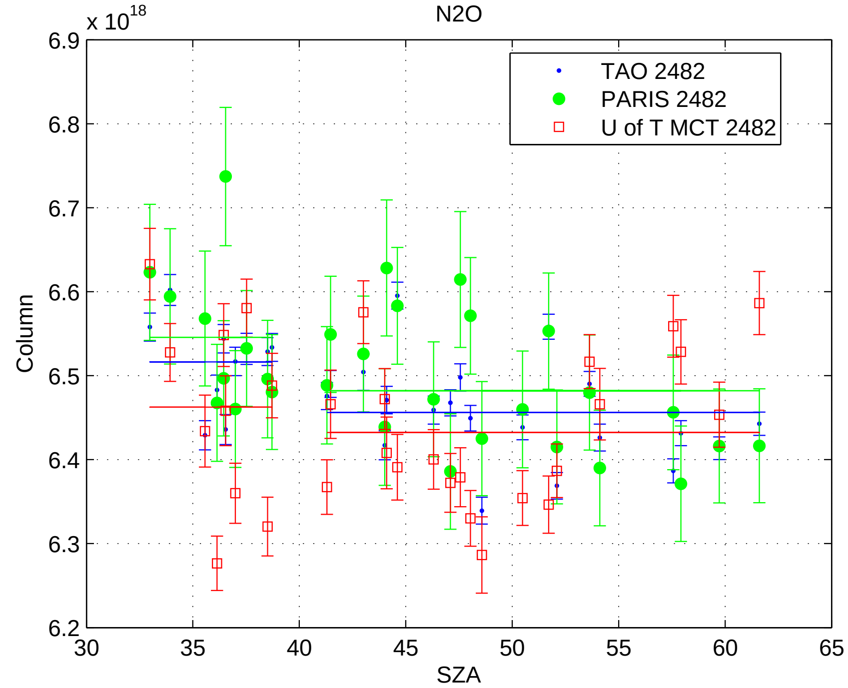

Figure 5.59: As in Figure 5.56, but for $N_2O$.

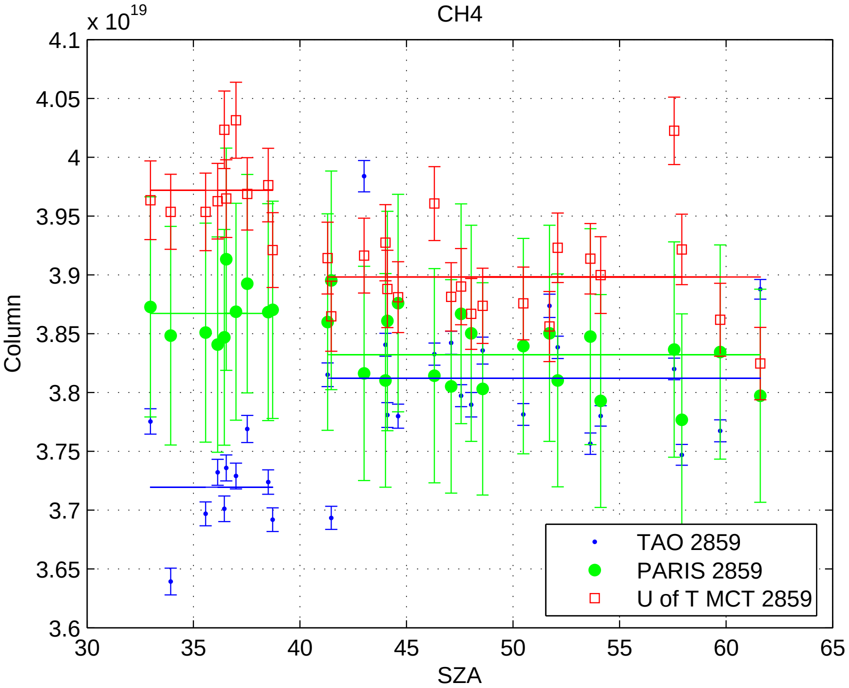

Figure 5.60: As in Figure 5.56, but for $CH_4$.

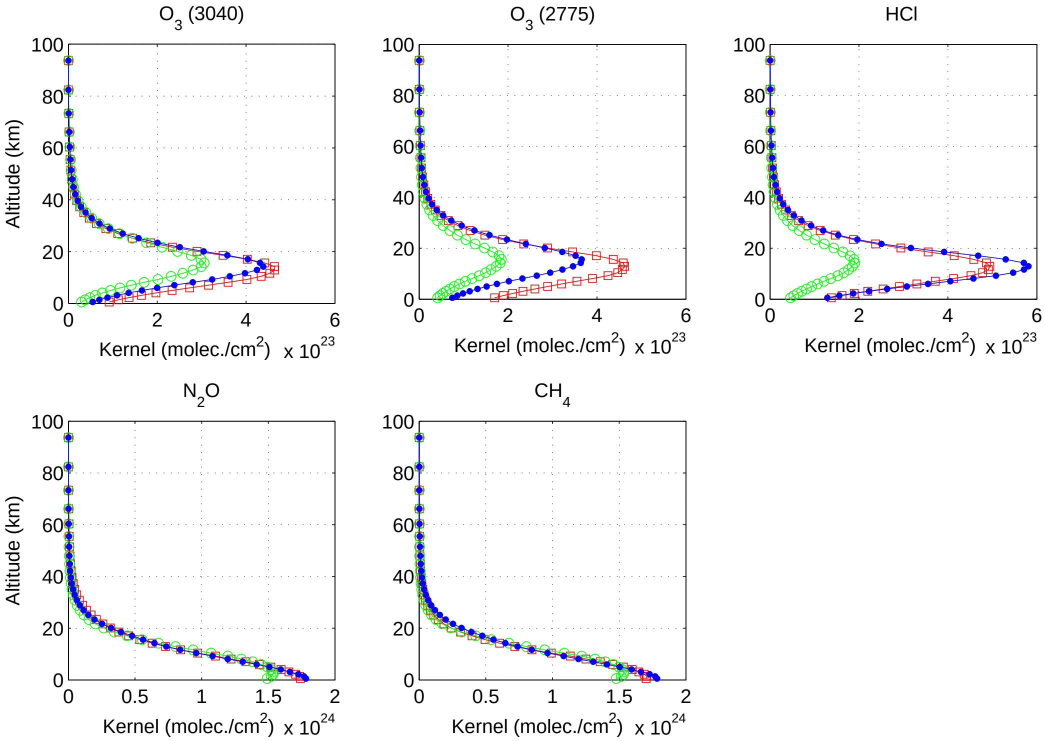

Figure 5.61: Density-weighted column averaging kernels for the three instruments: TAO-FTS (blue dots), U of T FTS (red squares) and the PARIS-IR (green circles), illustrating the sensitivity of the retrieved column at each altitude.

microwindow: −0.2% for the U of T FTS and −6.7% for PARIS-IR; for HCl: −1.4% for the U of T FTS and −8.4% for PARIS-IR; for $N_2O$: −0.01% for the U of T FTS and −0.5% for PARIS-IR; and for $CH_4$: −0.2% for the U of T FTS and −0.6% for PARIS-IR. The stratospheric species clearly show larger differences as we have also seen in Table 5.15. The differences in the stratospheric species, therefore, can be partially attributed to the lower sensitivity of the lower-resolution instruments to the stratosphere and the consequent increased reliance on the *a priori* in that region. It is therefore particularly important to choose appropriate microwindows and perform sufficient characterization of the lower-resolution instruments, to optimize the sensitivity.

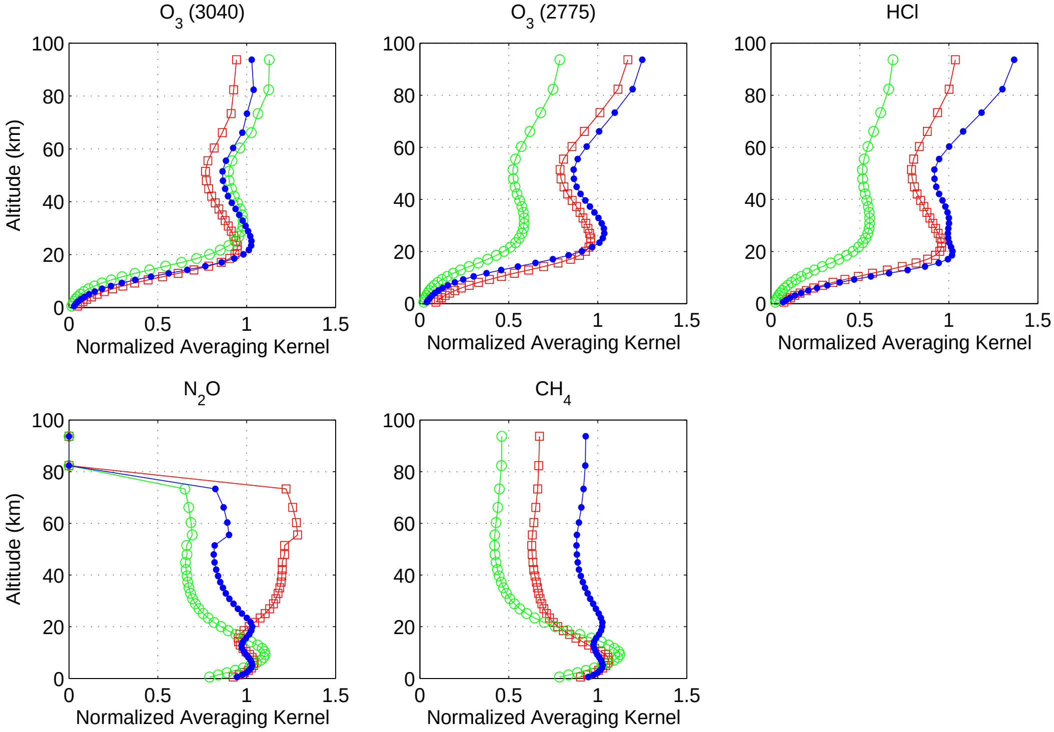

Figure 5.62: Normalized column averaging kernels. These panels show the normalized column averaging kernels for the three instruments: TAO-FTS (blue dots), U of T FTS (red squares) and the PARIS-IR (green circles).

## 5.6.4 Intercomparison Conclusions

Figures 5.56–5.60, summarized in Table 5.15, show that the lower-resolution instruments can measure total columns of $O_3$, $CH_4$, HCl, and $N_2O$ to within ~3% of the truth (taken here as the high-resolution TAO FTS) from the ground. The largest errors are from the stratospheric species, and these errors can be partially attributed to the averaging kernels of the lower-resolution instruments (Figures 5.61 and 5.63). The errors from the methane retrievals are possibly due to uncertainties in the spectroscopy.

Retrieving ILS PHS and EAP parameters from SFIT2 significantly changes and improves the column comparisons of the stratospheric species for the lower-resolution instruments. This is shown in Figure 5.44. The ILS information is less important for the tropospheric species. Also, retrieving the SFIT2 PHS and EAP parameters as part of the

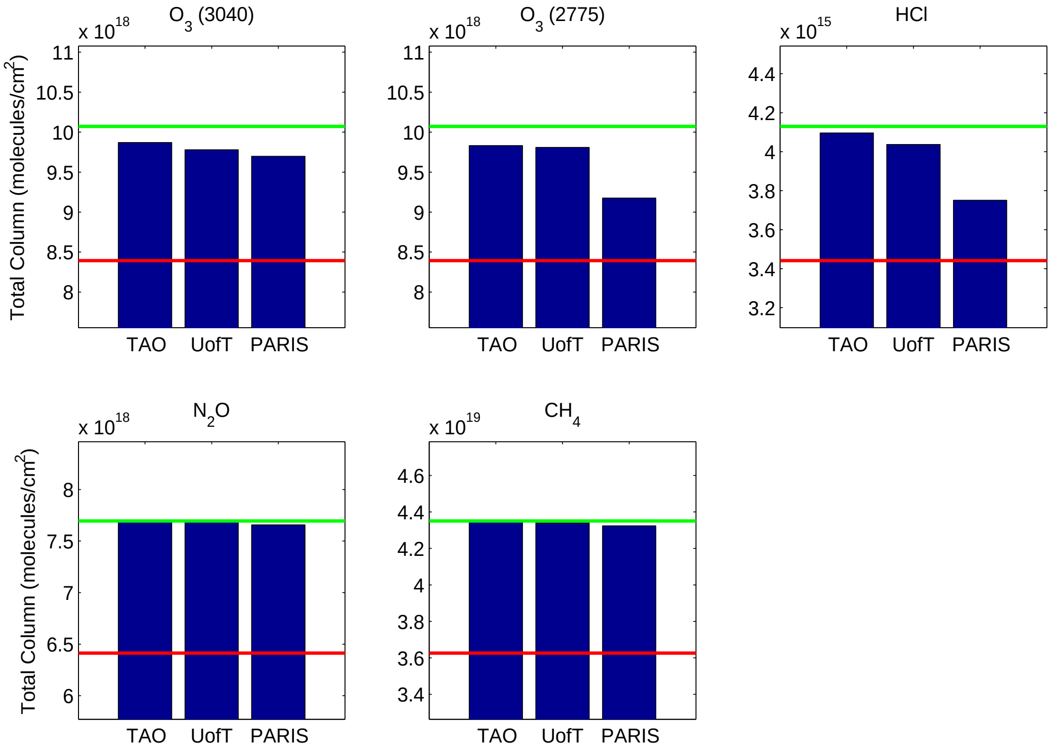

Figure 5.63: Total columns derived by applying the averaging kernels to a profile that is the *a priori* profile scaled up by 20% at each layer. The red lines indicate the *a priori* column amount and the green lines indicate the *a priori* column amount, scaled up by 20% (the “true” column value, in this case).

state vector can replace the LINEFIT ILS information for balloon-based measurements when retrieving the ILS from a gas cell is not feasible.

| Molecule | $O_3$ | | HCl | $N_2O$ | $CH_4$ |
|---|---|---|---|---|---|
| Microwindow | 3040 | 2775 | 2925 | 2482 | 2859 |
| PARIS-IR to TAO | 0.8 | **2.6** | **3.2** | 0.4 | 0.5 |
| U of T FTS to TAO | **3.3** | 0.7 | 1.7 | 0.4 | **2.3** |
| U of T FTS to PARIS-IR | **2.5** | **3.2** | 1.5 | 0.8 | **1.7** |
| Meier et al. [109, 2005] | 0.4<br>(3040) | | 0.7 | 0.1 | 0.2<br>(2904) |
| Griffith et al. [110, 2003] | 2.57<br>(3045.08-3045.38) | | 2.90 | 0.34 | 1.11<br>(2904) |
| Goldman et al. [108, 1999] | 1.5<br>(3045.08–3045.38) | | 1.6 | 1.1 | 0.2<br>(2904) |
| Paton-Walsh et al. [107, 1997] | N/A | | 0.5 | 1.0 | N/A |

Table 5.15: Percent differences of mean total column values from Figures 5.56–5.60 and results from previous intercomparisons. Bold PARIS-IR and U of T FTS percent differences indicate that the differences are significant to 95% by the Student's t-test (i.e. $t \geq 1.96$). The PARIS-IR and U of T FTS percent differences are from the TAO-FTS, for SZA >40 degrees. For the previous intercomparisons, brackets beneath the percent differences for each molecule indicate the microwindow retrieved, if it is different from Table 5.13. Here, for the Meier et al. [109], Griffith et al. [110], and Paton-Walsh et al. [107] papers, we cite mean percent differences between the two instruments over the duration of the intercomparison, whereas for Goldman et al. [108], we cite the maximum difference from the average of the three instruments involved for the November 11B data set.

# Chapter 6

# Summary

The MANTRA high-altitude balloon project is the unifying theme of this thesis. This project achieved three main things: first, a climatological description of turnaround, second, an electrical, mechanical and software overhaul of the U of T FTS and the results from MANTRA 2004, and third, an investigation of the effects of resolution on ground-based FTS measurements and assessment of the measurement capabilities of the U of T FTS.

An accurate prediction of stratospheric zonal wind turnaround is an important tool for a successful balloon campaign. Low stratospheric wind speeds allow for longer campaigns and for safer payload recoveries. The turnaround study was the first, and, to date, only climatological description and investigation of the predictability of late-summer turnaround. For this study, I initiated the project, processed the data and worked closely with the co-authors to elucidate the results. The study revealed that stratospheric zonal wind autocorrelations rapidly become statistically insignificant just before turnaround at the latitude of Vanscoy. This means that predicting turnaround over Vanscoy from zonal wind speeds earlier on in the summer is not possible, presumably because vertically-propagating Rossby waves eliminate the memory in any zonal wind anomalies just as turnaround occurs. This is an interesting result which has sparked further research about the dynamics of the stratosphere at this time of year. However, this result is not helpful for determining the optimal balloon launch date. The climatology of turnaround revealed that for every year between 1993 and 2002, sufficiently low wind speeds for a balloon launch at the latitude of Vanscoy were found from August 26 through September 5. This defines a useful launch window that should be valid well into the future. The MANTRA balloons have all been launched within or very close to this window. The 1998 launch was on August 24, the 2000 launch on August 29, the 2002 launch on September 3, and the 2004 launch on September 1.

The U of T FTS was successfully converted from a ground-based instrument into a robust instrument useful both on the ground and from high-altitude balloon platforms. The electrical system was removed and upgraded by Clive Midwinter and myself, retaining only the dynamic alignment system. I was responsible for designing and writing the software package, which controls the instrument, records housekeeping data and interferograms, and processes the interferograms into spectra. The renovation of the FTS was the first, to my knowledge, to retain the robust dynamic alignment system. Other attempts to update ABB Bomem DA-series instruments have involved removing all the electronics and substituting alternative dynamic alignment motor control.

The U of T FTS was on board the MANTRA 2002 payload prior to the bulk of the changes, and again on the MANTRA 2004 payload, where it recorded two spectra on each detector. Data from a full occultation would have been recorded if the payload's azimuth control had been functional. Neither of the other two FTS instruments on board the MANTRA 2004 payload recorded scientific data as a result of the communications loss and subsequent loss of payload pointing control. This shows that the software and hardware for the U of T FTS were well-designed for the balloon environment. This is the first Canadian FTS to have successfully flown on a balloon platform in ∼20 years.

The U of T FTS also recorded data on the ground during the MANTRA 2004 campaign. Total columns of ozone computed from the U of T FTS ground-based data were compared with those from the other ground-based instruments on-site. The total columns agree to within 7%. The MLS instrument on Aura had a number of overpasses during the MANTRA 2004 campaign, and partial column comparisons between the U of T FTS and MLS showed excellent agreement for $O_3$, CO, and $N_2O$, but not for HCl. MLS HCl agreements are also poor with the HALOE data: the reasons for this are still under investigation.

The ground-based intercomparison campaign held in Toronto in 2005 directly investigated the effect of spectral resolution on the retrieved total columns of $O_3$, HCl, $N_2O$ and $CH_4$—an effect that was previously unexamined. In order to properly validate satellite instruments, with different viewing geometries and instrument properties, we must first understand how well instruments that measure through the same atmospheric path can agree. Most satellite FTS instruments measure with lower resolution (ACE-FTS, MIPAS, ATMOS, etc.), and so understanding how reduced resolution affects the retrieval and what parameters most improve those retrievals is important.

The U of T FTS was compared with the TAO-FTS and PARIS-IR over four days of measurements[1]. It was previously noted that fully characterising instrument line shape information and using it as part of the forward model in SFIT2 is critical to properly retrieve stratospheric species such as $O_3$ and HCl, and somewhat less important for retrieving tropospheric species such as $N_2O$ and $CH_4$. This result was confirmed by our intercomparison, for which I was responsible for collecting and processing the U of T FTS data, comparing the data sets of the three instruments, and collaborating with the coauthors to draw conclusions from the results. The results show that it is even more crucial to include ILS information in the retrievals of stratospheric species for lower-resolution spectra. Further, the intercomparison study indicated that the lower-resolution instruments (PARIS-IR and the U of T FTS) cannot detect total columns of stratospheric species ($O_3$ and HCl) as accurately as the higher-resolution TAO-FTS can (up to ∼3% errors are seen). This low sensitivity to the stratospheric species is

---

[1] The U of T FTS and TAO-FTS also measured simultaneously over four months in the summer of 2005. A paper by Taylor et al. [121], which describes the comparison and explains the column amount discrepancies based on the different averaging kernels for the two instruments is currently in preparation.

directly attributable to the averaging kernels of the instruments. This is an important result, because it suggests that our retrieval method may not be capable of retrieving total columns of stratospheric species from lower-resolution ground-based spectra with an accuracy of better than 3%. It also highlights the importance of proper instrument characterization.

The study also revealed that calculating the phase error and effective apodization parameters as part of the SFIT2 atmospheric retrieval yielded comparable column results to defining the ILS parameters with gas cell measurements. Instrument line shapes for ground-based instruments do not change rapidly over time and so gas-cell measurements taken every few months suffice for proper ILS monitoring. Balloon-based FTS instrument line shapes, however, change much more rapidly, possibly even from spectrum to spectrum, and so gas-cell measurements made before and after a flight may not suffice for proper ILS monitoring. Since the SFIT2 phase error and effective apodization parameters are computed for each spectrum, this could be a useful method of monitoring the ILS changes from balloon-based measurements.

## 6.1 Suggested Future Work

### 6.1.1 U of T FTS

The U of T FTS is now a functional balloon and ground-based instrument. There are, however, a number of changes that would improve its functionality and data quality.

#### Solar tracking

A delta-tracker with a larger tracking range would have the advantage of being able to be used on the ground and on a balloon without additional optics. This would also make the FTS less dependent on payload azimuth control. A total lack of payload azimuth control will still result in data loss, but to a considerably lesser extent. Currently, I am

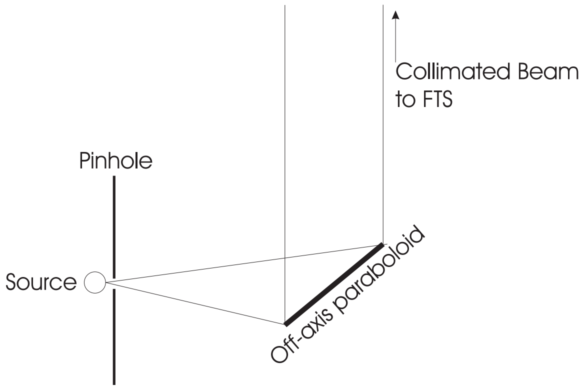

Figure 6.1: Blackbody plate.

working with Clive Midwinter to build a new suntracker, with software that computes the position of the sun and a camera that records images of the sun to perform fine adjustment to the calculated position.

### Detector Alignment

The detector alignment method must be improved. The current detector alignment mount has adjustment capability in three dimensions for both detectors, making the new system a vast improvement over the previous one. This facilitates more accurate, repeatable detector positioning. There are two things that currently inhibit proper detector alignment: the off-axis parabolic (OAP) mirror that focuses light onto the detectors, and the method of coupling blackbody radiation through a gas cell and into the FTS.

The current OAP is diamond-turned and has significant coma. Coma is an optical aberration in the mirror that causes the light at the focal point to possess a "tail" instead of a perfect, circular focus. This effect makes detector positioning difficult. The OAP ought to be replaced with a higher quality mirror.

In order to measure blackbody radiation through a gas cell, we replace the delta-tracker by a plate that couples blackbody radiation into the FTS (Figure 6.1). The plate has a pinhole placed directly in front of the blackbody source. The light is then collimated by an OAP and directed into the FTS. This is suboptimal. The standard NDACC HBr cell has only a 2 cm diameter window, which is too small to fill the FTS input window (which is 5 cm wide). When the cell is instead placed next to the pinhole, it increases significantly in temperature. Because spectral lines change shape with temperature, this is a significant source of error, especially since the temperature inside the cell cannot be accurately measured. The solution to this would be to either create a new gas cell that is large enough to be placed in the input aperture of the FTS, or to change the optical design of the blackbody-pinhole-OAP system. Using two OAPs with long focal lengths and placing the pinhole and HBr cell between them would allow for the cell to be placed in the focal plane of the beam without being near the blackbody source. Obtaining a blackbody with a measurable temperature would also be helpful.

The optical alignment of the FTS must be done iteratively. The detectors are adjusted to maximize the signal levels, and blackbody gas cell measurements are then recorded and analysed by LINEFIT or by another line shape calculation. The detectors are then adjusted further, and blackbody gas cell measurements are analysed again, until the best possible instrument line shape has been attained.

### Optical Components

A long-pass filter should be used between the detectors instead of a $CaF_2$ 50-50 beamsplitter to more efficiently separate the spectral regions of the two detectors. This would increase the signal-to-noise ratio of the spectra, because only the desired photons reach the detector. This will become especially important if the U of T FTS is required to measure $HNO_3$ or $ClONO_2$, two other molecules of importance to ozone depletion, which absorb outside of its current spectral range. The main FTS beamsplitter would have to be changed from $CaF_2$ to KBr, and the MCT detector would have to be replaced by one that can detect longer wavelengths.

We are currently only able to record the AC component from our detectors. We should record both AC and DC components from the detectors in the future. The

DC component will aid in the alignment procedure, since the DC levels at the MOPD increase as alignment is improved. The AC component cannot be as easily evaluated from an oscilloscope. The DC levels from the detector can also assist in estimating solar tracking precision. If the DC levels vary throughout a scan, this can indicate tracking errors, or the presence of clouds. In fact, dividing the interferogram by the DC signal can remove the influence of small clouds that pass through the solar beam during a scan.

### Noise Reduction

The interferograms of the U of T FTS are not photon-limited, as discussed in §4.5. The source of the extra noise in the spectra should be found. The first test should be to put a ripple attenuator module on the detector power supply to smooth out the high-frequency noise. This is a likely cause of the interferogram noise.

A second noise source is from the ADC converter. It should be replaced with 20-bit ADC to eliminate the need for gain changing. This would also ease interferogram processing as well.

### Timing Accuracy

Knowing the correct time on board the MANTRA 2004 balloon was a problem. BIOS clock times are notoriously unstable, and since retrievals are sensitive to the time, a better method of determining the correct time is necessary. Two possible solutions to this problem would be to use a GPS either as a time server or by recording a file with both GPS and computer time during the flight. The advantage to using a GPS as a time server is that it can be used for every instrument on board the payload, ensuring that all instruments are synchronized.

### 6.1.2 MLS Intercomparison

The HCl discrepancies between MLS and U of T FTS partial columns should be investigated further. Preliminary analysis has shown that the TAO-FTS also has a similar discrepancy with the MLS, but a more careful, long-term analysis must be attempted. The long-term analysis would preferably begin in August 2004 to ensure that the MLS performance has not changed throughout its lifetime. The discrepancies are interesting because the data from the HALOE instrument, which measures in the infrared, also disagree with MLS data in the same way, and the U of T FTS and TAO-FTS both use HALOE data for their *a priori* profiles. A complication lies in the fact that the MLS and ACE-FTS HCl profiles agree well, suggesting that the problem is not due to spectroscopic discrepancies between the microwave and the infrared [105].

### 6.1.3 Ballooning

Finally, I would like to stress the importance of a long-term Canadian balloon program that allows for more frequent launches with smaller payloads. Balloon campaigns are scientifically important in their own right, because they provide a platform for measuring various aspects of the atmosphere with very high vertical resolution. They also offer a unique opportunity to develop new space instrumentation. Balloon instruments are launched into a very similar environment to that of space, but with the opportunity to recover the instruments and improve on them for the next flight. This is not a luxury afforded to satellite instrument development. Further, the instruments that are developed for balloon platforms can be built in a shorter amount of time, with a lower cost, because they are not subject to the same rigours as space-qualified instrumentation. Balloon instrumentation, including scientific and support equipment, does require thorough testing prior to a balloon flight, but while this may minimize the risk of hardware failure during the balloon flight, it in no way eliminates the risk.

Smaller payloads and frequent launch opportunities would decrease the risk of the types of failures that afflicted the MANTRA 2004 campaign. A major challenge for the MANTRA campaigns was gondola pointing control—a problem that is made simpler with a lower payload mass. Launches every year, or, better, every six months, would allow for smaller payloads with fewer, carefully selected instruments, geared to answering focussed scientific questions. This would also allow for the timely re-flight of payloads that suffer from unforseen technical failures.

Suggested small balloon payloads would include a flight of the PARIS-IR and the Measurements of Atmospheric Extinction in the Stratosphere and Troposphere Retrieved by Occultation (MAESTRO) instrument that comprise the SCISAT-1 satellite [34]. These instruments should be launched with an ozone sonde for an ozone profile reference and a GPS for accurate time and location information. This small payload could be used for validating the SCISAT-1 satellite data, and may be able to address some of the questions arising from timing uncertainties on board the satellite. By flying an ozone sonde as well, the results would also investigate any biases in the PARIS-IR or MAESTRO ozone profiles.

A second suggestion for a small payload would be to fly the U of T FTS configured to measure $CO_2$. There has been considerable recent interest in the carbon budget, specifically in the amount of $CO_2$ that is in the atmosphere. There is a discrepancy between what is released into and what is found to remain in the atmosphere, and global $CO_2$ measurements are necessary to identify this sink. The Orbiting Carbon Observatory (OCO) satellite instrument aims to investigate this problem [122]. As a result, balloon measurements of $CO_2$ will be necessary for validation. The configuration of the U of T FTS would require replacing the germanium input filter and the detectors, since the best $CO_2$ absorption lines, from the perspective of minimal interfering species and line strength, are found in the near-infrared through to the visible. If an *in situ* $CO_2$ instrument were available, it would be a welcome addition to this payload.

# Bibliography

[1] D. J. Jacob. *Introduction to Atmospheric Chemistry.* Princeton University Press, 1999. ISBN 0-691-00185-5.

[2] J. T. Houghton, Y. Ding, D. J. Griggs, M. Noguer, P. J. van der Linden, X. D. K., and Maskell. *Climate Change 2001: The Scientific Basis.*

[3] WMO. Scientific Assessment of Ozone Depletion: 2002. Technical Report 47, WMO Global Ozone Research and Monitoring Project, Geneva, 2003.

[4] K. Strong, G. Bailak, D. Barton, M. R. Bassford, R. D. Blatherwick, S. Brown, D. Chartrand, J. Davies, J. R. Drummond, P. F. Fogal, E. Forsberg, R. Hall, A. Jofre, J. Kaminski, J. Kosters, C. Laurin, J. C. Mcconnell, C. T. Mcelroy, K. Menzies, C. Midwinter, F. J. Murcray, R. J. Olson, B. M. Quine, Y. Rochon, V. Savastiouk, B. Solheim, D. Sommerfeldt, A. Ullberg, S. Werchohlad, and D. Wunch. MANTRA — A balloon mission to study the odd-nitrogen budget of the stratosphere. *Atmos. Ocean*, 43(4):283–299, December 2005.

[5] D. W. Fahey, R. S. Gao, L. A. Del Negro, E. R. Keim, S. R. Kawa, R. J. Salawitch, P. O. Wennberg, T. F. Hanisco, E. J. Lanzendorf, K. K. Perkins, S. A. Lloyd, W. H. Swartz, M. H. Proffitt, J. J. Margitan, J. C. Wilson, R. M. Stimpfle, R. C. Cohen, C. T. McElroy, C. R. Webster, M. Loewenstein, J. W. Elkins, and T. P. Bui. Ozone destruction and production rates between spring and autumn in the

Arctic stratosphere. *Geophys. Res. Lett.*, 27:2605–2608, September 2000. doi: 10.1029/2000GL011404.

[6] R. Zander, G. Roland, L. Delbouille, A. Sauval, C. B. Farmer, and R. H. Norton. Column abundance and the long-term trend of hydrogen chloride (HCl) above the Jungfraujoch Station. *J. Atmos. Chem.*, 5(4):395–404, 1987.

[7] M. B. McElroy, R. J. Salawitch, and K. Minschwaner. The changing stratosphere. *Planet. Space Sci.*, 40:373–401, 1992.

[8] J. B. Liley, P. V. Johnston, R. L. McKenzie, A. J. Thomas, and I. S. Boyd. Stratospheric $NO_2$ variations from a long time series at Lauder, New Zealand. *J. Geophys. Res.*, 105(D9):11633–11640, 2000.

[9] M. de Mazière, M. van Roozendael, C. Hermans, P. C. Simon, P. Demoulin, G. Roland, and R. Zander. Quantitative evaluation of the post-Pinatubo $NO_2$ reduction and recovery, based on 10 years of FTIR and UV-visible spectroscopic measurements at the Jungfraujoch. *J. Geophys. Res.*, 103(D9):10849–10858, 1998.

[10] C. A. McLinden, S. C. Olsen, M. J. Prather, and J. B. Liley. Understanding trends in stratospheric $NO_y$ and $NO_2$. *J. Geophys. Res.*, 106:27787–27794, November 2001. doi: 10.1029/2000JD000100.

[11] W. J. Randel, F. Wu, and J. M. Russell. Space-time patterns of trends in stratospheric constituents derived from UARS measurements. *J. Geophys. Res.*, 104(D3):3711–3728, 1999.

[12] F. T. Barath, M. C. Chavez, R. E. Cofield, D. A. Flower, M. A. Frerking, M. B. Gram, W. M. Harris, J. R. Holden, R. F. Jarnot, and W. G. Kloezeman. The Upper Atmosphere Research Satellite microwave limb sounder instrument. *J. Geophys. Res.*, 98(D6):10–751, 1993.

[13] W. Evans, J. Kerr, D. Wardle, J. McConnell, B. Ridley, and H. Schiff. Intercomparison of NO, $NO_2$, and $HNO_3$ measurements with photochemical theory. *Atmosphere*, 14:189–98, 1976.

[14] W. F. J. Evans, J. B. Kerr, C. T. McElroy, R. S. Obrien, D. I. Wardle, and B. A. Ridley. The odd nitrogen mixing ratio in the stratosphere. *Geophys. Res. Lett.*, 4: 235–238, 1977.

[15] W. F. J. Evans, C. T. McElroy, J. B. Kerr, and J. C. McConnell. Simulation of nitrogen constituent measurements from the August 28, 1976, Stratoprobe III flight. *J. Geophys. Res.*, 86(C12):12066–12070, 1981.

[16] W. F. J. Evans, C. T. McElroy, J. B. Kerr, and J. C. McConnell. Simulation of the October 23, 1980 Stratoprobe flight. *Geophys. Res. Lett.*, 9:223–226, 1982.

[17] W. F. J. Evans, J. V. Kerr, C. T. McElroy, R. S. O'Brien, and J. C. McConnell. Measurements of $NO_2$ and $HNO_3$ during a stratospheric warming at 54 in February 1979. *Geophys. Res. Lett.*, 9(4):493–496, 1982.

[18] W. F. J. Evans, C. T. McElroy, and I. E. Galbally. The conversion of $N_2O_5$ to $HNO_3$ at high latitudes in winter. *Geophys. Res. Lett.*, 12:825–828, 1985.

[19] J. B. Kerr and C. T. McElroy. Measurement of atmospheric nitrogen dioxide from the AES stratospheric balloon program. *Atmosphere*, 14:166–171, 1976.

[20] J. B. Kerr, C. T. McElroy, and W. F. J. Evans. Mid-latitude summertime measurements of stratospheric $NO_2$. *Can. J. Phys.*, 60:196–200, 1982.

[21] B. A. Ridley, S. H. Luu, D. R. Hastie, H. I. Schiff, J. C. McConnell, W. F. J. Evans, C. T. McElroy, J. B. Kerr, H. Fast, and R. O'Brien. Stratospheric odd nitrogen-Measurements of $HNO_3$, NO, $NO_2$, and $O_3$ near 54 deg N in winter. *J. Geophys. Res.*, 89:4797–4820, 1984.

[22] J. D. Haigh and J. A. Pyle. Ozone perturbation experiments in a two-dimensional circulation model. *Quart. J. Roy. Meteorol. Soc.*, 108(457):551–574, 1982.

[23] IPCC/TEAP. Safeguarding the Ozone Layer and the Global Climate System. Special report, Intergovernmental Panel on Climate Change, 2005. Prepared by Working Groups I and III of the Intergovernmental Panel on Climate change and the Technical and Economic Assessment Panel.

[24] C. N. Banwell. *Fundamentals of Molecular Spectroscopy*. McGraw-Hill Book Company, London, 2nd edition, 1972.

[25] G. L. Stephens. *Remote Sensing of the Lower Atmosphere: An Introduction*. Oxford University Press, 1994. ISBN 0-19-508188-9.

[26] D. G. Andrews, J. R. Holton, and C. B. Leovy. *Middle Atmosphere Dynamics*, volume 40 of *International Geophysics Series*. Academic Press, Toronto, 1987. ISBN 0–12–058576–6.

[27] J. T. Houghton. *The Physics of Atmospheres*. Cambridge University Press, 2 edition, 1997. ISBN 0-521-33956-1.

[28] J. Notholt, G. Toon, N. Jones, D. Griffith, and T. Warneke. Spectral line finding program for atmospheric remote sensing using full radiation transfer. *J. Quant. Spectrosc. Radiat. Transfer*, 97(1):112–125, 2006.

[29] K.-N. Liou. *An Introduction to Atmospheric Radiation*, volume 26 of *International Geophysics Series*. Academic Press, 1980. ISBN 0–12–451450–2.

[30] X. Huang and Y. L. Yung. A Common Misunderstanding about the Voigt Line Profile. *J. Atmos. Sci.*, 61(13):1630–1632, 2004.

[31] L. S. Rothman, D. Jacquemart, A. Barbe, D. C. Benner, M. Birk, L. R. Brown, M. R. Carleer, C. C. Jr., K. Chance, L. H. Coudert, V. Dana, V. M. Devi, J.-M.

Flaud, R. Gamache, A. Goldman, J.-M. Hartmann, K. W. Jucks, A. G. Maki, J.-Y. Mandin, S. T. Massie, J. Orphal, A. Perrin, C. Rinsland, M. A. H. Smith, J. Tennyson, R. N. Tolchenov, R. A. Toth, J. V. Auwera, P. Varanasi, and G. Wagner. The HITRAN 2004 molecular spectroscopic database. *J. Quant. Spectrosc. Radiat. Transfer*, 96:139–204, 2005.

[32] N. Jacquinet-Husson, N. A. Scott, A. Chédin, K. Garceran, R. Armante, A. A. Chursin, A. Barbe, M. Birk, L. R. Brown, C. Camy-Peyret, C. Claveau, C. Clerbaux, P. F. Coheur, V. Dana, L. Daumont, M. R. Debacker-Barilly, J. M. Flaud, A. Goldman, A. Hamdouni, M. Hess, D. Jacquemart, P. Köpke, J. Y. Mandin, S. Massie, S. Mikhailenko, V. Nemtchinov, A. Nikitin, D. Newnham, A. Perrin, V. I. Perevalov, L. Regalia-Jarlot, A. Rublev, F. Schreier, I. Schult, K. M. Smith, S. A. Tashkun, J. L. Teffo, R. A. Toth, V. G. Tyuterev, J. Vander Auwera, P. Varanasi, and G. Wagner. The 2003 edition of the GEISA/IASI spectroscopic database. *J. Quant. Spectrosc. Radiat. Transfer*, 95:429–467, November 2005.

[33] P. F. Fogal, R. D. Blatherwick, F. J. Murcray, and J. R. Olson. Infra-red FTS measurements of $CH_4$, $N_2O$, $O_3$, $HNO_3$, HCl, CFC-11 and CFC-12 from the MANTRA balloon campaign. *Atmos. Ocean*, 43(4):351–359, 2005.

[34] P. F. Bernath, C. T. McElroy, M. C. Abrams, C. D. Boone, M. Butler, C. Camy-Peyret, M. Carleer, C. Clerbaux, P. F. Coheur, R. Colin, P. DeCola, M. DeMazière, J. R. Drummond, D. Dufour, W. F. J. Evans, H. Fast, D. Fussen, K. Gilbert, D. E. Jennings, E. J. Llewellyn, R. P. Lowe, E. Mahieu, J. C. McConnel, M. McHugh, S. D. McLeod, R. Michaud, C. Midwinter, R. Nassar, F. Nichitiu, C. Nowlan, C. P. Rinsland, Y. J. Rochon, N. Rowlands, K. Semeniuk, P. Simon, R. Skelton, J. J. Sloan, M. A. Soucy, K. Strong, P. Tremblay, D. Turnbull, K. A. Walker, I. Walkty, D. A. Wardle, V. Wehrle, R. Zander, and J. Zou. Atmospheric Chemistry

Experiment (ACE): Mission overview. *Geophys. Res. Lett.*, 32:L15S01, 2005. doi: 10.1029/2005GL022386.

[35] D. Fu, K. A. Walker, K. Sung, C. D. Boone, M. A. Soucy, and P. F. Bernath. The portable atmospheric research interferometric spectrometer for the infrared, PARIS-IR. *J. Quant. Spectrosc. Radiat. Transfer*, 2006.

[36] M. R. Schoeberl, A. R. Douglass, E. Hilsenrath, M. Luce, J. Bamett, R. Beer, J. Waters, J. Gille, P. F. Levelt, and P. DeCola. The EOS Aura Mission. In *Geoscience and Remote Sensing Symposium*, volume 1, pages 227–232. IGARSS '01. IEEE 2001 International, 2001.

[37] J. W. Waters, L. Froidevaux, R. S. Harwood, R. F. Jarnot, H. M. Pickett, W. G. Read, P. H. Siegel, R. E. Cofield, M. J. Filipiak, D. A. Flower, J. R. Holden, G. K. Lau, N. J. Livesey, G. L. Manney, H. C. Pumphrey, M. L. Santee, D. L. Wu, D. T. Cuddy, R. R. Lay, M. S. Loo, V. S. Perun, M. J. Schwartz, P. C. Stek, R. P. Thurstans, M. A. Boyles, K. M. Chandra, M. C. Chavez, G.-S. Chen, B. V. Chudasama, R. Dodge, R. A. Fuller, M. A. Girard, J. H. Jiang, Y. Jiang, B. W. Knosp, R. C. LaBelle, J. C. Lam, K. A. Lee, D. Miller, J. E. Oswald, N. C. Patel, D. M. Pukala, O. Quintero, D. M. Scaff, W. V. Snyder, M. C. Tope, P. A. Wagner, and M. J. Walch. The Earth Observing System Microwave Limb Sounder (EOS MLS) on the Aura satellite. *IEEE Trans. Geosci. Remote Sens.*, 2005.

[38] D. Wunch, M. P. Tingley, T. G. Shepherd, J. R. Drummond, G. W. K. Moore, and K. Strong. Climatology and Predictability of the Late Summer Stratospheric Zonal Wind Turnaround over Vanscoy, Saskatchewan. *Atmos. Ocean*, 43(4):301–313, December 2005.

[39] D. Wunch, C. Midwinter, J. R. Drummond, C. T. McElroy, and A.-F. Bagès. The

University of Toronto's Balloon-Borne Fourier Transform Spectrometer. *Rev. Sci. Inst.*, 77(9):093104, September 2006.

[40] D. Wunch, J. R. Taylor, D. Fu, P. Bernath, J. R. Drummond, C. Midwinter, K. Strong, and K. A. Walker. Simultaneous ground-based observations of $O_3$, HCl, $N_2O$ and $CH_4$ over Toronto by three FTIRs with different resolutions. *Atmospheric Chemistry and Physics Discussions*, 6:10883–10928, October 2006.

[41] V. E. Fioletov and T. G. Shepherd. Seasonal persistence of midlatitude total ozone anomalies. *Geophys. Res. Lett.*, 30, 2003. 10.1029/2002GL016739.

[42] B. Cushman-Roisin. *Introduction to Geophysical Fluid Dynamics.* Prentice Hall, Inc., 1994. ISBN 0-13-353301-8.

[43] T. G. Shepherd. Large-Scale Atmospheric Dynamics for Atmospheric Chemists. *Chem. Rev.*, 103(12):4509–4531, 2003.

[44] E. Kalnay, M. Kanamitsu, R. Kistler, W. Collins, D. Deaven, L. Gandin, M. Iredell, S. Saha, G. White, J. Woollen, Y. Zhu, A. Leetmaa, B. Reynolds, M. Chelliah, W. Ebisuzaki, W. Higgins, J. Janowiak, K. C. Mo, C. Ropelewski, J. Wang, R. Jenne, and D. Joseph. The NCEP/NCAR 40-year reanalysis project. *Bull. Amer. Meteorol. Soc.*, 77:437–471, 1996.

[45] R. Swinbank and A. O'Neill. A stratosphere-troposphere data assimilation system. *Mon. Weather Rev.*, 122:686–702, 1994.

[46] A. C. Lorenc, S. P. Ballard, R. S. Bell, N. B. Ingleby, P. L. F. Andrews, D. M. Barker, J. R. Bray, A. M. Clayton, T. Dalby, D. Li, T. J. Payne, and F. W. Saunders. The Met Office global 3-dimensional variational data assimilation scheme. *Quart. J. Roy. Meteorol. Soc.*, 126:2992–3912, 2000.

[47] S. R. Beagley, J. de Grandpré, J. N. Koshyk, N. A. McFarlane, and T. G. Shepherd. Radiative-dynamical climatology of the first-generation Canadian Middle Atmosphere Model. *Atmos. Ocean*, 35:293–331, 1997.

[48] J. de Grandpré, S. R. Beagley, V. I. Fomichev, E. Griffioen, J. C. McConnell, A. S. Medvedev, and T. G. Shepherd. Ozone climatology using interactive chemistry: Results from the Canadian Middle Atmosphere Model. *J. Geophys. Res.*, 105: 26475–26491, 2000.

[49] J. Austin, D. Shindell, S. R. Beagley, C. Brühl, M. Dameris, E. Manzini, T. Nagashima, P. Newman, S. Pawson, G. Pitari, E. Rozanov, C. Schnadt, and T. G. Shepherd. Uncertainties and assessments of chemistry-climate models of the stratosphere. *Atmos. Chem. Phys.*, 3:1–27, 2003.

[50] R. Kistler, E. Kalnay, W. Collins, S. Saha, G. White, J. Woollen, M. C. W. Ebisuzaki, M. Kanamitsu, V. K. H. van den Dool, R. Jenne, and M. Fiorino. The NCEP/NCAR 50-year reanalysis: monthly means CD-ROM and documentation. *Bull. Amer. Meteorol. Soc.*, 82:247–267, 2001.

[51] M. de Mazière. Atmospheric Observations in the Perspective of Changing Climate and Environment, and the Synergy Between Ground-Based, Airborne and Space-Based Measurements. *LNP Vol. 607: Exploring the Atmosphere by Remote Sensing Techniques*, 607:14–49, 2003.

[52] C. P. Rinsland, E. Mahieu, R. Zander, N. B. Jones, M. P. Chipperfield, A. Goldman, J. Anderson, J. M. Russell, P. Demoulin, J. Notholt, G. C. Toon, J.-F. Blavier, B. Sen, R. Sussmann, S. W. Wood, A. Meier, D. W. T. Griffith, L. S. Chiou, F. J. Murcray, T. M. Stephen, F. Hase, S. Mikuteit, A. Schulz, and T. Blumenstock. Long-term trends of inorganic chlorine from ground-based infrared solar spectra:

Past increases and evidence for stabilization. *J. Geophys. Res.*, 108(D8):10, April 2003. doi: 10.1029/2002JD003001.

[53] J. Notholt, G. Toon, F. Stordal, S. Solberg, N. Schmidbauer, E. Becker, A. Meier, and B. Sen. Seasonal variations of atmospheric trace gases in the high Arctic at 79°N. *J. Geophys. Res.*, 102:12855–12862, 1997. doi: 10.1029/97JD00337.

[54] C. P. Rinsland, A. Goldman, B. J. Connor, T. M. Stephen, N. B. Jones, S. W. Wood, F. J. Murcray, S. J. David, R. D. Blatherwick, R. Zander, E. Mahieu, and P. Demoulin. Correlation relationships of stratospheric molecular constituents from high spectral resolution, ground-based infrared solar absorption spectra. *J. Geophys. Res.*, 105:14637–14652, 2000. doi: 10.1029/2000JD900139.

[55] M. Trolier, J. W. C. White, P. P. Tans, K. A. Masarie, and P. A. Gemery. Monitoring the isotopic composition of atmospheric $CO_2$: Measurements from the NOAA Global Air Sampling Network. *J. Geophys. Res.*, 101:25897–25916, 1996. doi: 10.1029/96JD02363.

[56] D. W. T. Griffith, I. Jamie, M. Esler, S. R. Wilson, S. D. Parkes, C. Waring, and G. W. Bryant. Real-time field measurements of stable isotopes in water and $CO_2$ by Fourier transform infrared spectrometry. *Isot. Environ. Health Stud.*, 42(1): 9–20, 2006.

[57] C. Camy-Peyret. Balloon-borne infrared Fourier transform spectrscopy for measurements of atmospheric trace species. *Spectrochim. Acta*, 51A(7):1143–1152, 1995.

[58] A. Goldman, A. Barbe, V. G. Tyuterev, M. R. De Backer-Barilly, J. W. Hannigan, M. T. Coffey, C. P. Rinsland, and R. D. Blatherwick. Identification of enhanced absorption by $^{16}O_3$ lines around $5\mu m$ in high-resolution FTIR solar spectra. *J. Quant. Spectrosc. Radiat. Transfer*, 96:241–250, December 2005.

[59] C. B. Farmer, O. F. Raper, and R. Norton. Spectroscopic detection and vertical distribution of HCl in the troposphere and lower stratosphere. *Geophys. Res. Lett.*, 3:13–16, 1976.

[60] C. P. Rinsland, R. E. Boughner, J. C. Larsen, A. Goldman, F. J. Murcray, and D. G. Murcray. Stratospheric NO and $NO_2$ profiles at sunset from analysis of high-resolution balloon-borne infrared solar absorption spectra obtained at 33 deg N and calculations with a time-dependent photochemical model. Technical report, August 1984.

[61] A. Goldman, J. R. Gillis, F. J. Murcray, D. G. Murcray, and C. P. Rinsland. Stratospheric $HNO_3$ quantification from line-by-line nonlinear least-squares analysis of high-resolution balloon-borne solar absorption spectra in the 870$\text{cm}^{-1}$ region. *Appl. Opt.*, 19:3252–3255, 1984.

[62] C. P. Rinsland, A. Goldman, F. J. Murcray, D. G. Murcray, M. A. H. Smith, R. K. Seals, Jr., J. C. Larsen, and P. L. Rinsland. Stratospheric N2O mixing ratio profile from high-resolution balloon-borne solar absorption spectra and laboratory spectra near 1880$\text{cm}^{-1}$. *Appl. Opt.*, 23:4351–4355, December 1982.

[63] A. Kleinböhl, H. Bremer, M. von König, H. Küllmann, K. F. Künzi, A. P. H. Goede, E. V. Browell, W. B. Grant, G. C. Toon, T. Blumenstock, B. Galle, B.-M. Sinnhuber, and S. Davies. Vortexwide denitrification of the Arctic polar stratosphere in winter 1999/2000 determined by remote observations. *J. Geophys. Res.*, 108(D5): 8305, 2003. doi: 10.1029/2001JD001042.

[64] P. R. Griffiths and J. A. de Haseth. *Fourier Transform Infrared Spectrometry*, volume 83 of *Chemical Analysis: A series of monographs on analytical chemistry and its applications*. John Wiley & Sons, 1986. ISBN 0-471-09902-3.

[65] C. J. H. Bernardo. *Measurement of Instrument Line Shape Functions of High-Resolution FTIR Spectrometers and their Application to the Analysis of Spectra.* PhD thesis, University of Wollongong, 2001.

[66] S. P. Davis, M. C. Abrams, and J. W. Brault. *Fourier Transform Spectrometry.* Academic Press, 2001. ISBN 0-12-042510-6.

[67] J. Chamberlain. *The Principles of Interferometric Spectroscopy.* John Wiley & Sons, 1979. ISBN 0-471-99719-6.

[68] R. J. Bell. *Introductory Fourier Transform Spectroscopy.* Academic Press, Inc., 1972.

[69] G. Guelachvili. Distortions in Fourier spectra and diagnosis. In G. A. Vanasse, editor, *Spectrometric Techniques*, volume 2. Academic Press, New York, 1981.

[70] J. W. Cooley and J. W. Tukey. An Algorithm for the Machine Calculation of Complex Fourier Series. *Mathematics of Computation*, pages 297–301, 1964.

[71] W. L. Briggs and V. E. Henson. *The DFT: An Owner's Manual for the Discrete Fourier Transform.* Society for Industrial and Applied Mathematics, 1995. ISBN 0-89871-342-0.

[72] P. Raspollini, P. Ade, B. Carli, and M. Ridolfi. Correction of instrument line-shape distortions in Fourier transform spectroscopy. *Appl. Opt.*, 37(17):3698–3704, June 1998.

[73] M. L. Forman, W. H. Steel, and G. A. Vanasse. Correction of Asymmetric Interferograms obtained in Fourier Spectroscopy. *J. Opt. Soc. Amer.*, 56(1):5–10, Jan 1966.

[74] F. Hase, T. Blumenstock, and C. Paton-Walsh. Analysis of the instrumental line

shape of high-resolution Fourier transform IR spectrometers with gas cell measurements and new retrieval software. *Appl. Opt.*, 38(15):3417–3422, May 1999.

[75] J. Kauppinen and P. Saarinen. Line-shape distortions in misaligned cube corner interferometers. *Appl. Opt.*, 31(1):69–74, January 1992.

[76] P. Saarinen and J. Kauppinen. Spectral line-shape distortions in Michelson interferometers due to off-focus radiation source. *Appl. Opt.*, 31(13):2353–2359, May 1992.

[77] *DA5 Spectroradiometer User's Guide.* ABB Bomem Inc., 585, boul. Charest Est, suite 300, Québec, QC, CANADA G1K 9H4, 2-0 edition, November 2000. IMZ9707.

[78] *Balloon-Borne and Air-Borne Interferometer System Model BBDA 2.01-1: Operation and Service Manual.* Bomem, Inc., March 1980.

[79] F. J. Murcray, J. J. Kosters, R. D. Blatherwick, J. Olson, and D. G. Murcray. High resolution solar spectrometer system for measuring atmospheric constituents. *Appl. Opt.*, 29(10):1520–1525, April 1990.

[80] B. M. Quine, K. Strong, A. Wiacek, D. Wunch, J. A. Anstey, and J. R. Drummond. Scanning the Earth's Limb from a High-Altitude Balloon: the Development and Flight of a New Balloon-Based Pointing System. *J. Atmos. Ocean. Technol.*, 19: 618–632, May 2002.

[81] T. Hawat, C. Camy-Peyret, and R. Torguet. Suntracker for atmospheric remote sensing. *Opt. Eng.*, 37(5):1633–1642, May 1998.

[82] C. D. Rodgers. *Inverse Methods for Atmospheric Sounding: Theory and Practice*, volume 2 of *Series on Atmospheric, Oceanic and Planetary Physics.* World Scientific Co. Pte. Ltd., 2000. ISBN 981-02-2740-X.

[83] C. D. Rodgers and B. J. Connor. Intercomparison of remote sounding instruments. *J. Geophys. Res.*, 108(D3):4116, February 2003. doi: 10.1029/2002JD002299.

[84] F. Hase, J. W. Hannigan, M. T. Coffey, A. Goldman, M. Höpfner, N. B. Jones, C. P. Rinsland, and S. W. Wood. Intercomparison of retrieval codes used for the analysis of high-resolution, ground-based FTIR measurements. *J. Quant. Spectrosc. Radiat. Transfer*, 87:25–52, 2004.

[85] B. J. Connor, N. B. Jones, S. W. Wood, J. G. Keys, C. P. Rinsland, and F. J. Murcray. Retrieval of HCl and $HNO_3$ profiles from ground-based FTIR data using SFIT2. In R. Bojkov and G. Visconti, editors, *Proceedings of the XVIII Quadrennial Ozone Symposium*, pages 485–488, L'Aquila, Italy, 1998. Parco Scientifico e Technologico d'Abruzzio.

[86] N. S. Pougatchev, B. J. Connor, and C. P. Rinsland. Infrared measurements of the ozone vertical distribution above Kitt Peak. *J. Geophys. Res.*, 100:16689–16698, 1995. doi: 10.1029/95JD01296.

[87] C. P. Rinsland, M. A. H. Smith, P. L. Rinsland, A. Goldman, J. W. Brault, and G. Stokes. Ground-based infrared spectroscopic measurements of atmospheric hydrogen cyanide. *J. Geophys. Res.*, 87:11119–11125, 1982.

[88] R. D. McPherson, K. H. Bergman, R. E. Kistler, G. E. Rasch, and D. S. Gordon. The NMC operational global data assimilation system. *Mon. Weather Rev.*, 107: 1445–1461.

[89] M. Schoeberl, P. Newman, R. N. Nagatani, and L. Lait. Goddard Automailer — NASA Goddard Space Flight Center Code 916. science@hyperion.gsfc.nasa.gov.

[90] W. O. Gallery, F. X. Kneizys, and S. A. Clough. Air mass computer program for atmospheric transmittance/radiance calculation: FSCATM. *AFGL-TR-0208 Environmental Research papers*, March 1983.

[91] A. Meier, A. Goldman, P. S. Manning, T. M. Stephen, C. P. Rinsland, N. B. Jones, and S. W. Wood. Improvements to air mass calculations for ground-based infrared measurements. *J. Quant. Spectrosc. Radiat. Transfer*, 83:109–113, 2004.

[92] A. Wiacek. *First Trace Gas Measurements Using Fourier Transform Infrared Solar Absorption Spectroscopy at the University of Toronto Atmospheric Observatory.* PhD thesis, University of Toronto, 2006.

[93] A. Wiacek, J. R. Taylor, K. Strong, R. Saari, T. E. Kerzenmacher, N. B. Jones, and D. W. T. Griffith. Ground-based solar absorption FTIR spectroscopy: a novel optical design instrument at a new NDSC complementary station, characterization of retrievals and first results. *J. Atmos. Ocean. Technol.*, in press.

[94] J. M. Russell, L. L. Gordley, L. Deaver, R. Thompson, and J. H. Park. An overview of the halogen occultation experiment (HALOE) and preliminary results. *Adv. Space Res.*, 14:9–13, 1994.

[95] B. Carli, D. Alpaslan, M. Carlotti, E. Castelli, S. Ceccherini, B. M. Dinelli, A. Dudhia, J. M. Flaud, M. Hoepfner, V. Jay, L. Magnani, H. Oelhaf, V. Payne, C. Piccolo, M. Prosperi, P. Raspollini, J. Remedios, M. Ridolfi, and R. Spang. First results of MIPAS/ENVISAT with operational level 2 code. *Adv. Space Res.*, 33:1012–1019, 2004.

[96] G. C. Toon. The JPL MkIV interferometer. *Optics & Photonics News*, 2(10):19–21, 1991.

[97] M. T. Coffey, A. Goldman, J. W. Hannigan, W. G. Mankin, W. G. Schoenfeld, C. P. Rinsland, C. Bernardo, and D. W. T. Griffith. Improved vibration-rotation (0-1) HBr line parameters for validating high resolution infrared atmospheric spectra measurements. *J. Quant. Spectrosc. Radiat. Transfer*, 60:863–867, 1998.

[98] F. T. Barath, M. C. Chavez, R. E. Cofield, D. A. Flower, M. A. Frerking, M. B. Gram, W. M. Harris, J. R. Holden, R. F. Jarnot, and W. G. Kloezeman. The Upper Atmosphere Research Satellite microwave limb sounder instrument. *J. Geophys. Res.*, 98:10751, June 1993.

[99] M. R. Bassford, K. Strong, C. A. McLinden, and C. T. McElroy. Ground-based measurements of ozone and $NO_2$ during MANTRA 1998 using a zenith-sky spectrometer. *Atmos. Ocean*, 43(4):325–338, 2005.

[100] J. Pommereau and F. Goutail. $O_3$ and $NO_2$ ground-based measurements by visible spectrometry during Arctic winter and spring 1988. *Geophys. Res. Lett.*, 15:891–894, 1988.

[101] C. T. McElroy. A spectroradiometer for the measurement of direct and scattered solar irradiance from on-board the NASA ER-2 high-altitude research aircraft. *Geophys. Res. Lett.*, 22:1361–1364, 1995. doi: 10.1029/95GL01391.

[102] M. Schneider. *Continuous Observations of Atmospheric Trace Gases by Ground-based FTIR Spectroscopy and Izaña Observatory, Tenerife Island.* PhD thesis, Institut für Meteorologie und Klimaforschung, May 2002.

[103] T. G. Kyle and R. Blatherwick. Smearing of interferograms in Fourier transform spectroscopy. *Appl. Opt.*, 23(2):261–263, 1984.

[104] N. J. Livesey, W. G. Read, M. J. Filipiak, L. Froidevaux, R. S. Harwood, J. H. Jiang, C. Jimenez, H. M. Pickett, H. C. Pumphrey, M. L. Santee, M. J. Schwartz, J. W. Waters, and D. L. Wu. Earth Observing System Microwave Limb Sounder Version 1.5 Level 2 data quality and description document. Technical report, Jet Propulsion Laboratory, 2005.

[105] L. Froidevaux, N. J. Livesey, W. G. Read, Y. B. Jiang, C. C. Jimenez, M. J. Filipiak, M. J. Schwartz, M. L. Santee, H. C. Pumphrey, J. H. Jiang, et al. Early

validation analyses of atmospheric profiles from EOS MLS on the Aura satellite. *IEEE Trans. Geosci. Remote Sens.*, 44(5), May 2006.

[106] L. S. Rothman, N. Jacquinet-Husson, C. Boulet, and A. M. Perrin. History and future of the molecular spectroscopic databases. *Comptes rendus. Physique*, 6(8): 897–907, 2005.

[107] C. Paton-Walsh, W. Bell, T. Gardiner, N. Swann, P. Woods, J. Notholt, H. Schütt, B. Galle, W. Arlander, and J. Mellqvist. An uncertainty budget for ground-based Fourier transform infrared column measurements of HCl, HF, $N_2O$ and $HNO_3$ deduced from results of side-by-side instrument intercomparisons. *J. Geophys. Res.*, 102(D7):8867–8873, April 1997.

[108] A. Goldman, C. Paton-Walsh, W. Bell, G. C. Toon, J.-F. Blavier, B. Sen, M. T. Coffey, J. W. Hannigan, and W. G. Mankin. Network for the Detection of Stratospheric Change Fourier transform infrared intercomparison at Table Mountain Facility, November 1996. *J. Geophys. Res.*, 104:30481–30503, 1999.

[109] A. Meier, C. Paton-Walsh, W. Bell, T. Blumenstock, F. Hase, A. Goldman, A. Steen, R. Kift, P. Woods, and Y. Kondo. Evidence of reduced measurement uncertainties from an FTIR instrument intercomparison at Kiruna, Sweden. *J. Quant. Spectrosc. Radiat. Transfer*, 96:75–84, 2005.

[110] D. W. T. Griffith, N. B. Jones, B. McNamara, C. Paton-Walsh, W. Bell, and C. Bernardo. Intercomparison of NDSC ground-based solar FTIR measurements of atmospheric gases at Lauder, New Zealand. *J. Atmos. Ocean. Technol.*, 20: 1138–1153, 2003.

[111] M. J. Kurylo and R. J. Zander. The NDSC – Its status after ten years of operation. In *Proceedings of XIX Quadrennial Ozone Symposium, Hokkaido University, Sapporo, Japan*, pages 167–168, 2000.

[112] E. Mahieu, R. Zander, P. Duchatelet, J. W. Hannigan, M. T. Coffey, S. Mikuteit, F. Hase, T. Blumenstock, A. Wiacek, K. Strong, J. R. Taylor, R. Mittermeier, H. Fast, C. D. Boone, S. D. McLeod, K. A. Walker, P. F. Bernath, and C. P. Rinsland. Comparisons between ACE-FTS and ground-based measurements of stratospheric HCl and $ClONO_2$ loadings at northern latitudes. *Geophys. Res. Lett.*, 32:L15S08, 2005. doi: 10.1029/2005GL022396.

[113] B. Dils, M. de Mazière, J. F. Müller, T. Blumenstock, M. Buchwitz, R. de Beek, P. Demoulin, P. Duchatelet, H. Fast, C. Frankenberg, A. Gloudemans, D. Griffith, N. Jones, T. Kerzenmacher, I. Kramer, E. Mahieu, J. Mellqvist, R. L. Mittermeier, J. Notholt, C. P. Rinsland, H. Schrijver, D. Smale, A. Strandberg, A. G. Straume, W. Stremme, K. Strong, R. Sussmann, J. Taylor, M. van den Broek, V. Velazco, T. Wagner, T. Warneke, A. Wiacek, and S. Wood. Comparisons between SCIAMACHY and ground-based FTIR data for total columns of CO, $CH_4$, $CO_2$ and $N_2O$. *Atmos. Chem. Phys.*, 6:1953–1976, June 2006.

[114] A. Wiacek, K. Strong, N. B. Jones, J. R. Taylor, R. L. Mittermeier, and H. Fast. First detection of meso-thermospheric Nitric Oxide (NO) by ground-based FTIR solar absorption spectroscopy. *Geophys. Res. Lett.*, 33(L03811), 2006. doi: 10.1029/2005GL024897.

[115] T. E. Kerzenmacher, K. A. Walker, K. Strong, R. Berman, P. F. Bernath, C. D. Boone, J. R. Drummond, H. Fast, A. Fraser, K. MacQuarrie, C. Midwinter, K. Sung, C. T. McElroy, R. L. Mittermeier, J. Walker, and H. Wu. Measurements of $O_3$, $NO_2$ and temperature during the 2004 Canadian Arctic ACE validation campaign. *Geophys. Res. Lett.*, 32:L16S07, 2005. doi: 10.1029/2005GL023032.

[116] C. P. Rinsland, N. B. Jones, B. J. Connor, J. A. Logan, N. S. Pougatchev, A. Goldman, F. J. Murcray, T. M. Stephen, A. S. Pine, R. Zander, E. Mahieu, and P. Demoulin. Northern and southern hemisphere ground-based infrared spectroscopic

measurements of tropospheric carbon monoxide and ethane. *J. Geophys. Res.*, 103 (28):197–218, November 1998. doi: 10.1029/98JD02515.

[117] N. S. Pougatchev, B. J. Connor, N. B. Jones, and C. P. Rinsland. Validation of ozone profile retrievals from infrared ground-based solar spectra. *Geophys. Res. Lett.*, 23(13):1637–1640, 1996.

[118] H. von Storch and F. W. Zwiers. *Statistical Analysis in Climate Research.* Cambridge University Press, 1999. ISBN 0 521 45071 3.

[119] L. R. Brown, D. C. Benner, J. P. Champion, V. M. Devi, L. Fejard, R. R. Gamache, T. Gabard, J. C. Hilico, B. Lavorel, M. Loete, G. C. Mellau, A. Nikitin, A. S. Pine, A. Predoi-Cross, C. P. Rinsland, O. Robert, R. L. Sams, M. A. H. Smith, S. A. Tashkun, and V. G. Tyuterevk. Methane line parameters in HITRAN. *J. Quant. Spectrosc. Radiat. Transfer*, 82:219–238, 2003.

[120] J. Worden, S. S. Kulawik, M. W. Shephard, S. A. Clough, H. Worden, K. Bowman, and A. Goldman. Predicted errors of tropospheric emission spectrometer nadir retrievals from spectral window selection. *J. Geophys. Res.*, 109:9308, May 2004. doi: 10.1029/2004JD004522.

[121] J. R. Taylor, D. Wunch, C. Midwinter, A. Wiacek, J. R. Drummond, and K. Strong. Extended intercomparison of simultaneous ground-based FTIR observations at the Toronto Atmospheric Observatory. *J. Quant. Spectrosc. Radiat. Transfer*, 2006. In progress.

[122] D. Crisp, R. M. Atlas, F.-M. Breon, L. R. Brown, J. P. Burrows, P. Ciais, B. J. Connor, S. C. Doney, I. Y. Fung, D. J. Jacob, C. E. Miller, D. O'Brien, S. Pawson, J. T. Randerson, P. Rayner, R. J. Salawitch, S. P. Sander, B. Sen, G. L. Stephens, P. P. Tans, G. C. Toon, P. O. Wennberg, S. C. Wofsy, Y. L. Yung, Z. Kuang, B. Chudasama, G. Sprague, B. Weiss, R. Pollock, D. Kenyon, and S. Schroll. The

Orbiting Carbon Observatory (OCO) mission. *Adv. Space Res.*, 34:700–709, 2004. doi: 10.1016/j.asr.2003.08.062.